NASA
Technical Paper 1266

AVRADCO
Technical Report 78-50

A Laser Velocimeter Flow Survey Above a Stalled Wing

Warren H. Young, Jr., James F. Meyers,
and Danny R. Hoad

DECEMBER 1978

NASA

U.S. ARMY AVRADCOM

NASA
Technical Paper 1266

AVRADCOM
Technical Report 78-50

A Laser Velocimeter Flow Survey Above a Stalled Wing

Warren H. Young, Jr.
Structures Laboratory, AVRADCOM Research and Technology Laboratories
Langley Research Center
Hampton, Virginia

James F. Meyers
Langley Research Center
Hampton, Virginia

Danny R. Hoad
Structures Laboratory, AVRADCOM Research and Technology Laboratories
Langley Research Center
Hampton, Virginia

National Aeronautics
and Space Administration

**Scientific and Technical
Information Office**

1978

CONTENTS

SUMMARY

A laser velocimeter operating in the backscatter mode was used to survey the flow about a stalled wing installed in the Langley V/STOL tunnel. Mean velocities and magnitudes of velocity fluctuations were calculated from measurements of two orthogonal components of velocity. Free shear mixing layers above and below a large separated flow region were defined. Velocity power spectra were calculated at two points in the flow field.

The flow-field survey was carried out about a rectangular aspect-ratio-8 wing with an NACA 0012 airfoil section. The wing angle of attack was 19.4°, the Mach number was 0.148, and the nominal Reynolds number was 1×10^6.

The prominent features of the flow about the wing are a reversed velocity region; free shear mixing layers above, and behind the trailing edge, below the reversed velocity region; and a jetlike flow from below the airfoil lower surface.

INTRODUCTION

An extensive investigation into the process of dynamic stall by the Aeromechanics Laboratory, AVRADCOM Research and Technology Laboratories, summarized in reference 1, has delineated the features of the stalling process. The processes involved in recovery from dynamic stall, typical of the retreating blade of a helicopter rotor, are considerably less well understood. Because an understanding of dynamic stall recovery should benefit from a flow survey in the highly stalled regime of even a static airfoil, the present experiment was designed to define the separated flow field about a fully stalled, rigidly mounted airfoil.

Reference 2 summarizes a recent series of experiments that measured the mean flow about a static, balance mounted airfoil up to and beyond stall. The present experiment complements a recent investigation in the Langley high-speed 7- by 10-foot tunnel described in reference 3. The present experiment differs from the investigation of reference 3 primarily because that study was performed at a higher (0.49) Mach number, used surface pressure measurements, and had directional ambiguity in the velocity measurements. The principal finding of that test was the identification of a system of strong, discrete vortices. These vortices were generated near the airfoil crest at regular time intervals and were accelerated downstream by the flow over the airfoil upper surface.

The investigations at low angles of attack described by Hoad and coauthors in references 4 and 5 were performed immediately before the present experiment. The apparatus and data reduction were identical except for the velocity spectral measurements.

For the present test, a fringe-type laser velocimeter was installed in the Langley V/STOL tunnel. The laser velocimeter measured two components of velocity at 289 points in the flow field. At two points velocity power spectra were calculated. The measurements were carried out in a vertical plane through the wing center span. The wing had an NACA 0012 cross section and was set at an angle of attack of 19.4°. The nominal Reynolds number was 1×10^6. Because the wing was rectangular and had an aspect ratio of 8, the flow at the center span was treated as two-dimensional.

SYMBOLS

A_u	lag product for autocovariance calculation at lag time Δt, m^2/sec^2
C_i	number of velocity measurements in ith histogram interval as fraction of D
$C(\Delta t)$	autocovariance at lag time Δt, m^2/sec^2
c	wing chord, 0.3048 m
D	number of velocity measurements in one ensemble
D_{sv}	diameter of sample volume, m
D.R.	average data rate in ensemble, measurements/sec
E	excess, equation (5)
$H(\Delta t)$	number of lag products at lag time Δt
L_{fr}	fringe spacing, m
L_{sv}	length of sample volume, m
N	distance from airfoil measured along normal to surface, fraction of chord
N_o	value of N for which U_c is 0
R_c	airfoil Reynolds number, based on chord
S_R	skew, equation (4)
s	distance along airfoil surface measured from leading edge, fraction of chord
T	period, sec

T_R reset time of high-speed burst counter, sec

t time, sec

U velocity component, m/sec (see fig. 1)

U_R resultant velocity, $\sqrt{U_L^2 + V_L^2}$, m/sec

U_T tunnel wind speed, m/sec

U_c velocity component parallel to chord, m/sec

U_s velocity component parallel to airfoil surface, m/sec

U_∞ free-stream velocity (corrected for tunnel flow angularity), m/sec

V velocity component, m/sec (see fig. 1)

V_{fr} velocity of fringes due to Bragg cell, m/sec

X_c, Y_c coordinate axes relative to wing chord, m (see fig. 1)

X_f, Y_f coordinate axes relative to free stream, m (see fig. 1)

x_c distance downstream from wing leading edge along chord, m

x_f distance along X_f-axis, m

y_c distance above wing surface (measured perpendicular to wing chord), m

y_f distance along Y_f-axis, m

α_R flow angle, $\tan^{-1} \frac{V_f}{U_f}$, deg

α_s angle between N and vertical, deg

α_w wing angle of attack, deg

Δt interarrival time between two consecutive velocity measurements, sec

ΔU_i width of ith histogram interval, m/sec

$\Delta \tau$ minimum lag time, sec

δU_L statistical uncertainty in velocity component U_L, m/sec

δV_L statistical uncertainty in velocity component V_L, m/sec

$\delta \sigma$ uncertainty in calculation of standard deviation, m/sec

ε error, percent

η similarity variable for N, $\frac{N - N_o}{s}$

θ angle between crossing laser beams, deg

λ laser radiation wavelength, nm

σ standard deviation, m/sec

σ_R resultant of the two individual components of standard deviation, $\sqrt{\sigma_u^2 + \sigma_v^2}$, m/sec

Subscripts:

a experimental time-averaged data

B data corrected for Bragg bias and velocity bias

e ensemble averaged data

f directions parallel and normal to free stream (see fig. 1)

i ith measurement in ensemble

L directions of laser measurement (see fig. 1)

l lth measurement in ensemble

R resultant

u data in direction of U_L component

v data in direction of V_L component

A bar over a symbol denotes a theoretical time average.

APPARATUS

The laser velocimeter is described in reference 4. For completeness and to provide additional background for the velocity spectral measurements, a brief description is presented here.

Laser Velocimeter Optical System

A fringe-type laser velocimeter optics system operating in the backscatter mode was used for these tests, which eased the maintenance of optical alignment by using common components for both transmitting and collecting optics. The

backscatter mode allowed the use of simplified scanning mechanisms. The characteristics of the optical system are listed in table I.

Two components of velocity were measured. Unlike the method of reference 3, where polarization separation was used to make simultaneous measurements of both components, the present test measured the two components consecutively due to crosstalk. The two measurement directions were 45° above and below the horizontal as shown in figure 1. Each component was measured separately by splitting the laser output beam into three laser beams, one dedicated to each component and a third, shared. The two beams that measure a velocity component were aligned in the plane of that component direction and focused by a lens to the point, so that a fringe pattern was formed (fig. 2). As a micrometer-sized particle passed through the fringe pattern, light was scattered with varying intensity. The collecting optics intercepted part of this scattered light and sent it to a photomultiplier tube. The frequency of oscillation of the electrical signal output of the photomultiplier tube was proportional to the particle velocity divided by the fringe spacing L_{fr}. The fringe spacing was determined by measuring the angle between the two crossing beams θ and by applying the formula

$$L_{fr} = \frac{\lambda}{2 \sin (\theta/2)}$$

where λ is the wavelength of the laser light.

The fringes were caused to move at a speed of 132 m/sec by a 5-MHz Bragg cell placed in the third, shared laser beam. The Bragg cell eliminates the directional ambiguity of the experiment of reference 3.

The argon-ion continuous wave laser and the laser velocimeter optical system were located in the tunnel test chamber immediately outside the test section wall. The laser was operated with an output power of 4.0 watts using the 514.5-nm wavelength. The laser velocimeter had a focal length of 3.8649 m (sufficient to reach the center span location on the wing) and a collecting solid angle of 0.00108 sr. The sample volume was 2.29 cm long with a diameter of 0.314 mm yielding 12 stationary fringes with a fringe spacing of 26.5 μm.

The optical system was mounted on a movable table to allow movement of the sample volume in the horizontal and vertical directions under computer control. The sample volume location could be measured to within 1 mm. The overall assembly, including the traversing system, laser, and optical system, is shown in figure 3.

Laser Velocimeter Electronics System

The electronics system is discussed in greater detail in reference 4. A preliminary discussion of some of the effects of the electronic system on the velocity measurements is contained in reference 6.

The interface between the optics system and electronics system was an S-20 photomultiplier tube and signal conditioning electronics. The laser velocimeter data acquisition system, shown as a block diagram in figure 4, measures the frequency contained in each signal burst from the optics system, converts the frequency to velocity, develops velocity histograms, computes the mean velocity and standard deviation of the velocity fluctuations, and stores the raw velocity data and tunnel parameters on magnetic tape for later, more complete data reduction.

High-speed burst counter.- A burst is the transient output of the photomultiplier that is caused by the passage of one particle through the sample volume. The high-speed burst counter is a device designed to measure the period of a high-frequency signal (1 kHz to 100 MHz) contained in a burst of the type received from a laser velocimeter. An idealized burst received from the laser velocimeter is illustrated in figure 5(a). The pedestal (dc bias) is removed by high-pass filters so that the burst is symmetric about 0 volts (fig. 5(b)). A double threshold comparator is used to convert the burst into a digital pulse train (fig. 5(c)). In order for the comparator to work, the signal must cross the positive threshold before crossing 0 volts with a negative slope, and the signal must cross the negative threshold before crossing 0 volts with a positive slope. No other combination will operate the comparator. The first pulse in the digital pulse train is used to clear the counter circuits, the second is used to arm the counters, and the third triggers the counters to begin counting pulses from the 500-MHz reference clock. When the 10th digital pulse occurs, the counters are halted. Thus, the counter now contains the measurement of the period average of eight signal cycles based on a reference clock of 500 MHz, yielding a period average measurement with a resolution of 2 nsec.

Data gathering system.- The data from the high-speed burst counter is input to the laser velocimeter autocorrelation buffer interface (described in appendix A of ref. 4) which stores the velocity data and measures the time between the arrival of each datum and the immediately preceding datum (i.e., interarrival time) to a resolution of 0.1 μsec. The interarrival time is recorded only if it is less than 0.655 sec. When either 4096 data points are gathered or 1.0 min of measurement time elapses, the data gathering process halts and the data are sent to the computer. The raw data are converted to velocity values in the computer and stored, together with the interarrival times, on magnetic tape. The statistical quantities (e.g., mean, standard deviation, and skew) are computed on-line and are output on a line printer together with the sample volume location, tunnel parameters, and time of day. The histogram of the data record is determined and output on-line on a cathode ray tube. The total time required for measurement, data transfer, storage, computation, and output is less than 2 min.

Wing and Wind Tunnel

The model wing was installed horizontally in the Langley V/STOL tunnel. The test section was closed and had a cross section of about 4.4 m by 6.6 m. The clear-tunnel free-stream measurements of reference 4 established a vertical

low angularity of 0.6°. The velocity measurements have been referenced to the free-stream coordinate axes X_f and Y_f rather than to the horizontal and vertical.

The model wing was aerodynamically similar to the model in reference 3 and is shown in figure 6. The model was an untwisted, unswept, untapered wing with an aspect ratio of 8 and a 0.3048-m chord. Two mounts, each at 50 percent semispan, were used to stiffen the model and to minimize dynamic response. All the measurements were made in the plane of wing center span so that the spanwise velocity was assumed negligible. The airfoil cross section was an NACA 0012 and no transition strip was used. The relationship between the airfoil section, free-stream direction, and the two laser velocimeter measurement directions is shown in figure 1.

For data measurements near the wing leading edge, the laser beams were angled a few degrees downstream. For the measurements near the trailing edge, the optics system was angled upstream. Due to the limitations on the vertical traverse of the laser velocimeter optics system, it was necessary to raise the wing on shim blocks for one series of measurements. The original angle of attack was 19.40° and, after the wing was raised, it was reset to 9.43°. The nominal angle of attack is taken as 19.4°. The accuracy of the angle-of-attack measurement was estimated to be ±0.03°. Thus, the maximum change in angle of attack caused by raising the wing was 0.09°.

The nominal tunnel conditions were a tunnel velocity of 51 m/sec, a Mach number of 0.148, and a Reynolds number of 1×10^6. Throughout the test the tunnel velocity varied from 50.6 to 51.9 m/sec, and Reynolds number varied from 0.97×10^6 to 1.04×10^6. To obtain more accurate nondimensionalization, the tunnel conditions were recorded for each run.

The tunnel flow was seeded by a smoke generator located in the tunnel settling chamber upstream of the screens. The smoke generator vaporized kerosene which condensed in the tunnel airflow to form a smoke plume of kerosene seed particles.

A limited number of video tape recordings of the smoke flow about the wing center span were made at a reduced tunnel speed of about 15 m/sec. Motion pictures were used to produce consecutive photographs for flow visualization.

DATA ACQUISITION AND REDUCTION

Statistical Quantities

The data reduction performed on-line consisted of calculation of the velocity mean, standard deviation, skew, excess, statistical uncertainty in the mean, and statistical uncertainty in the standard deviation. Also, to aid in the interpretation of the data, velocity histograms (a discrete approximation of the velocity probability density function) were computed and plotted on-line on a graphics cathode ray tube.

The mean of each velocity data ensemble U_e approximates the theoretical time-averaged velocity $\bar{U}$ under the following assumptions:

1. The period of all the Fourier components of the velocity fluctuations is much less than the time of measurement (i.e., the velocity sample is representative of a stationary condition in time at the measurement location).

2. The laser velocimeter is equally likely to measure all velocity magnitudes.

3. The number of velocity measurements D is large to minimize the statistical uncertainties.

Under the same assumptions, the standard deviation σ approximates the root-mean-square value of the deviation from the average velocity. That is

$$\sigma^2 \approx \lim_{T\to\infty} \frac{1}{T} \int_0^T \left[U(t) - \bar{U}\right]^2 dt \tag{1}$$

The formulas for the calculation of the ensemble mean and the square of the standard deviation (variance) are

$$U_e = \frac{\sum U_i}{D} \tag{2}$$

and

$$\sigma^2 = \frac{\sum (U_i - U_e)^2}{D} \tag{3}$$

Except for bimodal histograms, the first four moments of the ensemble give a quantitative measure of histogram shape. The higher ensemble moments were computed for skew S_R and excess E by applying the following formulas:

$$S_R = \frac{\sum (U_i - U_e)^3}{D\sigma^3} \tag{4}$$

$$E = \frac{\sum (U_i - U_e)^4}{D\sigma^4} - 3 \tag{5}$$

The statistical uncertainties in U_L and σ_u for a 95-percent confidence limit due to the third approximation (finite number of measurements in the ensemble) were calculated (ref. 7) as

$$\delta U_L = \frac{2\sigma_u}{\sqrt{D_u}}$$

and

$$\delta\sigma_u = \sigma_u\sqrt{\frac{2}{D_u}\left(1 + \frac{E_u}{2}\right)}$$

where E is the statistical excess computed from the data ensemble. The calculations of δV_L and $\delta\sigma_v$ were performed in a similar fashion.

The error caused by the second assumption was evaluated by recomputing the velocity mean compensated for velocity weighting. Reference 8 shows that if the seed particles are uniformly distributed in the flow, higher velocity flow passes more gas per unit time (and thus more particles) through the sample volume than lower velocity flow. Conversely, use of a Bragg cell weights the ensemble toward the lower velocities since a low-velocity particle remains in the sample volume for more time (e.g., a stationary particle yields an infinite number of measurements). Using the equation for A_i derived in the appendix, the ensemble mean was compensated for both one-component velocity bias and Bragg bias by calculating the mean velocity as

$$U_B = \frac{\sum A_i U_i}{\sum A_i} \tag{6}$$

where

$$A_i = \frac{10L_{fr} + T_R V_{fr} + T_R U_i}{D_{sv}(V_{fr} + U_i)}$$

The bias problem can be avoided by approximating the definition of the time-averaged mean $\bar{U}$ by a trapezoidal quadrature. The definition of $\bar{U}$ is

$$\bar{U} = \lim_{T\to\infty} \frac{1}{T}\int_0^T U(t)\, dt$$

and the approximation is

$$U_a = \frac{\sum (U_i + U_{i+1})\, \Delta t_i}{2\sum \Delta t_i} \tag{7}$$

where Δt_i is the interarrival time between measurements i and i + 1. The error for the quadrature approximation for randomly sampled data has not been formulated.

Although the skew and excess are not as readily interpreted in terms of the time variation of velocity as the mean or standard deviation, they have been calculated for several flows. For example, in reference 9 large positive values of skew were found on the high-speed side of a free shear mixing layer and large negative values were found on the low-speed side. The skew and maximums in excess were attributed to intermittency at the edge of the mixing layer.

These statistical quantities can be interpreted visually by viewing the probability density function of the velocity field at the measurement location. The probability density function was approximated by placing the velocity measurements in histogram form. That is, the measurements of each velocity component were sorted into velocity bins of width ΔU_i. The ordinate of the histogram C_i is the percentage of measurements within the ensemble which lie between $U_i - (\Delta U_i/2)$ and $U_i + (\Delta U_i/2)$.

Instrument Precision

The overall precision of the measurement of a single seed particle velocity is obtained by determining the accuracies of all variables in the system which affect the accuracy of each velocity measurement. Reference 3 gives these error sources as the cross-beam angle measurement, diverging fringes, time jitter, clock synchronization, and quantizing error. The cross-beam angle measurement error is an unknown bias error based on the uncertainty in locating the center of each laser beam when the cross-beam angle is determined. This error is estimated to yield a ±1.12-percent uncertainty in the measured velocity. The diverging fringes, resulting from the difference in location of the focus point of each laser beam and the crossover point, yield both a bias error (-0.50 percent) and a random error (±0.37 percent).

In the present system a double threshold technique with zero crossing detection is used which eliminates the time jitter error. The clock synchronization error (time difference between the start pulse of the high-speed burst counter and the first reference clock pulse that is counted) yields a bias error (0.29 percent) and a random error (±0.29 percent). The quantizing error is nonexistent in the present test since the 10-bit digital output from the high-speed burst counter is not truncated. These errors yield a total instrument precision of -1.33 percent to 0.91 percent bias and ±0.47 percent random uncertainty.

In large velocity gradients, measured velocity errors may occur if the measurement point is not at the desired location. The two-component mechanical traversing system had a placement uncertainty of ±1 mm which yielded a worst case (based on the measured velocity flow field) uncertainty of ±2 percent.

Tunnel Seeding

The tunnel was seeded by a kerosene vaporizer mounted upstream in the settling chamber. The measured particle size obtained using the technique described in reference 3 is shown in figure 7(a). A computer simulation by Meyers (ref. 10) of the laser velocimeter and the scattering intensity from the kerosene particles gave the probability of a successful measurement of velocity if a single kerosene particle passes through the sample volume. Figure 7(b) presents this probability. The product of the probability of occurrence of a particular particle size (fig. 7(a)) times the probability of a measurement for that particle size (fig. 7(b)) is the fraction of measurements caused by that particle size (fig. 7(c)). Most of the measurements were made from particles about 3.5 μm in diameter, although a significant number were made from particles about 1.9 μm in diameter. The particle drag equations of Walsh (ref. 11) were used to plot the tracking errors shown in figure 8. The dynamic response of the 1.9-μm particles is accurate up to 1000 Hz but the 3.5-μm particles have acceptable particle tracking errors up to only about 300 Hz. Since the frequency range of interest, based on the pressure frequency spectra of reference 3, should lie below 300 Hz, the particle tracking errors are acceptable.

Velocity Frequency Spectra

Technique.- The calculation of velocity power spectra from laser velocimeter measurements is in a preliminary stage of development, and no error analysis of the spectra is available. The results should be viewed as qualitative. During the present test, two locations were chosen for preliminary spectra measurements to try to find the proposed discrete shed vortices found in reference 3.

The calculation of the velocity power spectra follows the technique developed by Mayo (ref. 12). The technique is based on the Fourier transform of the autocovariance function developed from the measurement ensemble. The autocovariance $C(m\Delta\tau)$ of a uniformly sampled signal is found by using the equation

$$C(m\Delta\tau) = \lim_{D\to\infty} \frac{1}{2D+1} \sum_{n=-D}^{D} V_n V_{n+m}^*$$

where V_n is the nth value in an ensemble of D values, the $*$ denotes the complex conjugate, and $\Delta\tau$ is the uniform lag time. However, the measurement of velocity using a laser velocimeter is a Poisson distributed random sample in time of velocity and not a uniform sample. The problem of randomly sampled data is handled by measuring the time between velocity measurements and by using these times to determine the delay function. First, since the autocovariance function is desired, the ensemble mean is calculated and subtracted from each velocity measurement. Then two arrays are established: the first is $A_u(m)$ to sum the paired products $V(t_i)\ V(t_i+m\Delta\tau)$ (the complex conjugate notation

is dropped since the velocity measurements are real) and the second is $H_u(m)$ to sum the number of occurrences of the time delay $m\Delta\tau$, where $\Delta\tau$ is the minimum time delay selected. For example, if the time between two measurements is $t_i - t_l$, then the delay increment is defined by

$$m = \frac{t_i - t_l}{\Delta\tau} + 0.5$$

where m is the integer obtained by truncation of the fraction. If m is within the range of the desired autocovariance function, 511 in the present test, the array location $H_u(m)$ is incremented by 1 and the array location $A_u(m)$ is incremented by the velocity product $V_i V_l$.

When the measurement ensemble is processed in this manner, the autocovariance function is found by using the equation

$$C(m\Delta\tau) = \frac{A_u(m)}{H_u(m)}$$

for $m = 0, 1, \ldots, 511$. This expression has been shown to be an unbiased estimate of the autocovariance function (ref. 12) if the true mean velocity has been subtracted from the data.

The resulting autocovariance function is folded so as to form an even function, and is multiplied by a Bartlett (i.e., triangular) window function. A fast Fourier transform yields the velocity power spectra measurement.

Measurements.- The data from the laser velocimeter high-speed burst counters were gathered by a digital buffer interface described in detail by Clemmons in appendix A of reference 4. This interface also measured the time between measurements with a triple-range clock which automatically shifted clocks to yield a total measurement time range from 1.0 μsec to 0.655 sec, with resolutions of 0.1 μsec, 1.0 μsec, and 10.0 μsec depending on the clock selected. When 4000 velocity measurements were gathered, about 10 sec for the spectra tests, the data were transferred to the minicomputer for processing and storage.

PRESENTATION OF RESULTS

The flow field is arbitrarily divided into regions for purposes of the discussion of results. There is no clear boundary between the regions and the division is only for convenience of detailed discussion. The leading-edge region is upstream of the nose of the airfoil. The crest region is above the airfoil from the leading edge to about the quarter chord. The mixing layer region is above the airfoil and downstream of the quarter chord. It includes a reversed velocity region, a free shear mixing layer, and an outer flow above

both. The trailing-edge region includes the interaction between the flow from the upper and lower surfaces.

All 289 runs (ensembles of measurements of both velocity components at one location) are organized into scans as shown in figure 9. The scan lines (except scan 19) were designed to be either perpendicular to the wing surface or perpendicular to the extended chord line before or behind the wing. The runs in each scan, tunnel conditions, and the location of each scan line are shown in table II. The values shown are averages taken over the runs in each scan.

The discussion of the results of this investigation is presented in the following order:

Flow-field overview (figs. 10 to 14)

Flow visualization (figs. 15 to 18)

Basic data:
  Histograms (figs. 19 to 25)
  Statistical moments (figs. 26 to 44)

Velocity frequency spectra (figs. 45 to 48)

Leading-edge region (figs. 19 and 20)

Crest region (figs. 20, 21, and 49)

Mixing layer region (figs. 50 to 59)

Trailing-edge region (figs. 60 to 64)

Wake formation

DISCUSSION OF RESULTS

Flow-Field Overview

Plots of the entire flow field are presented in figures 10 to 14. Figure 10 is an arrow plot of the mean velocity field. The tail of each arrow is a measurement point. The length and direction of each arrow defines the magnitude and direction of the resultant mean velocity vector. The most prominent feature of the flow is the large region of reversed flow. Since measurements are not available close enough to the airfoil upper surface and since transition is free, it is not possible to pinpoint the origin of the separated region. The origin appears to lie between scans 4 and 6. The upper boundary of the separated region is a region of high velocity gradients. The lower boundary behind the airfoil is a region of even larger velocity gradients caused by high-velocity flow coming from the lower surface of the airfoil.

Other aspects of the flow field are presented in figures 11 to 14. These figures were constructed by using a spline fit to each scan, spline fits between scans, and linear interpolation between points on a fine grid. The contour of zero resultant mean velocity in figure 11 outlines the reversed velocity region. The negative values denote flow toward the airfoil leading edge.

The angle of the resultant mean velocity with respect to the free stream is shown in figure 12. Large variations in angle appear in the reversed flow region. The flow angle of the outer flow (outside the reversed flow region and areas of high shear) varies smoothly from positive angles around the leading edge and airfoil crest to negative angles over the aft part of the airfoil. This outer flow is more easily visualized by the mean flow streamlines in figure 13.

Figure 14 shows contours of resultant standard deviation about the mean σ_R which is given by $\sigma_R^2 = \sigma_u^2 + \sigma_v^2$. The value of σ_R^2 approximates $\overline{U^2} + \overline{V^2}$ where U and V are two perpendicular components of the unsteady velocity variation with time and the bar denotes a time average. Thus, σ_R can be interpreted as a two-dimensional turbulent intensity. The largest values occur in the turbulent regions of high velocity gradients. Relative maximum values of resultant standard deviation occur above the reversed flow region. In the reversed flow region, the unsteady part of the velocity is comparable in magnitude to the mean velocity.

Flow Visualization

A more extensive view of the flow pattern was provided by the vapor screen flow visualization setup shown in figure 15. A vertical sheet of laser light illuminated the plane of the wing center span. The smoke was photographed by a tunnel sidewall television camera placed slightly behind and above the wing trailing edge. Figure 16 shows that the camera placement caused the wing tip to hide the wing leading edge, but the wing upper surface is clearly shown (the bright line is the reflection of the light sheet). To increase the smoke density, tunnel speed was reduced to about 15 m/sec. The entire wake region fluctuated rapidly, but observers estimated the average wake closure point to be about one chord length behind the trailing edge and near the height of the leading edge.

The large changes in the smoke pattern are demonstrated by figures 17(a), (b), and (c). Consecutive photographs of the television picture (at a nominal frame time of 40 msec) show the wake region filling with smoke. Investigators observed that the smoke in the wake region came forward from the wake closure region. The photograph for figure 17(d) was taken a few seconds after the smoke plume had moved well above the airfoil. Below and immediately above the wake region the smoke has been convected downstream, but smoke remains in the wake region. The poor convective transfer of smoke between the outer flow and wake region also occurred at the tunnel test speed of 51 m/sec. This is demonstrated by figure 18 which shows that low average data rate contours coincide with the upper boundary of the region of low smoke density shown in figure 16.

The flow visualization indicated that much of the unsteadiness in the flow affected large regions of the flow. The large changes observed in the boundaries of the wake region also indicate that one of the sources of unsteadiness in the flow was large-scale fluctuations.

Basic Data

Statistical moments.- The histograms for each run are shown in figures 19 to 25. At the beginning of each figure, the measurement location is indicated by the tail of a mean velocity vector. The statistical moments for some of the runs are plotted in figures 26 to 44 and are listed in table III. The curves for the higher moments, skew and excess, do not show as much consistency and smoothness as the velocity and standard deviation curves. This may be attributed partly to the decrease in accuracy expected for the higher moment calculations. Table III gives three values each for U_L and V_L. The means of the ensemble averaged data, $U_{L,e}$ and $V_{L,e}$, are compared to the means found by accounting for the velocity bias, $U_{L,B}$ and $V_{L,B}$. The differences are usually less than the statistical uncertainties due to the finite number of measurements, $\delta U_{L,e}$ and $\delta V_{L,e}$, and much less than the standard deviations, σ_u and σ_v. Therefore, the values $U_{L,e}$ and $V_{L,e}$ were used throughout this report as the calculated values for U_L and V_L. The time-averaged velocities, $U_{L,a}$ and $V_{L,a}$, are also tabulated. The deviations of the time-averaged velocities from the ensemble means are significant in the regions of low velocity (fig. 11), large standard deviation (fig. 14), and low data rate (fig. 18). Even though the time average is a more direct calculation than the ensemble mean, it is marred by several defects. At data rates less than about 50 measurements per second, the likelihood of exceeding the maximum time of the interarrival clock becomes significant. When the maximum clock time of 0.655 sec is exceeded, the clock resets, causing a break in the continuous timing. This break forces the calculation of a series of integrals and loss of accuracy. The time-averaged and ensemble mean values agree well (typically within 1 percent) for runs with high data rates (above 200 per second). Although no error analysis has been developed for the time-average calculation for randomly sampled data, the calculation appears to be accurate for high data rates at least.

The basic data are converted into more convenient forms in table IV. The velocities are converted into free-stream coordinate components and into a resultant velocity. The location of the measurement is shown in three coordinate systems: free-stream, airfoil chord oriented, and airfoil surface coordinates.

Data consistency.- The nominal tunnel test conditions were $U_T = 51$ m/sec, $M_T = 0.148$, and $R_C = 1 \times 10^6$. The tunnel velocity deviation from the nominal over the 5-day duration of the test was less than ±2 percent and, in addition, many of the results are normalized by the tunnel velocity which was measured by a pitot probe when the laser velocimeter data were acquired. The Reynolds number, however, deviated as much as ±4 percent from the nominal value, and no normalization procedure is available.

The largest inconsistency in the data was caused by raising the wing to change the scan mechanism limits as shown in figure 9. The process of raising the wing increased the angle of attack less than 0.09°. Scans 13, 14, 15, and 19 were interrupted by the change. The resulting discontinuity in the measurements is apparent in figure 10 for scan 19. Runs 270 and 273 to 289 were made for the raised condition. Even though the intermeshed points were removed before the contour plots were made, the discontinuity is also obvious in figures 11 to 14.

Velocity Frequency Spectra

The frequency content of the velocity was measured at two points in the flow field using the technique presented previously. The two points, marked by crosses in figure 14, were chosen to be near the mixing layers above the upper surface and behind the trailing edge and to be in regions where high data rates were more easily obtainable. Both U_L and V_L components were measured. The results are presented in figures 45 to 48.

Each spectrum is based on 30 000 or more measurements. The autocovariance function was based on 512 time delays with a $\Delta\tau$ of 0.25 msec. The value of the autocovariance function for each time delay was based on 4000 or more paired products (figs. 45(a), 46(a), 47(a), and 48(a)). The measured power spectra shown in figures 45(c), 46(c), 47(c), and 48(c) have a frequency resolution of 4 Hz and a frequency range from 0 to 1.0 kHz. The high peaks in the zeroth frequency, or dc value, may indicate that the ensemble means that were subtracted from the data were not the true velocity means.

The points above the mixing layer show large excursions in amplitude, but the trend appears to be declining amplitude as frequency increases. The calculation scheme used, i.e., Fourier transform of the autocovariance, does not force the spectral amplitude to be positive. Any negative values that occur are probably due to statistical variabilities in the calculations based on a limited amount of data. At this time, the relationship of spectral uncertainty as a function of particle arrival rate, number of measurements, and spectral bandwidth is unknown. Thus these spectral measurements are viewed for only a qualitative indication of the frequency content in the velocity flow field. It is tentatively concluded that there are no dominant, discrete frequencies present and that most of the flow unsteadiness is concentrated in the frequencies below 0.4 kHz. The results of reference 3 showed a discrete frequency that corresponded to a Strouhal number of 0.6 based on the length $c \sin \alpha$. Therefore, the large amplitude response expected at 0.3 kHz was not found in the present experiment.

For the points near the trailing-edge wake, an even sharper decline in amplitude with frequency is apparent. Most of the power is contained in frequencies below 0.2 kHz.

Leading-Edge Region

The mean flow velocities for scans 1, 2, and 3 are affected in magnitude and direction by the presence of the wing. The histograms (fig. 19) show more detailed trends. The V_L component histograms are skewed in a positive sense (toward higher velocities), but most of the U_L components tend to have broader, shorter histograms in the region above the airfoil. The histograms become narrower and taller (i.e., smaller standard deviation) toward the bottom of the scans. The contour plot of resultant standard deviation (fig. 14) shows that there is more unsteadiness in the flow near the airfoil leading edge and that away from the airfoil surface, the unsteadiness decreases.

The histograms of the scans below the airfoil (scans -4, -5, and -6 in figs. 20 and 21) show similar trends. The V_L components become particularly broad near the airfoil lower surface. The transition to broad histograms occurs at about run 82 in scan -6. Runs 83 and 84 have bimodal or double-peaked histograms. This pattern indicates that there are two flow states with different velocities and that the flow alternates between the two states. A precursor of these bimodal histograms can be seen in scan -4 (the V_L components of runs 59 and 60) but not in scan -5. The flow state with the higher velocity is apparently dominant closer to the airfoil surface. Thus, the bimodal histograms are not caused by the penetration of an oscillating separation bubble, and no discrete vortices are passing through the region. The bimodal histograms in the present case are probably associated with unsteady fluctuations in the airfoil circulation which may result from unsteady separation phenomena.

Crest Region

The crest region encompasses scans 4 to 9; it is the transition between the leading-edge and mixing layer regions. The crest region histograms (figs. 20 and 21) continue many of the trends observed in the leading-edge region. The positive skew of the V_L component continues through scans 4, 5, and 6 for the histograms farthest above the airfoil surface. Scans 6 to 9 show less skew of the V_L component and show negative skew of the U_L component.

As the airfoil surface is approached, the histograms become broader. This trend is more pronounced for the downstream scans. Some of the histograms nearest the surface are bimodal. Run 51 of scan 4, run 66 of scan 5, run 79 of scan 6, and run 112 of scan 9 are bimodal in the V_L component. Run 80 and runs in scans that are farther downstream become extremely broad near the airfoil surface. This rapid change in standard deviation with height causes a concentration of contour lines in figure 14. The mean flow angles also increase rapidly (fig. 12) in this region. Figure 49 shows velocity profiles of the magnitude of the component parallel to the airfoil surface. The vertical scale in figure 49 represents the normal distance from airfoil surface.

Figure 49, together with the histograms, shows that the flow field in the crest region contains a layer of high velocity gradients and that the flow is very unsteady within that layer. The layer begins with, or is preceded by, a

region with bimodal histograms which are characteristic of two alternating flow states. Aft of scan 6, the height of the layer above the airfoil surface increases rapidly, and the thickness of the layer also increases. The increase in thickness is evident in the spreading in the downstream direction of the contour lines of both resultant mean velocity (fig. 11) and resultant standard deviation (fig. 14). It can also be inferred that the flow beneath the layer is reversed (i.e., there is a velocity component toward the nose of the airfoil surface) in the area near the airfoil surface and aft of the airfoil crest. The crest region contains the origin of the free shear mixing layer and the reversed velocity region. The growth in height of both continues into the mixing layer region.

Mixing Layer Region

Flow evolution for a typical scan.- The histograms of scan 13 are typical of the scans in the mixing layer region. The arrow plot in figure 10 indicates that run 155 was located in the far-field, inviscid flow. However, the histograms for run 155 show that the flow at this point is much more unsteady than it is at the uppermost points in the leading-edge and crest regions. The histograms become broader, and the component mean velocities smaller, from runs 155 to about runs 162 or 163. As more of the histogram appears in the negative velocity region (runs 163 to about 167) the broadening decreases. The mean velocity is in the reversed direction for runs 167 to 173.

General features of the mixing layer.- The contours of constant resultant mean velocity in figure 50 were drawn by a linear interpolation over triangles with vertices at the run points. The continuity of the mixing layer from the crest region into the mixing layer region can be seen. Contours of constant resultant standard deviation are shown in figure 14. The unsteadiness of the reversed velocity region is comparable in magnitude to the magnitude of the resultant mean velocity. Figures 51 and 52 are contour plots of the skew. Although the values of skew and excess do not fall into as well-defined patterns as the velocity and standard deviation, the locus of relative extremums on each plot falls in the mixing layer. The extremums are summarized in figure 53. The minimums of excess fall between the contour lines $U_R = 0.1$ and 0.3. The maximum values of resultant standard deviation and skew generally fall between $U_R = 0.5$ and 0.8.

Similarity in the mixing layer.- The general features of the mixing layer in the context of the entire flow field have been outlined. In order to isolate the mixing layer region and to analyze it in more depth, examination of only the component of velocity parallel to the airfoil mean chord line U_C is used. The other two alternatives, resultant mean velocity and velocity parallel to the airfoil surface, have proved less useful.

The chordwise velocity profiles are presented in figure 54. The similarity in the shape of the profiles for scans 10 to 15 resembles that of the development of a free shear mixing layer. The data for scan 19 were taken along a vertical line; the discontinuity in the profile was caused by the angle-of-attack change after raising the wing. In order to examine the similarity of the profiles, three changes were made in the ordinate. First, the distance

from the airfoil surface measured along a normal to the surface N was used. The second adjustment compensated for the curvature of the mixing layer by referencing the ordinate to N_o (the value of N at the line $U_c = 0$ as shown in fig. 55). The distance $N - N_o$ is thus the height, along the scan line, from the point where $U_c = 0$. The final adjustment to the ordinate accounted for the increase in height of the mixing layer in the downstream direction.

Figure 56 shows two attempts to form a similarity parameter based on distance downstream s. The first attempt was based upon the observation that the theoretical spreading rate of some laminar free shear mixing layers is proportional to the square root of the distance downstream divided by a Reynolds number. Satisfactory coalescence of the velocity profiles (with the exception of part of scan 19) was achieved by referencing s to a virtual origin of 0.25 (the quarter chord). The second attempt used the similarity parameter $\eta = \frac{N - N_o}{s}$. Although there is no significant improvement in the coalescence, this parameter was judged more convenient for the following reasons: (1) This parameter is more appropriate for turbulent flows. (2) The origin of the mixing layer is apparently at neither $s = 0.25$ nor $s = 0$, but as indicated in the discussion of the crest region, it is closer to the latter. Measurements near enough to the surface to define the $U_c = 0$ (or $U_s = 0$) line in the crest region are necessary to define a more precise value for the virtual origin. (3) The simpler parameter seems preferable because of the limited length of the mixing layer available for analysis, the inconsistency of the data, and the deterioration of the coalescence for the downstream scans.

Figure 57 is an expansion of figure 56(b). The similarity of the profiles of resultant standard deviation (fig. 58) and skew (fig. 59(a)) deteriorate for the downstream profiles. Most of the scans have maximum values of resultant standard deviation near $\eta = 0.2$ and maximum values of skew between $\eta = 0.1$ and 0.2. The profiles of the U_L and V_L components of excess (fig. 59(b)) show some similarity.

Summary of mixing layer characteristics.- The following conclusions have been drawn from the examination of the mixing layer region: (a) A free shear mixing layer originates near the crest of the airfoil and forms the upper boundary of a highly unsteady reversed velocity region. (2) The similarity parameter η is adequate, within the limited length of the mixing layer region and consistency of the data, for coalescence of the profiles of mean velocity and resultant standard deviation. (3) The resultant standard deviation (which is a measure of the unsteadiness of the flow) is largest in the upper part of the mixing layer, typically at about $U_c = 0.7$. The maximum resultant standard deviation increases from a value of about 35 percent of the free-stream velocity at the beginning of the mixing layer region to about 43 percent for the downstream scans.

Trailing-Edge Region

The velocity vectors behind the airfoil in figure 10 show that there is an abrupt transition between the reversed velocity region and the jetlike flow

from the lower side of the airfoil. The mean flow streamlines (fig. 13) show that the jet is entraining the air from the reversed velocity region and sweeping it downstream.

The steps in the transition from reversed flow to jetlike flow are apparent in the histograms for scan 19 (fig. 25). The histogram for run 282 is in the reversed velocity region. The transition begins at runs 285 and 286 as the mean velocities increase. Run 285 shows a continuing increase in mean velocity and a very large increase in flow unsteadiness. The mean velocities have near-maximum values at run 286, and the flow unsteadiness has begun to decrease toward the rather small values seen at run 287. The histogram shapes at run 287 have the appearance of the histograms upstream of the airfoil. The order of events as the scan is traversed from top to bottom is an increase (from negative to positive values) in mean velocity, a maximum in unsteadiness, and finally the continuing increase in mean velocity and decrease in unsteadiness to values approaching the free stream.

In figure 60, an enlargement of the velocity vectors is presented to allow a detailed examination of the transition region behind the trailing edge. The jetlike flow appears initially to follow the direction of the tangent line to the lower surface and then to curve upward. The height of the transition region increases rapidly in the downstream direction. Scan 16 shows that just behind the trailing edge the flow makes the transition from fully reversed to fully downstream within a height of less than 3 mm. The flow unsteadiness also increases rapidly in the downstream direction (fig. 61). The region of high velocity gradient coincides with the largest values of resultant standard deviation. Figure 62 contains the chordwise velocity profiles plotted against vertical height for the three scans that traverse the transition region. The profiles are characteristic of a free shear mixing layer. The length surveyed in the downstream direction is too small to assess the profile similarity quantitatively. Qualitatively, the velocity profiles and the profiles of resultant standard deviation (fig. 63) show similar shapes from scan to scan. Even the profiles of skew (fig. 64) show considerable similarity. There is a maximum in each skew profile above $y_f/c = 0$ and a minimum below. This is consistent with the skew profile pattern in the free shear mixing layer above the reversed velocity region.

The free shear mixing layer behind the trailing edge forms the boundary between the reversed velocity region and the jetlike flow from the lower side of the airfoil. The major characteristics of the trailing-edge region are as follows: (1) The high-speed flow from the lower surface is initially parallel to the tangent line of the lower surface. (2) The high-speed jetlike flow entrains and accelerates the fluid in the reversed velocity region in a free shear mixing layer. (3) The flow unsteadiness was maximum in the part of the mixing layer with the largest velocity gradient, and the maximum resultant standard deviation increases in the downstream direction. (4) The thickness of the mixing layer increases in the downstream direction. The profiles of mean velocity, resultant standard deviation, and skew show similarity of shape along the length of the mixing layer.

Wake Formation

The flow visualization results and figure 13 indicate that the mixing layers above the airfoil and behind the trailing edge continue downstream to near a wake closure point. The reversed velocity region is expected to continue downstream and form part of the core of the wake. The boundaries of the wake core and the smoke-free region from the flow visualization appear to be nearly coincident.

Reference 3 identified discrete vortices above the airfoil by the presence of a pattern of double-peaked histograms near the airfoil crest and by a discrete frequency in the surface pressure. In addition, cross-correlation of the pressures along the chord indicated the convection of the discrete vortices. In the present test no discrete frequency peaks were identified in the velocity spectra above the airfoil, and no pattern of double-peaked histograms was found. These failures do not preclude the existence of discrete vortices because the failures could be due to the vortex convection being random in time and space. Cross-correlations, which can detect random, discrete vortices, are not available in the present test. Thus the results of the present test neither support nor refute the presence of discrete convected vortices in the mixing layer.

CONCLUSIONS

A flow survey of the flow field above a stalled wing was conducted by means of a directionally sensitive laser velocimeter that used the backscatter mode of operation to measure two components of velocity at 289 points. Ensemble statistics were calculated together with the statistical uncertainties in the means and standard deviations, and histograms were formed for trend analysis. At two locations sufficient data were taken to form velocity frequency spectra. The model was an aspect-ratio-8 wing tested in the Langley V/STOL tunnel at an angle of attack of 19.4°, a nominal Reynolds number of 1×10^{6}, and a Mach number of 0.148.

The prominent features of the flow about the wing are a reversed velocity region; free shear mixing layers above and, behind the trailing edge, below the reversed velocity region; and a jetlike flow from below the airfoil lower surface. Analysis of the velocity measurements led to the following conclusions:

1. The flow upstream of the leading edge anticipated the presence of the airfoil not only by decreased velocity magnitude and changes in flow angle but also by increased unsteadiness and a skew toward higher velocities.

2. A large reversed velocity region began near the airfoil crest, increased in height over the airfoil surface, and continued downstream as part of the wake core. The flow unsteadiness (as indicated by the resultant standard deviation) in the reversed velocity region was the same order of magnitude as the mean velocity in the reversed velocity region.

3. The upper boundary and, downstream of the trailing edge, the lower boundary of the reversed velocity region were two free shear mixing layers. The largest values of flow unsteadiness were measured in the mixing layers. This unsteadiness and the mixing layer height increased in the downstream direction. Profiles of mean velocity, resultant standard deviation, and skew showed a similar pattern of development in the downstream direction. No evidence of the presence of discrete vortices was found in either mixing layer.

4. The lower mixing layer was caused by a jetlike flow from the lower surface of the airfoil. This flow was initially parallel to the lower surface tangent line, but it then curved upward and entrained fluid from the reversed velocity region. The unsteadiness of the flow was maximum in the region of large velocity gradients.

5. The upper mixing layer originated near the crest of the airfoil. Aft of 35 percent chord, a similarity parameter adequately accounted for the downstream development of the profiles of velocity and resultant standard deviation. The unsteadiness was maximum in the upper part of the mixing layer, typically where the velocity parallel to the chord was about 70 percent of the free-stream velocity. This maximum in resultant standard deviation increased downstream to a maximum value of about 43 percent of the free-stream velocity.

6. Wake contraction began near the trailing edge where the mixing layers above and below the airfoil began to curve toward each other.

Langley Research Center
National Aeronautics and Space Administration
Hampton, VA 23665
October 12, 1978

APPENDIX

COMPENSATION FOR LASER VELOCIMETER BIAS ERROR

There are two major sources of bias error present in a laser velocimeter measurement data ensemble, velocity bias and Bragg cell bias. If the seeding particles are uniformly distributed in the flow field, a higher flow velocity passes more particles through the laser velocimeter sample volume than lower flow velocities. Thus, the data are biased toward the higher velocities. This effect was studied by Tiederman and McLaughlin, and their results are presented in reference 8. On the other hand, when a Bragg cell is used in the laser velocimeter to give the system directional-sensing capabilities, a bias toward the lower velocities occurs. Since the Bragg cell moves the fringe pattern, multiple measurements can be obtained from the same seed particle as it passes through the sample volume. The extreme of this effect occurs when a particle is stationary in the sample volume which allows an infinite number of measurements to be made.

Since the particles pass through the laser velocimeter sample volume at a rate proportional to the velocity of the flow, the bias toward higher velocities can be corrected by including a multiplication factor in the standard statistical mean calculation to give

$$V_{e,corrected} = \frac{\sum a_i V_i}{\sum a_i}$$

where $a_i = 1/V_i$. Thus, the equation for calculating the corrected ensemble mean is

$$V_{e,corrected} = \frac{\sum (1/V_i) V_i}{\sum (1/V_i)} = \frac{D}{\sum (1/V_i)}$$

On the other hand, the measurement rate of a laser velocimeter system, which is equipped with a Bragg cell for directionality in the velocity measurements, is inversely proportional to the velocity of the flow. The number of multimeasurements made of a single particle as it traverses the sample volume is found by dividing the transit time of the particle passing through the sample volume by the time required for a single laser velocimeter measurement. The time for a single measurement t_m is found by using the equation

$$t_m = \frac{10 L_{fr}}{V_{fr} + V_i} + T_R$$

where L_{fr} is the fringe spacing, V_{fr} is the velocity of the moving fringes due to the Bragg effect, and T_R is the reset time of the high-speed burst

counter. The factor of 10 is included since 10 fringe crossings are required to make a measurement. The particle transit time t_t is defined as the time required for the particle to pass through the sample volume as defined by the $1/e^2$ laser power boundaries and is written

$$t_t = \frac{D_{sv}}{V_i}$$

where D_{sv} is the sample volume diameter. Thus, the number of measurements n_i is expressed as

$$n_i = \frac{t_t}{t_m} = \frac{\frac{D_{sv}}{V_i}}{\frac{10L_{fr}}{V_{fr} + V_i} + T_R} = \frac{D_{sv}(V_{fr} + V_i)}{V_i\left[10L_{fr} + T_R(V_{fr} + V_i)\right]}$$

The correction factor b_i then becomes

$$b_i = \frac{1}{n_i}$$

and the corrected ensemble mean is

$$V_B = \frac{\sum b_i V_i}{\sum b_i}$$

The ensemble mean V_B corrected for both velocity bias and Bragg bias is then expressed as

$$V_B = \frac{\sum a_i b_i V_i}{\sum a_i b_i} = \frac{\sum A_i V_i}{\sum A_i}$$

where

$$A_i = \frac{1}{V_i} \frac{V_i\left[10L_{fr} + T_R(V_{fr} + V_i)\right]}{D_{sv}(V_{fr} + V_i)}$$

$$= \frac{10L_{fr} + T_R(V_{fr} + V_i)}{D_{sv}(V_{fr} + V_i)}$$

APPENDIX

Based on the characteristics of the present laser velocimeter with the assumption that the velocity was perpendicular to the V fringes, the value of A_i was calculated for velocities from -50 m/sec to 100 m/sec. The results are shown in figure A1.

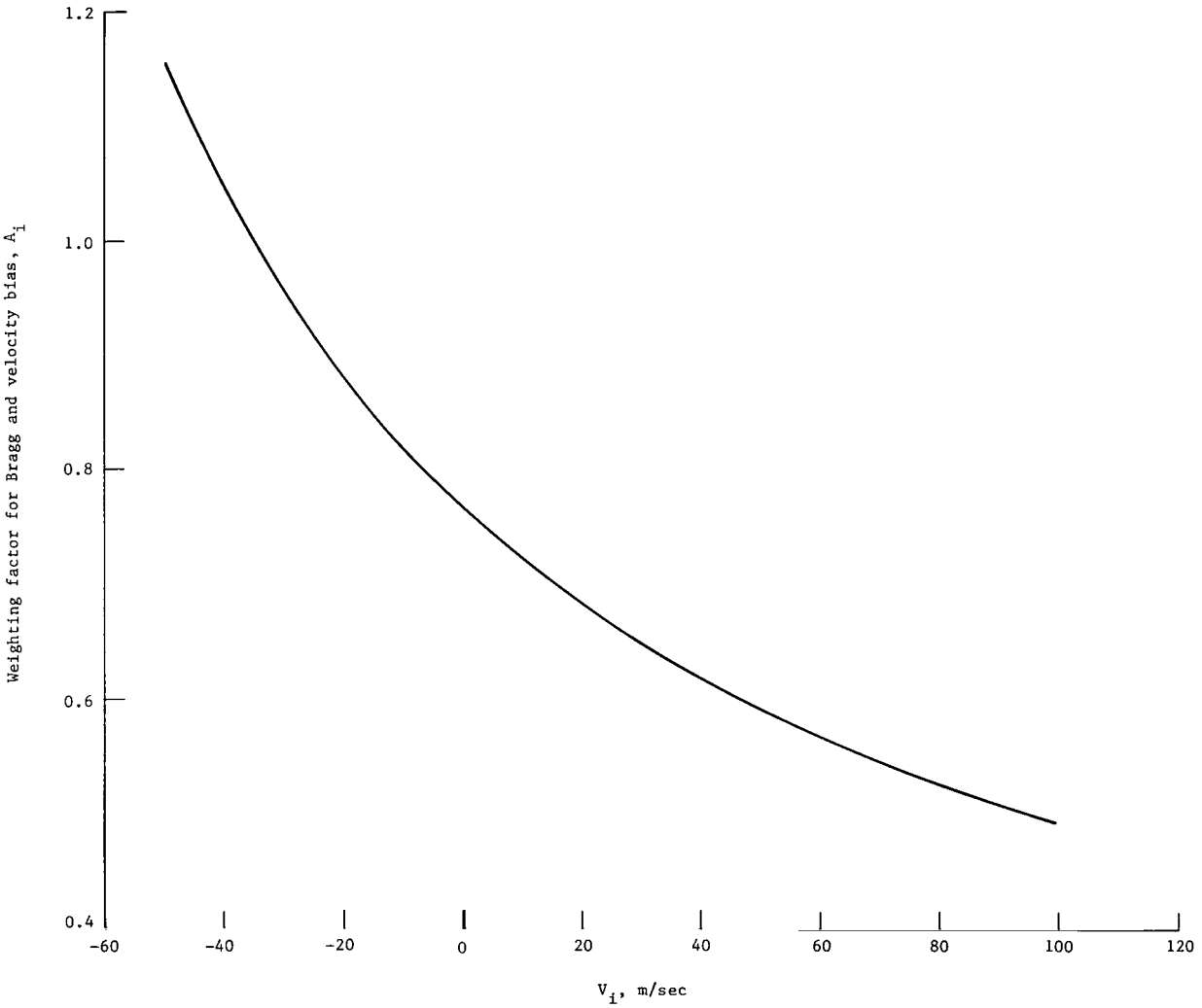

Figure A1.- Weighting factor for removal of one-component Bragg and velocity bias.

REFERENCES

1. McAlister, Kenneth W.; Carr, Lawrence W.; and McCroskey, William J.: Dynamic Stall Experiments on the NACA 0012 Airfoil. NASA TP-1100, 1978.

2. Seetharam, H. C.; and Wentz, W. H., Jr.: Experimental Investigation of Subsonic Turbulent Separated Boundary Layers on an Airfoil. J. Aircr., vol. 14, no. 1, Jan. 1977, pp. 51-55.

3. Young, Warren H., Jr.; Meyers, James F.; and Hepner, Timothy E.: Laser Velocimeter Systems Analysis Applied to a Flow Survey Above a Stalled Wing. NASA TN D-8408, 1977.

4. Hoad, Danny R.; Meyers, James F.; Young, Warren H., Jr.; and Hepner, Timothy E. (appendix A by James I. Clemmons, Jr.): Laser Velocimeter Survey About a NACA 0012 Wing at Low Angles of Attack. NASA TM-74040, 1978.

5. Hoad, Danny R.; Meyers, James F.; Young, Warren H., Jr.; and Hepner, Timothy E.: Correlation of Laser Velocimeter Measurements Over a Wing With Results of Two Prediction Techniques. NASA TP-1168, 1978.

6. Young, Warren H., Jr.; Meyers, James F.; and Hoad, Danny R.: Laser Velocimeter Data Interpretation by Histogram and Spectral Analysis. Proceedings of the Twenty-Third Conference on the Design of Experiments in Army Research Development and Testing, ARO Rep. 78-2, U.S. Army, July 1978, pp. 183-211.

7. Yule, G. Udny; and Kendall, M. G.: An Introduction to the Theory of Statistics. Charles Griffin & Co., Ltd., 1940.

8. Tiederman, W. G.; McLaughlin, D. K.; and Reischman, M. M.: Individual Realization Laser Doppler Technique Applied to Turbulent Channel Flow. Turbulence in Liquids, G. K. Patterson and J. L. Zakin, eds., Univ. of Missouri-Rolla, 1975, pp. 172-185.

9. Spencer, B. W.; and Jones, B. G.: Statistical Investigation of Pressure and Velocity Fields in the Turbulent Two-Stream Mixing Layer. AIAA Paper No. 71-613, June 1971.

10. Meyers, James F.; and Walsh, Michael J.: Computer Simulation of a Fringe Type Laser Velocimeter. Proceedings of the Second International Workshop on Laser Velocimetry, Volume I, H. D. Thompson and W. H. Stevenson, eds., Eng. Exp. Stn. Bull. No. 144, Purdue Univ., 1974, pp. 471-510.

11. Walsh, Michael J.: Influence of Particle Drag Coefficient on Particle Motion in High-Speed Flow With Typical Laser Velocimeter Applications. NASA TN D-8120, 1976.

12. Mayo, W. T., Jr.; Shay, M. T.; and Riter, S.: The Development of New Digital Data Processing Techniques for Turbulence Measurements With a Laser Velocimeter. AEDC-TR-74-53, U.S. Air Force, Aug. 1974. (Available from DDC as AD 784 891.)

TABLE I.- LASER VELOCIMETER CHARACTERISTICS

Laser wavelength, λ, nm	514.5
Input lens focal length, m	3.8649
Cross-beam angle, θ, deg	1.1139
Transmission coefficient, beam A	0.15
Transmission coefficient, beam B	0.16
Transmission coefficient, beam C	0.12
Input laser power, watts	4.0
Diameter of laser beam at input lens, m	0.0081
Receiving lens focal length, m	3.8649
Rotation angle of receiver, horizontal, deg	180.0
Rotation angle of receiver, vertical, deg	0
Effective receiving lens diameter, m	0.127
Transmission coefficient, receiver	0.42
Bragg frequency, MHz	5.0
Photomultiplier quantum efficiency	0.14
Photomultiplier gain	60 000
Counter threshold voltage, volts	0.015
Low-pass filter cutoff, MHz	8.0
High-pass filter cutoff, MHz	0.5
Counter count comparison accuracy	0.02
System gain, dB	-4.0
Counter reset time, T_R, μsec	0.4
Diameter of sample volume, D_{SV}, mm	0.314
Length of sample volume, L_{SV}, cm	2.29

TABLE II.- SUMMARY OF SCANS

Scan	Runs		Day	Time		Mach number	R_c	U_T, m/s	Scan location, percent chord	α_{scan}, deg	s_{scan}, percent chord
	From	To		Start	Stop						
1	1	16	137	0850	0916	0.148	1.01×10^6	50.9	-16.3	18.8	------
2	17	28	136	1818	1838	.148	1.02	50.8	-7.9	19.1	------
3	29	38	137	0921	0940	.148	1.00	51.1	-3.9	16.8	------
+4	39	51	137	1242	1305	.147	.97	51.6	.6	-20.8	1.85
[a]-4	52	60	137	1032	1201	.148	.98	51.4	.8	56.1	-2.15
+5	61	66	137	1007	1022	.148	.99	51.3	.3	14.4	1.60
[a]-5	67	69	137	1026	1030	.148	.99	51.3	.6	20.9	-1.87
+6	70	80	137	1308	1414	.147	.97	51.5	4.3	-.2	5.34
[a]-6	81	84	137	1210	1235	.148	.97	51.5	3.9	42.7	-6.01
7	85	94	138	1326	1354	.148	.97	51.8	9.3	9.3	11.64
8	95	103	138	1410	1446	.148	.97	51.9	15.7	11.4	18.13
9	104	112	138	1450	1505	.148	.97	51.9	24.7	16.1	27.20
10	113	124	138	1511	1528	.148	.97	51.8	35.7	19.2	38.25
11	125	138	138	1533	1624	.148	.97	51.7	48.3	21.9	50.80
12	139	154	138	1628	1652	.149	.98	51.8	60.6	23.7	63.16
13	155	168	138	1715	1742	.148	.99	51.5			
[b]13	169	170	138	1007	1009	.148	.99	51.5	75.6	24.9	78.29
[b]13	171	173	139	1833	1837	.149	1.02	51.2			
14	174	190	139	0918	1005	.149	1.00	51.4	85.8	26.0	88.63
[b]14	191	197	139	1839	1850	.149	1.02	51.1			
+15	198	204	139	1042	1300	.148	.99	51.5	96.3	26.1	99.20
[b]+15	205	213	140	0853	0907	.149	1.04	50.7			
[a]-15	214	218	140	1007	1016	.148	1.03	50.6	94.9	2.4	-97.82
[b]16	219	240	140	1023	1217	.148	1.03	50.7	102.5	18.2	------
[b]17	241	252	140	1222	1243	.148	1.02	50.8	108.4	19.3	------
[b]18	253	256	140	1246	1250	.148	1.01	50.8	114.2	17.6	------
19	257	269	139	1306	1324	.148	.99	51.5			
[b]19	270	270	140	0952	0954	.148	1.03	50.6	(c)	.5	------
19	271	271	139	1325	1327	.148	.99	51.5			
[b]19	272	289	140	0911	0948	.148	1.03	50.6			

[a]Negative denotes that part of scan below wing.

[b]Wing was raised and wing angle of attack increased less than 0.09°.

[c]Direction of scan 19 was vertical, not perpendicular to airfoil surface.

TABLE III.- HISTOGRAM MOMENTS AND TIME-AVERAGED VELOCITIES

Run	Scan (a)	$U_{L,e}$ m/s	$\delta U_{L,e}$ m/s	$V_{L,e}$ m/s	$\delta V_{L,e}$ m/s	$U_{L,B}$ m/s (b)	$V_{L,B}$ m/s (b)	$U_{L,a}$ m/s	$V_{L,a}$ m/s	σ_u m/s	$\delta\sigma_u$ m/s	σ_v m/s	$\delta\sigma_v$ m/s	$S_{R,u}$	$S_{R,v}$	E_u	E_v	D_u	D_v	D.R. meas/sec u	D.R. meas/sec v
1	1	39.8	.1	28.3	.0	40.0	28.4	40.3	28.0	2.2	.0	2.2	.0	-.50	1.05	-.2	1.1	1468	1953	24	32
2	1	40.8	.0	27.9	.0	40.9	28.0	41.1	27.4	1.9	.0	2.3	.0	-.86	.97	.5	.7	4073	3978	129	147
3	1	39.7	.0	27.9	.0	39.8	28.0	40.1	27.5	2.0	.0	2.4	.0	-.46	.76	-.3	.1	2429	2960	40	49
4	1	38.6	.0	27.6	.0	38.7	27.7	39.1	27.2	1.9	.0	2.5	.0	-.07	.83	-.4	.2	2374	3032	39	50
5	1	38.7	.0	27.3	.0	38.7	27.3	39.0	26.9	1.8	.0	2.5	.0	-.51	.85	.2	.4	3898	4075	64	168
6	1	37.9	.0	27.4	.0	38.0	27.4	38.3	27.2	1.6	.0	2.4	.0	-.37	.63	.1	.1	4078	4079	147	184
7	1	37.2	.0	27.1	.0	37.3	27.1	37.3	26.7	1.5	.0	2.2	.0	-.20	.61	.1	.4	4078	4075	164	198
8	1	36.9	.0	26.6	.0	36.9	26.6	37.1	26.0	1.4	.0	2.2	.0	-.25	.69	.6	.4	4083	4077	181	228
9	1	36.2	.0	26.6	.0	36.3	26.6	36.3	26.3	1.3	.0	2.4	.0	-.15	.85	.4	.5	4082	4073	173	187
10	1	35.6	.0	26.2	.0	35.6	26.3	35.6	25.9	1.2	.0	2.3	.0	-.14	1.03	.0	.9	4065	4074	189	214
11	1	35.0	.0	26.6	.0	35.1	26.5	35.1	26.2	1.3	.0	2.2	.0	.11	.74	.6	.5	4086	4065	199	234
12	1	34.6	.0	26.2	.0	34.6	26.2	34.5	26.0	1.2	.0	2.0	.0	.12	.98	.4	1.2	4076	4068	211	229
13	1	34.1	.0	26.5	.0	34.1	26.4	34.0	26.3	1.2	.0	1.8	.0	.13	.74	.5	.6	4075	4054	229	205
14	1	33.7	.0	26.8	.0	33.6	26.9	33.6	26.6	1.2	.0	1.8	.0	.17	1.08	.2	1.4	4054	4075	255	237
15	1	33.2	.0	27.4	.0	33.2	27.4	33.1	27.1	1.1	.0	1.7	.0	.34	.55	.6	.3	4073	4059	250	234
16	1	32.9	.0	27.7	.0	32.9	27.7	32.8	27.6	1.1	.0	1.6	.0	.32	.61	.4	.5	4049	4067	239	227
17	2	41.8	.0	23.6	.0	41.8	23.5	42.0	23.3	1.9	.0	1.9	.0	-.46	.74	-.1	.5	2002	2232	33	37
18	2	40.8	.0	24.0	.0	40.8	23.9	41.2	23.9	2.0	.0	2.5	.0	-.35	.50	-.3	-.2	4081	4065	152	192
19	2	39.8	.0	23.5	.0	39.8	23.5	40.0	22.8	1.9	.0	2.6	.0	-.22	.36	-.3	-.4	4083	4077	151	193
20	2	38.8	.0	22.7	.0	38.8	22.7	39.0	22.2	1.6	.0	2.8	.0	-.15	.40	-.0	-.5	4075	4072	147	181
21	2	37.3	.0	22.5	.0	37.3	22.4	37.5	21.6	1.3	.0	2.7	.0	-.04	.43	.0	-.4	4081	4070	154	196
22	2	36.0	.0	21.8	.0	36.0	21.7	36.2	21.4	1.1	.0	2.8	.0	.04	.45	.4	-.4	4087	4064	148	189
23	2	34.5	.0	21.6	.0	34.5	21.5	34.4	21.0	1.1	.0	2.9	.0	.25	.76	.3	.2	4067	4078	169	182
24	2	33.3	.0	21.7	.0	33.3	21.5	33.3	21.3	1.1	.0	2.4	.0	.35	.81	.2	.5	4056	3271	149	54
25	2	32.0	.0	22.7	.0	32.0	22.6	31.8	22.4	1.2	.0	2.2	.0	.57	.92	.7	.8	4078	3962	166	177
26	2	31.7	.0	23.9	.0	31.6	23.8	30.7	23.5	1.4	.0	2.1	.0	.59	.62	.7	.1	4052	4034	189	161
27	2	31.5	.0	25.0	.0	31.2	25.0	22.4	24.7	1.6	.0	2.0	.0	.29	.59	.4	-.0	3973	3910		155
28	2	31.5	.0	26.1	.0	31.0	26.0	31.3	25.6	1.6	.0	2.0	.0	-.13	.62	.1	.2	3927	3180		53
29	3	42.5	.0	21.2	.0	42.6	21.1	42.8	20.8	2.2	.0	2.1	.0	-.48	.73	.0	.4	4078	4049	146	181
30	3	42.2	.0	19.7	.0	42.2	19.6	42.5	19.3	2.2	.0	2.4	.0	-.44	.72	-.2	.1	4077	4045	145	176
31	3	41.1	.0	17.9	.0	41.1	17.8	41.4	17.2	2.1	.0	2.9	.0	-.29	.67	-.3	-.1	3974	4066	132	170
32	3	38.4	.0	16.0	.1	38.4	15.7	38.5	15.6	1.7	.0	3.0	.0	-.18	.71	-.2	.0	3358	2883	55	48
33	3	35.2	.0	16.0	.1	35.2	15.6	35.3	16.1	1.0	.0	3.0	.1	-.02	.86	-.3	.7	2335	1762	38	29
34	3	32.7	.0	17.1	.1	32.6	16.8	32.6	16.6	1.0	.0	2.9	.1	.19	.71	.1	.8	1175	1499	19	24
35	3	31.1	.0	19.0	.0	31.1	18.8	28.5	18.6	1.2	.0	2.4	.0	.32	.46	.0	-.0	1598	2546	26	42
36	3	29.8	.0	20.2	.0	29.2	20.0	26.8	19.8	1.6	.0	2.0	.0	-.45	.50	-.3	.3	3384	2809	56	46
37	3	29.5	.0	22.0	.0	28.5	21.9	27.5	21.8	1.9	.0	1.8	.0	-.58	.65	-.6	.7	3828	3675	63	61
38	3	28.6	.0	23.5	.0	27.9	23.4	28.4	23.2	1.7	.0	1.6	.0	-.03	.52	.3	.4	3915	4048		197
39	4	39.8	.1	28.6	.0	39.9	28.6	40.0	28.4	2.0	.1	2.2	.0	-.04	.64	-.4	.3	660	4085	11	213
40	4	41.3	.0	27.4	.0	41.3	27.4	41.7	27.1	2.1	.0	2.2	.0	-.35	.54	-.3	.1	4082	4073	134	157
41	4	41.4	.0	26.7	.0	41.4	26.6	41.8	26.4	2.2	.0	2.1	.0	-.42	.49	-.3	.0	4086	3893	134	64
42	4	41.5	.0	26.1	.0	41.5	26.0	42.0	25.6	2.2	.0	2.3	.0	-.25	.53	-.4	.0	4090	4074	138	162
43	4	42.0	.0	25.0	.0	42.0	24.9	42.4	24.4	2.2	.0	2.4	.0	-.19	.59	-.5	-.0	4088	4074	134	162
44	4	42.2	.0	24.1	.0	42.2	24.1	42.7	23.1	2.4	.0	2.8	.0	-.24	.79	-.6	.1	4089	4032	136	161
45	4	42.2	.0	22.9	.0	42.2	22.8	42.6	22.3	2.4	.0	2.6	.0	-.27	.46	-.4	-.3	4090	4038	140	158
46	4	42.2	.0	21.8	.0	42.2	21.8	42.7	19.9	2.5	.0	3.0	.0	-.06	.37	-.5	-.3	4092	3727	147	62
47	4	42.3	.0	20.1	.1	42.3	19.9	42.8	19.6	2.8	.0	3.5	.0	-.05	.41	-.4	-.2	4091	3948	132	165
48	4	42.5	.0	18.0	.1	42.5	17.8	43.1	17.0	2.9	.0	4.7	.1	.28	.66	-.4	.1	4092	2960	137	49
49	4	42.6	.1	14.9	.1	42.5	14.4	43.3	13.8	3.2	.0	4.7	.1	.22	.80	-.6	.7	4091	2450	127	40
50	4	42.1	.1	12.1	.1	42.0	11.7	42.8	10.9	3.2	.0	5.5	.1	.43	.97	-.3	.6	3549	2147	59	35
51	4	40.4	.1	13.8	.7	40.3	13.2	41.0	10.2	2.2	.1	8.4	.4	.51	.79	.8	-1.0	763	134	12	2
52	-4	30.9	.0	24.5	.0	29.5	24.4		24.4	1.8	.0	1.5	.0	-.97	.53	-.8	.4	3707	3445	61	57
53	-4	30.6	.0	24.6	.0	29.6	24.5	-43.9	24.4	1.6	.0	1.5	.0	-.33	.66	.4	.8	3694	2515	61	41
54	-4	30.8	.0	24.0	.0	30.1	23.9	21.1	23.8	1.5	.0	1.6	.0	-.34	.56	-.2	.3	3702	2512	61	41
55	-4	31.3	.0	23.1	.0	30.4	22.9		22.8	1.9	.0	1.7	.0	-.57	.65	-.2	.7	3795	4020	63	199
56	-4	29.1	.0	21.4	.1	29.1	21.1	25.3	21.0	1.4	.0	2.0	.1	.78	.92	.3	1.8	1758	913	29	15
57	-4	29.7	.3	23.8	.1	29.7	23.7	29.3	23.2	2.3	.2	4.2	.0	.56	.52	-.1	-.5	71	4092	1	189
58	-4	31.8	.0	24.7	.1	31.8	24.6	31.4	23.7	1.9	.0	5.0	.1	.17	.19	-.1	-1.1	2339	1485	38	24
59	-4	30.9	.0	21.3	.1	30.8	21.1	30.2	21.3	1.6	.0	3.0	.0	.17	.57	.2	.6	2033	2497	33	41
60	-4	29.9	.1	20.1	.1	29.9	19.8	28.3	20.2	1.8	.0	3.5	.1	.20	.98	.0	1.0	726	865	12	14
61	5	46.0	.1	19.4	.0	46.0	19.2	46.3	19.0	3.6	.0	2.4	.0	-.27	.81	-.5	1.0	3960	4017	121	159
62	5	47.8	.1	16.8	.0	47.8	16.5	48.2	16.5	3.2	.0	2.2	.0	-.38	.51	-.3	.7	4078	4000	141	139
63	5	48.5	.1	13.4	.0	48.5	12.9	49.0	13.2	3.7	.0	2.4	.0	-.46	.56	.0	1.3	3283	2446	54	40
64	5	48.0	.1	7.9	.1	47.9	5.9	48.8	6.7	4.6	.0	8.4	.2	-.11	-2.07	-.6	10.4	4088	4000	140	145
65	5	44.1	.1	7.6	.1	44.0	6.6	44.7	5.8	3.8	.0	4.8	.1	.32	1.41	-.4	3.8	3584	1677	59	27
66	5	41.2	.1	14.3	1.2	41.1	13.7	41.4	12.8	2.5	.1	10.1	.4	.49	.35	.6	-1.6	429	70	7	1
67	-5	25.0	.1	17.6	.1	24.8	17.0	24.4	17.0	2.6	.1	2.7	.1	.71	.87	.9	1.7	1019	912	16	15
68	-5	24.7	.1	19.6	.0	24.6	19.3	24.1	19.5	2.2	.0	1.8	.0	.64	1.16	-.1	2.3	1475	2159	24	35
69	-5	24.4	.0	21.4	.0	24.2	21.2	24.2	21.1	2.0	.0	1.4	.0	.68	.77	.5	1.6	2793	3167	46	52
70	6	44.4	.1	28.1	.1	44.5	28.0	44.8	27.9	2.1	.1	1.6	.1	-.59	.48	-.3	.5	664	591	11	9
71	6	42.6	.1	28.4	.1	42.5	28.3	43.0	28.1	2.8	.0	2.3	.0	.20	.38	-.6	-.2	1475	1162	24	19

[a]Negative denotes that part of scan below wing.
[b]Corrected for velocity bias including Bragg effects.

TABLE III.- Continued

Run	Scan (a)	$U_{L,e}$ m/s	$\delta U_{L,e}$ m/s	$V_{L,e}$ m/s	$\delta V_{L,e}$ m/s	$U_{L,B}$ m/s (b)	$V_{L,B}$ m/s (b)	$U_{L,a}$ m/s	$V_{L,a}$ m/s	σ_u m/s	$\delta\sigma_u$ m/s	σ_v m/s	$\delta\sigma_v$ m/s	$S_{R,u}$	$S_{R,v}$	E_u	E_v	D_u	D_v	D.R. meas/sec u	D.R. meas/sec v
72	6	46.3	.0	26.5	.0	46.3	26.4	46.7	26.4	2.4	.0	1.6	.0	-.66	.36	-.0	.4	4060	4074	165	173
73	6	47.8	.0	24.6	.0	47.9	24.5	48.2	24.5	2.2	.0	1.5	.0	-.67	.15	.1	.2	4051	2198	145	36
74	6	50.1	.1	22.5	.0	50.3	22.4	50.3	21.8	2.0	.1	2.0	.0	-.73	.68	.4	.8	924	3484	15	58
75	6	46.6	.1	23.3	.1	46.5	23.2	48.1	22.3	4.8	.0	4.0	.0	-.01	.47	-1.0	-.6	4095	2880	140	48
76	6	50.4	.1	18.2	.0	50.4	18.0	51.2	18.1	4.1	.0	2.4	.0	-.60	.57	-.3	.5	4088	4032	149	135
77	6	53.6	.1	14.1	.0	53.9	13.9	54.8	14.1	4.4	.1	2.9	.0	-.85	.39	.3	1.5	4056	3651	134	60
78	6	57.0	.1	10.4	.1	57.3	10.1	57.7	10.6	3.5	.0	4.1	.1	-.75	1.10	.7	4.7	3991	4012	150	145
79	6	45.2	.6	13.4	.6	44.6	13.0	49.9	15.5	11.2	.4	8.4	.3	-.37	.41	-.1	-1.0	312	196	5	3
80	6	3.5	.4	-1.3	.2	2.3	-1.7	3.4	.1	10.1	.3	5.2	.1	.74	.53	.1	.7	649	845	10	14
81	-6	24.4	.0	23.5	.0	24.3	23.4	23.7	23.5	2.2	.0	1.5	.0	1.11	.96	1.8	2.1	4050	4009	172	182
82	-6	23.4	.0	24.9	.1	23.2	24.9	23.0	23.7	2.6	.0	3.9	.0	1.02	.81	1.4	-.4	3822	4088	63	220
83	-6	26.9	.1	25.0	.1	26.8	24.9	26.6	24.2	4.4	.1	4.1	.0	.35	.21	-.6	-1.1	2551	1707	42	28
84	-6	30.9	.3	26.7	.2	30.3	26.7	30.1	25.6	4.4	.2	4.7	.1	-.79	-.52	-.4	-1.0	299	562	4	9
85	7	47.1	.1	29.5	.0	47.2	29.6	47.4	29.8	1.7	.0	1.7	.0	-.61	.02	.4	.4	728	2074	12	34
86	7	45.0	.1	29.2	.0	44.9	29.2	44.8	28.9	2.9	.1	1.7	.0	-.40	.01	-.4	.1	1010	1392	16	23
87	7	45.8	.1	28.3	.0	45.8	28.3	46.7	28.4	3.2	.1	1.9	.0	-.30	.25	-.6	.4	1202	1808	20	30
88	7	45.7	.1	27.5	.1	45.6	27.5	46.1	27.4	3.7	.1	2.3	.1	-.24	.60	-.4	.6	1017	1349	16	22
89	7	47.2	.2	25.7	.0	47.2	25.7	48.0	25.3	3.8	.1	2.3	.0	-.36	.42	-.5	.3	619	4075	10	136
90	7	49.7	.1	25.2	.0	49.6	25.1	50.3	25.0	3.5	.0	2.7	.0	-.37	.39	-.2	.1	3395	3635	56	60
91	7	50.8	.1	23.9	.1	50.7	23.9	51.4	23.6	4.1	.1	3.5	.1	-.35	.59	-.2	.2	2319	2218	38	36
92	7	48.7	.1	23.5	.1	48.8	23.6	49.5	23.3	4.7	.1	5.1	.1	-.16	.01	-.5	.3	1671	2224	27	37
93	7	42.1	.2	20.8	.2	42.7	20.8	43.1	21.0	6.7	.2	7.0	.1	-.56	-.16	1.2	.1	792	1365	13	22
94	7	24.8	1.2	15.6	.3	23.9	14.9	29.8	18.7	13.5	.5	10.0	.2	-.02	-.19	-1.3	-.3	136	1205	2	20
95	8	48.3	.0	31.4	.0	48.3	31.4	48.7	31.8	2.2	.0	2.2	.0	-.90	.07	.7	-.1	4068	4085	175	205
96	8	48.1	.1	29.7	.0	48.1	29.7	48.5	29.9	2.6	.1	2.0	.0	-.31	.34	-.2	.2	1087	1811	18	30
97	8	49.9	.0	30.0	.0	50.0	30.0	50.4	30.3	2.8	.0	2.7	.0	-.58	.27	-.2	-.1	4075	4075	118	149
98	8	51.1	.1	29.7	.1	51.0	29.6	51.4	29.3	4.8	.1	3.3	.1	-.32	-.23	-.3	-.6	3791	493	63	8
99	8	46.1	.1	28.2	.1	46.0	28.2	47.6	29.0	7.6	.1	7.1	.1	-.80	-.47	1.4	.4	3995	4038	207	177
100	8	43.3	.2	25.3	.2	43.2	25.0	44.8	26.7	9.6	.1	9.1	.1	-.88	-.58	.2	.0	3005	2345	50	39
101	8	33.9	.3	20.5	.3	32.9	19.6	36.7	24.2	14.0	.1	12.0	.2	-.18	-.25	-1.2	-.5	2725	2250	45	37
102	8	19.8	.3	12.7	.3	18.4	11.5	27.7	15.3	15.5	.2	13.3	.2	.79	.29	-.6	-.3	2160	1449	36	24
103	8	11.6	.4	6.5	.4	10.1	5.4	23.4	7.0	13.4	.3	11.1	.3	1.09	.51	.6	-.1	1389	644	23	10
104	9	49.6	.0	33.5	.0	49.7	33.4	49.9	33.5	1.8	.0	2.3	.0	-.47	-.02	.6	-.2	4051	4078	142	159
105	9	50.7	.0	32.6	.1	50.8	32.5	51.0	32.8	1.9	.0	2.6	.0	-.63	.18	.9	-.3	2073	2172	34	36
106	9	51.7	.0	32.6	.1	51.8	32.7	51.8	33.1	2.4	.0	3.5	.0	.02	.18	.3	-.2	4056	4062	241	187
107	9	49.6	.1	33.7	.1	49.8	33.8	49.9	34.6	3.4	.0	5.6	.1	-.23	-.16	.6	-.2	4031	3586	123	59
108	9	45.1	.1	32.4	.2	45.5	32.6	45.9	34.2	6.6	.1	8.0	.1	-.92	-.60	1.1	.3	2522	2112	42	35
109	9	32.4	.4	24.6	.4	31.6	23.5	35.2	28.6	12.7	.2	14.2	.2	-.21	-.40	-.8	-.7	1174	1450	19	24
110	9	18.7	.5	14.2	.6	17.7	12.7	25.1	17.3	13.0	.3	14.3	.4	.80	.46	-.2	-.2	749	642	12	10
111	9	7.8	.3	9.6	.9	6.1	8.5	9.6	11.3	8.3	.3	13.4	.6	.77	.52	1.5	.0	575	223	9	3
112	9	3.3	.4	.9	2.0	1.4	-.3	4.7	1.9	7.3	.4	15.3	1.5	.93	1.45	1.9	.3	395	56	6	0
113	10	49.5	.0	35.4	.1	49.5	35.4	49.6	35.6	1.9	.0	2.6	.0	-.11	-.07	.5	-.2	2709	2478	45	41
114	10	50.0	.0	34.8	.1	50.1	35.0	50.2	35.5	2.3	.0	3.2	.0	-.00	.16	.2	.1	4056	3370	102	56
115	10	46.9	.1	36.2	.1	47.1	36.4	47.0	37.6	3.7	.1	5.9	.1	-.30	-.36	.5	.3	3045	2473	50	41
116	10	43.1	.1	34.5	.2	43.4	34.5	43.6	35.9	5.8	.1	8.4	.2	-.54	-.76	.5	.5	2848	1443	47	24
117	10	36.5	.4	28.2	.6	36.2	28.2	38.1	32.6	10.2	.2	11.5	.3	-.72	-.20	-.1	-.7	814	415	13	6
118	10	28.5	.4	22.7	.8	27.7	21.4	30.4	25.0	12.4	.2	14.5	.5	-.15	-.08	-.9	-.7	1041	302	17	5
119	10	19.4	.5	19.3	.7	18.5	17.7	24.7	25.4	12.8	.3	15.1	.4	.48	.13	-.2	-.6	768	440	12	7
120	10	11.4	.4	11.1	1.0	10.3	9.3	17.3	15.7	10.8	.3	17.5	.6	.76	.41	.5	-.8	652	295	10	4
121	10	5.3	.3	3.6	.6	3.9	2.3	4.9	4.1	8.3	.2	11.8	.4	.57	.66	.8	.2	885	426	14	7
122	10	1.3	.2	-.3	.4	.6	-1.7	4.1	-.9	6.4	.2	9.2	.4	.56	.31	.5	.8	917	463	15	7
123	10	-.5	.2	-3.9	.4	-1.0	-4.4	.1	-7.8	5.2	.1	6.8	.3	-.14	-.06	-.5	1.2	466	311	7	5
124	10	-.9	.2	-3.8	.4	-1.2	-4.3	-1.4	-4.1	4.5	.1	6.4	.4	.30	.45	-.3	1.2	504	234	8	3
125	11	48.7	.1	36.4	.2	48.6	36.8	48.5	37.0	2.1	.1	3.1	.1	.07	.12	.4	-.4	447	365	7	6
126	11	46.3	.1	38.9	.1	46.4	39.1	46.9	37.9	3.3	.0	6.2	.1	.00	-.41	.5	.7	4035	4045	284	435
127	11	42.2	.1	39.3	.1	42.4	39.4	42.7	39.7	4.8	.1	6.9	.1	-.45	-.59	.5	.5	1272	2584	21	43
128	11	35.1	.3	33.9	.8	34.9	33.2	36.4	35.1	9.4	.1	11.4	.6	-.41	-.68	-.6	-.2	1414	189	23	3
129	11	22.9	.3	24.5	.4	21.9	22.9	25.5	29.2	11.8	.2	16.0	.3	.04	-.26	-.6	-.4	1651	1309	27	21
130	11	18.2	.3	17.9	.5	17.4	16.2	22.1	21.9	10.5	.2	16.4	.3	.37	.31	-.3	-.9	1453	946	24	15
131	11	12.4	.3	15.4	.6	11.5	14.0	14.4	19.9	8.5	.3	15.1	.4	.45	.29	.8	-.3	800	653	13	10
132	11	8.7	.2	3.4	.4	7.3	1.8	10.4	8.2	7.2	.2	10.8	.3	.52	.64	.5	.3	997	628	16	10
133	11	3.9	.2	2.8	.3	3.1	1.3	6.4	7.3	6.0	.1	8.5	.2	.17	.33	.2	.4	1282	953	21	15
134	11	3.0	.3	.7	.3	2.4	-.9	4.8	-1.7	6.3	.2	8.3	.3	.26	.35	-.5	1.9	369	576	6	9
135	11	1.5	.2	-3.6	.4	.9	-4.1	2.1	-3.5	4.6	.1	7.0	.4	-.06	.91	1.1	2.5	875	330	14	5
136	11	-.4	.3	-5.2	.2	-.7	-6.7	-1.1	-6.9	4.6	.2	3.5	.2	.33	-.97	.7	.5	289	206	4	3
137	11	-2.4	.1	-5.4	.3	-2.6	-5.8	-2.3	-8.3	1.9	.1	4.4	.2	-.46	-.97	2.2	-.3	232	269	3	4
138	11	-1.2	.2	-6.8	.4	-1.2	-7.0	-1.5	-9.4	4.7	.1	7.0	.2	.50	.41	.2	-.6	641	293	10	4
139	12	45.4	.0	41.0	.1	45.4	41.3	45.5	41.5	3.2	.0	4.9	.1	-.04	-.41	.3	.4	4061	4041	158	141
140	12	42.7	.1	40.6	.1	42.8	41.1	42.9	41.3	3.9	.1	6.1	.1	-.12	-.37	.4	.1	3096	2632	51	43
141	12	38.1	.1	38.9	.2	38.2	39.1	38.5	37.2	6.1	.1	8.9	.2	-.36	-.86	.1	.9	2873	2080	47	34
142	12	31.0	.2	31.7	.4	30.7	30.9	32.5	33.8	8.1	.1	13.6	.3	-.29	-.62	-.4	-.2	1855	1275	30	21
143	12	23.7	.2	25.4	.5	23.3	23.7	25.3	26.6	9.3	.1	14.9	.3	.13	-.20	-.5	-.7	1590	1010	26	16
144	12	16.7	.3	18.0	.5	16.1	16.6	19.9	24.6	8.4	.2	14.8	.3	.23	.40	.1	-.5	1045	760	17	12

[a]Negative denotes that part of scan below wing.
[b]Corrected for velocity bias including Bragg effects.

TABLE III.- Continued

Run	Scan	$U_{L,e}$ m/s	$\delta U_{L,e}$ m/s	$V_{L,e}$ m/s	$\delta V_{L,e}$ m/s	$U_{L,B}$ m/s	$V_{L,B}$ m/s	$U_{L,a}$ m/s	$V_{L,a}$ m/s	σ_u m/s	$\delta\sigma_u$ m/s	σ_v m/s	$\delta\sigma_v$ m/s	$S_{R,u}$	$S_{R,v}$	E_u	E_v	D_u	D_v	D.R. meas/sec u	D.R. meas/sec v
	(a)					(b)	(b)														
145	12	10.1	.2	10.5	.4	9.3	8.9	12.9	14.2	7.4	.2	13.0	.4	.32	.83	.3	.6	1268	897	21	14
146	12	7.1	.4	5.0	.5	6.7	3.0	10.9	9.0	7.1	.3	12.5	.4	.46	.81	1.0	1.0	361	623	6	10
147	12	4.8	.2	.9	.5	4.6	-.6	6.1	3.6	4.3	.1	8.2	.4	.32	.61	1.0	.6	744	247	12	4
148	12	2.1	.2	-1.7	.3	1.3	-2.3	2.6	-3.5	4.7	.2	6.5	.2	-.56	.09	.5	-.5	516	446	8	7
149	12	1.6	.4	-.9	.3	.8	-1.5	-.7	-3.9	4.7	.3	5.9	.2	-.13	-.36	-.0	-.1	142	482	2	8
150	12	.1	.2	-5.3	.3	-.1	-5.9	-.3	-7.3	4.2	.1	6.3	.3	-.23	.95	-.6	1.4	526	390	6	6
151	12	.3	.2	-6.9	.2	.2	-6.9	.5	-8.6	4.0	.1	4.1	.2	-.26	-.71	.5	.3	511	379	8	6
152	12	-1.6	.2	-8.7	.2	-1.3	-8.8	-1.2	-9.2	4.2	.2	4.0	.1	.04	-.18	.3	-.4	417	347	6	5
153	12	-1.9	.3	-7.5	.3	-1.6	-7.8	-2.0	-9.0	3.5	.2	4.1	.2	-.08	-.86	-.6	-.3	162	189	2	3
154	12	-2.1	.3	-8.1	.3	-1.8	-8.0	-2.7	-9.2	4.0	.2	3.8	.1	.18	-.08	-.3	-.8	231	201	3	3
155	13	42.9	.1	42.9	.1	42.9	43.3	42.8	43.6	3.5	.1	5.4	.1	.10	-.40	.2	.3	2506	2964	41	49
156	13	39.4	.2	45.5	.1	39.6	45.8	39.7	44.3	4.7	.2	6.8	.1	-.02	-.54	.4	.5	525	3526	8	58
157	13	36.6	.1	41.6	.2	36.8	41.6	36.7	41.9	5.4	.1	10.0	.2	-.37	-.80	.5	.7	2367	2316	39	38
158	13	31.6	.2	39.2	.2	31.4	38.5	32.3	40.6	7.7	.1	12.8	.2	-.41	-.88	-.2	.3	2288	3445	38	57
159	13	26.1	.1	40.6	.3	27.5	39.6	28.1	41.9	8.3	.1	14.1	.2	-.35	-.88	-.2	.1	3212	2231	53	37
160	13	21.5	.2	33.7	.5	20.8	32.2	24.5	34.3	9.4	.1	16.1	.3	-.06	-.42	-.2	-.6	1834	1007	30	16
161	13	16.3	.2	22.5	.5	15.6	20.1	18.5	30.9	9.1	.1	18.5	.3	.30	.04	-.3	-.8	1701	1405	28	23
162	13	11.4	.3	18.9	.7	10.5	16.9	15.8	25.0	9.6	.2	16.5	.5	.16	.34	.2	-.4	1132	528	18	8
163	13	6.6	.3	10.8	.5	7.7	9.1	12.4	15.5	8.8	.2	16.0	.5	.36	.60	.1	-.3	876	441	14	7
164	13	5.1	.3	6.5	1.0	4.2	4.7	7.0	12.0	7.6	.2	17.3	.7	.25	.85	-.1	-.2	639	303	10	5
165	13	2.8	.3	2.4	1.0	2.4	1.1	3.7	3.9	7.1	.2	14.4	.7	.02	.49	.1	-.1	596	191	9	3
166	13	1.0	.4	2.9	.9	.5	.2	1.4	.8	6.6	.3	5.9	.8	.03	.05	-.4	.9	237	41	3	0
167	13	.9	.4	-2.5	.9	.2	-2.8	.1	-4.4	6.0	.3	9.7	.5	-.43	-.07	.0	-.8	183	122	3	2
168	13	-2.2	.3	-7.7	.4	-2.4	-7.9	-1.5	-8.9	5.3	.2	3.4	.3	.47	-1.40	-.4	1.0	237	81	3	1
169	13	-.9	.4	.8	1.2	-.7	-.7	-3.4	2.5	6.8	.3	13.6	.9	-.48	.44	.5	.2	337	124	5	2
170	13	-1.1	.6	-2.4	.8	-2.1	-3.2	-3.9	-4.6	9.0	.5	10.8	.7	-.83	.64	.6	.8	196	192	3	3
171	13	-2.2	.1	-6.7	.2	-2.2	-6.8	-3.3	-9.9	4.9	.1	6.2	.2	-.11	.11	-.2	.1	1281	882	21	14
172	13	-2.0	.1	-9.4	.2	-1.9	-9.6	-2.6	-10.1	4.3	.1	4.2	.1	-.03	-.57	-.2	-.2	989	484	16	8
173	13	-4.0	.3	-8.8	.2	-3.6	-8.9	-4.3	-10.2	4.3	.2	4.8	.2	-.29	-.28	-.2	.4	208	411	3	6
174	14	39.1	.1	46.6	.3	39.1	47.0	39.2	47.5	4.4	.1	6.3	.3	.02	-.75	.3	1.4	861	401	14	6
175	14	38.3	.1	46.9	.1	38.4	47.1	38.3	47.4	4.2	.0	6.2	.1	-.03	-.59	.2	.6	4075	3952	175	107
176	14	35.9	.1	46.5	.2	36.0	46.8	35.8	47.5	4.9	.1	7.5	.1	-.18	-.71	.1	.6	4049	2439	141	40
177	14	33.2	.1	44.4	.3	33.2	44.6	33.4	46.6	5.9	.1	10.7	.2	-.32	-1.08	.2	1.3	2428	1511	40	25
178	14	30.5	.2	42.2	.4	30.6	42.1	30.5	42.2	6.6	.2	12.4	.3	-.36	-.83	.3	.3	1073	1150	17	19
179	14	22.6	.3	35.9	.8	22.3	34.5	23.7	36.7	7.9	.2	15.7	.4	-.04	-.51	-.1	-.7	700	430	11	7
180	14	15.9	.5	31.8	2.2	15.2	14.9	18.2	29.7	8.9	.3	18.0	.8	-.00	-.28	-.4	-1.4	324	66	5	1
181	14	22.2	.7	39.1	.6	2.5	38.0	10.2	42.4	9.7	.5	14.8	.5	-.16	-.87	.0	.3	197	623	3	10
182	14	19.0	.4	36.1	.8	18.6	35.6	20.3	40.7	9.1	.2	15.1	.5	.06	-.41	-.5	-.4	568	323	9	5
183	14	14.2	.4	30.1	1.0	13.6	28.1	16.4	40.0	11.2	.3	18.1	.5	.09	-.19	-.3	-1.0	662	336	11	5
184	14	11.2	.5	27.5	1.3	10.6	25.7	13.3	36.8	9.5	.3	18.3	.7	.01	.03	.1	-.7	441	201	7	3
185	14	8.4	.6	19.2	1.6	7.7	16.5	10.1	26.3	10.0	.4	20.3	.8	.35	.26	.1	-1.0	329	157	5	2
186	14	1.6	.6	21.9	1.6	1.3	20.5	3.4	27.9	8.4	.5	16.9	.9	.74	.50	-.0	-.7	172	109	2	1
187	14	3.0	.7	13.6	1.9	2.4	11.5	4.0	18.3	8.9	.4	19.2	1.1	.49	.29	-.5	-.8	158	102	2	1
188	14	3.3	.3	14.3	1.0	2.6	12.9	2.5	20.1	7.7	.2	15.0	.7	.06	.62	.1	.2	493	217	8	3
189	14	.4	.4	9.7	.8	-.3	3.8	1.0	9.8	7.9	.3	15.0	.5	.02	.37	.5	-.4	507	352	8	5
190	14	.6	.6	6.3	2.2	-.1	4.0	.9	4.2	8.8	.5	19.5	1.0	-.38	.16	.6	-1.2	210	75	3	1
191	14	.2	.4	-7.0	.6	.0	-6.6	-2.0	-7.6	4.4	.3	5.9	.5	-.17	.16	.3	.8	139	108	2	1
192	14	-1.7	.4	-8.4	.6	-2.0	-8.6	-1.9	-9.2	5.0	.2	4.6	.4	.10	-.87	-.9	.4	126	69	2	1
193	14	-.9	.2	-5.4	.5	-1.2	-5.8	-1.3	-7.3	6.6	.1	9.4	.3	.10	.45	-.3	-.4	1227	435	20	7
194	14	-3.7	.4	-8.3	.3	-3.3	-8.7	-3.7	-9.5	5.5	.2	6.3	.2	-.15	.38	-.4	.0	193	345	3	5
195	14	-2.7	.2	-7.5	.4	-2.8	-7.1	-2.6	-10.2	5.9	.1	5.7	.2	-.32	-.34	-.4	-.5	869	233	14	3
196	14	-1.8	.2	-10.3	.8	-1.7	-10.6	-3.9	-10.4	5.3	.2	6.1	.4	-.52	-.40	.1	-.8	615	61	10	1
197	14	-3.8	.3	-12.5	1.0	-3.5	-12.8	-3.6	-15.8	4.7	.1	6.7	.3	.14	-.18	-1.2	-1.5	258	44	4	0
198	15	25.4	.2	40.1	.4	25.2	40.0	24.9	42.0	7.7	.2	13.5	.3	-.25	-.60	0.0	-.1	1264	1097	21	18
199	15	16.6	.4	28.3	1.1	16.0	26.3	17.4	36.6	9.6	.3	19.2	.6	-.22	-.39	-.1	-.6	653	318	10	5
200	15	11.3	.3	26.9	.7	10.7	24.6	12.4	40.3	9.5	.2	19.0	.4	-.15	-.27	-.0	-.8	783	745	13	12
201	15	6.3	.5	19.4	.8	5.3	17.4	10.5	25.8	8.5	.3	18.4	.4	.18	.14	-.2	-.8	279	593	4	9
202	15	1.8	.4	12.7	.9	1.1	9.5	.8	21.6	9.6	.3	18.7	.6	.10	.22	-.2	-.6	504	403	8	6
203	15	.7	.4	7.3	1.3	.2	5.0	.9	13.5	8.8	.3	17.4	.9	-.01	.25	.1	0.0	394	189	6	3
204	15	-3.0	.4	-.3	.9	-3.7	-2.1	-4.4	.1	8.9	.3	13.5	.7	.17	.40	.1	.4	421	222	7	3
205	15	-2.4	.2	.1	.3	-2.4	-.8	-3.4	.8	6.3	.1	10.0	.3	-.15	.11	.3	.5	1214	865	20	14
206	15	-2.0	.2	-3.2	.4	-2.4	-3.7	-3.9	-4.4	7.3	.1	9.3	.3	-.31	.19	-.5	.1	1193	614	19	10
207	15	-3.6	.3	-2.6	.3	-3.8	-3.3	-5.5	-3.9	7.3	.2	8.2	.2	-.09	.07	-.3	-.2	464	603	7	10
208	15	-4.3	.2	-4.3	.3	-4.4	-4.8	-6.5	-3.8	7.2	.1	8.4	.2	.12	.23	-.4	.1	1240	688	20	11
209	15	-3.8	.2	-6.5	.3	-4.1	-6.5	-5.7	-9.4	6.7	.1	7.3	.2	0.00	-.00	.0	-.4	1329	551	22	9
210	15	-4.4	.3	-4.8	.3	-4.7	-5.5	-5.8	-5.5	6.6	.2	8.4	.2	.02	.46	.4	-.1	518	598	8	9
211	15	-5.2	.2	-7.0	.2	-5.4	-7.1	-6.9	-8.9	6.8	.2	5.7	.2	-.24	.08	.4	.2	813	545	13	9
212	15	-4.9	.5	-6.4	.3	-4.8	-6.7	-6.4	-7.6	6.1	.3	6.7	.2	-.27	-.06	-.8	.6	147	571	2	9
213	15	-4.6	.2	-7.3	.3	-4.8	-7.8	-5.8	-9.6	5.8	.1	5.4	.3	-.10	.35	-.2	2.2	1110	471	18	7
214	-15	31.6	.0	45.8	.0	31.7	45.9	31.9	46.5	2.3	.0	1.9	.0	-.15	-.65	-.0	.5	4082	4052	194	163
215	-15	31.1	.0	45.5	.0	31.2	45.6	31.3	45.8	2.1	.0	1.9	.0	-.21	-.51	.2	.1	3517	3669	58	61
216	-15	30.9	.0	45.6	.0	31.0	45.7	31.2	45.8	2.0	.0	1.9	.0	-.15	-.52	.5	.2	1881	2084	31	34
217	-15	30.7	.0	46.2	.0	30.8	46.3	30.9	46.5	2.0	.0	1.8	.0	-.28	-.36	-.0	0.0	4072	4044	167	129

[a]Negative denotes that part of scan below wing.
[b]Corrected for velocity bias including Bragg effects.

TABLE III.- Concluded

Run	Scan (a)	$U_{L,e}$ m/s	$\delta U_{L,e}$ m/s	$V_{L,e}$ m/s	$\delta V_{L,e}$ m/s	$U_{L,B}$ m/s (b)	$V_{L,B}$ m/s (b)	$U_{L,a}$ m/s	$V_{L,a}$ m/s	σ_u m/s	$\delta\sigma_u$ m/s	σ_v m/s	$\delta\sigma_v$ m/s	$S_{R,u}$	$S_{R,v}$	E_u	E_v	D_u	D_v	D.R. meas/sec u	D.R. meas/sec v
218	-15	30.3	.1	45.8	.1	30.5	45.8	30.4	46.1	1.9	.1	1.9	.0	-.13	-.38	.2	-.2	556	642	9	10
219	16	-1.8	.2	-1.6	.5	-2.0	-2.6	-3.9	-.6	7.2	.2	9.8	.3	-.12	-.11	-.1	-.0	978	448	16	7
220	16	-1.7	.9	-3.5	.8	-1.9	-4.7	-1.4	-3.3	6.6	.7	9.7	.7	-.17	.77	.3	1.1	51	145	0	2
221	16	-7.7	.3	-3.4	.5	-7.8	-4.5	-9.5	-3.2	7.4	.2	10.1	.4	.23	.36	.1	-.0	537	357	8	5
222	16	-7.5	.2	-2.9	.5	-7.8	-4.0	-8.5	-5.0	6.4	.2	9.0	.3	.17	.01	.4	-.5	671	293	11	4
223	16	-9.0	.3	-5.9	.7	-9.2	-7.2	-10.8	-8.3	6.9	.2	7.9	.6	.22	.51	.3	.8	617	137	10	2
224	16	-7.8	.2	-6.4	.3	-7.8	-6.0	-9.5	-7.4	6.5	.2	4.3	.2	-.10	-.17	-.1	.1	720	273	12	4
225	16	-7.6	.3	-7.5	.3	-7.6	-7.5	-11.6	-7.7	5.2	.2	3.7	.2	-.64	-.75	-.4	.2	290	215	4	3
226	16	-7.9	.3	-4.7	.2	-8.0	-4.6	-9.5	-4.8	5.1	.2	2.9	.1	-.42	-.04	-.4	-.4	380	196	6	3
227	16	-4.1	.2	-1.1	.3	-4.4	-1.2	-4.4	-1.3	5.7	.2	4.9	.1	.76	.45	.6	-.7	567	357	9	5
228	16	-5.8	.2	-5.2	.2	-5.5	-5.0	-7.7	-5.7	4.7	.1	4.0	.2	.09	.25	-.4	1.1	524	298	8	4
229	16	-1.7	.3	1.7	.3	-2.0	1.3	-2.8	2.3	5.7	.2	4.9	.2	.08	.27	-.5	-.1	430	275	7	4
230	16	9.3	.5	16.6	.5	8.7	15.8	10.7	17.2	8.9	.4	9.0	.4	.05	.66	.1	.1	290	319	4	5
231	16	28.3	.3	41.6	.4	28.3	41.5	30.0	44.7	6.0	.2	8.6	.4	-.17	-1.14	-.4	1.3	565	405	9	6
232	16	29.2	.5	43.8	.6	29.2	44.3	30.6	46.4	6.4	.3	6.8	.4	-.79	-.50	.0	.2	166	133	2	2
233	16	32.9	.1	48.7	.1	33.0	48.8	33.7	49.4	3.0	.1	2.7	.1	-.77	-1.28	.2	1.0	1893	1511	31	25
234	16	34.0	.1	48.1	.1	34.1	48.2	34.6	49.2	3.0	.1	3.8	.1	-1.26	-.99	1.6	-.2	2324	2182	38	36
235	16	32.7	.0	48.1	.0	32.8	48.1	33.3	48.9	2.9	.0	3.0	.0	-.55	-.87	-.1	-.1	4066	3878	202	64
236	16	31.9	.0	47.7	.0	31.9	47.8	32.4	48.1	2.5	.0	1.9	.0	-.04	-.41	-.3	.0	4087	4055	327	267
237	16	31.6	.0	47.3	.0	31.6	47.4	31.9	47.7	2.5	.0	2.0	.0	-.08	-.47	-.2	.2	4083	4031	286	178
238	16	31.9	.0	47.1	.0	31.9	47.3	32.3	47.5	2.4	.0	1.9	.0	-.16	-.48	-.2	.1	4083	4031	246	169
239	16	32.1	.0	46.3	.0	32.1	46.4	32.4	46.7	2.2	.0	1.9	.0	-.05	-.59	-.2	.4	4077	4034	208	136
240	16	32.3	.0	45.9	.0	32.3	46.0	32.6	46.2	2.3	.0	1.8	.0	-.01	-.55	-.2	.4	4083	4047	212	138
241	17	-10.1	.7	-7.4	.6	-10.3	-8.4	-13.4	-8.5	9.0	.4	9.6	.4	.29	.05	-.8	-.4	166	238	2	3
242	17	-11.3	.4	-4.0	.8	-11.7	-4.5	-13.7	-3.9	7.9	.2	8.8	.7	.01	.07	-.7	1.0	382	128	6	2
243	17	-12.2	.4	-4.7	.4	-12.6	-5.1	-12.9	-7.9	8.3	.3	8.1	.3	.38	-.49	.0	.2	482	365	8	6
244	17	-9.8	.4	-6.6	.7	-10.1	-6.4	-12.7	-7.3	8.3	.2	7.7	.4	.09	-.06	-.3	-.3	480	134	8	2
245	17	-11.8	.3	-2.2	.7	-12.0	-2.4	-14.1	-2.9	6.1	.2	6.8	.5	-.36	.46	.3	-.2	503	88	8	1
246	17	-9.9	.3	-3.6	.4	-10.3	-4.1	-10.5	-3.0	6.2	.2	6.1	.3	.21	.46	.3	.1	566	266	9	4
247	17	7.3	.6	13.4	.5	6.2	13.2	9.9	14.0	11.1	.4	6.3	.4	.27	-.05	-.4	.4	371	143	6	2
248	17	32.1	.4	39.2	.4	32.7	38.8	35.1	40.9	9.4	.3	9.5	.3	-.64	-.98	.2	.3	510	493	8	8
249	17	35.9	.1	48.5	.1	36.0	48.6	36.5	48.8	3.8	.1	2.5	.1	-.88	-.99	.6	1.9	2373	1394	39	23
250	17	34.5	.0	48.0	.0	34.6	48.1	34.9	48.2	2.6	.0	1.6	.0	-.20	-.43	-.1	.5	4082	3209	202	53
251	17	34.2	.0	47.5	.0	34.2	47.6	34.6	47.7	2.5	.0	1.4	.0	-.16	-.45	-.2	.7	4080	2975	176	49
252	17	34.2	.0	47.4	.0	34.3	47.5	34.6	47.6	2.5	.0	1.4	.0	-.13	-.37	-.0	.4	4083	3010	183	50
253	18	32.2	.5	39.6	.5	32.5	39.2	33.6	42.0	10.6	.3	8.4	.4	-.77	-1.16	-.1	.4	484	295	8	4
254	18	37.3	.1	45.6	.2	37.3	45.8	37.9	46.1	3.5	.1	2.7	.1	-.73	-.05	.3	-.6	821	160	13	2
255	18	36.8	.0	48.0	.0	36.8	48.1	37.2	47.7	2.7	.0	1.5	.0	-.27	-.08	.2	.3	3550	2104	59	35
256	18	36.9	.1	47.5	.0	36.9	47.6	36.9	47.8	2.6	.0	1.4	.0	-.34	-.41	.0	1.1	2345	1210	39	20
257	19	39.8	.1	45.8	.1	40.0	46.1	39.6	46.7	4.0	.0	5.0	.1	-.11	-.33	.2	.3	3904	2831	151	47
258	19	38.6	.1	45.2	.1	39.0	45.7	38.3	46.7	4.7	.1	6.3	.1	-.33	-.39	.5	.6	2341	1749	39	29
259	19	37.4	.1	44.1	.2	37.4	44.7	37.6	45.0	5.4	.1	7.8	.2	-.40	-.74	.1	1.0	2135	1392	35	23
260	19	34.8	.1	43.7	.2	35.1	44.4	34.4	45.4	6.1	.1	8.7	.2	-.42	-.70	.3	.8	1825	1550	30	25
261	19	31.9	.2	42.6	.3	31.8	42.3	32.1	46.4	7.5	.1	11.5	.3	-.42	-1.04	.2	.7	1376	1166	22	19
262	19	30.6	.3	42.7	.4	30.3	42.9	31.6	45.2	8.3	.2	11.1	.3	-.37	-.94	-.2	.9	1095	887	18	14
263	19	27.2	.3	38.8	.5	26.7	37.9	26.1	42.1	9.8	.2	14.3	.3	-.34	-.59	-.3	-.5	852	966	14	16
264	19	21.7	.3	37.8	.5	21.2	37.0	23.1	42.8	10.4	.2	14.9	.3	-.09	-.68	-.6	-.1	1081	915	18	15
265	19	20.8	.3	32.6	.7	20.0	30.2	22.3	37.7	10.7	.2	17.8	.4	-.42	-.57	-.3	-.3	1166	720	19	12
266	19	16.4	.4	29.5	.7	15.6	27.5	14.4	35.7	10.6	.3	18.6	.4	-.20	-.39	.2	-.6	720	783	12	13
267	19	12.7	.3	26.1	.7	11.8	23.8	14.7	34.8	10.3	.2	18.9	.3	-.20	.01	-.1	-1.0	1030	825	17	13
268	19	9.8	.4	25.4	.7	8.9	23.2	10.2	30.9	10.9	.3	18.6	.5	-.18	-.40	-.4	-.4	773	648	12	10
269	19	10.2	.4	21.8	.9	9.2	19.8	9.5	29.9	11.2	.3	18.7	.5	-.12	-.00	-.2	-.7	635	441	10	7
270	19	.9	.3	5.1	.4	.2	4.0	.2	13.3	7.9	.2	11.9	.3	-.27	.08	-.2	.2	949	734	15	12
271	19	2.2	.4	24.4	.5	1.4	22.0	3.2	27.0	10.9	.3	20.1	.3	-.09	-.28	-.3	-.8	698	1882	11	31
272	19	-1.8	.2	.4	.7	-2.1	-.9	-.4	1.5	8.3	.2	12.9	.5	-.10	.28	-.1	0.0	1130	365	18	6
273	19	-5.2	.4	-5.2	1.9	-6.0	-5.3	-6.3	-1.8	8.1	.2	9.1	1.0	-.05	-.13	-.3	-.8	459	24	7	0
274	19	-5.3	.2	-2.9	.4	-5.6	-4.1	-9.0	-4.5	7.7	.1	9.8	.3	-.23	.02	-.1	.1	1463	539	24	8
275	19	-7.5	.2	-3.0	.4	-7.7	-4.0	-9.6	-4.4	7.8	.2	11.7	.3	.07	.57	-.1	-.2	1057	721	17	12
276	19	-9.1	.3	-4.3	.3	-9.3	-5.2	-11.3	-5.9	8.3	.2	8.7	.2	.04	.42	-.3	-.0	988	719	16	11
277	19	-11.0	.3	-4.0	.3	-11.3	-4.8	-10.9	-6.4	7.5	.2	8.7	.2	.31	.18	.1	-.2	820	640	13	10
278	19	-10.5	.2	-6.5	.3	-11.0	-6.5	-12.1	-8.3	7.9	.2	7.2	.2	.27	-.06	.1	-.5	1200	662	20	11
279	19	-12.2	.2	-7.3	.2	-12.6	-7.6	-13.9	-8.0	6.0	.2	5.9	.2	-.31	.07	1.0	-.2	776	567	12	9
280	19	-12.2	.2	-6.7	.3	-12.7	-6.9	-13.3	-6.7	6.3	.2	6.4	.2	-.25	.55	-.3	.3	674	472	11	7
281	19	-9.8	.3	-5.8	.5	-10.2	-6.0	-11.3	-5.5	7.1	.2	6.0	.3	-.05	-.43	.3	-.6	737	143	12	2
282	19	-7.8	.3	-5.3	.3	-8.3	-5.3	-9.3	-5.7	8.1	.3	5.2	.2	-.06	-.18	.1	-.3	547	427	9	7
283	19	2.2	.5	5.9	.3	1.1	5.6	4.7	6.3	11.9	.3	6.3	.2	.49	.67	-.2	.2	543	416	9	6
284	19	-6.5	.5	-1.1	.5	-7.2	-1.6	-8.8	-2.9	8.4	.4	6.6	.3	.49	-.04	.1	-.1	267	203	4	3
285	19	9.6	1.2	15.2	.7	7.6	14.4	13.5	17.3	16.3	.8	8.5	.5	.40	.39	-.3	-.2	197	156	3	2
286	19	31.9	.5	36.4	.4	31.3	35.9	34.4	38.3	13.7	.3	10.3	.3	-.75	-1.02	-.2	.2	768	848	12	14
287	19	38.3	.0	47.6	.0	33.4	47.7	38.6	47.9	2.8	.0	1.9	.0	-.47	-.28	1.0	.7	4061	4038	171	135
288	19	37.1	.0	47.3	.0	37.2	47.3	37.5	47.4	2.8	.0	1.6	.0	-.30	.03	0.0	.2	4079	4051	208	163
289	19	37.0	.0	47.0	.0	37.1	47.0	37.3	47.0	2.6	.0	1.5	.0	-.36	-.01	.1	.5	4083	4060	186	138

[a]Negative denotes that part of scan below wing.
[b]Corrected for velocity bias including Bragg effects.

TABLE IV.- VELOCITIES FROM ENSEMBLE AVERAGES

Run	Scan	$\frac{U_f}{U_T}$	$\frac{V_f}{U_T}$	$\frac{U_R}{U_T}$	α_R, deg	$\frac{x_f}{c}$	$\frac{y_f}{c}$	$\frac{x_c}{c}$	$\frac{y_c}{c}$	α_s, deg	s	N
1	1	.95	.15	.96	9.0	1.048	.540	-.168	.161	-29.9	.017	.228
2	1	.95	.17	.97	10.0	1.048	.525	-.163	.147	-31.7	.016	.215
3	1	.94	.15	.95	9.3	1.055	.504	-.163	.125	-35.9	.014	.202
4	1	.92	.14	.93	8.8	1.062	.486	-.163	.106	-40.2	.012	.192
5	1	.92	.15	.93	9.2	1.069	.465	-.163	.083	-45.8	.009	.181
6	1	.91	.14	.92	8.6	1.077	.446	-.163	.063	-51.3	.007	.174
7	1	.90	.13	.91	8.3	1.083	.426	-.163	.042	-57.4	.005	.168
8	1	.89	.13	.90	8.6	1.089	.407	-.163	.022	-63.5	.003	.164
9	1	.87	.13	.88	8.2	1.095	.388	-.162	.002	-70.0	.000	.162
10	1	.86	.12	.87	8.0	1.102	.366	-.162	-.021	-64.0	-.002	.163
11	1	.86	.11	.86	7.2	1.110	.348	-.162	-.041	-83.5	-.005	.167
12	1	.84	.11	.85	7.2	1.117	.328	-.162	-.062	-89.8	-.007	.173
13	1	.84	.10	.85	6.6	1.122	.308	-.160	-.082	-95.4	-.009	.178
14	1	.84	.09	.84	5.9	1.129	.289	-.161	-.102	-100.5	-.011	.188
15	1	.84	.07	.84	4.9	1.139	.268	-.163	-.125	-105.2	-.014	.203
16	1	.84	.06	.84	4.3	1.144	.250	-.162	-.144	-109.1	-.016	.213
17	2	.91	.24	.95	14.9	.982	.453	-.077	.101	-24.7	.021	.121
18	2	.90	.22	.93	13.9	.990	.437	-.079	.084	-30.1	.017	.110
19	2	.88	.22	.91	13.8	.996	.417	-.078	.063	-37.4	.013	.097
20	2	.86	.21	.88	14.0	1.005	.398	-.080	.041	-47.6	.008	.089
21	2	.83	.20	.86	13.4	1.018	.379	-.086	.019	-60.0	.004	.088
22	2	.81	.19	.83	13.2	1.018	.358	-.079	-.000	-70.6	-.050	-.000
23	2	.78	.17	.80	12.4	1.023	.339	-.078	-.021	-83.0	-.004	.080
24	2	.77	.15	.78	11.3	1.031	.320	-.079	-.041	-93.6	-.008	.087
25	2	.76	.12	.77	9.0	1.038	.298	-.078	-.064	-104.3	-.013	.097
26	2	.78	.10	.78	7.4	1.044	.280	-.077	-.083	-111.3	-.017	.108
27	2	.79	.08	.79	5.9	1.051	.261	-.078	-.103	-116.6	-.021	.123
28	2	.80	.07	.81	4.7	1.059	.241	-.079	-.124	-121.1	-.024	.139
29	3	.89	.29	.93	17.9	.962	.422	-.048	.078	-22.4	.022	.084
30	3	.86	.30	.91	19.3	.964	.405	-.043	.061	-26.7	.019	.069
31	3	.82	.31	.88	20.8	.963	.385	-.036	.044	-32.4	.016	.052
32	3	.75	.30	.81	21.8	.972	.365	-.038	.021	-49.1	.008	.042
33	3	.71	.26	.76	20.0	.978	.344	-.036	-.000	-70.2	-.000	.036
34	3	.69	.21	.72	16.7	.984	.326	-.036	-.019	-90.9	-.007	.040
35	3	.69	.16	.71	13.0	.992	.306	-.037	-.041	-106.8	-.014	.051
36	3	.69	.12	.70	10.2	.994	.287	-.033	-.060	-118.0	-.022	.060
37	3	.71	.10	.72	7.6	1.007	.267	-.038	-.083	-123.3	-.026	.082
38	3	.72	.06	.72	4.9	1.013	.246	-.037	-.104	-128.4	-.032	.098
39	4	.94	.14	.95	8.8	1.004	.529	-.123	.165	-21.9	.023	.199
40	4	.94	.18	.96	10.8	.993	.500	-.102	.142	-21.9	.023	.168
41	4	.94	.19	.96	11.6	.986	.484	-.091	.129	-21.8	.023	.151
42	4	.93	.20	.95	12.3	.982	.469	-.082	.116	-22.4	.022	.135
43	4	.92	.22	.95	13.7	.974	.453	-.069	.104	-22.0	.023	.117
44	4	.91	.24	.94	14.6	.966	.438	-.057	.092	-21.4	.023	.100
45	4	.90	.26	.93	16.0	.964	.423	-.050	.079	-23.1	.022	.086
46	4	.88	.27	.92	17.1	.957	.407	-.038	.066	-23.0	.022	.069
47	4	.86	.30	.91	19.0	.951	.391	-.027	.052	-23.6	.021	.051
48	4	.83	.33	.90	21.4	.945	.375	-.015	.040	-23.6	.021	.034
49	4	.79	.37	.88	25.1	.942	.368	-.010	.034	-24.0	.021	.026
50	4	.75	.40	.85	28.3	.941	.360	-.007	.027	-26.6	.019	.019
51	4	.75	.36	.83	25.5	.936	.352	-.000	.021	-25.6	.020	.010
52	-4	.77	.08	.77	6.0	1.038	.249	-.061	-.110	-122.6	-.026	.117
53	-4	.76	.07	.76	5.6	1.036	.249	-.060	-.110	-123.0	-.026	.116
54	-4	.75	.08	.76	6.4	1.033	.258	-.060	-.099	-120.7	-.024	.108
55	-4	.75	.11	.76	8.0	1.018	.266	-.049	-.087	-120.9	-.024	.091
56	-4	.70	.10	.70	8.0	1.002	.275	-.036	-.074	-121.6	-.025	.073
57	-4	.74	.07	.74	5.7	.989	.284	-.027	-.060	-120.9	-.024	.057
58	-4	.78	.09	.78	6.6	.989	.284	-.027	-.061	-121.2	-.024	.057
59	-4	.72	.12	.73	9.8	.980	.288	-.019	-.054	-121.8	-.025	.047
60	-4	.69	.13	.70	10.5	.974	.293	-.016	-.047	-120.9	-.024	.040
61	5	.91	.36	.97	21.5	.921	.408	-.004	.079	-7.2	.042	.060
62	5	.90	.42	.99	25.0	.921	.395	.001	.062	-7.9	.040	.047
63	5	.86	.47	.98	28.9	.922	.379	.005	.039	-9.2	.038	.032
64	5	.78	.55	.95	35.1	.928	.363	.004	.023	-14.6	.030	.017
65	5	.72	.50	.87	34.6	.934	.355	.002	.017	-21.6	.023	.011
66	5	.77	.36	.85	25.3	.934	.350	.002	.011	-24.4	.021	.007
67	-5	.59	.10	.60	9.2	.954	.285	.005	-.036	-131.5	-.037	.029
68	-5	.61	.06	.61	6.0	.960	.269	.005	-.053	-134.7	-.043	.044
69	-5	.63	.04	.63	3.2	.967	.253	.004	-.071	-136.8	-.048	.060
70	6	1.00	.21	1.02	12.1	.901	.545	-.031	.215	-1.0	.058	.196
71	6	.98	.18	.99	10.7	.903	.513	-.022	.184	-1.3	.057	.164

TABLE IV.- Continued

Run	Scan	$\frac{U_f}{U_T}$	$\frac{V_f}{U_T}$	$\frac{U_R}{U_T}$	$\alpha_{R'}$, deg	$\frac{x_f}{c}$	$\frac{y_f}{c}$	$\frac{x_c}{c}$	$\frac{y_c}{c}$	$\alpha_{s'}$, deg	s	N
72	6	1.00	.26	1.03	14.6	.904	.498	-.018	.169	-1.6	.056	.149
73	6	1.00	.31	1.04	17.2	.903	.463	-.006	.137	-1.7	.055	.114
74	6	1.00	.37	1.07	20.2	.901	.431	.007	.093	-1.3	.057	.082
75	6	.96	.31	1.01	17.8	.900	.414	.014	.072	-1.1	.057	.065
76	6	.94	.43	1.04	24.6	.902	.396	.018	.052	-1.8	.055	.047
77	6	.94	.53	1.08	29.7	.903	.381	.022	.035	-2.2	.054	.032
78	6	.93	.63	1.12	34.0	.902	.373	.025	.026	-2.1	.054	.024
79	6	.81	.43	.91	27.9	.902	.365	.028	.017	-2.2	.054	.016
80	6	.03	.06	.07	64.3	.902	.357	.031	.009	-2.1	.054	.008
81	-6	.66	.01	.66	.5	.967	.237	.010	-.081	-139.6	-.056	.072
82	-6	.66	-.03	.66	-2.5	.953	.247	.019	-.060	-140.5	-.059	.055
83	-6	.71	.02	.71	1.6	.944	.260	.024	-.043	-140.2	-.058	.039
84	-6	.79	.05	.79	3.5	.938	.267	.027	-.033	-140.2	-.058	.030
85	7	1.05	.23	1.08	12.3	.805	.557	.056	.221	9.2	.118	.216
86	7	1.01	.20	1.03	11.4	.810	.543	.055	.206	9.0	.115	.201
87	7	1.01	.23	1.04	12.7	.812	.509	.065	.171	9.3	.118	.167
88	7	1.00	.24	1.03	13.4	.818	.478	.070	.138	9.2	.117	.135
89	7	1.00	.28	1.04	15.8	.823	.444	.076	.104	9.2	.118	.102
90	7	1.02	.32	1.07	17.5	.828	.428	.077	.086	9.1	.116	.085
91	7	1.02	.36	1.08	19.2	.829	.412	.081	.070	9.2	.117	.068
92	7	.99	.33	1.04	18.7	.831	.395	.085	.052	9.2	.117	.051
93	7	.86	.28	.91	18.1	.834	.386	.085	.043	9.1	.116	.042
94	7	.55	.12	.57	12.2	.836	.378	.086	.035	9.0	.116	.034
95	8	1.09	.22	1.11	11.3	.737	.554	.121	.227	13.3	.169	.226
96	8	1.06	.24	1.09	12.7	.738	.514	.133	.188	13.7	.176	.187
97	8	1.09	.26	1.12	13.4	.744	.479	.139	.153	13.8	.179	.152
98	8	1.10	.28	1.14	14.2	.750	.446	.144	.119	13.9	.180	.118
99	8	1.01	.23	1.04	13.0	.761	.414	.145	.085	13.8	.178	.084
100	8	.94	.24	.97	14.1	.767	.406	.141	.076	13.5	.174	.075
101	8	.75	.17	.77	13.2	.765	.398	.147	.069	13.8	.178	.068
102	8	.44	.09	.45	11.8	.765	.390	.149	.060	13.8	.179	.060
103	8	.25	.07	.26	15.0	.767	.382	.150	.052	13.9	.179	.052
104	9	1.13	.21	1.15	10.4	.626	.544	.229	.246	17.5	.262	.246
105	9	1.14	.23	1.16	11.6	.628	.513	.237	.217	17.7	.268	.217
106	9	1.15	.25	1.18	12.2	.636	.481	.240	.184	17.8	.270	.184
107	9	1.14	.20	1.15	10.2	.647	.450	.240	.150	17.8	.269	.150
108	9	1.06	.16	1.07	8.7	.657	.436	.235	.134	17.6	.264	.134
109	9	.78	.10	.78	7.2	.655	.420	.242	.119	17.8	.271	.119
110	9	.45	.06	.45	7.3	.663	.403	.241	.101	17.7	.268	.101
111	9	.24	-.03	.24	-6.5	.667	.388	.242	.085	17.8	.270	.085
112	9	.06	.03	.07	28.8	.672	.372	.242	.068	17.8	.269	.068
113	10	1.16	.18	1.18	8.8	.500	.536	.351	.280	20.5	.370	.280
114	10	1.16	.20	1.18	9.6	.501	.505	.360	.251	20.7	.379	.251
115	10	1.14	.13	1.14	6.7	.514	.474	.358	.217	20.6	.379	.217
116	10	1.06	.11	1.07	5.7	.518	.460	.359	.202	20.7	.379	.202
117	10	.88	.10	.89	6.7	.524	.444	.358	.186	20.7	.379	.185
118	10	.70	.07	.70	5.9	.529	.427	.359	.167	20.7	.380	.167
119	10	.53	-.00	.53	-.5	.537	.411	.357	.150	20.7	.379	.150
120	10	.31	.00	.31	.3	.543	.396	.356	.134	20.6	.378	.134
121	10	.12	.02	.12	10.3	.547	.381	.358	.118	20.7	.380	.118
122	10	.01	.02	.03	56.9	.553	.364	.358	.100	20.7	.380	.100
123	10	-.06	.05	.08	141.2	.559	.350	.356	.085	20.7	.379	.085
124	10	-.06	.04	.07	147.4	.566	.334	.355	.068	20.7	.379	.068
125	11	1.16	.15	1.17	7.6	.346	.545	.492	.346	22.7	.498	.345
126	11	1.17	.09	1.17	4.4	.348	.517	.500	.319	22.8	.506	.319
127	11	1.11	.03	1.12	1.5	.361	.486	.499	.286	22.8	.507	.285
128	11	.94	.01	.94	.4	.375	.455	.495	.252	22.8	.506	.251
129	11	.65	-.03	.65	-2.5	.387	.424	.494	.218	22.8	.507	.218
130	11	.49	-.00	.49	-.1	.395	.409	.492	.202	22.8	.505	.201
131	11	.38	-.05	.38	-6.8	.402	.394	.490	.184	22.7	.505	.184
132	11	.17	.07	.18	23.3	.408	.378	.490	.167	22.8	.505	.167
133	11	.09	.02	.09	9.4	.413	.362	.491	.151	22.8	.507	.151
134	11	.05	.03	.06	31.6	.419	.348	.489	.135	22.8	.507	.135
135	11	-.03	.07	.07	110.9	.427	.333	.487	.118	22.8	.505	.118
136	11	-.09	.08	.12	137.6	.433	.316	.487	.101	22.8	.506	.101
137	11	-.11	.04	.11	157.9	.438	.302	.487	.086	22.8	.507	.085
138	11	-.11	.08	.13	144.1	.445	.287	.485	.069	22.8	.506	.069
139	12	1.18	.05	1.18	2.3	.208	.531	.628	.388	24.1	.622	.387
140	12	1.14	.02	1.14	.8	.207	.507	.636	.367	24.2	.631	.365
141	12	1.05	-.02	1.05	-1.2	.217	.487	.634	.345	24.1	.631	.344
142	12	.86	-.02	.86	-1.2	.228	.463	.631	.318	24.1	.631	.317
143	12	.67	-.03	.67	-2.7	.239	.441	.629	.293	24.1	.630	.292
144	12	.47	-.02	.47	-2.8	.248	.419	.627	.270	24.1	.630	.269

TABLE IV.- Continued

Run	Scan	$\frac{U_f}{U_T}$	$\frac{V_f}{U_T}$	$\frac{U_R}{U_T}$	$\alpha_{R'}$, deg	$\frac{x_f}{c}$	$\frac{y_f}{c}$	$\frac{x_c}{c}$	$\frac{y_c}{c}$	$\alpha_{s'}$, deg	s	N
145	12	.28	-.01	.28	-1.7	.259	.396	.625	.244	24.1	.630	.243
146	12	.16	.03	.17	9.5	.269	.372	.623	.218	24.1	.631	.217
147	12	.08	.05	.09	33.9	.279	.351	.620	.194	24.1	.630	.193
148	12	.01	.05	.05	83.6	.289	.327	.619	.169	24.1	.631	.168
149	12	.01	.03	.04	74.2	.296	.312	.618	.152	24.1	.631	.151
150	12	-.08	.08	.11	133.8	.302	.296	.617	.135	24.1	.631	.134
151	12	-.09	.10	.13	131.8	.309	.283	.614	.120	24.1	.630	.119
152	12	-.14	.10	.17	144.9	.316	.268	.613	.103	24.1	.630	.103
153	12	-.13	.08	.15	148.9	.322	.252	.613	.086	24.1	.631	.086
154	12	-.14	.08	.16	149.0	.331	.236	.609	.068	24.1	.629	.068
155	13	1.18	-.01	1.18	-.6	.032	.534	.793	.466	25.3	.772	.463
156	13	1.16	-.10	1.17	-4.7	.033	.509	.800	.443	25.4	.781	.440
157	13	1.07	-.08	1.08	-4.3	.041	.489	.799	.421	25.4	.782	.419
158	13	.97	-.11	.98	-6.7	.053	.467	.795	.396	25.4	.781	.394
159	13	.94	-.18	.96	-10.9	.063	.442	.794	.369	25.4	.783	.367
160	13	.75	-.18	.77	-13.1	.073	.421	.791	.345	25.4	.782	.343
161	13	.53	-.09	.54	-9.7	.084	.399	.788	.321	25.4	.782	.319
162	13	.42	-.11	.43	-14.4	.095	.377	.786	.296	25.4	.782	.294
163	13	.27	-.03	.27	-7.3	.107	.354	.782	.270	25.4	.780	.269
164	13	.16	-.02	.16	-7.2	.115	.332	.781	.246	25.4	.782	.245
165	13	.07	.01	.07	4.2	.128	.309	.776	.220	25.4	.780	.219
166	13	.05	-.03	.06	-27.3	.139	.285	.774	.194	25.4	.781	.193
167	13	-.02	.05	.05	114.2	.149	.264	.772	.170	25.4	.781	.169
168	13	-.13	.08	.15	150.5	.157	.249	.770	.153	25.4	.781	.152
169	13	-.00	-.02	.02	-92.0	.164	.234	.768	.137	25.4	.781	.136
170	13	-.05	.02	.05	158.2	.170	.219	.767	.121	25.4	.781	.120
171	13	-.12	.06	.14	152.5	.178	.202	.765	.101	25.4	.782	.101
172	13	-.16	.10	.19	146.3	.185	.186	.764	.084	25.4	.782	.084
173	13	-.18	.07	.19	158.6	.189	.172	.764	.069	25.4	.784	.069
174	14	1.18	-.12	1.19	-5.6	-.093	.536	.910	.524	26.1	.877	.520
175	14	1.17	-.13	1.18	-6.3	-.093	.517	.916	.506	26.2	.885	.502
176	14	1.13	-.16	1.14	-7.9	-.085	.495	.916	.482	26.2	.887	.479
177	14	1.06	-.17	1.08	-8.8	-.071	.472	.910	.455	26.2	.885	.452
178	14	1.00	-.17	1.01	-9.7	-.063	.450	.910	.432	26.2	.887	.429
179	14	.80	-.19	.83	-13.4	-.051	.427	.906	.406	26.2	.887	.403
180	14	.65	-.23	.69	-19.1	-.040	.405	.904	.381	26.2	.887	.379
181	14	.84	-.24	.87	-16.0	-.039	.402	.903	.378	26.2	.887	.376
182	14	.76	-.24	.79	-17.8	-.030	.385	.901	.359	26.2	.887	.357
183	14	.61	-.22	.65	-20.3	-.021	.368	.897	.339	26.2	.885	.336
184	14	.53	-.23	.58	-23.4	-.012	.348	.896	.317	26.2	.886	.315
185	14	.38	-.15	.41	-22.0	-.003	.329	.893	.296	26.2	.886	.294
186	14	.32	-.28	.43	-41.4	.006	.311	.891	.275	26.2	.886	.273
187	14	.23	-.15	.27	-33.3	.015	.292	.889	.254	26.2	.887	.252
188	14	.24	-.15	.29	-32.5	.024	.272	.887	.233	26.2	.887	.231
189	14	.08	-.07	.11	-41.9	.034	.254	.883	.212	26.2	.887	.210
190	14	.09	-.08	.12	-40.2	.043	.236	.881	.191	26.2	.887	.190
191	14	-.09	.10	.14	132.6	.063	.216	.869	.165	26.1	.878	.164
192	14	-.14	.09	.17	145.9	.064	.200	.873	.150	26.1	.884	.149
193	14	-.09	.06	.11	143.6	.067	.186	.875	.135	26.2	.887	.135
194	14	-.17	.07	.19	157.1	.075	.172	.872	.119	26.2	.886	.118
195	14	-.14	.07	.15	154.2	.083	.158	.869	.103	26.2	.885	.102
196	14	-.17	.12	.20	144.4	.088	.143	.870	.087	26.2	.887	.087
197	14	-.22	.12	.26	151.5	.096	.129	.867	.071	26.2	.886	.071
198	15	.89	-.21	.92	-13.3	-.148	.406	1.005	.432	26.9	.978	.427
199	15	.61	-.17	.64	-15.2	-.147	.376	1.014	.403	27.0	.990	.400
200	15	.52	-.22	.57	-22.8	-.134	.346	1.012	.371	27.0	.992	.368
201	15	.35	-.18	.40	-27.7	-.120	.317	1.008	.338	27.0	.993	.335
202	15	.20	-.15	.25	-37.5	-.106	.288	1.004	.307	27.0	.993	.303
203	15	.11	-.09	.14	-40.2	-.090	.257	.999	.271	27.0	.993	.268
204	15	-.05	-.04	.06	-142.0	-.074	.228	.994	.237	27.0	.992	.235
205	15	-.03	-.03	.05	-132.2	-.075	.226	.996	.236	27.1	.994	.234
206	15	-.07	.02	.08	165.8	-.061	.199	.992	.205	27.1	.994	.203
207	15	-.09	-.01	.09	-172.0	-.044	.169	.986	.171	27.0	.992	.170
208	15	-.12	.00	.12	179.4	-.038	.155	.984	.155	27.0	.993	.154
209	15	-.14	.04	.15	164.9	-.029	.141	.980	.138	27.0	.991	.137
210	15	-.13	.01	.13	177.2	-.022	.125	.980	.121	27.0	.993	.120
211	15	-.17	.03	.17	171.0	-.013	.111	.975	.105	27.0	.991	.104
212	15	-.16	.02	.16	171.4	-.006	.097	.974	.088	27.0	.991	.088
213	15	-.17	.04	.17	166.9	-.000	.081	.973	.072	27.0	.993	.071
214	-15	1.08	-.21	1.10	-11.0	.053	-.074	.974	-.083	11.8	-.993	.082
215	-15	1.07	-.21	1.09	-11.2	.054	-.059	.969	-.068	11.8	-.989	.067
216	-15	1.07	-.22	1.09	-11.5	.053	-.044	.964	-.053	11.8	-.987	.052
217	-15	1.07	-.23	1.10	-12.0	.053	-.027	.959	-.036	11.8	-.983	.036

TABLE IV.- Concluded

Run	Scan	$\frac{U_f}{U_T}$	$\frac{V_f}{U_T}$	$\frac{U_R}{U_T}$	α_R, deg	$\frac{x_f}{c}$	$\frac{y_f}{c}$	$\frac{x_c}{c}$	$\frac{y_c}{c}$	α_s, deg	s	N
218	-15	1.06	-.23	1.08	-12.1	.051	-.018	.958	-.027	11.8	-.984	.027
219	16	-.05	-.00	.05	-178.0	-.087	.206	1.014	.223	19.4	1.044	.223
220	16	-.07	.03	.08	160.1	-.087	.174	1.024	.193	19.4	1.054	.193
221	16	-.16	-.05	.17	-162.6	-.077	.143	1.025	.161	19.4	1.055	.161
222	16	-.15	-.06	.16	-156.9	-.066	.112	1.025	.127	19.4	1.055	.127
223	16	-.21	-.04	.21	-169.2	-.055	.078	1.026	.092	19.4	1.056	.092
224	16	-.20	-.02	.20	-175.0	-.044	.048	1.026	.060	19.4	1.056	.060
225	16	-.21	.00	.21	179.5	-.034	.018	1.027	.028	19.4	1.056	.028
226	16	-.18	-.04	.18	-166.5	-.028	.009	1.023	.018	19.4	1.053	.018
227	16	-.07	-.04	.08	-150.2	-.028	.002	1.026	.011	19.4	1.055	.011
228	16	-.15	-.01	.15	-177.3	-.022	.003	1.020	.010	19.4	1.050	.010
229	16	.00	-.05	.05	-89.9	-.023	-.002	1.022	.006	19.4	1.052	.006
230	16	.36	-.11	.37	-16.4	-.022	-.005	1.023	.002	19.4	1.053	.002
231	16	.97	-.20	.99	-11.4	-.026	-.006	1.026	.003	19.4	1.056	.003
232	16	1.02	-.21	1.04	-11.9	-.022	-.010	1.024	-.002	19.4	-1.054	.002
233	16	1.14	-.23	1.16	-11.5	-.023	-.015	1.026	-.006	19.4	-1.056	.006
234	16	1.14	-.21	1.16	-10.4	-.023	-.015	1.026	-.006	19.4	-1.056	.006
235	16	1.12	-.23	1.14	-11.4	-.019	-.019	1.024	-.011	19.4	-1.054	.011
236	16	1.11	-.23	1.13	-11.9	-.017	-.029	1.026	-.022	19.4	-1.056	.022
237	16	1.10	-.23	1.12	-11.9	-.014	-.037	1.025	-.030	19.4	-1.055	.030
238	16	1.10	-.22	1.12	-11.5	-.013	-.045	1.027	-.038	19.4	-1.057	.038
239	16	1.09	-.21	1.11	-10.9	-.006	-.061	1.026	-.055	19.4	-1.055	.055
240	16	1.09	-.20	1.10	-10.5	-.006	-.073	1.029	-.067	19.4	-1.059	.067
241	17	-.24	-.04	.25	-171.7	-.146	.190	1.075	.228	19.4	1.104	.228
242	17	-.21	-.10	.24	-155.0	-.141	.150	1.084	.188	19.4	1.113	.188
243	17	-.24	-.10	.26	-156.5	-.130	.111	1.085	.148	19.4	1.115	.148
244	17	-.23	-.04	.23	-169.6	-.115	.072	1.084	.106	19.4	1.114	.106
245	17	-.20	-.13	.24	-146.2	-.102	.032	1.085	.064	19.4	1.115	.064
246	17	-.19	-.08	.21	-155.8	-.085	.013	1.076	.041	19.4	1.106	.041
247	17	.29	-.09	.30	-17.2	-.088	-.007	1.086	.023	19.4	1.115	.023
248	17	.99	-.11	1.00	-6.3	-.085	-.016	1.085	.013	19.4	1.115	.013
249	17	1.17	-.19	1.19	-9.1	-.080	-.027	1.085	.002	19.4	1.114	.002
250	17	1.15	-.20	1.16	-9.9	-.073	-.045	1.084	-.018	19.4	-1.114	.018
251	17	1.14	-.20	1.15	-9.9	-.066	-.065	1.084	-.039	19.4	-1.114	.039
252	17	1.13	-.20	1.15	-9.8	-.065	-.074	1.086	-.048	19.4	-1.115	.048
253	18	1.00	-.11	1.01	-6.5	-.142	-.022	1.141	.027	19.4	1.171	.027
254	18	1.15	-.13	1.16	-6.3	-.139	-.037	1.143	.011	19.4	1.173	.011
255	18	1.18	-.17	1.19	-8.2	-.133	-.054	1.143	-.006	19.4	-1.173	.006
256	18	1.17	-.16	1.18	-7.8	-.127	-.070	1.142	-.024	19.4	-1.172	.024
257	19	1.18	-.09	1.18	-4.6	-.147	.536	.961	.548	26.5	.922	.544
258	19	1.15	-.10	1.16	-5.1	-.148	.519	.967	.533	26.5	.930	.528
259	19	1.12	-.10	1.12	-5.3	-.147	.498	.973	.514	26.6	.938	.510
260	19	1.08	-.13	1.09	-7.1	-.148	.476	.982	.494	26.7	.948	.490
261	19	1.02	-.16	1.03	-8.8	-.148	.456	.988	.477	26.7	.956	.473
262	19	1.01	-.18	1.02	-10.0	-.147	.435	.994	.457	26.8	.965	.453
263	19	.91	-.17	.92	-10.6	-.149	.415	1.003	.441	19.4	1.032	.441
264	19	.82	-.23	.85	-15.8	-.147	.395	1.007	.421	19.4	1.037	.421
265	19	.73	-.17	.75	-13.0	-.147	.373	1.015	.400	19.4	1.045	.400
266	19	.63	-.19	.65	-16.5	-.146	.352	1.021	.380	19.4	1.051	.380
267	19	.53	-.19	.56	-19.7	-.146	.332	1.027	.362	19.4	1.057	.362
268	19	.48	-.22	.53	-24.4	-.147	.310	1.036	.341	19.4	1.066	.341
269	19	.44	-.16	.47	-20.5	-.146	.290	1.042	.322	19.4	1.072	.322
270	19	.08	-.06	.10	-35.1	-.148	.266	1.051	.299	19.4	1.081	.299
271	19	.36	-.31	.48	-40.4	-.146	.248	1.055	.282	19.4	1.085	.282
272	19	-.02	-.03	.04	-122.1	-.145	.205	1.068	.242	19.4	1.098	.242
273	19	-.15	.00	.15	179.8	-.145	.186	1.075	.223	19.4	1.104	.223
274	19	-.11	-.03	.12	-164.8	-.145	.165	1.082	.204	19.4	1.112	.204
275	19	-.15	-.06	.16	-157.7	-.146	.145	1.089	.185	19.4	1.119	.185
276	19	-.19	-.07	.20	-160.8	-.145	.124	1.096	.165	19.4	1.126	.165
277	19	-.21	-.10	.23	-155.6	-.144	.103	1.102	.145	19.4	1.132	.145
278	19	-.24	-.05	.24	-167.3	-.145	.083	1.109	.126	19.4	1.139	.126
279	19	-.27	-.07	.28	-166.3	-.144	.062	1.115	.106	19.4	1.145	.106
280	19	-.26	-.08	.27	-164.1	-.144	.041	1.122	.086	19.4	1.152	.086
281	19	-.22	-.05	.22	-166.4	-.142	.020	1.127	.066	19.4	1.157	.066
282	19	-.18	-.03	.18	-169.7	-.144	.020	1.129	.067	19.4	1.159	.067
283	19	.11	-.05	.12	-25.3	-.143	-.002	1.135	.046	19.4	1.165	.046
284	19	-.11	-.07	.13	-144.9	-.143	.010	1.131	.056	19.4	1.161	.056
285	19	.35	-.08	.35	-13.3	-.143	-.012	1.139	.036	19.4	1.169	.036
286	19	.95	-.07	.95	-4.4	-.145	-.021	1.143	.028	19.4	1.173	.028
287	19	1.20	-.14	1.21	-6.8	-.144	-.043	1.150	.007	19.4	1.179	.007
288	19	1.18	-.15	1.19	-7.5	-.144	-.064	1.157	-.012	19.4	-1.187	.012
289	19	1.17	-.15	1.18	-7.4	-.144	-.075	1.161	-.023	19.4	-1.190	.023

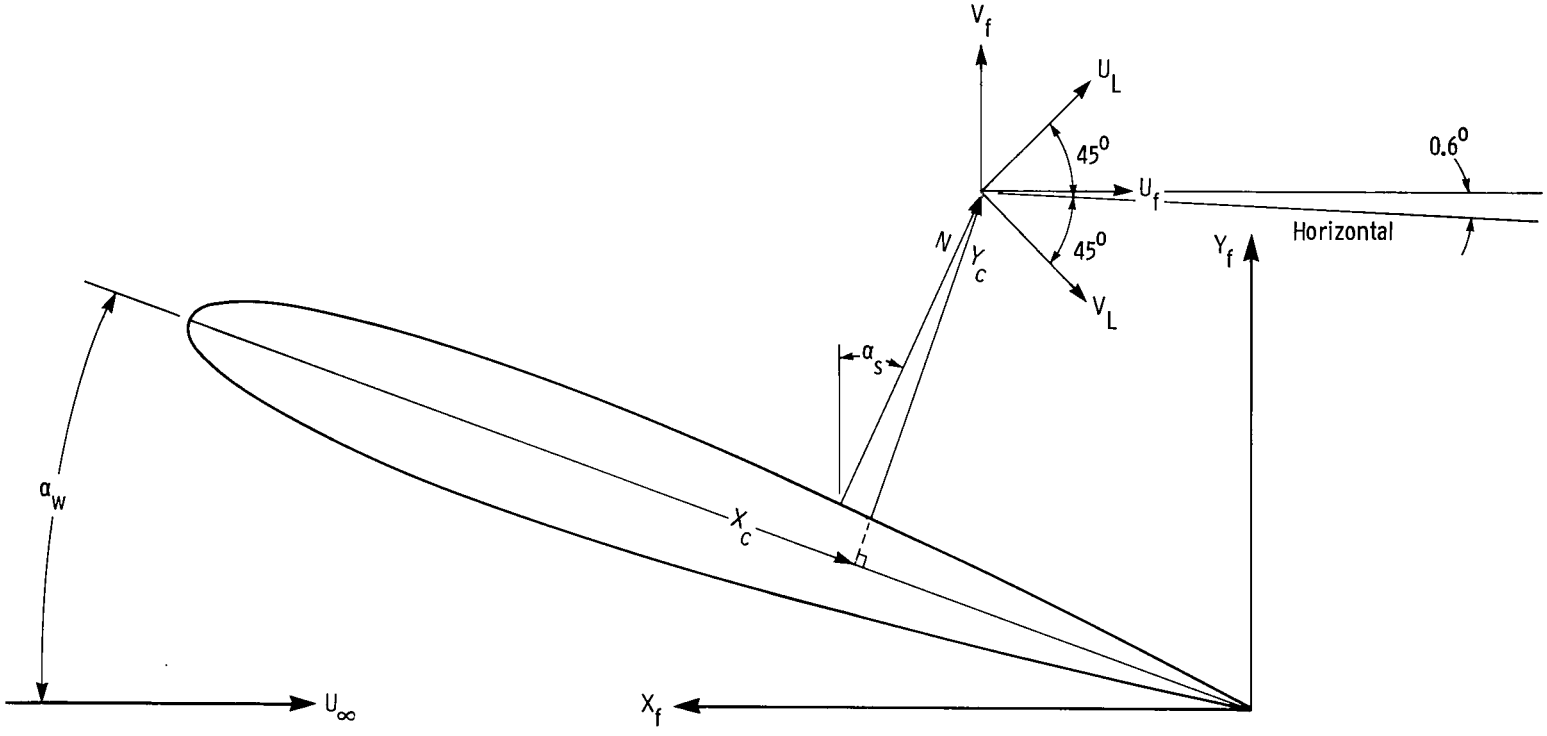

Figure 1.- Wing and laser velocimeter coordinate systems.

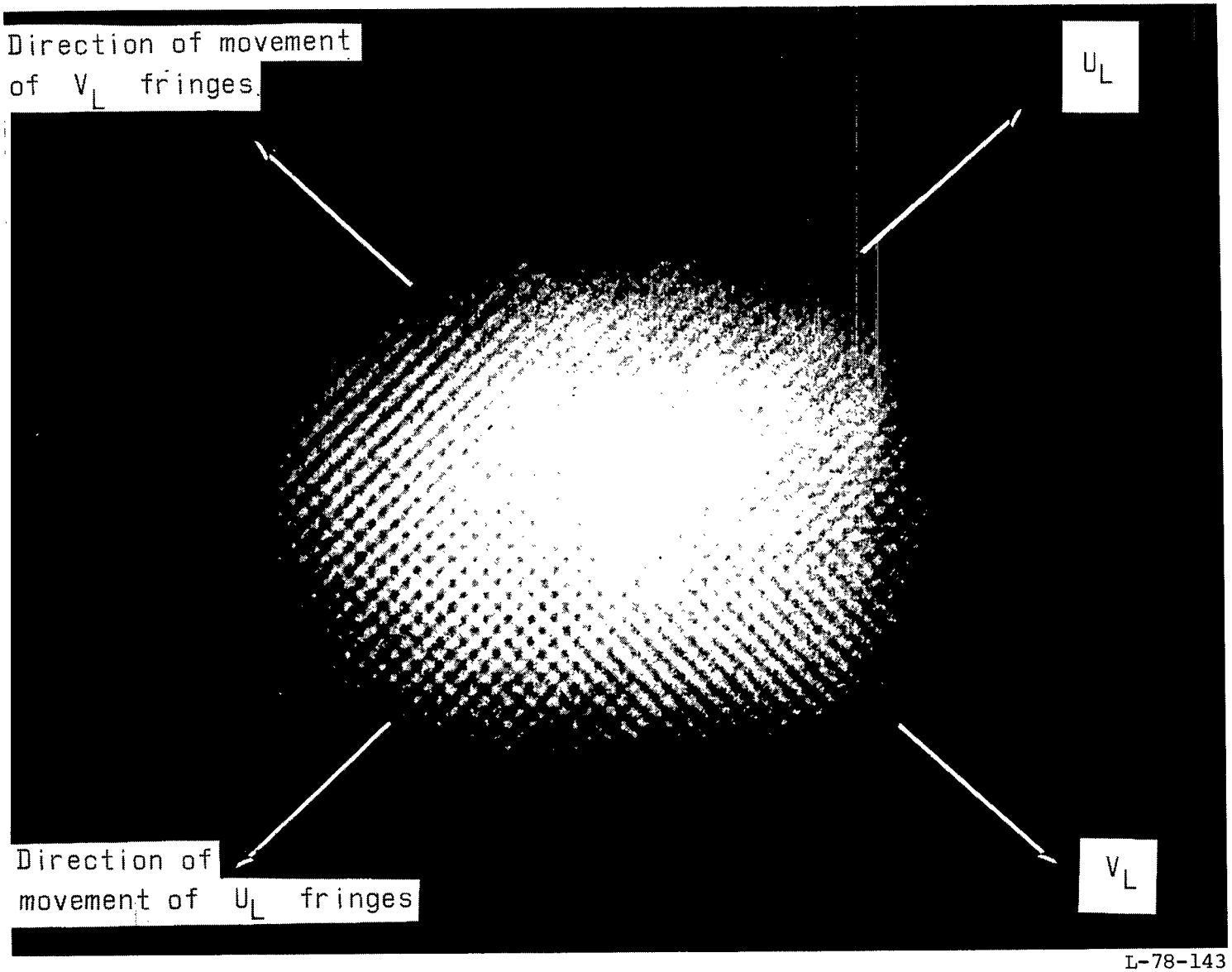

L-78-143

Figure 2.- Two-component fringes in sample volume.

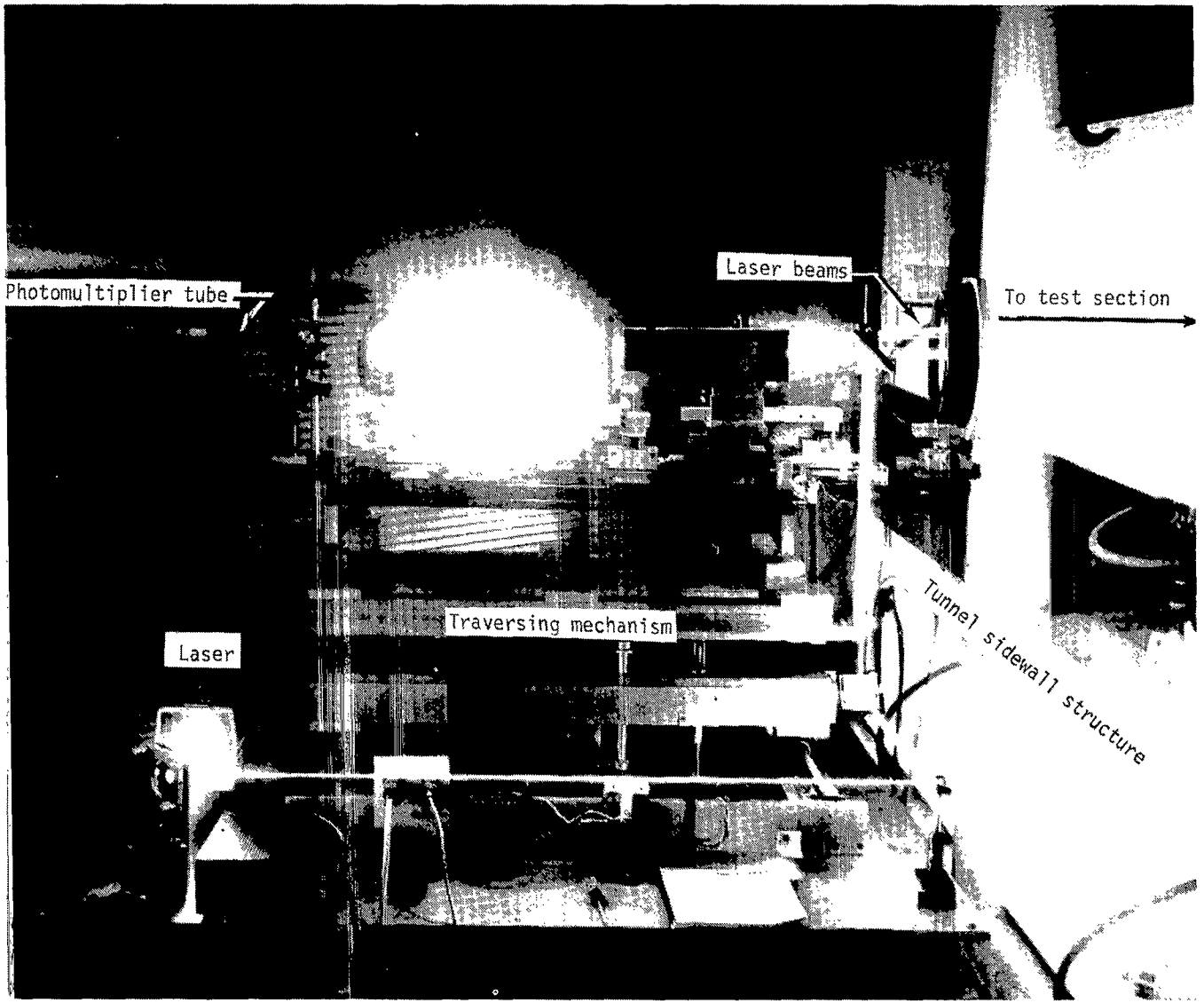

Figure 3.- Laser optical system mounted in test chamber.

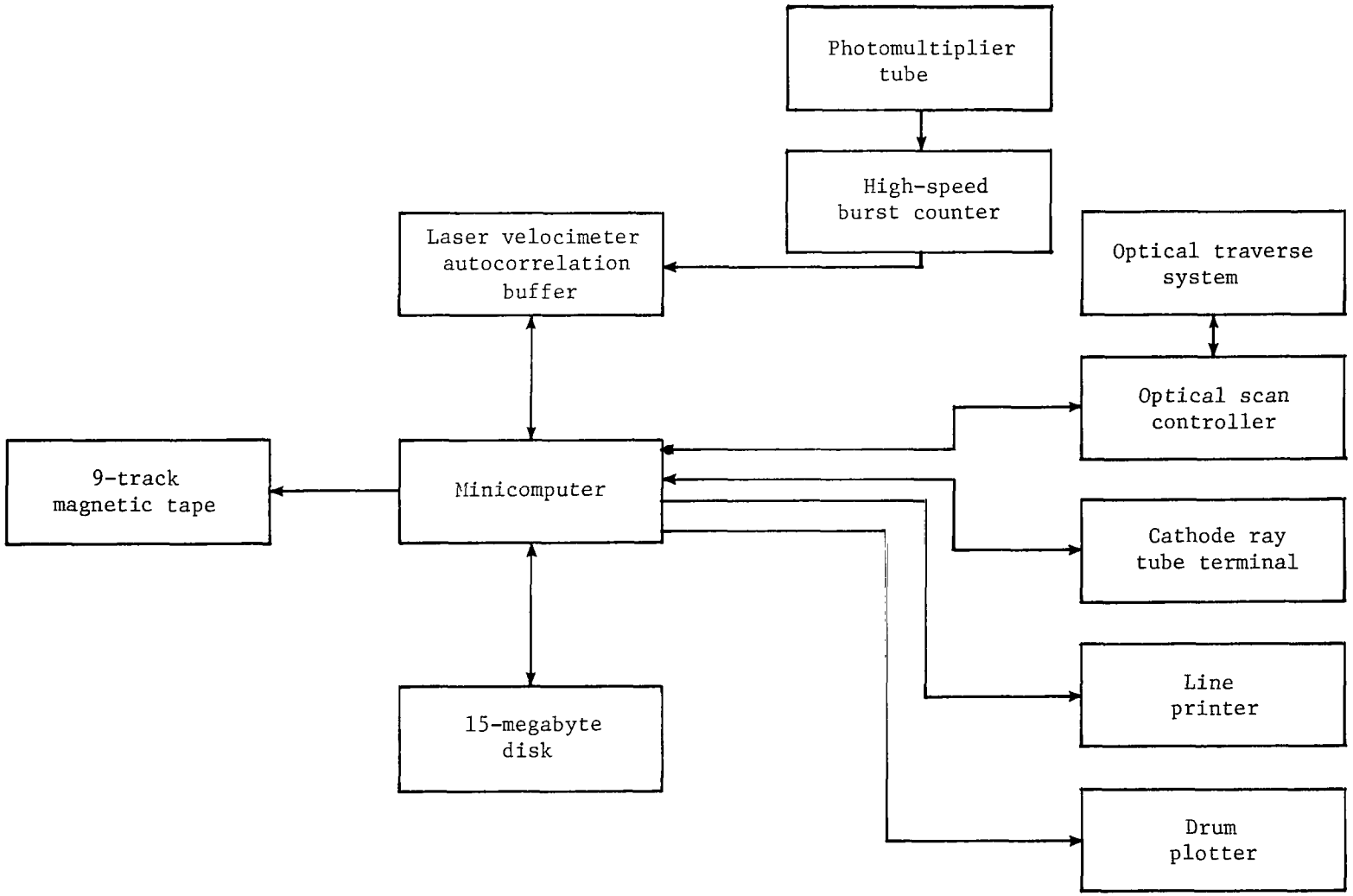

Figure 4.- Block diagram of laser velocimeter data acquisition system.

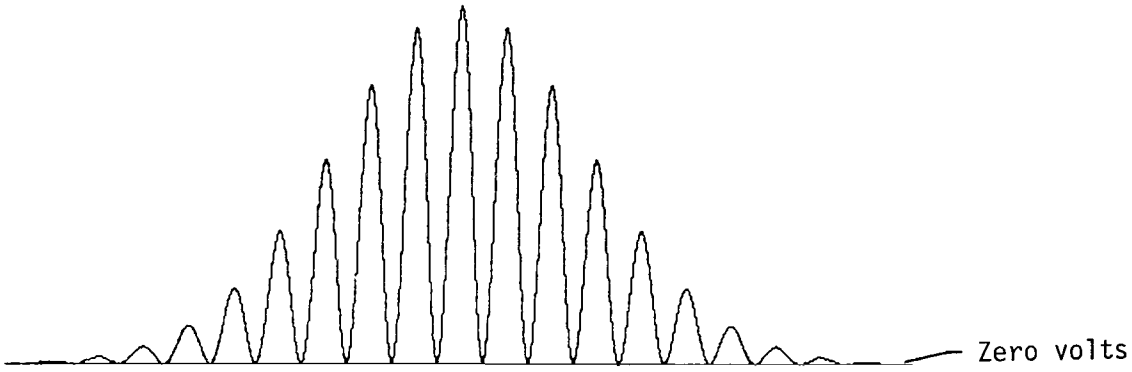

(a) Input signal from photomultiplier tube.

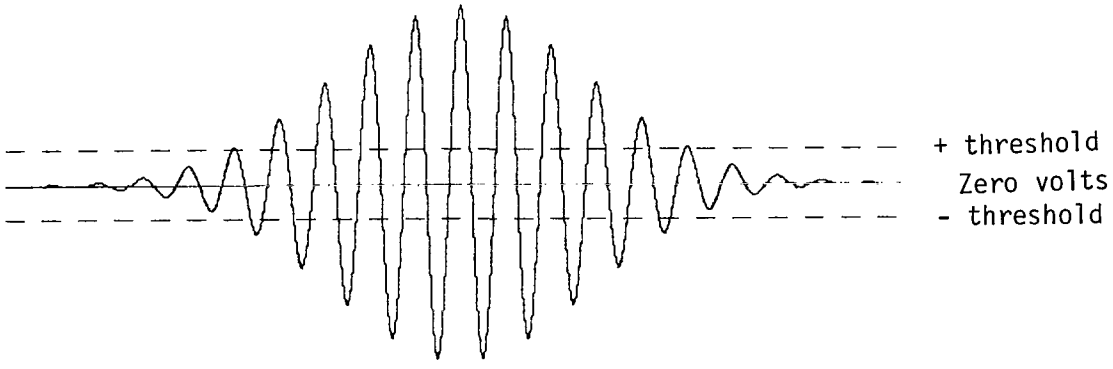

(b) Filtered signal and thresholds.

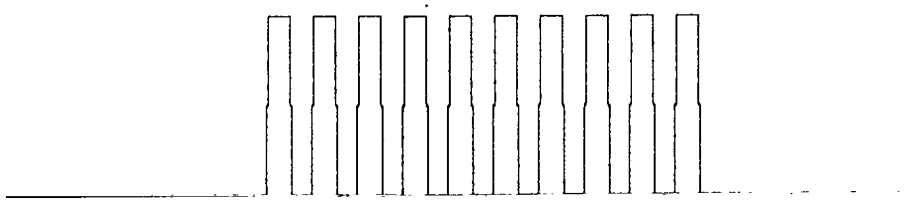

(c) Digital pulse train to trigger reference clock counter.

Figure 5.- Operation of high-speed burst counter.

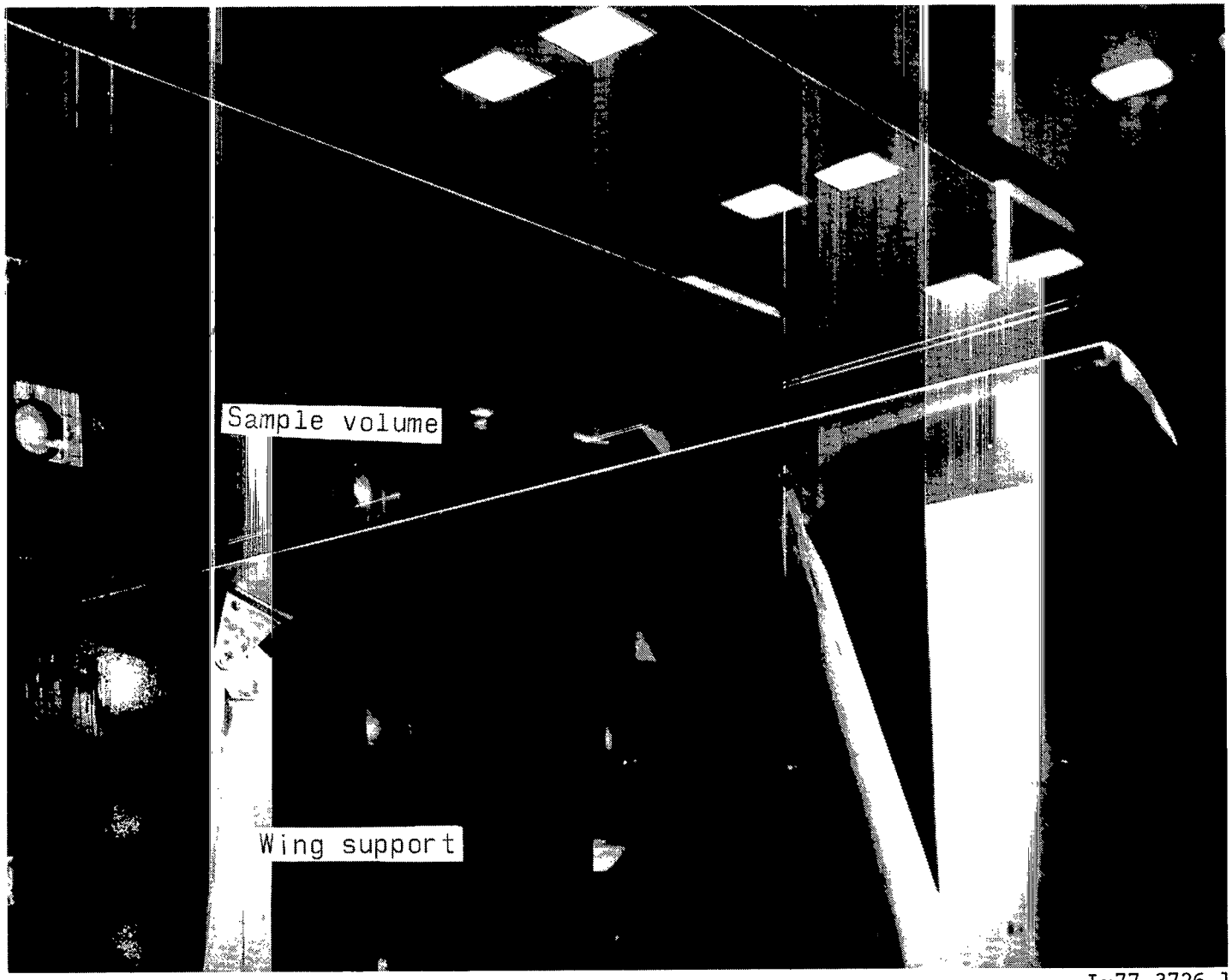

L-77-3726.1

Figure 6.- Model wing installed in Langley V/STOL tunnel.

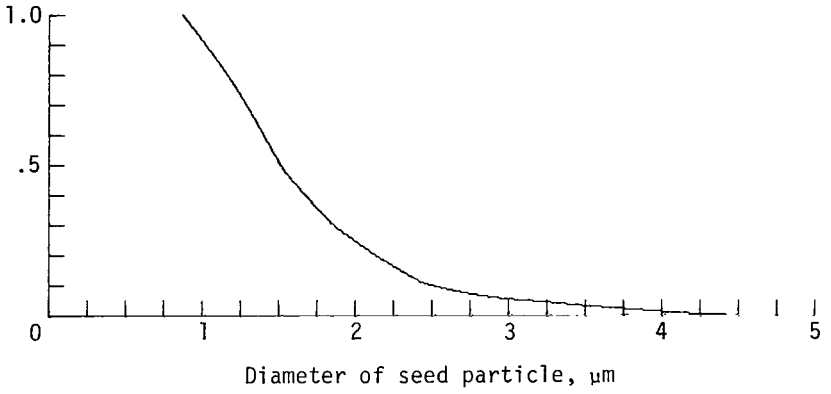

(a) Particle size from smoke generator.

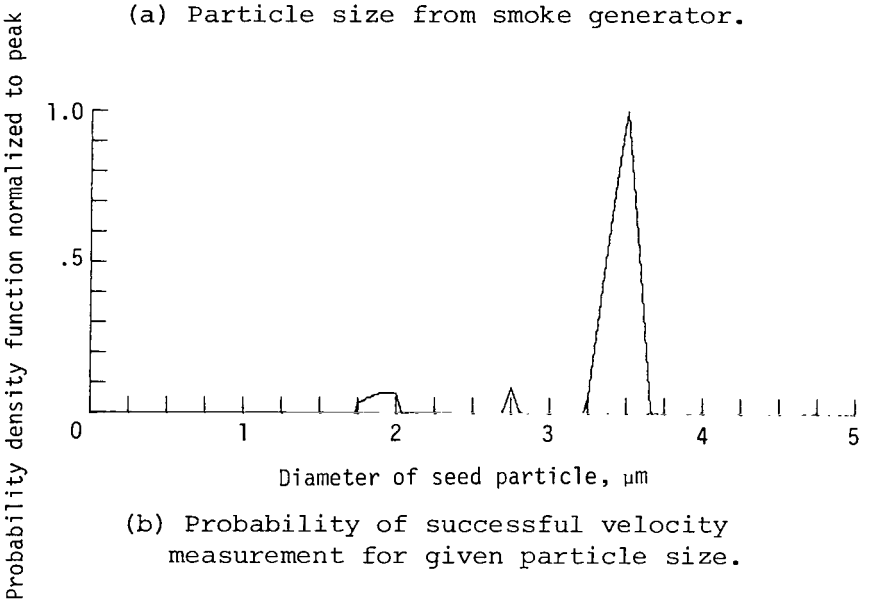

(b) Probability of successful velocity measurement for given particle size.

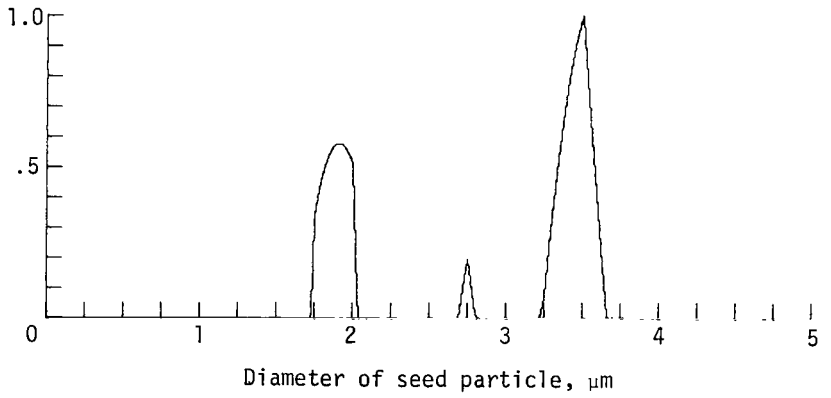

(c) Probability of successful velocity measurement for seed from smoke generator.

Figure 7.- Influence of seed size distribution and laser velocimeter optics on size of particles that generate successful velocity measurements.

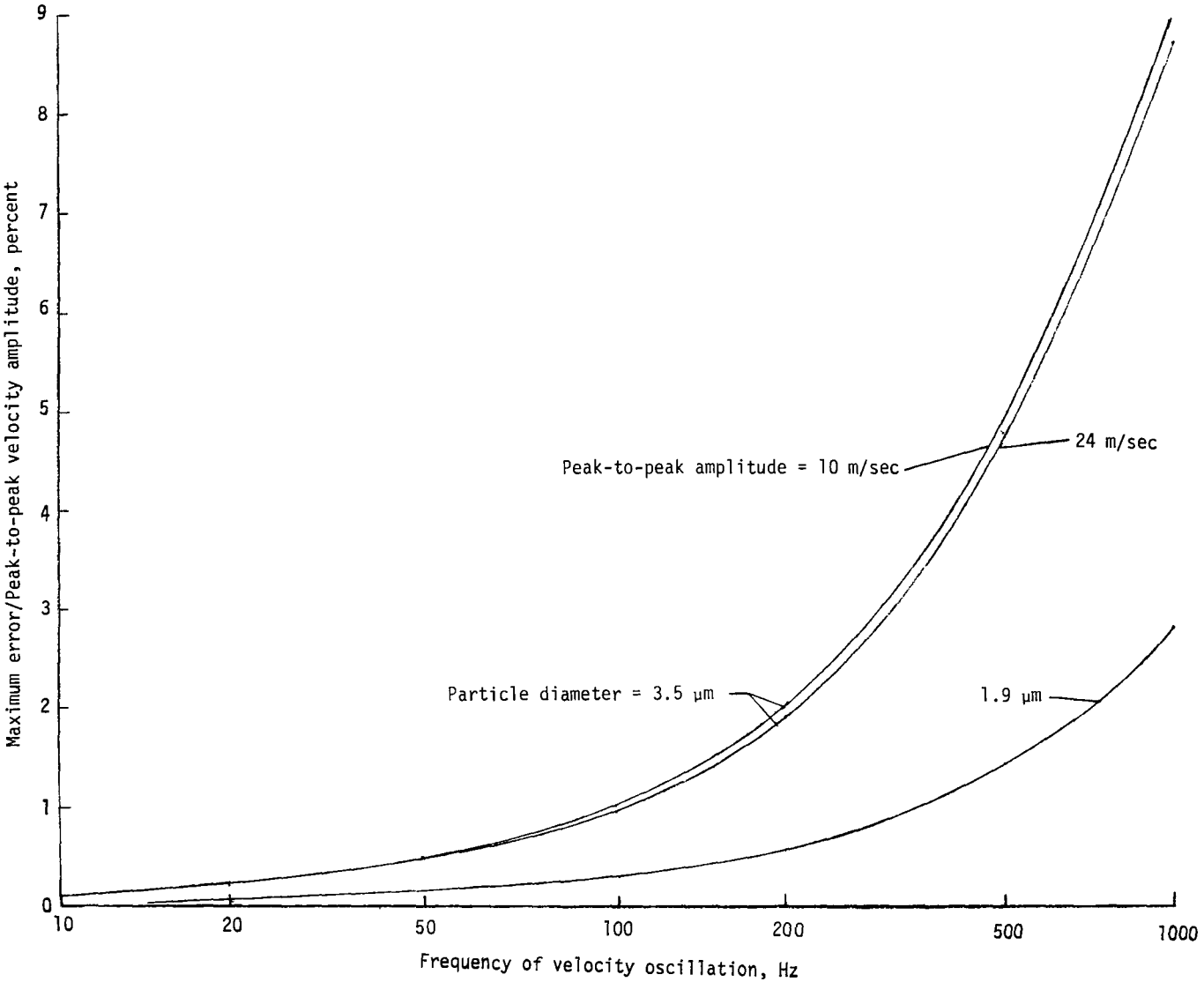

Figure 8.- Particle tracking errors for sinusoidal velocity fluctuations.

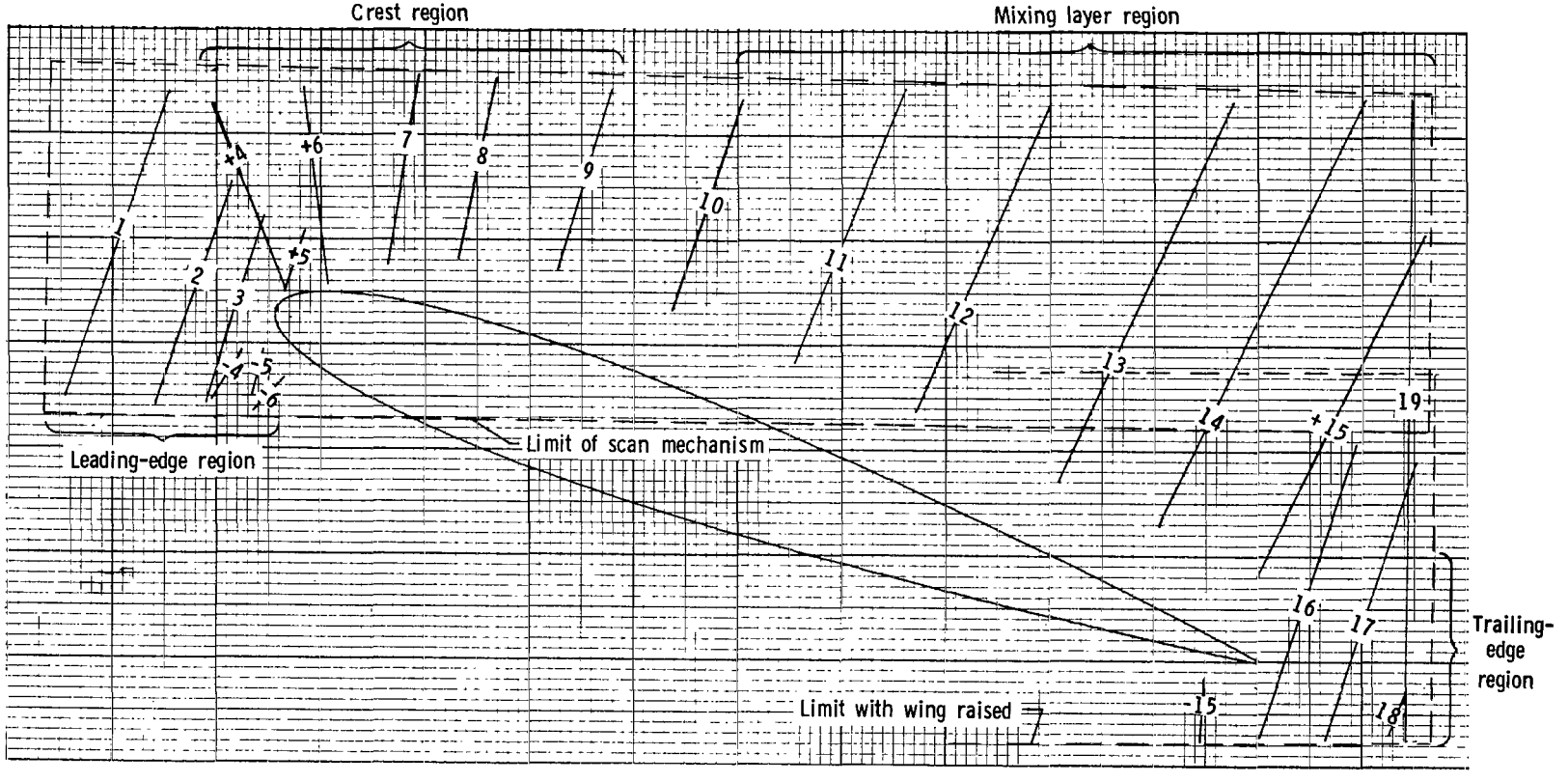

Figure 9.- Location of scan lines.

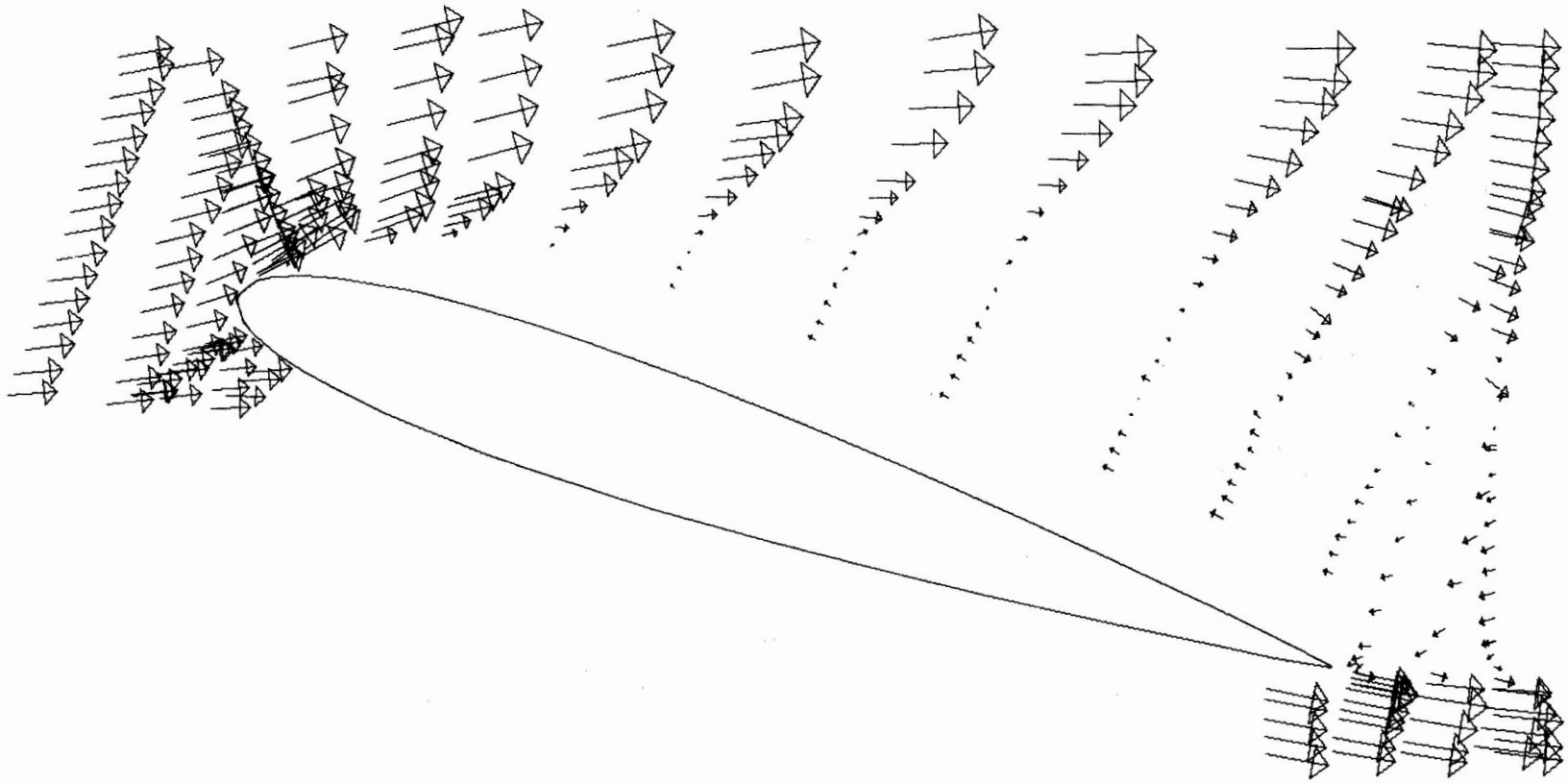

Figure 10.- Resultant vectors of mean velocity normalized by free-stream velocity.

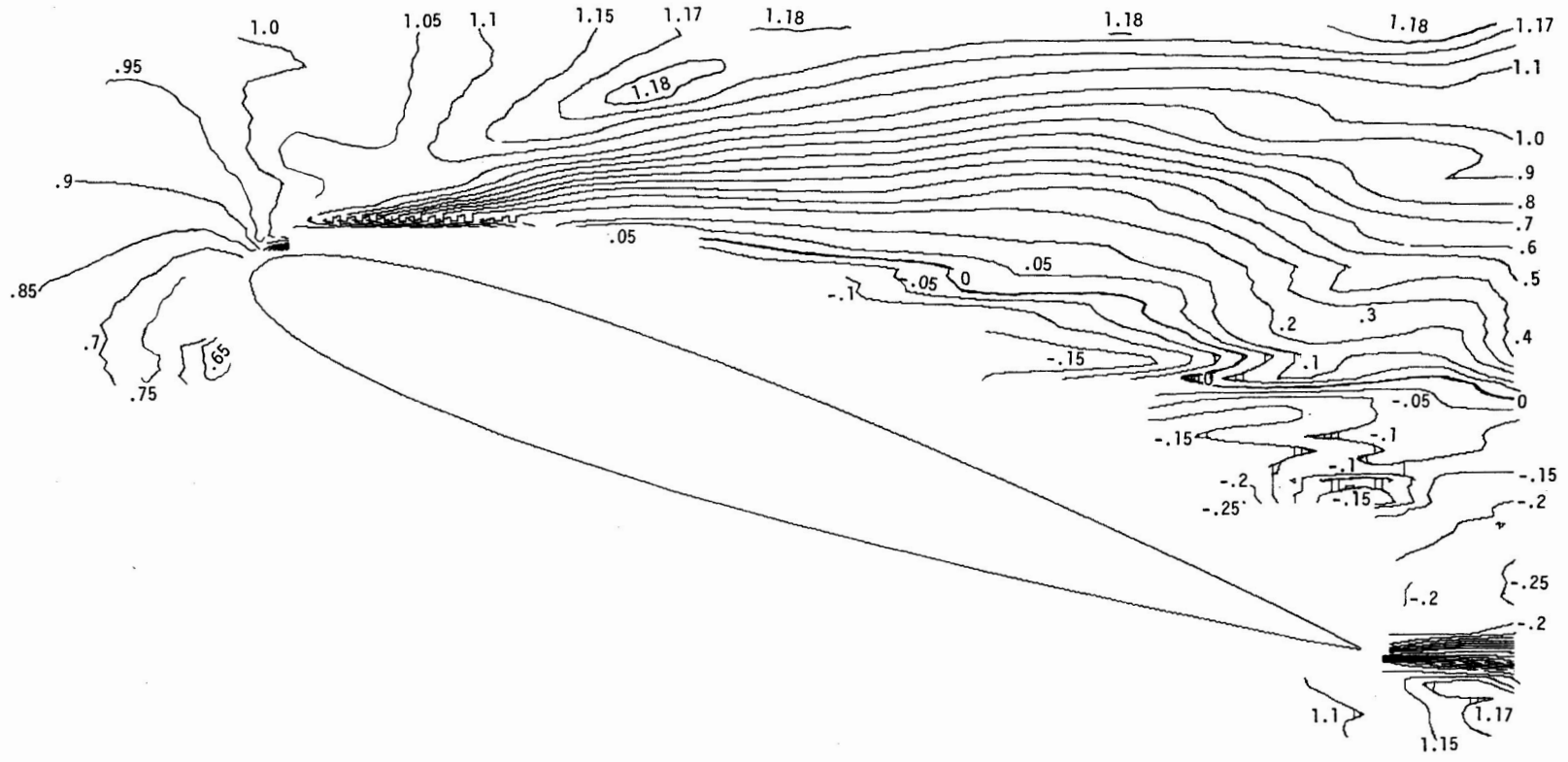

Figure 11.- Contours of constant resultant mean velocity normalized by free-stream velocity.

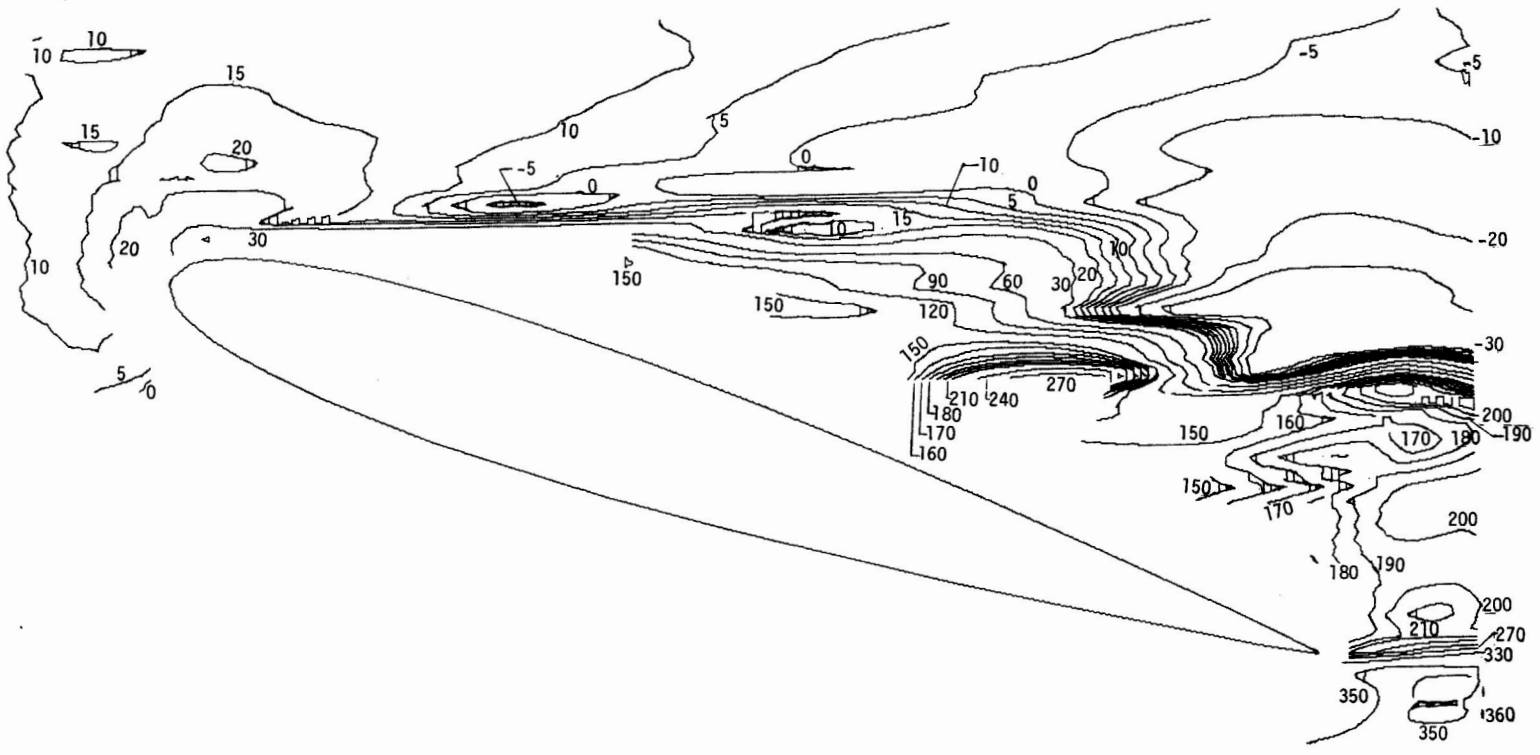

Figure 12.- Contours of constant values of angle (in degrees) of mean flow with respect to free-stream direction.

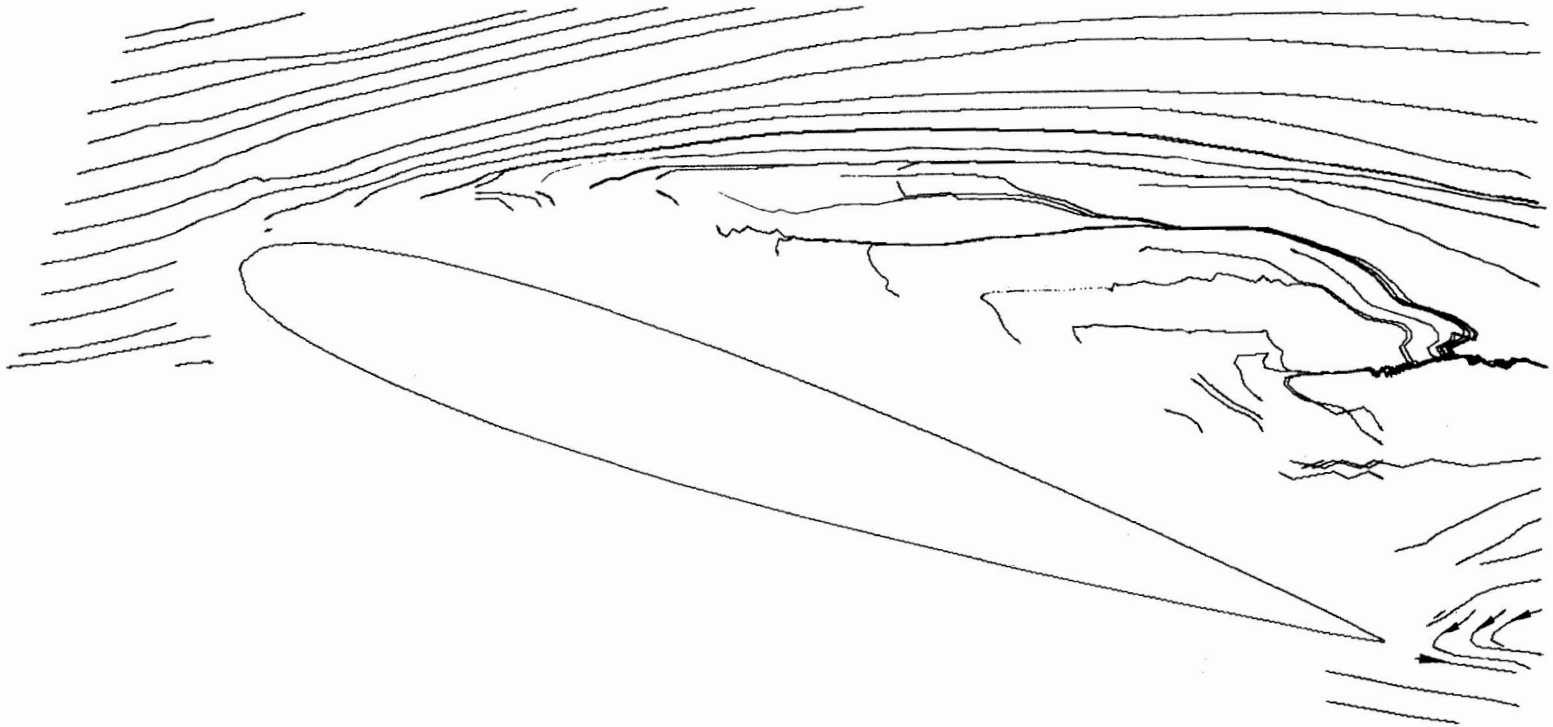

Figure 13.- Mean flow streamlines.

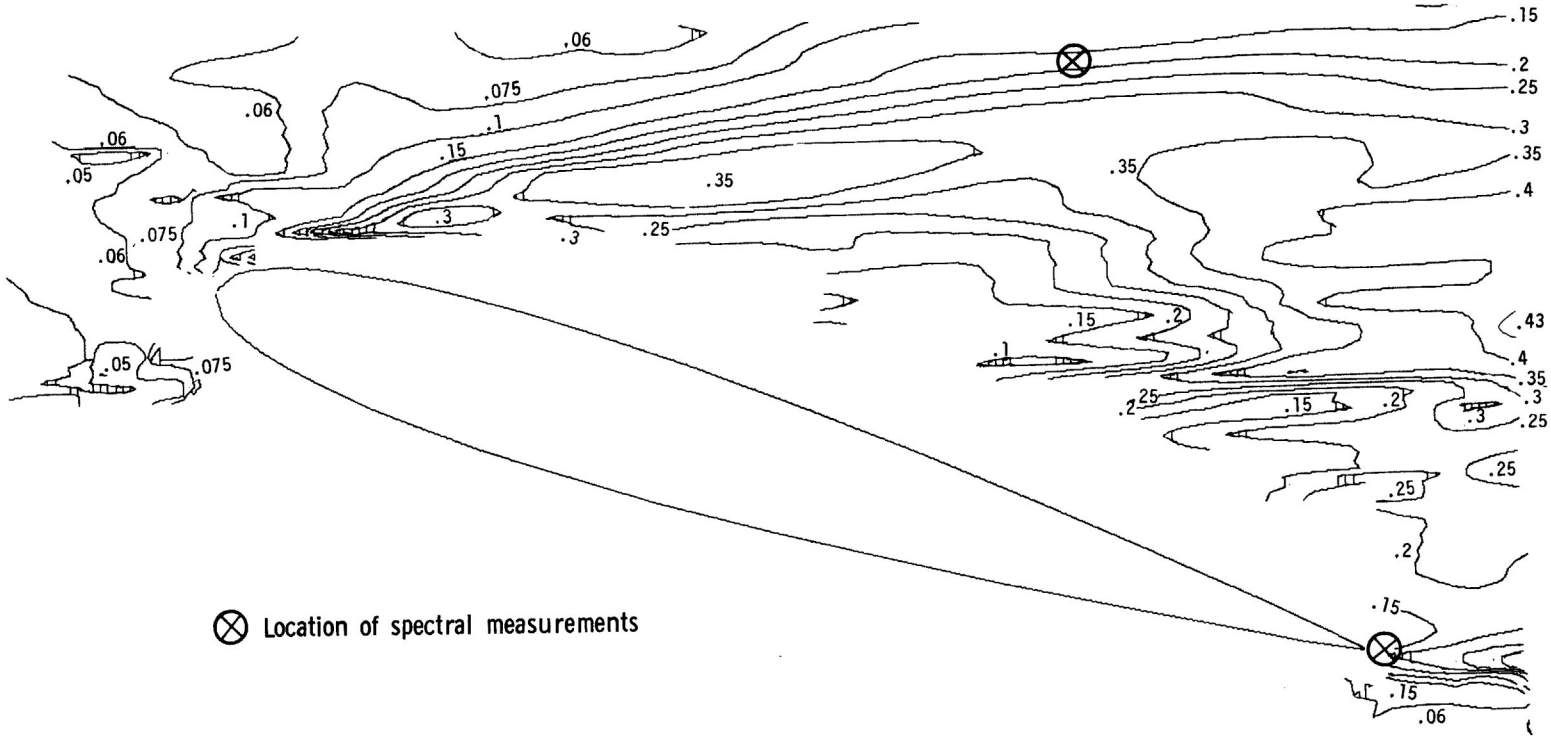

Figure 14.- Contours of constant values of resultant standard deviation of velocity normalized to free-stream velocity.

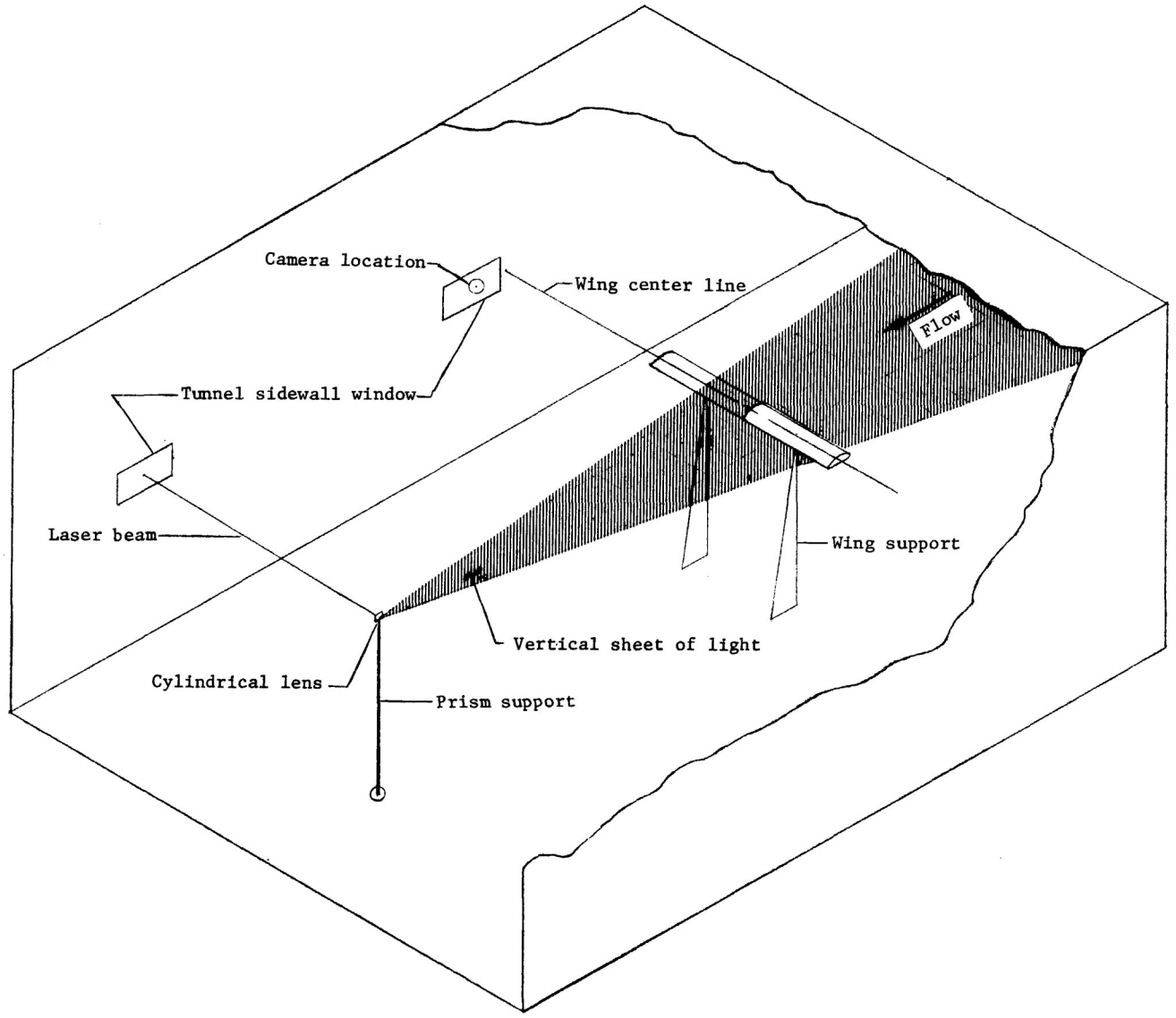

Figure 15.- Sketch of vapor screen flow visualization setup showing projection of vertical sheet of light through plane of wing center span.

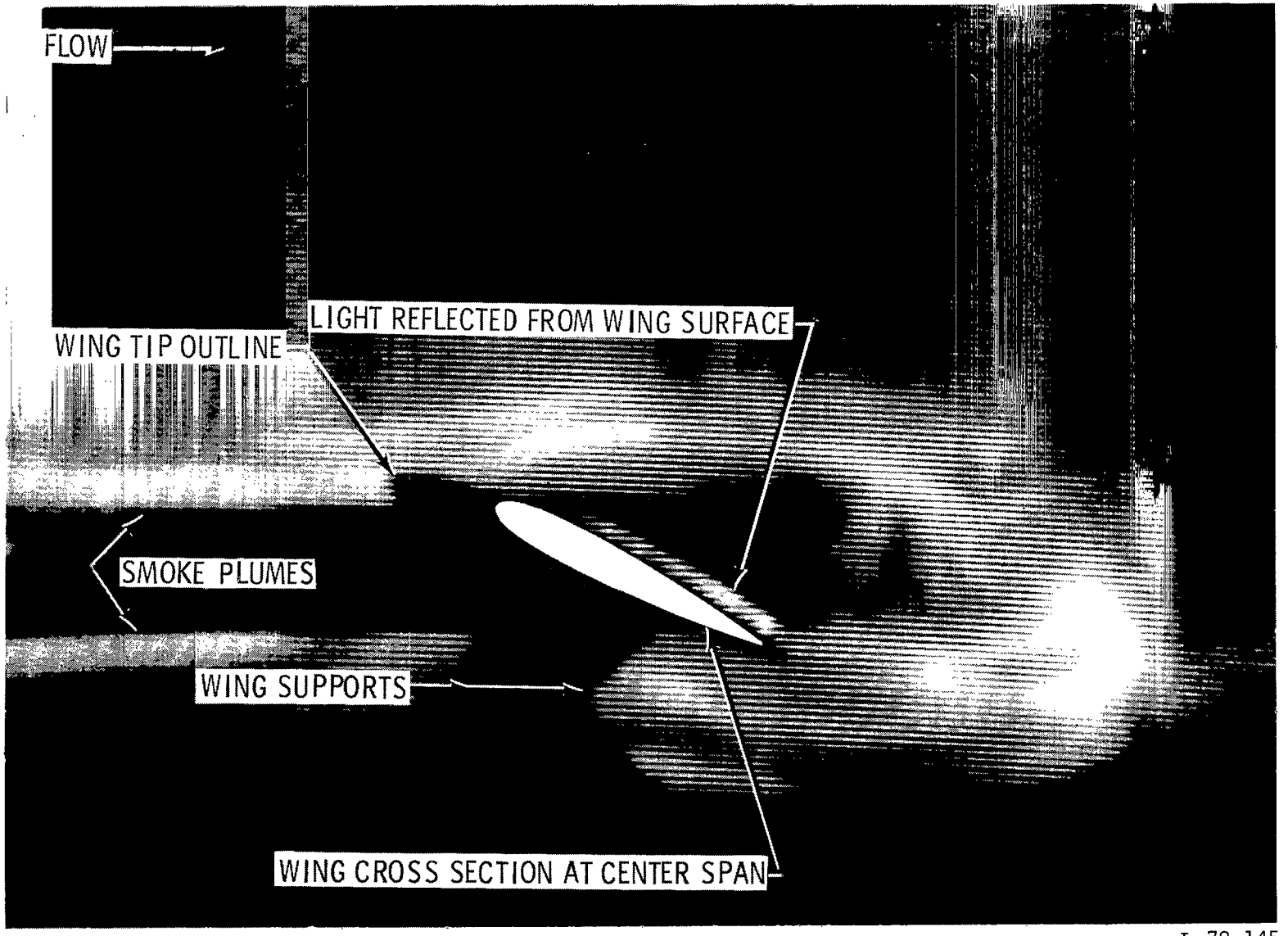

L-78-145

Figure 16.- Smoke flow visualization at wing center span for U_T = 15 m/sec.

(a) First frame.

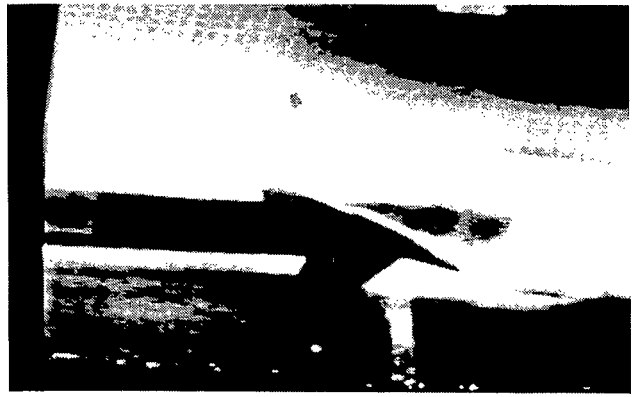

(b) Second frame.

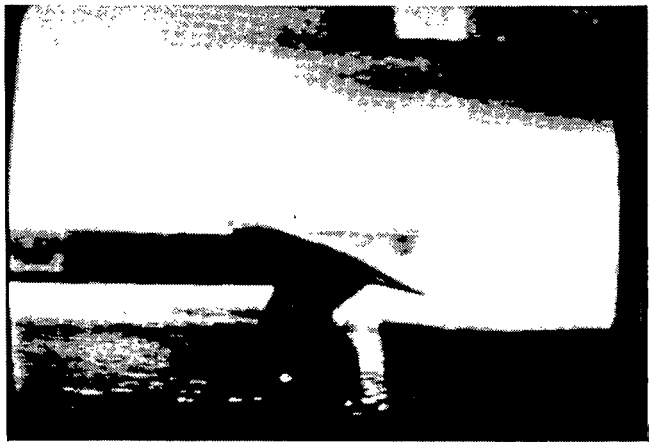

(c) Third frame.

(d) After smoke plume removal.

L-78-146

Figure 17.- Wake closure development in 40-msec frame time and effect of smoke plume removal.

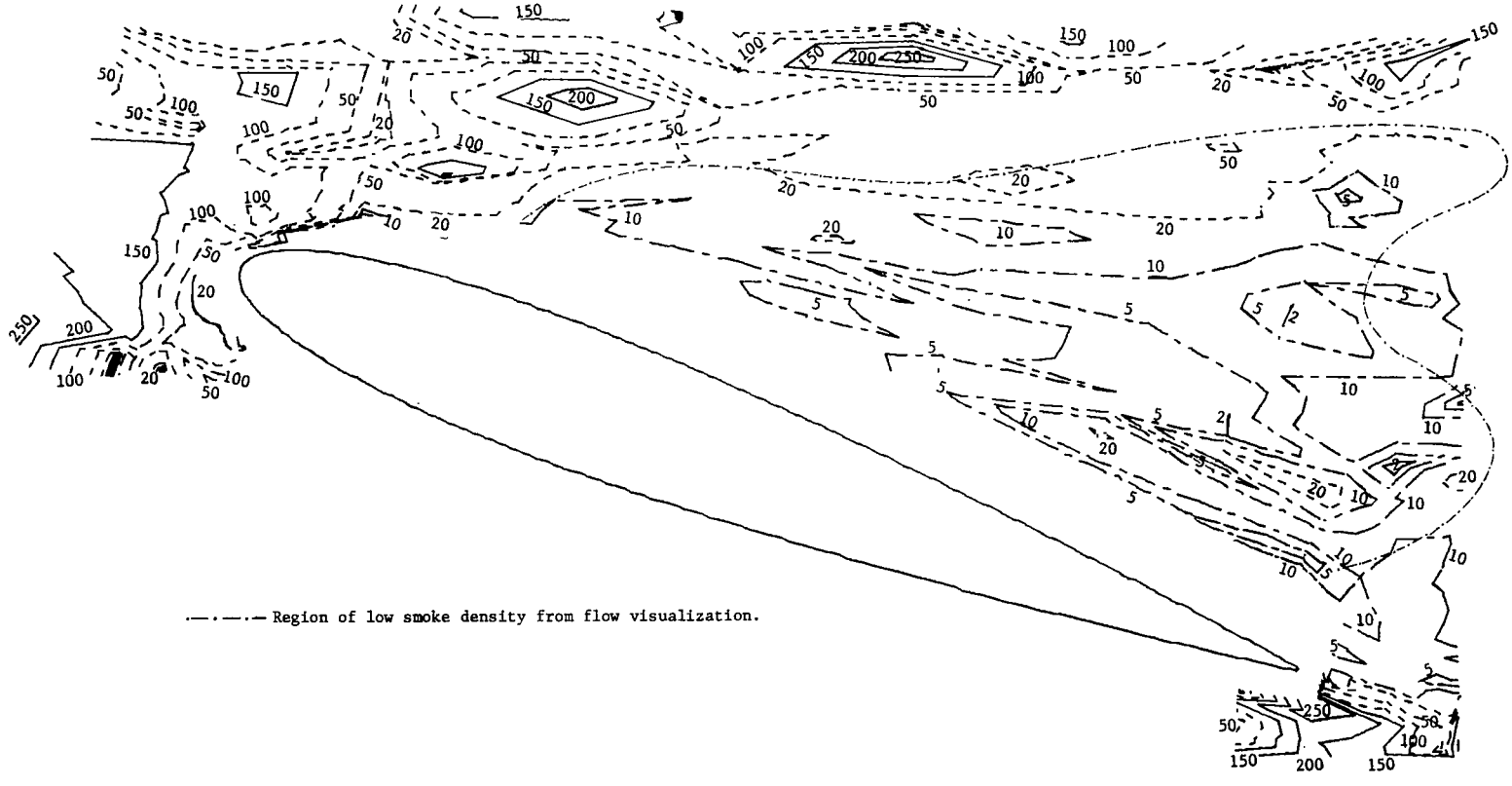

Figure 18.- Contours of constant data rate in samples per second.

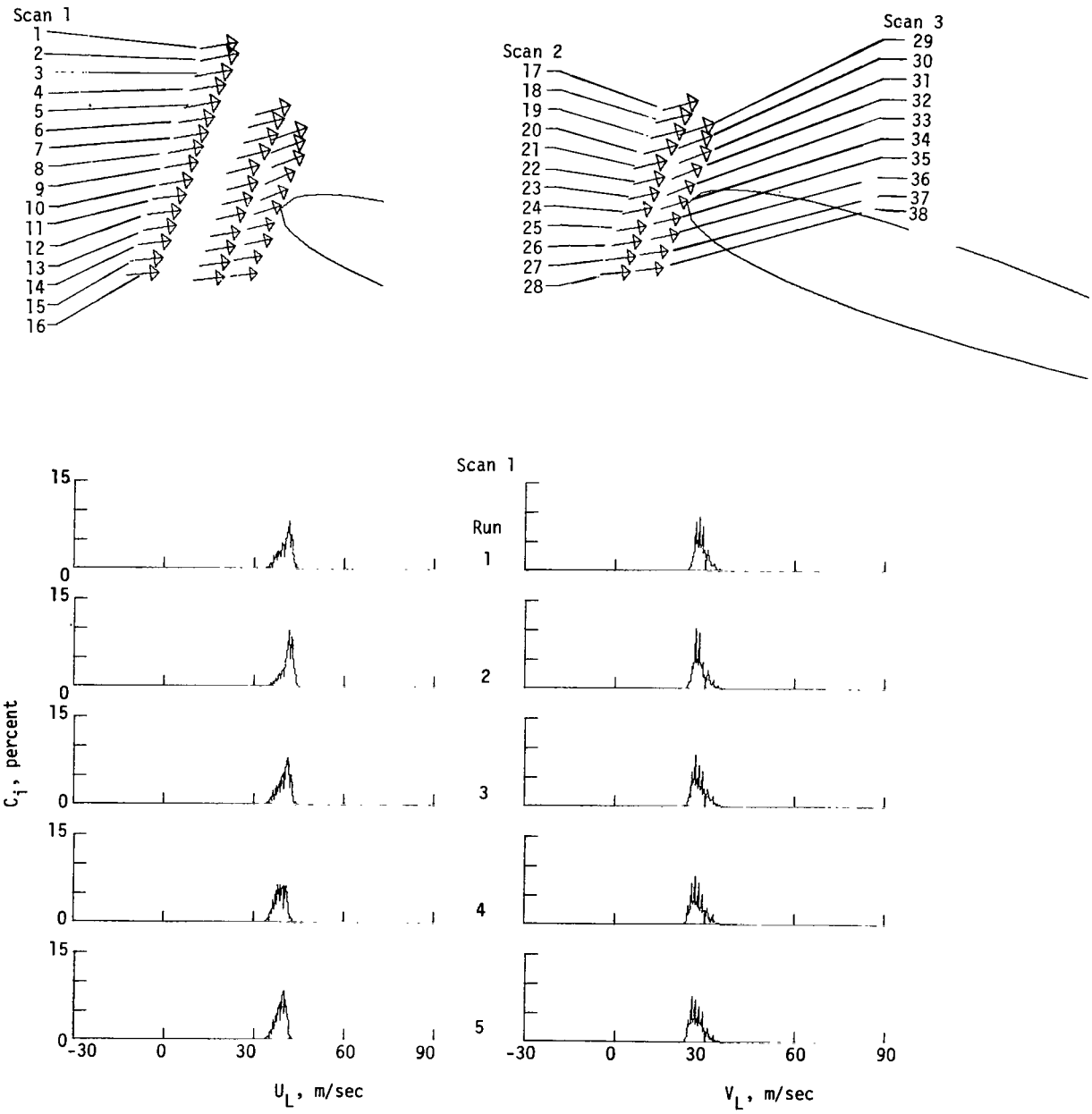

Figure 19.- Histograms in scans 1, 2, and 3.

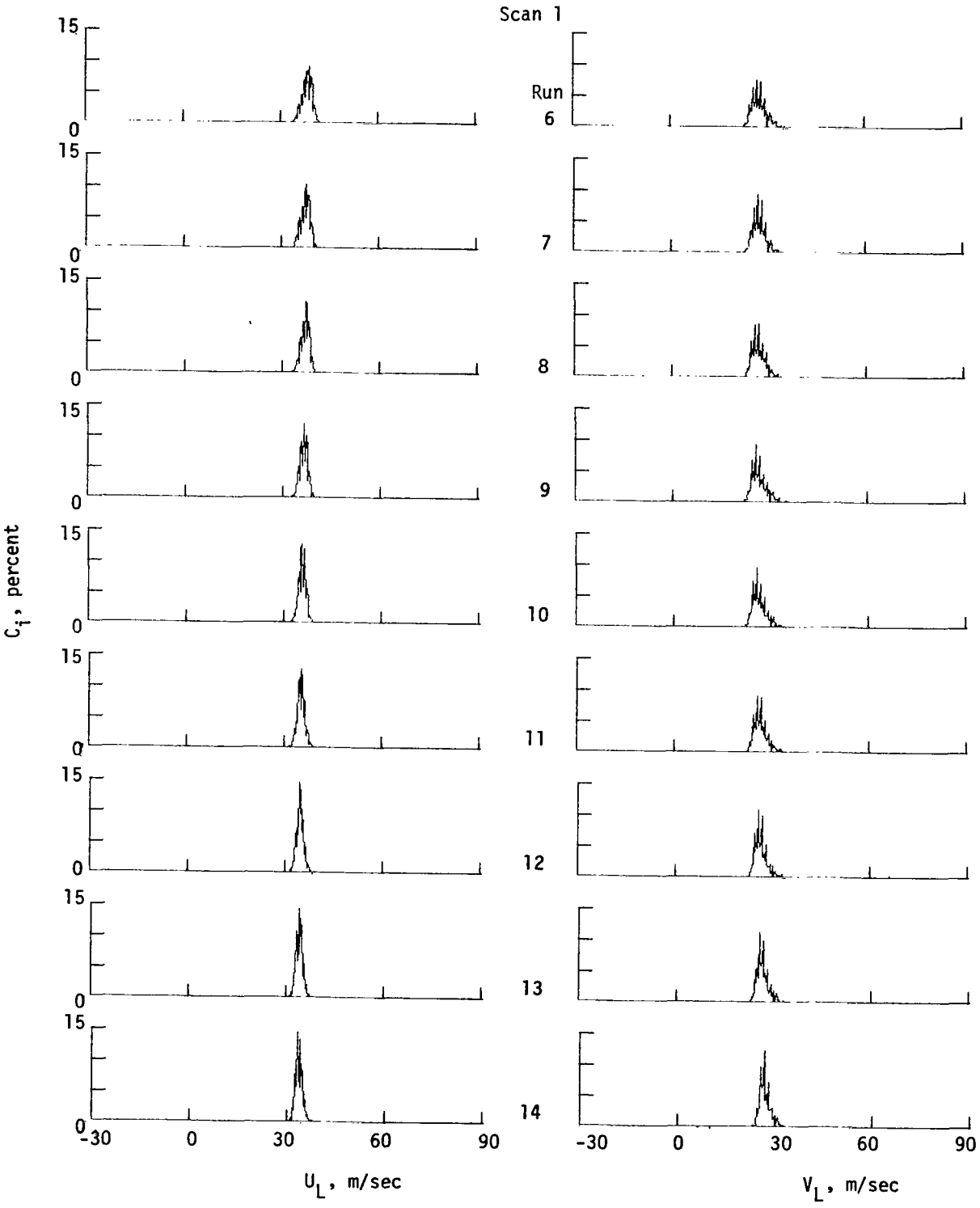

Figure 19.- Continued.

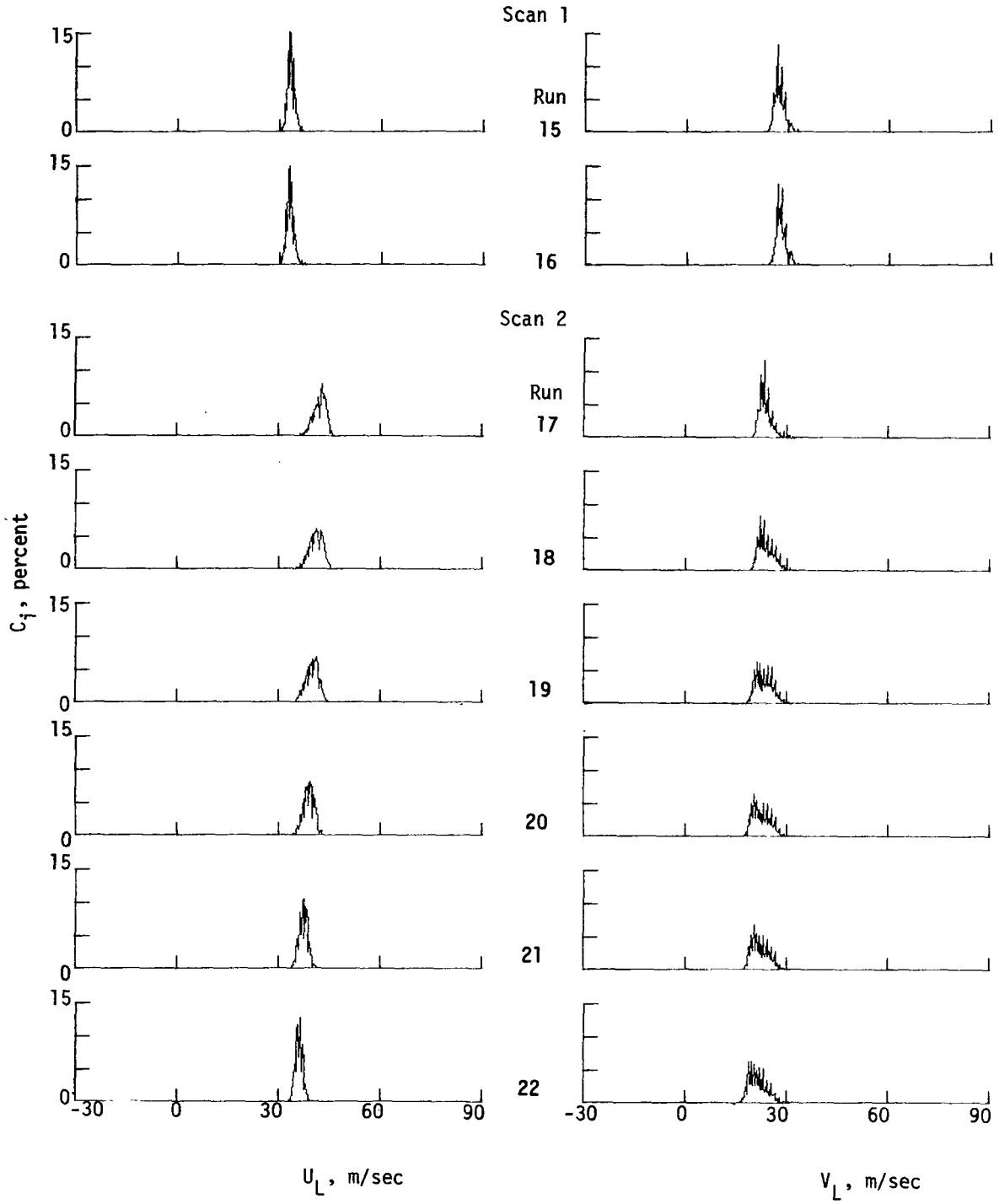

Figure 19.- Continued.

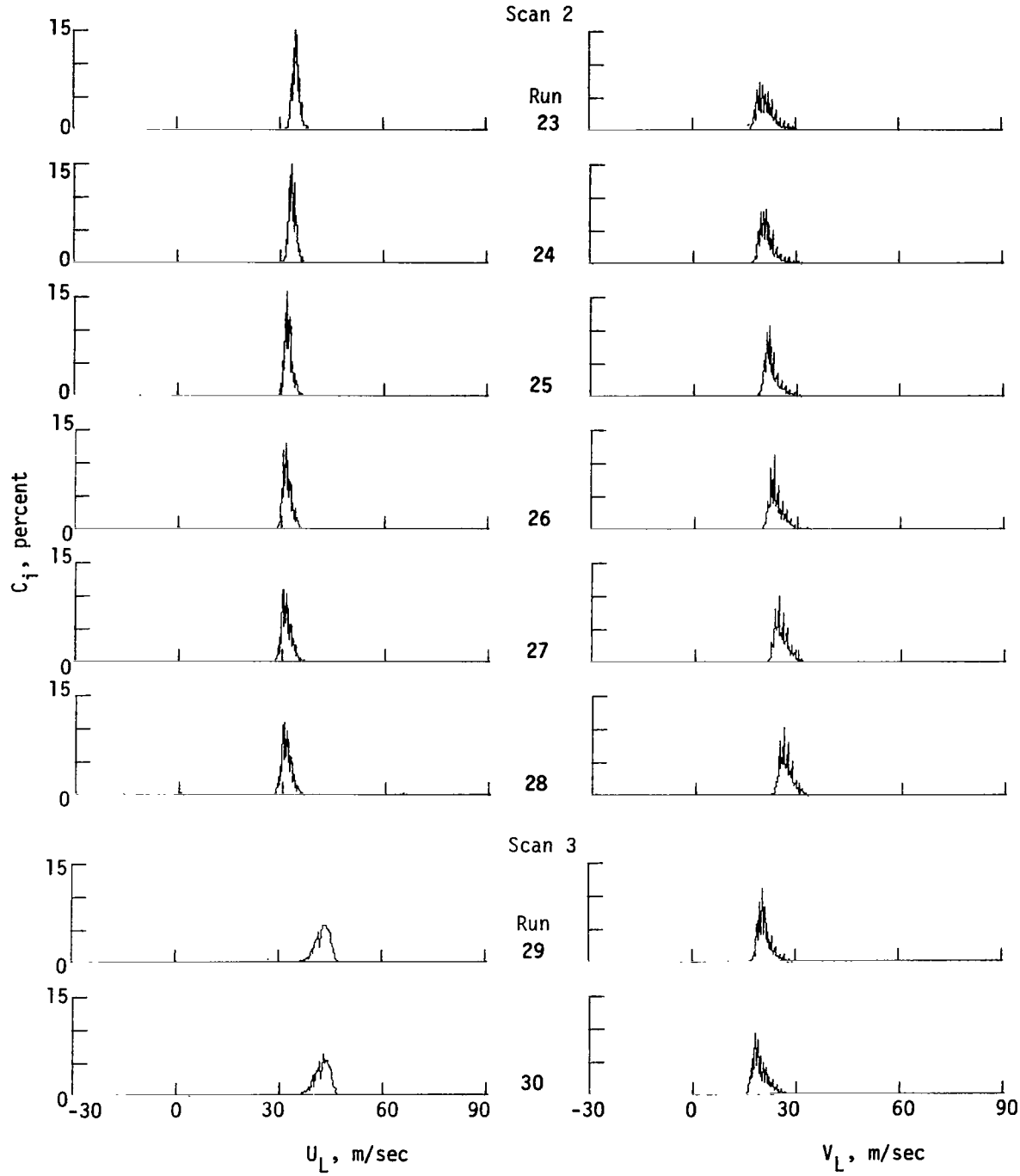

Figure 19.- Continued.

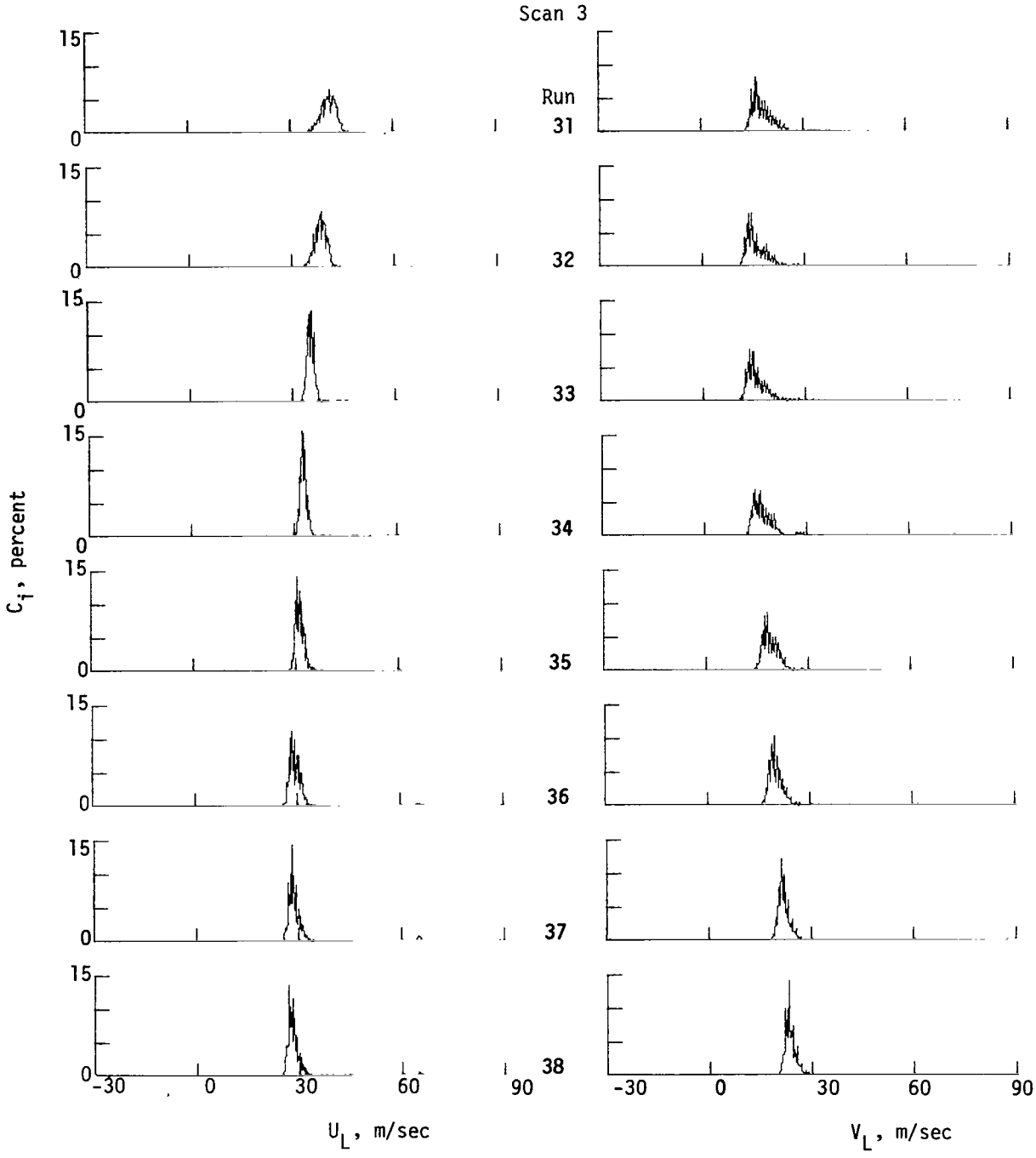

Figure 19.- Concluded.

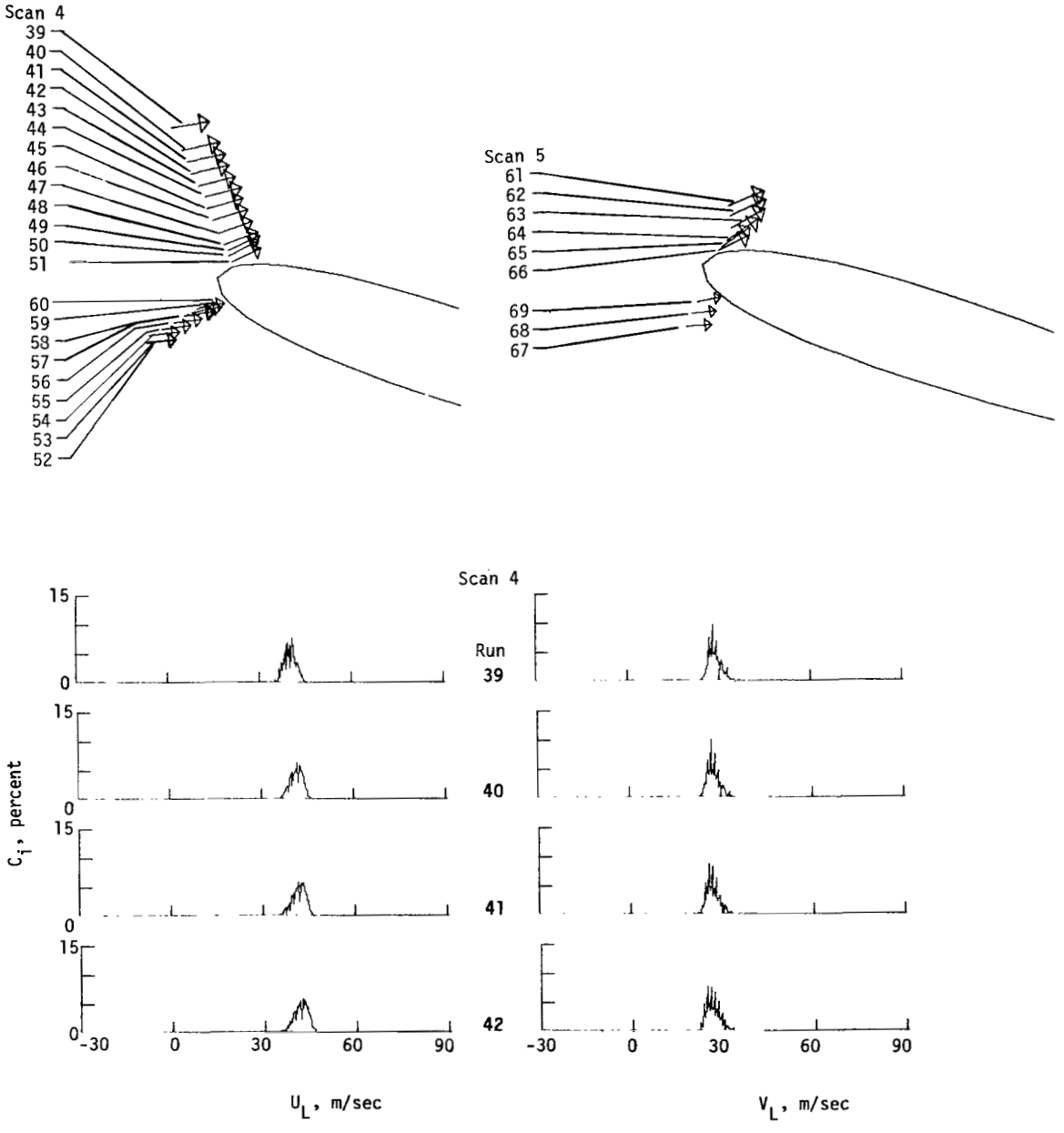

Figure 20.- Histograms in scans 4 and 5.

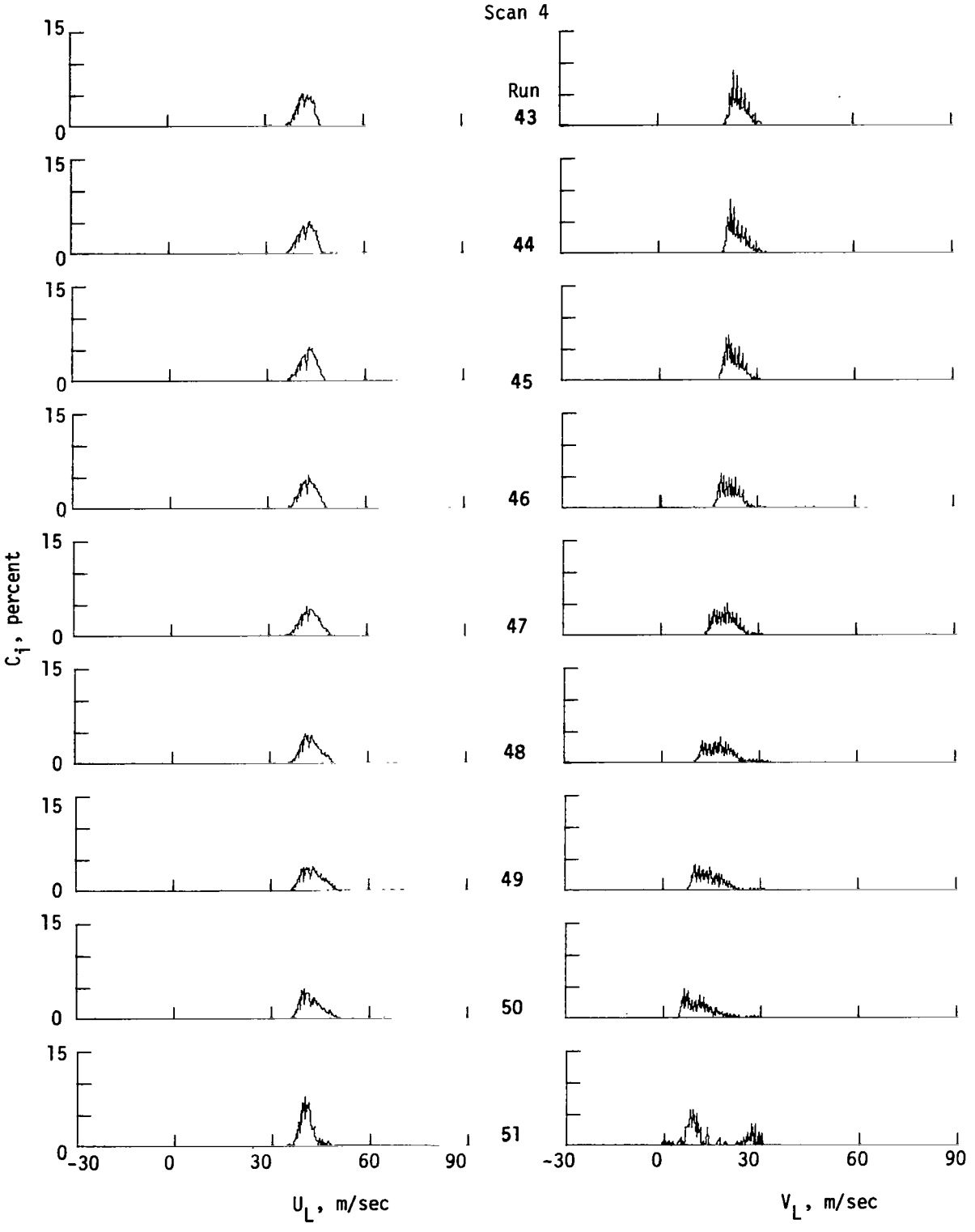

Figure 20.- Continued.

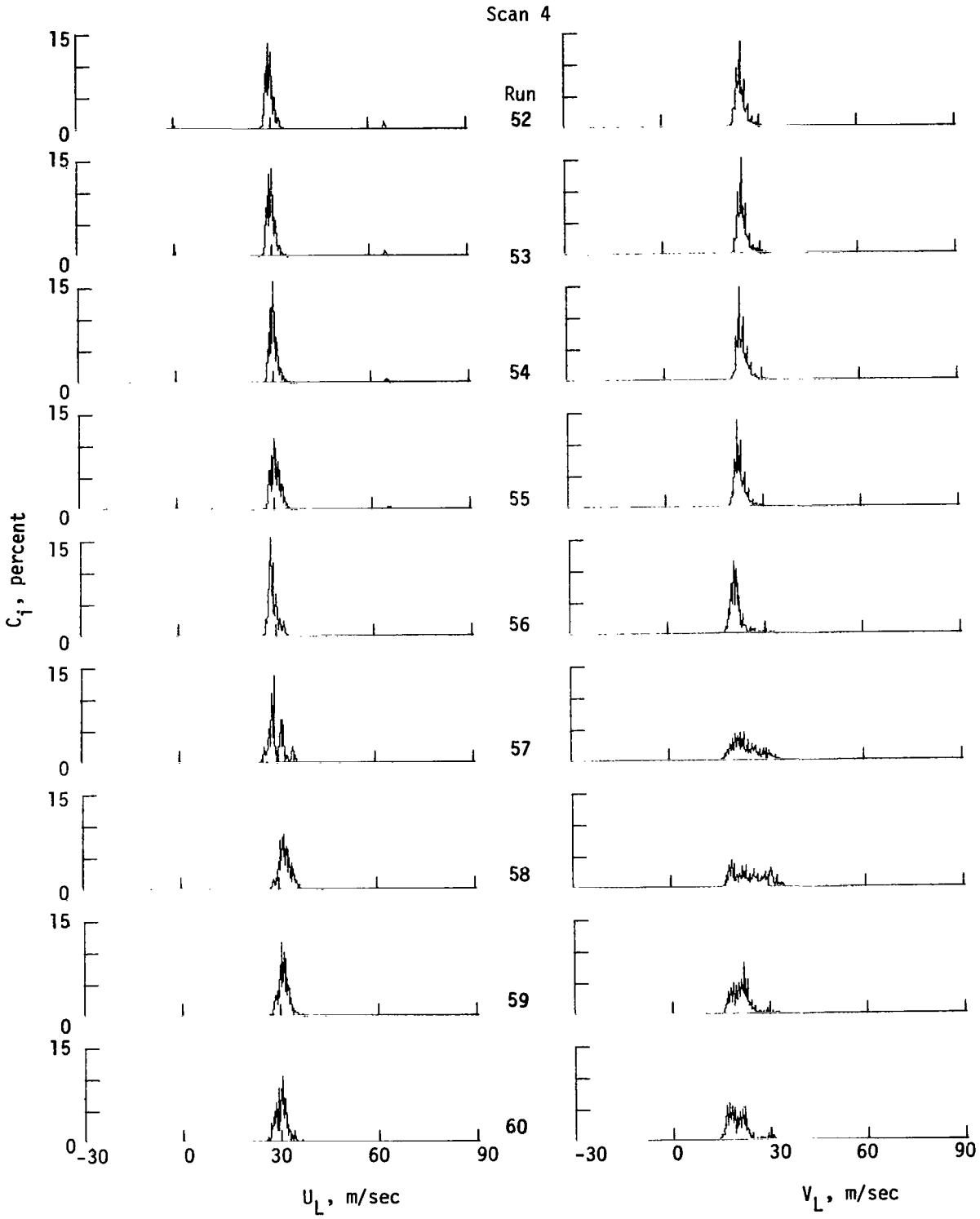

Figure 20.- Continued.

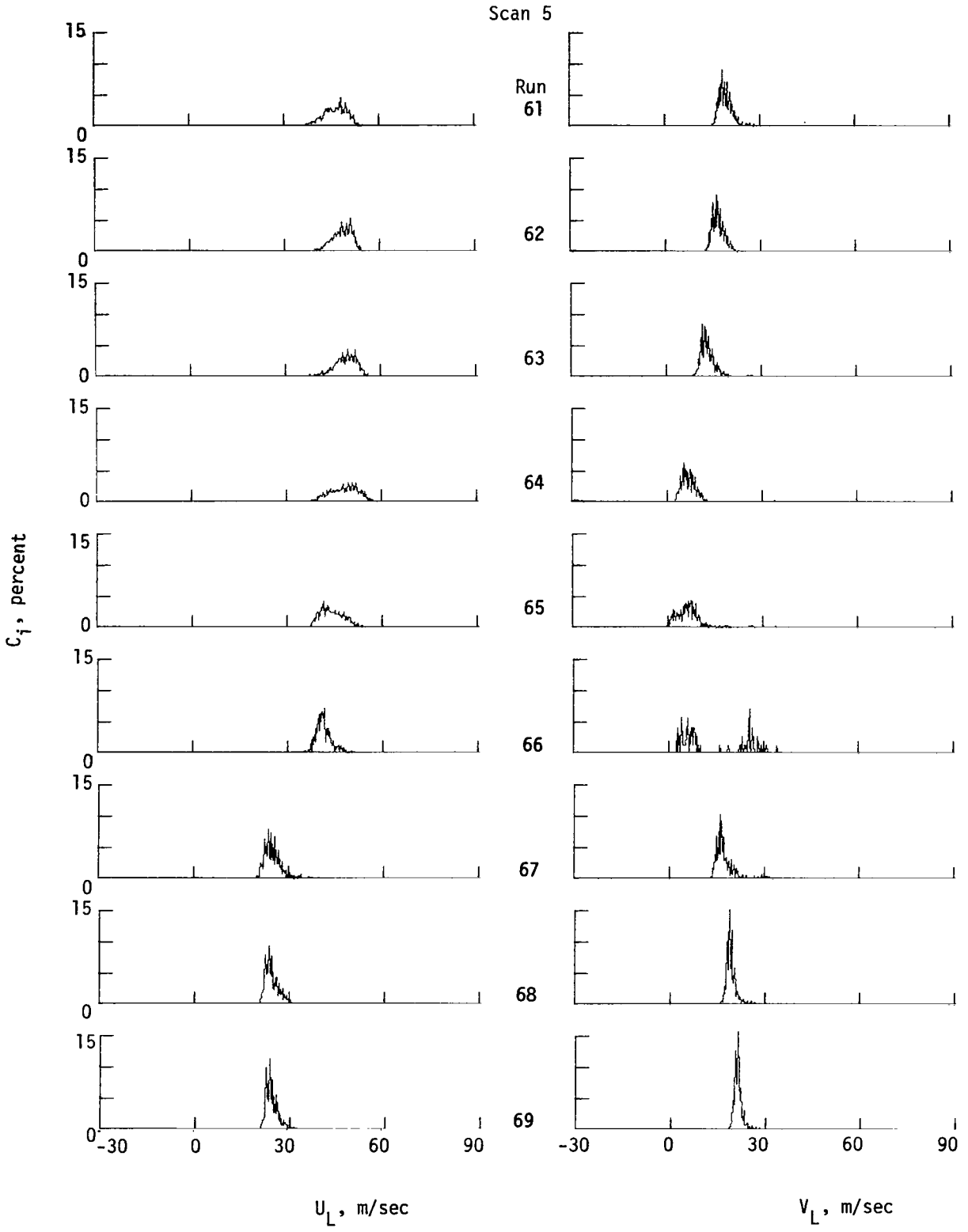

Figure 20.- Concluded.

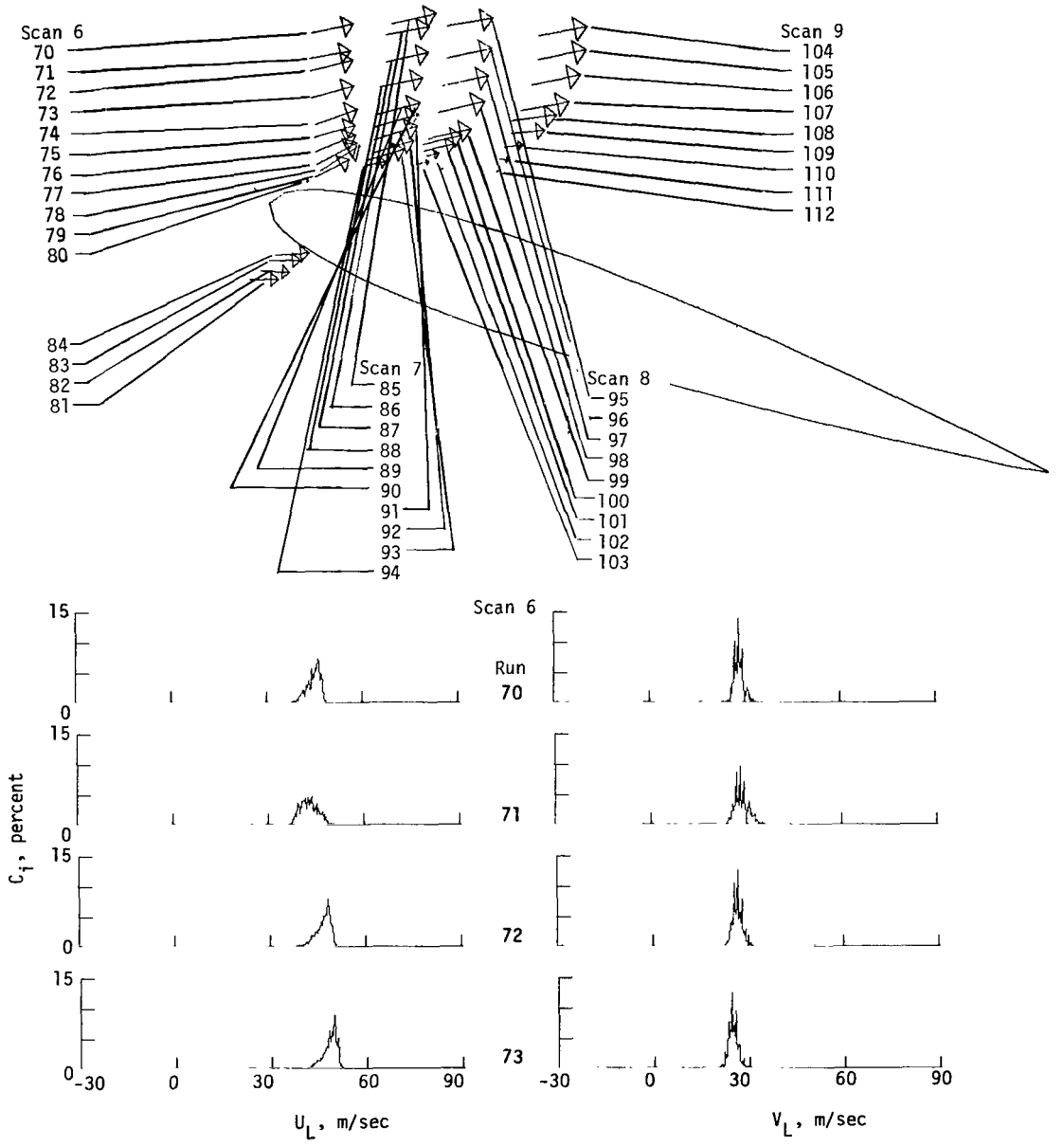

Figure 21.- Histograms in scans 6, 7, 8, and 9.

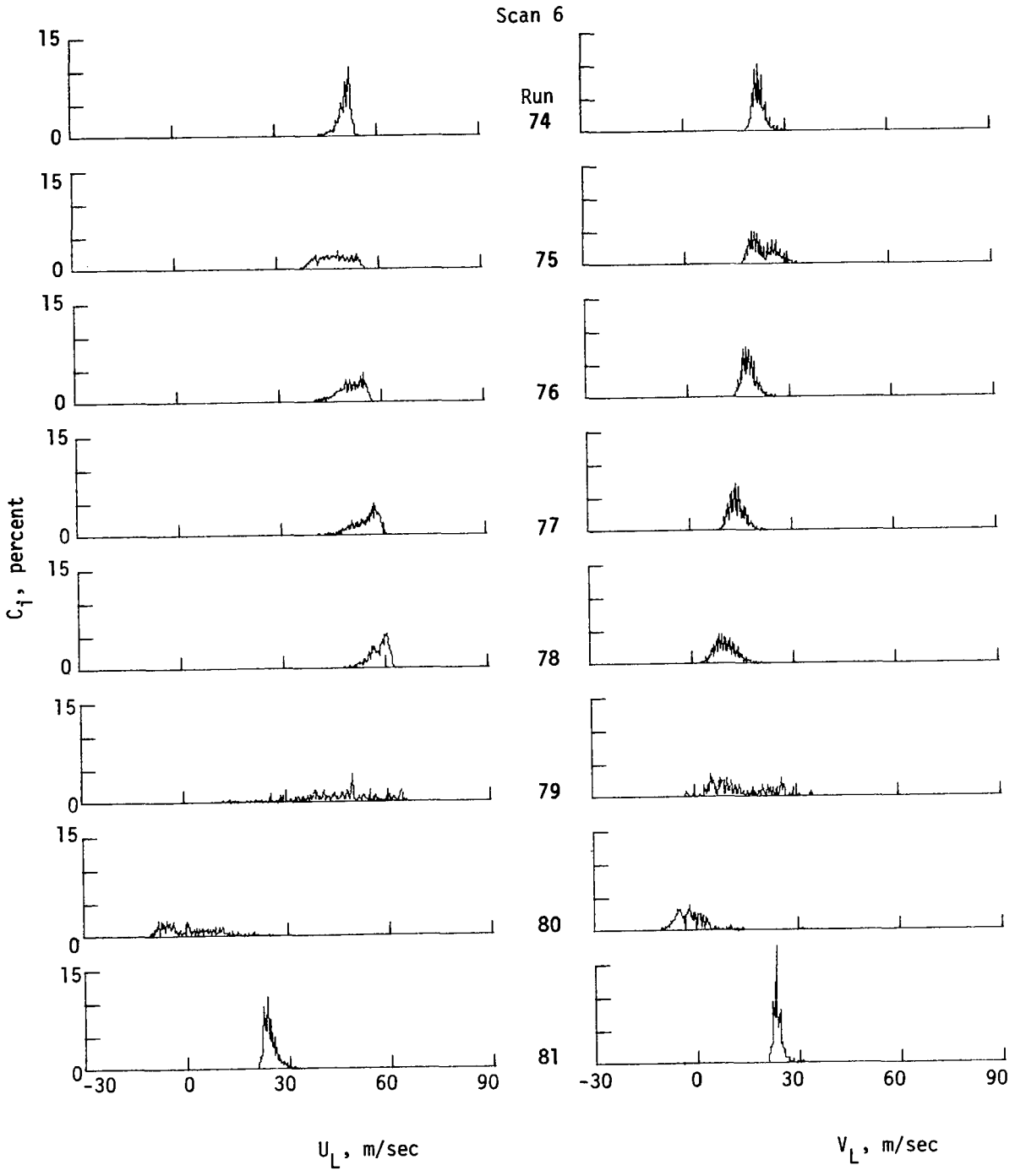

Figure 21.- Continued.

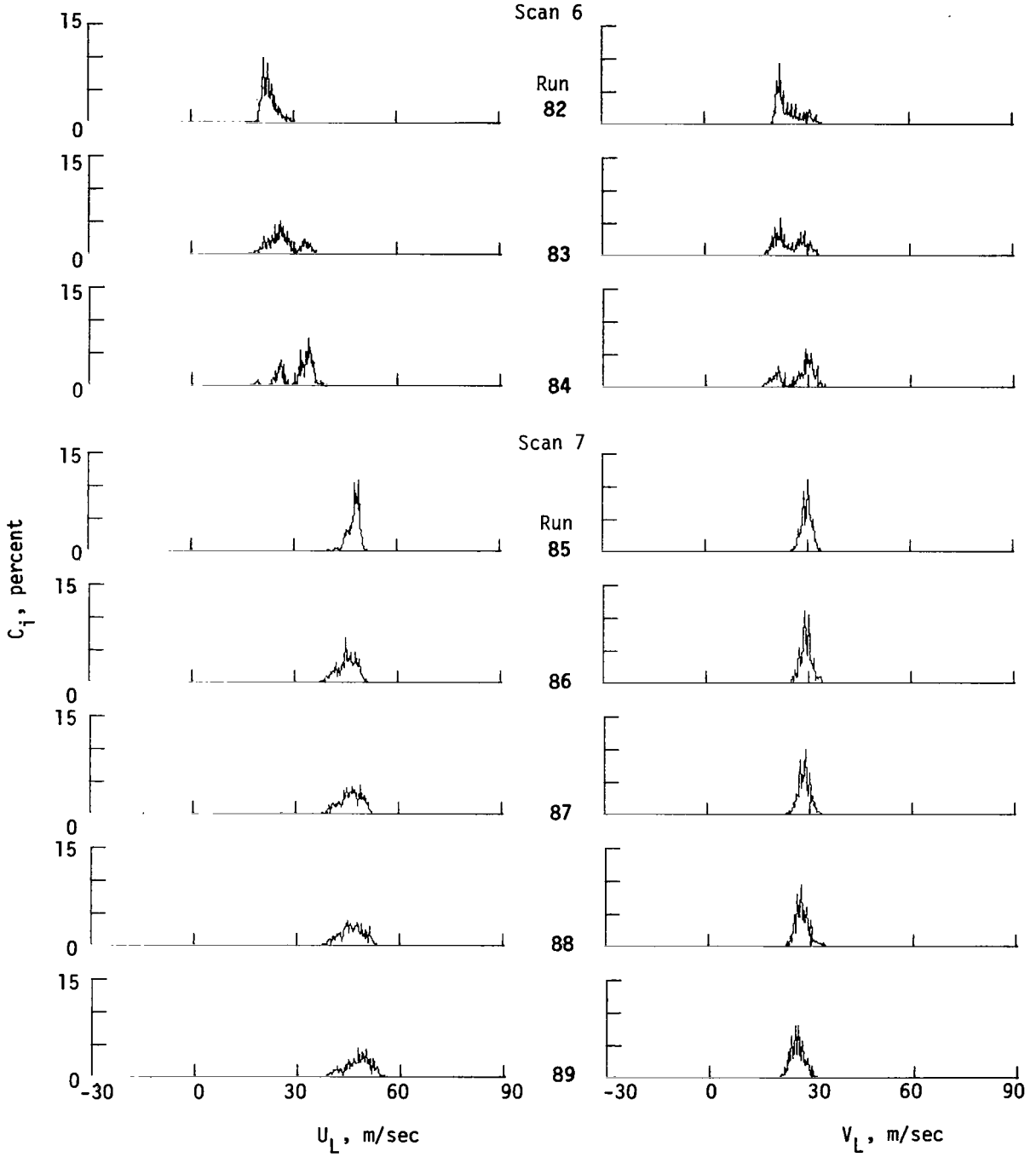

Figure 21.- Continued.

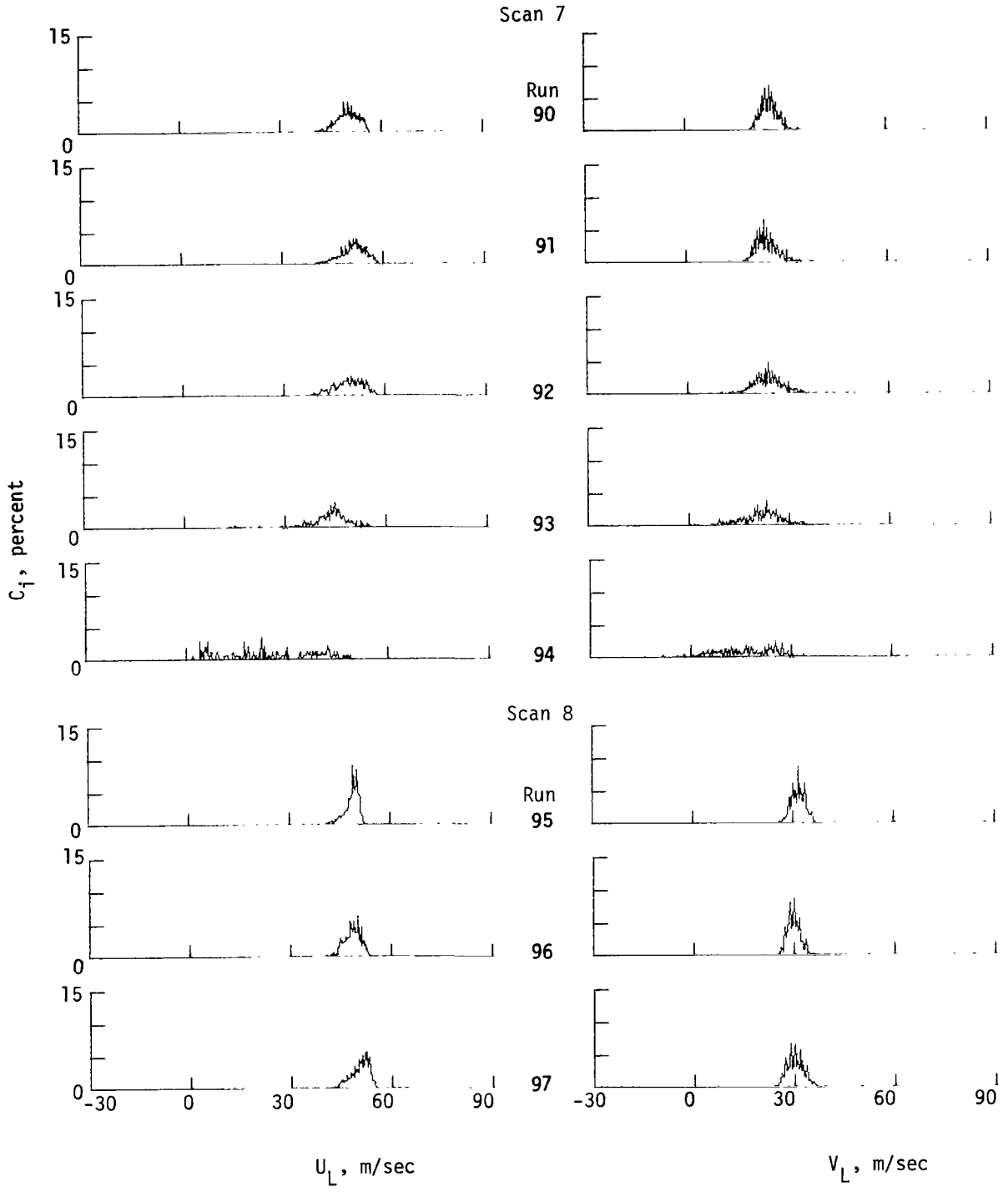

Figure 21.- Continued.

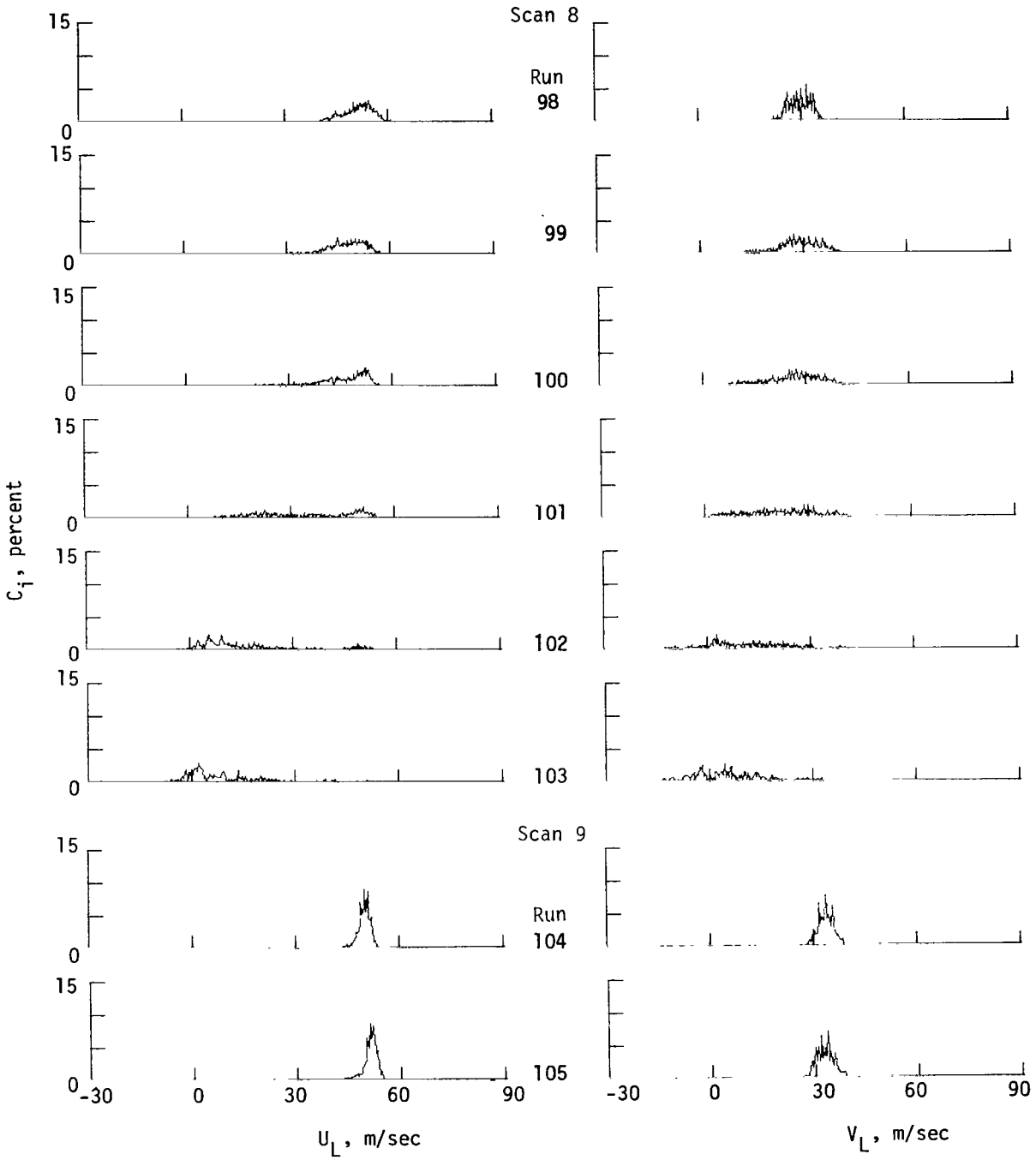

Figure 21.- Continued.

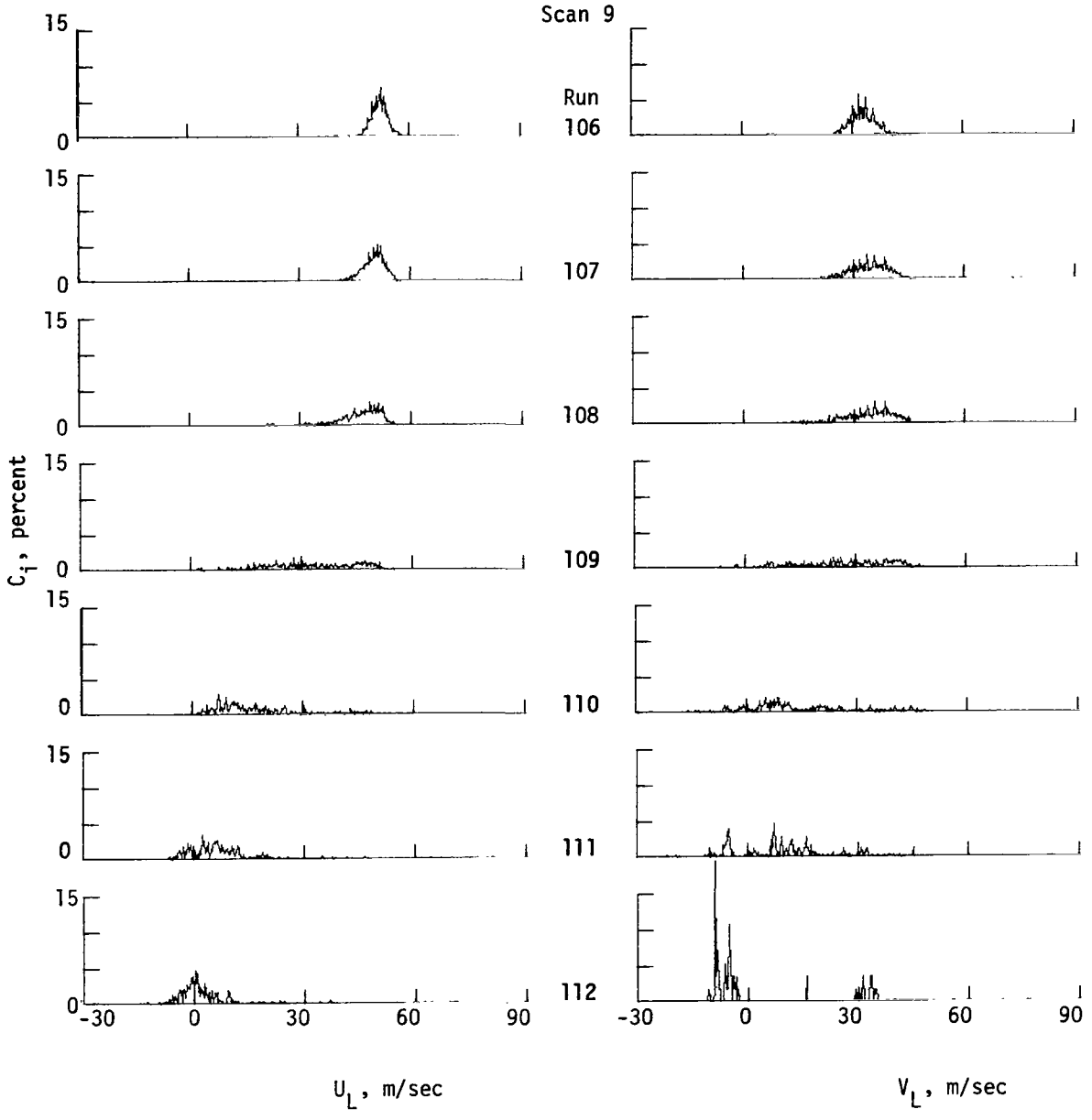

Figure 21.- Concluded.

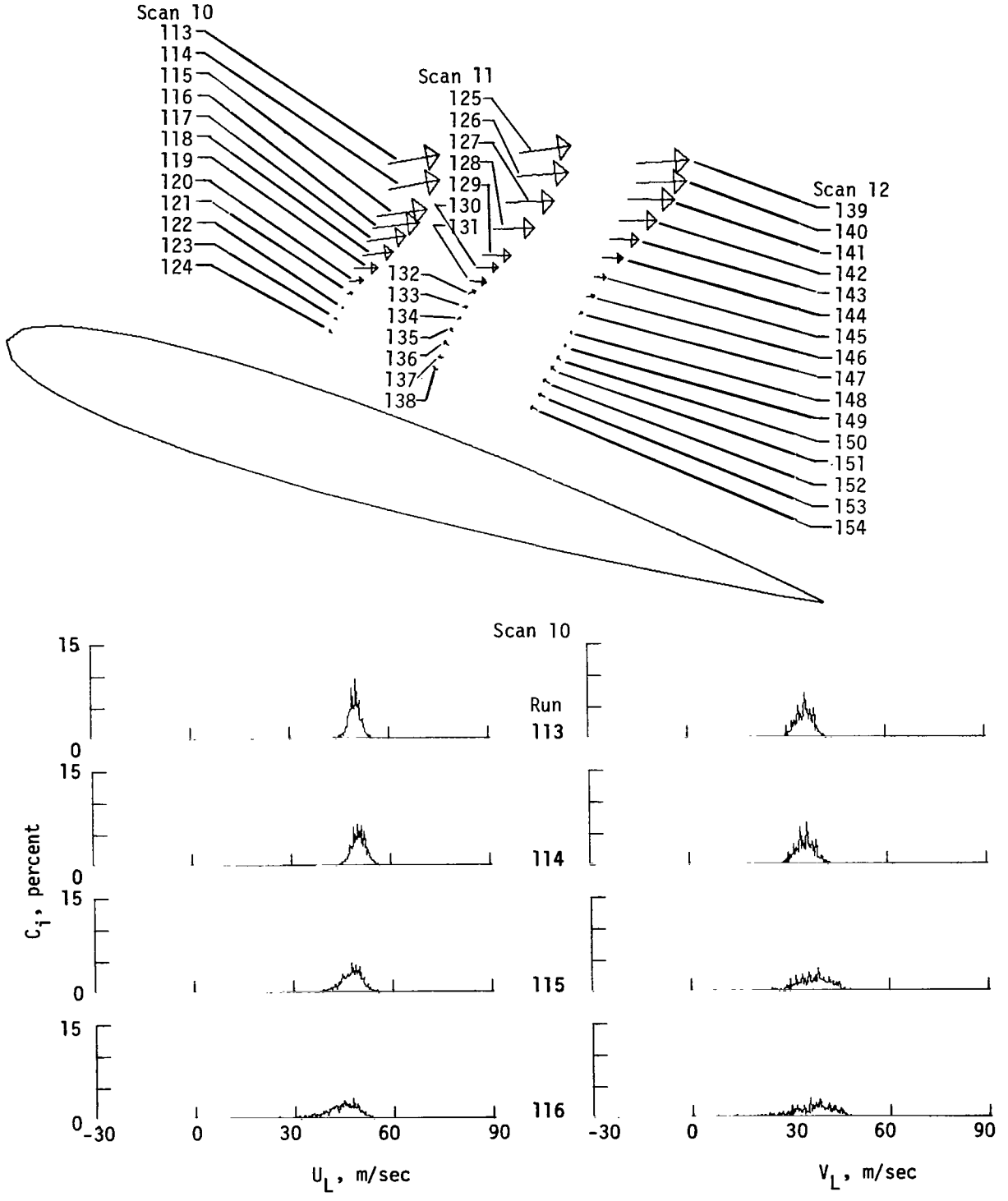

Figure 22.- Histograms in scans 10, 11, and 12.

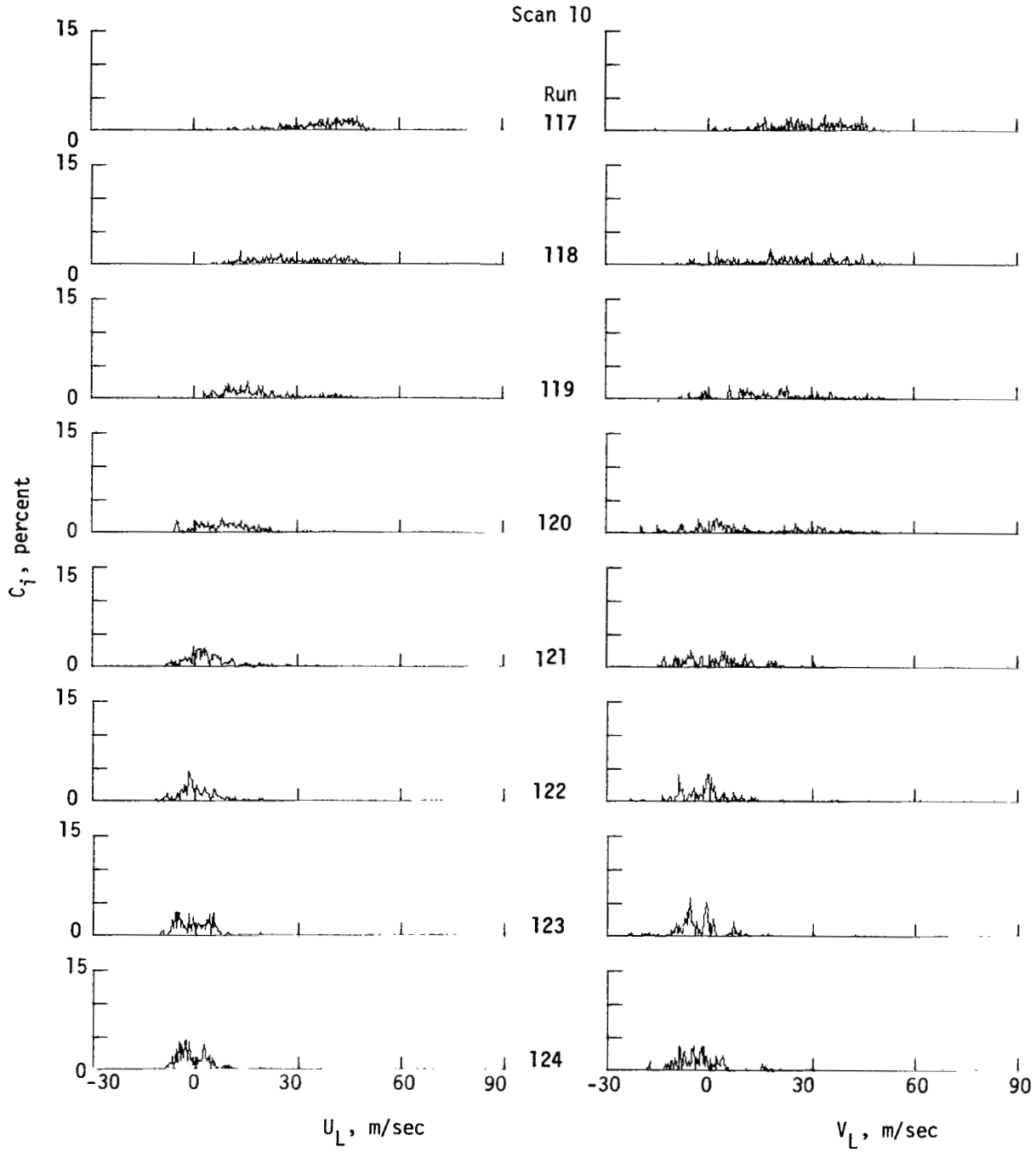

Figure 22.- Continued.

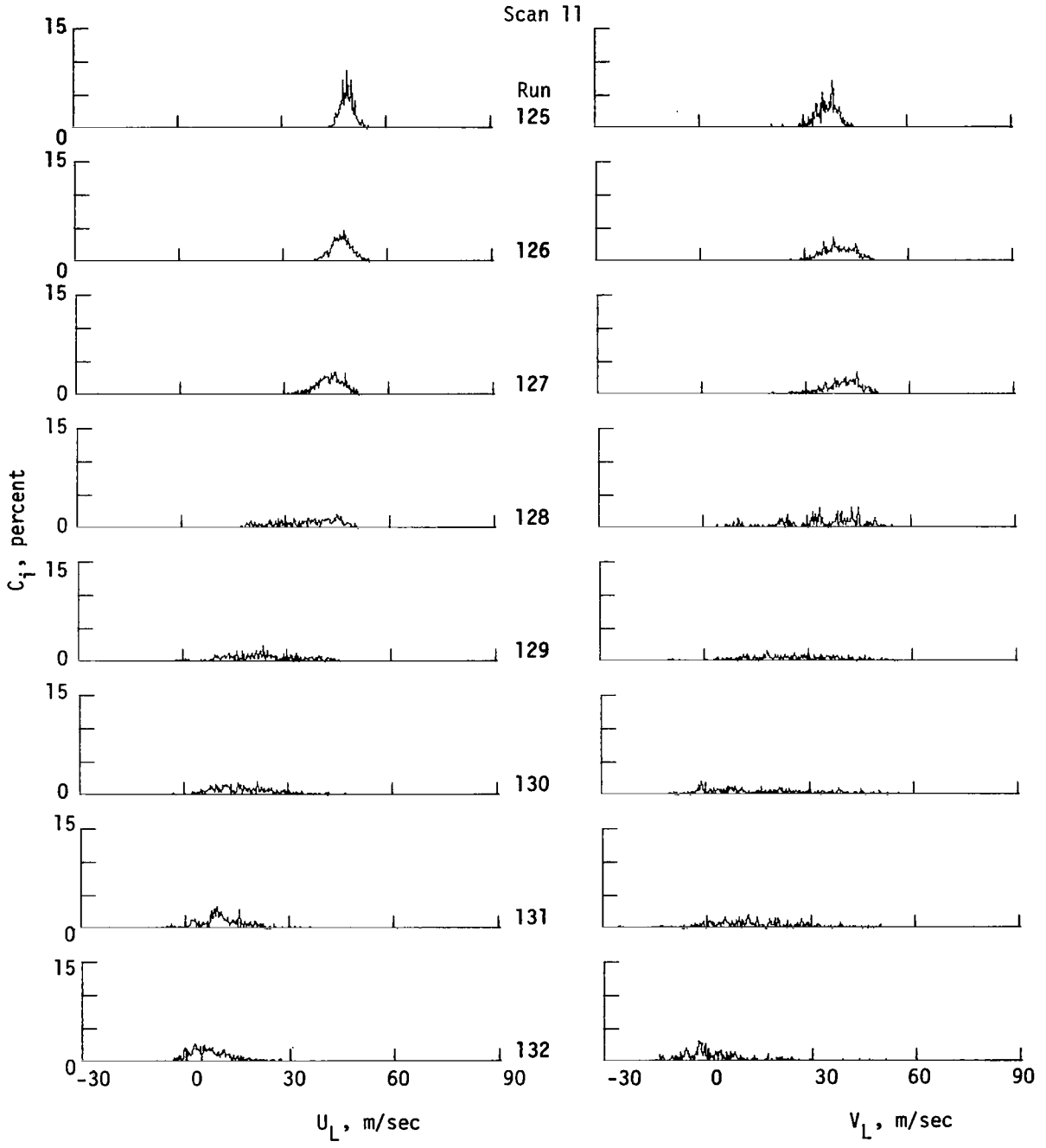

Figure 22.- Continued.

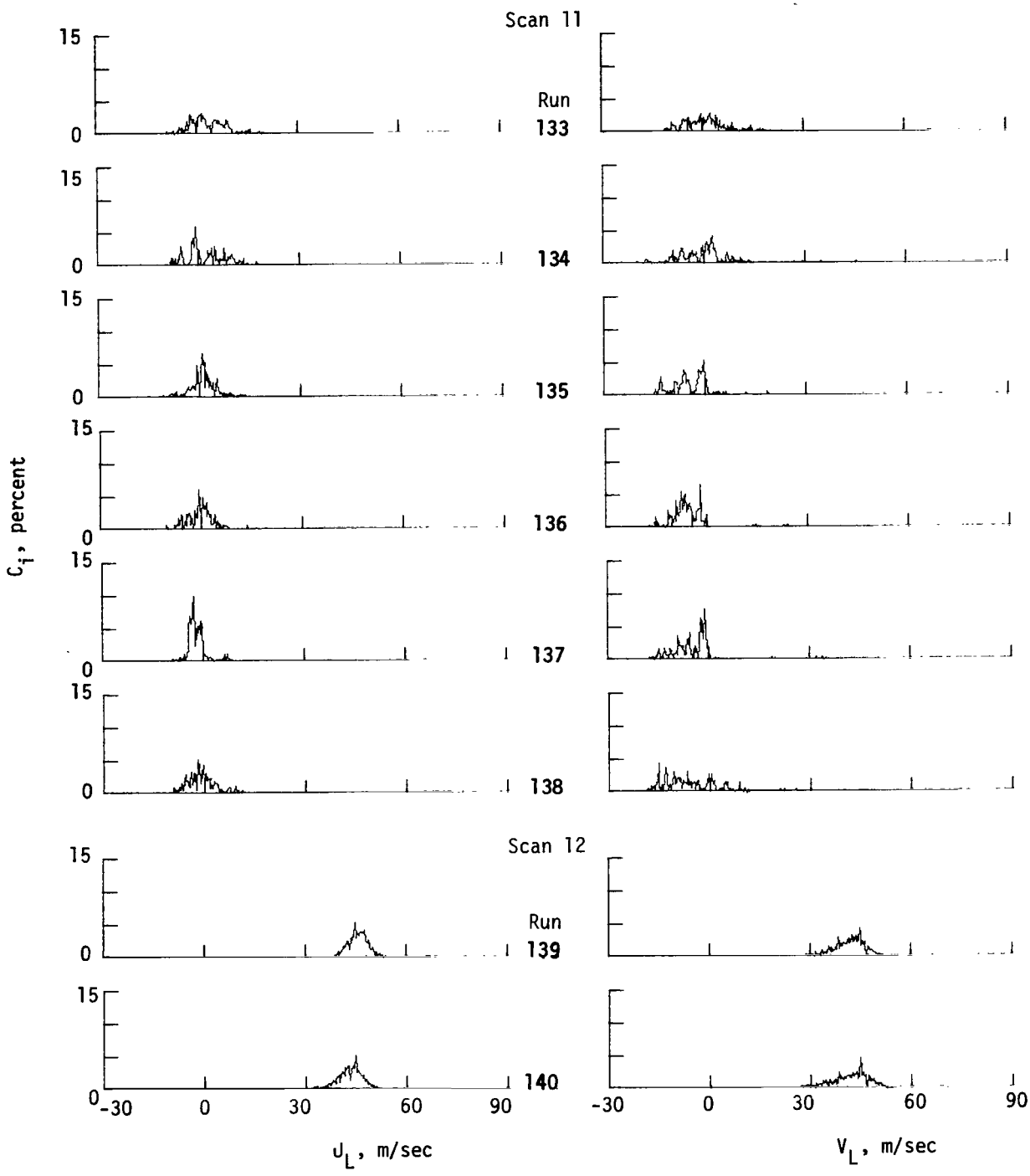

Figure 22.- Continued.

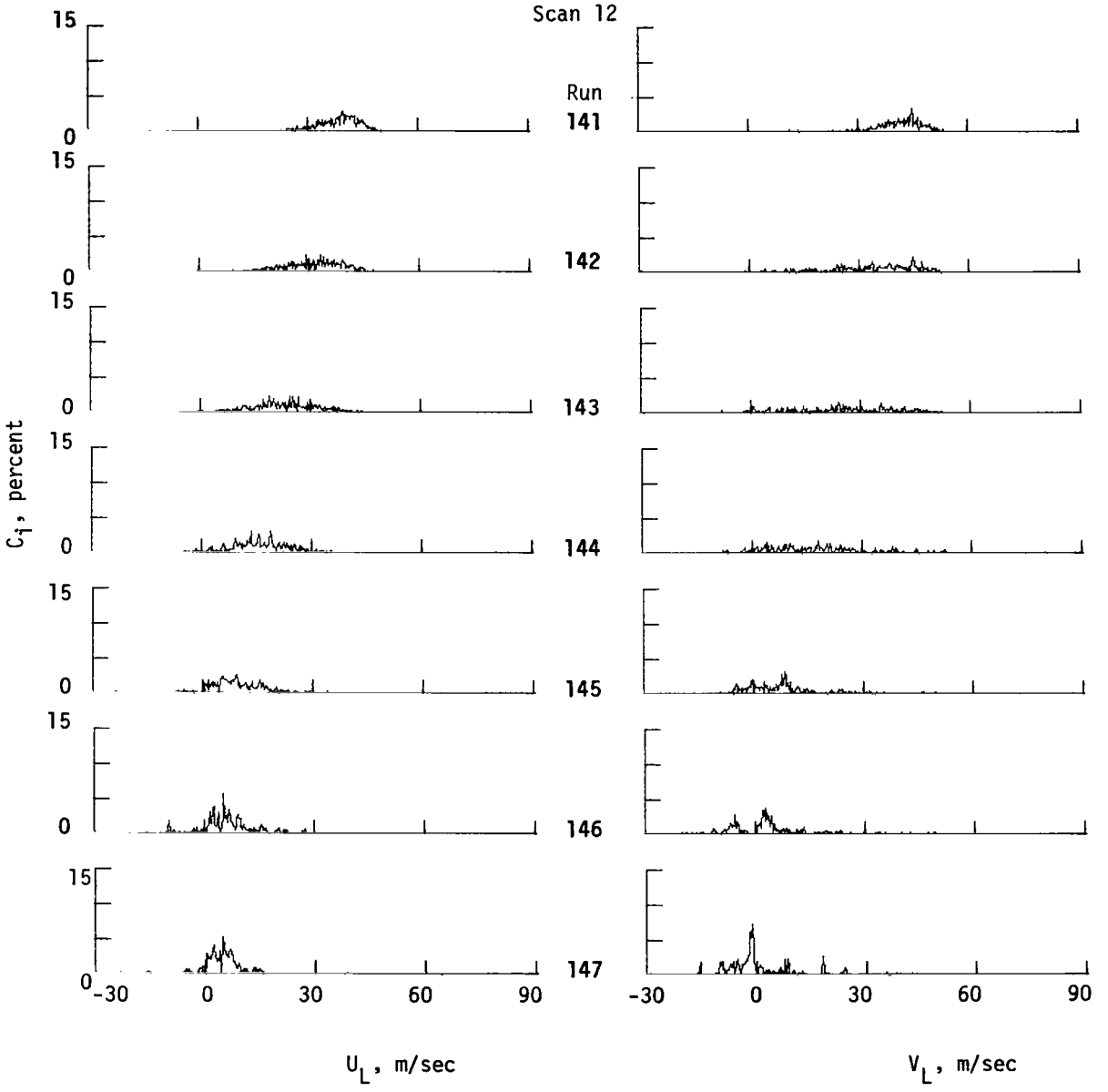

Figure 22.- Continued.

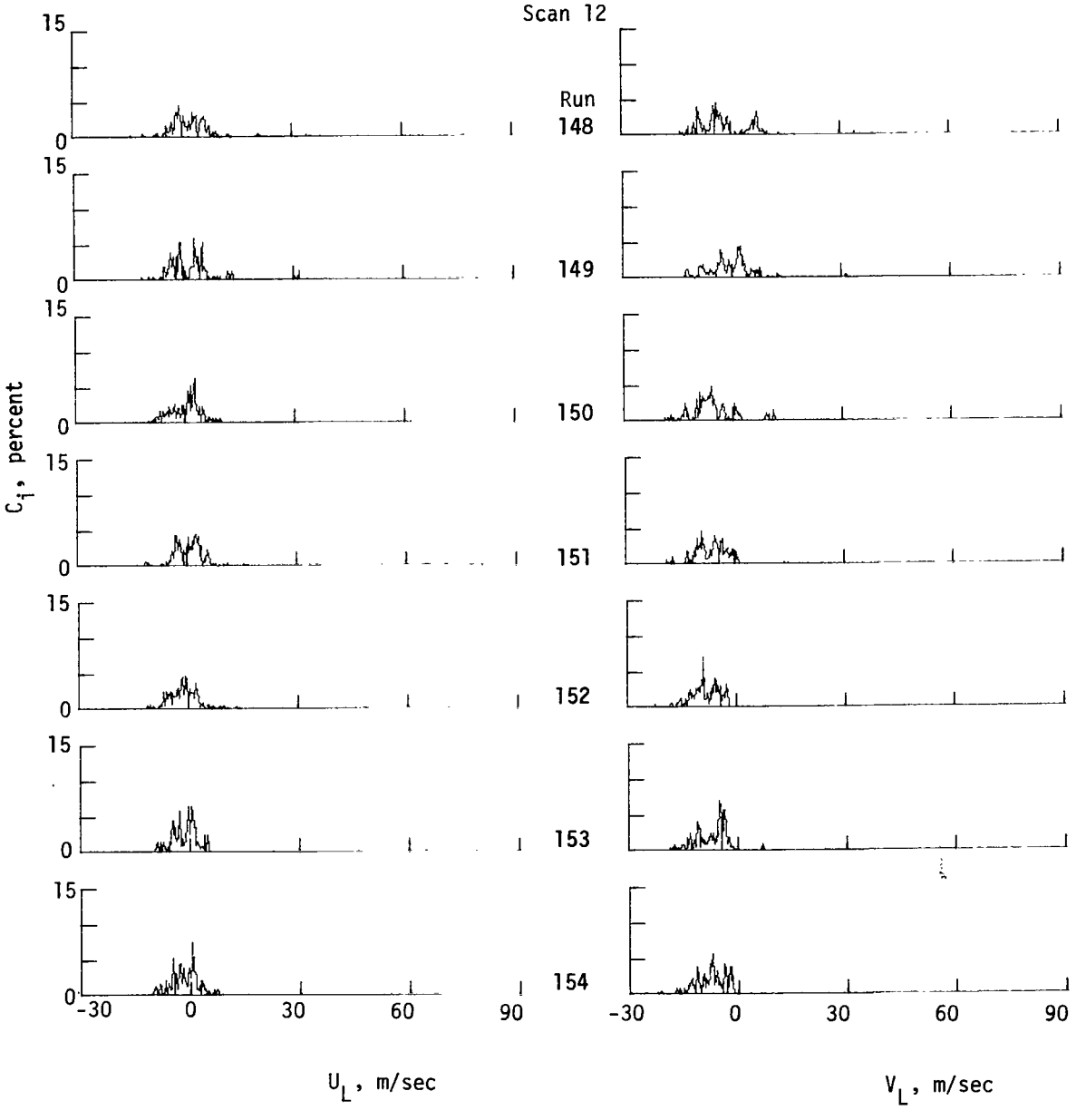

Figure 22.- Concluded.

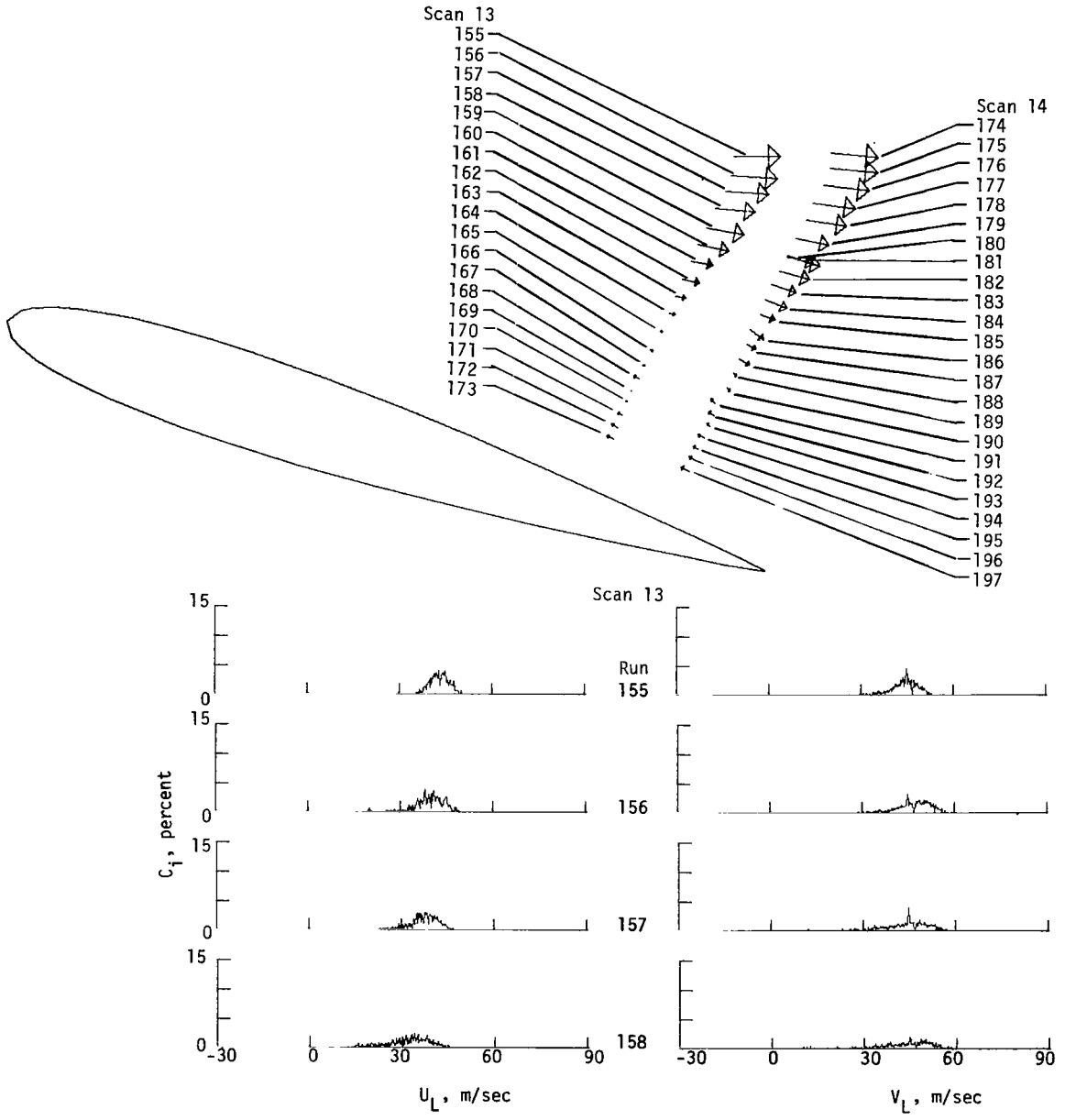

Figure 23.- Histograms in scans 13 and 14.

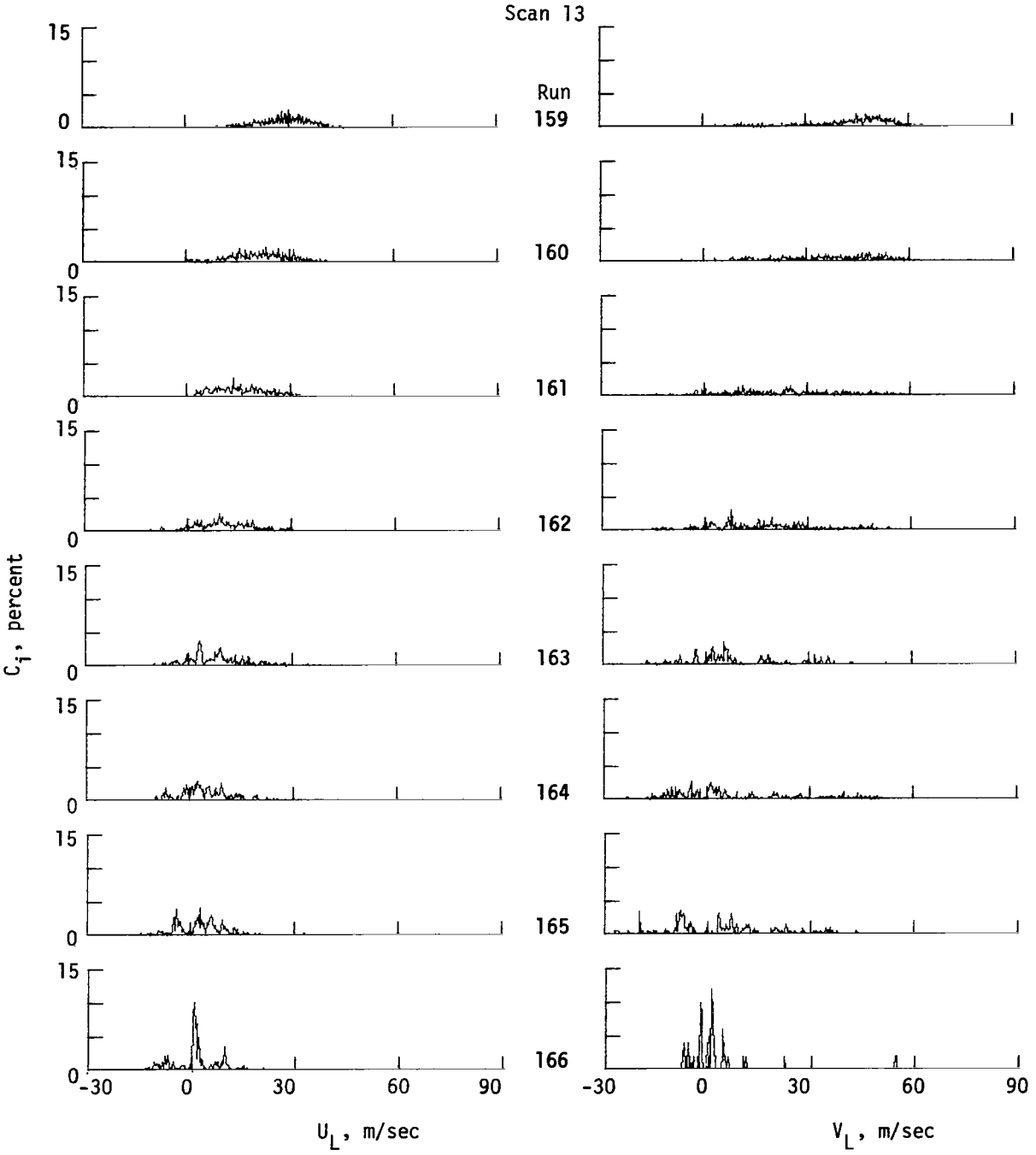

Figure 23.- Continued.

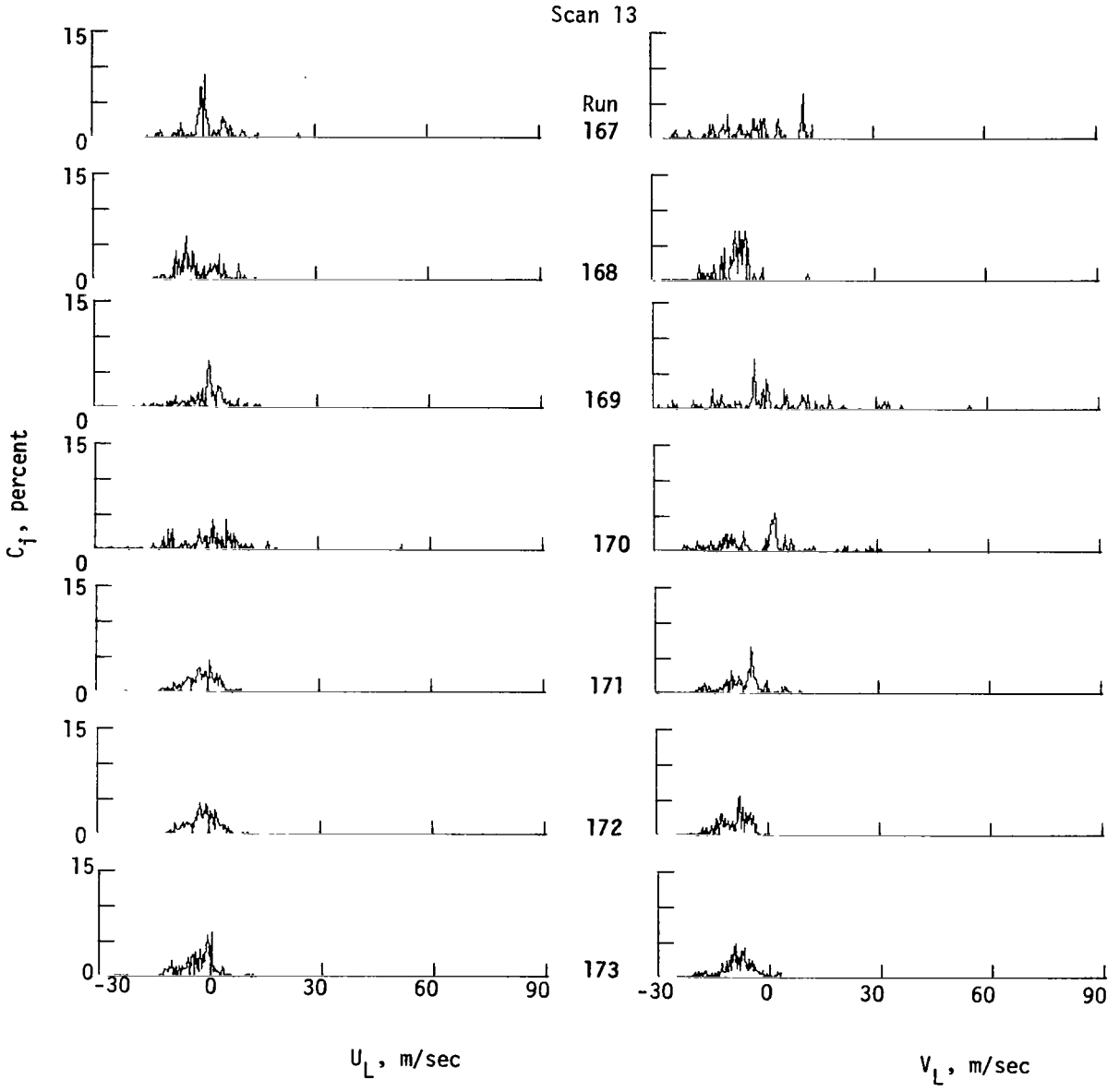

Figure 23.- Continued.

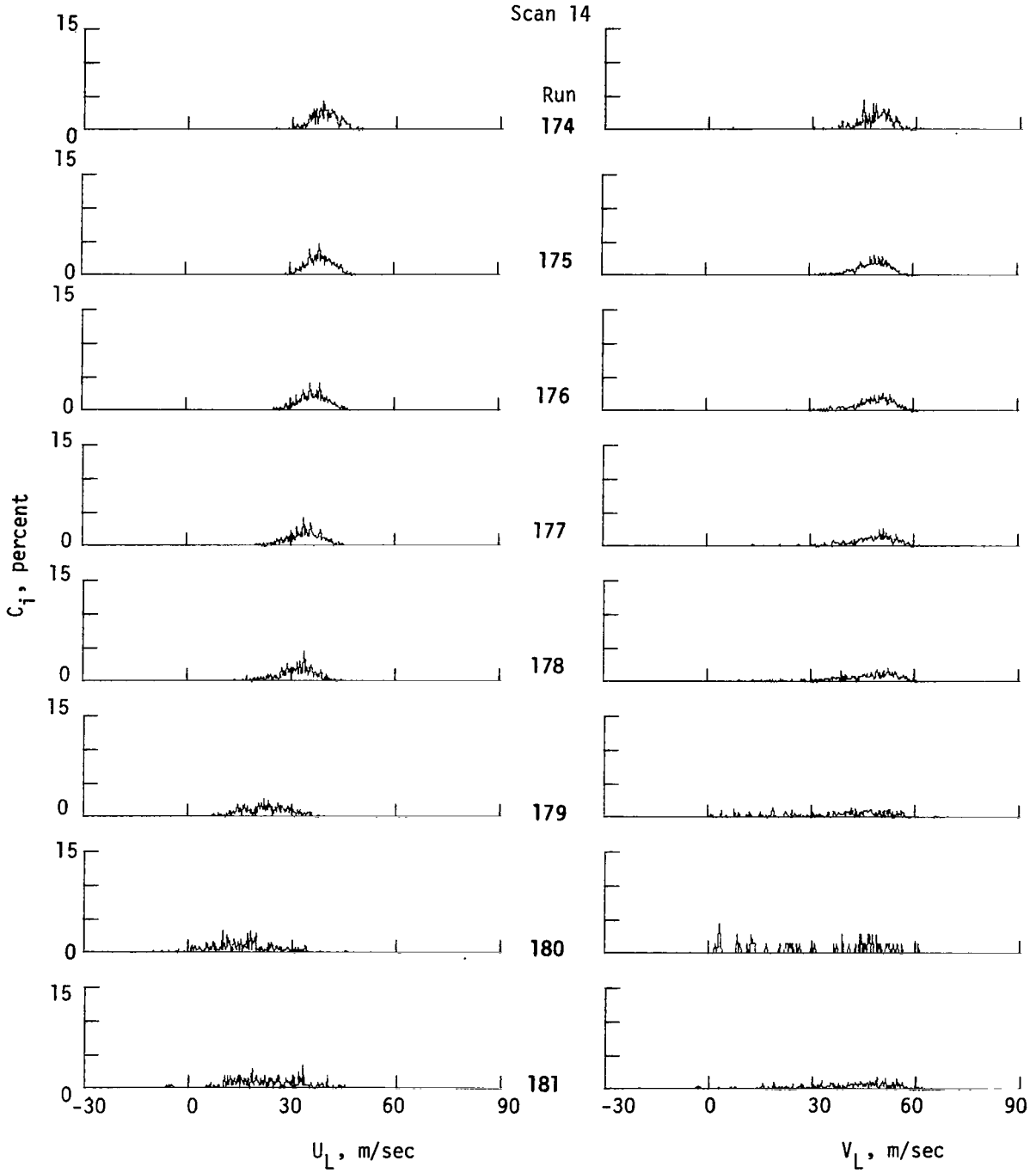

Figure 23.- Continued.

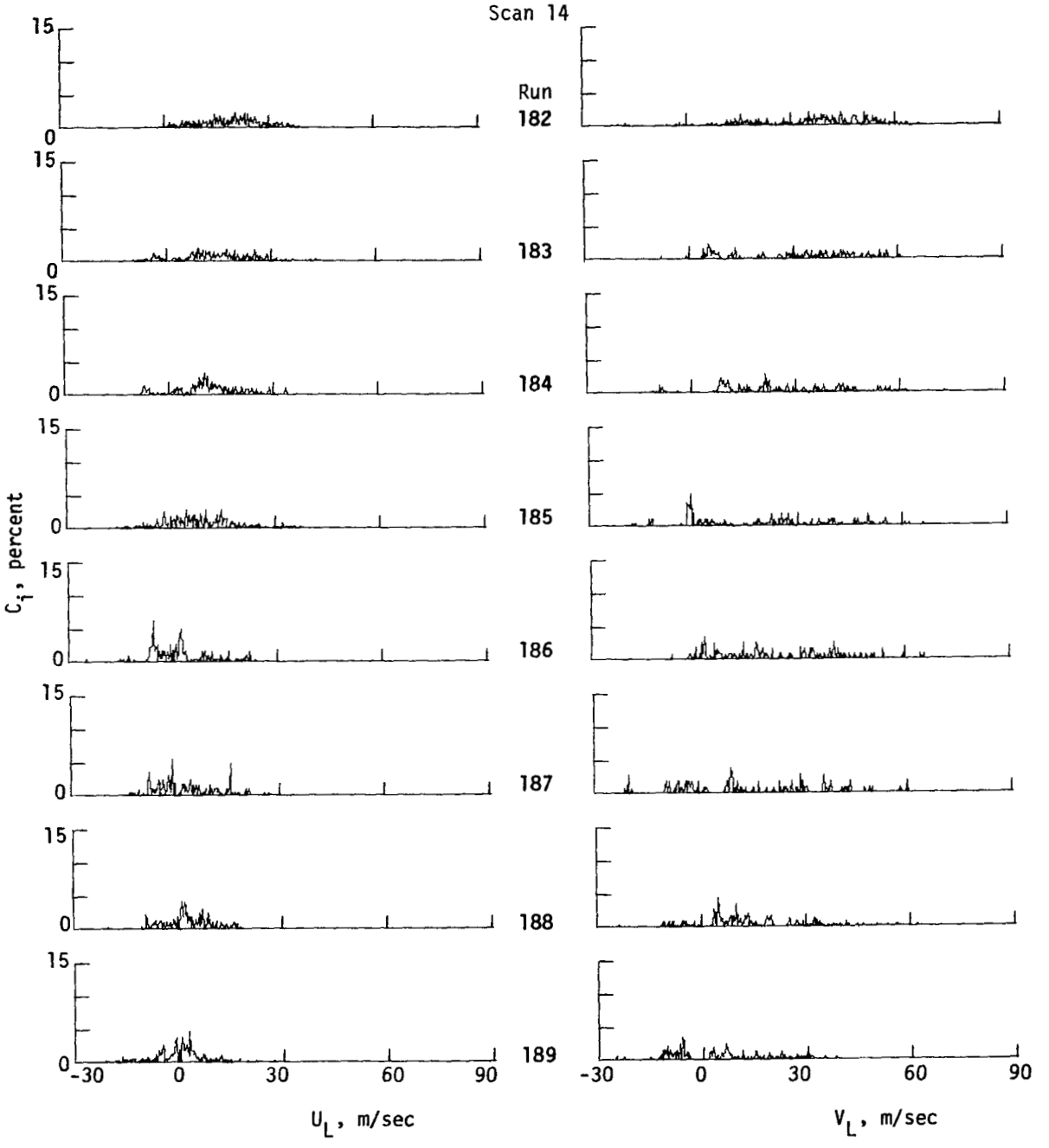

Figure 23.- Continued.

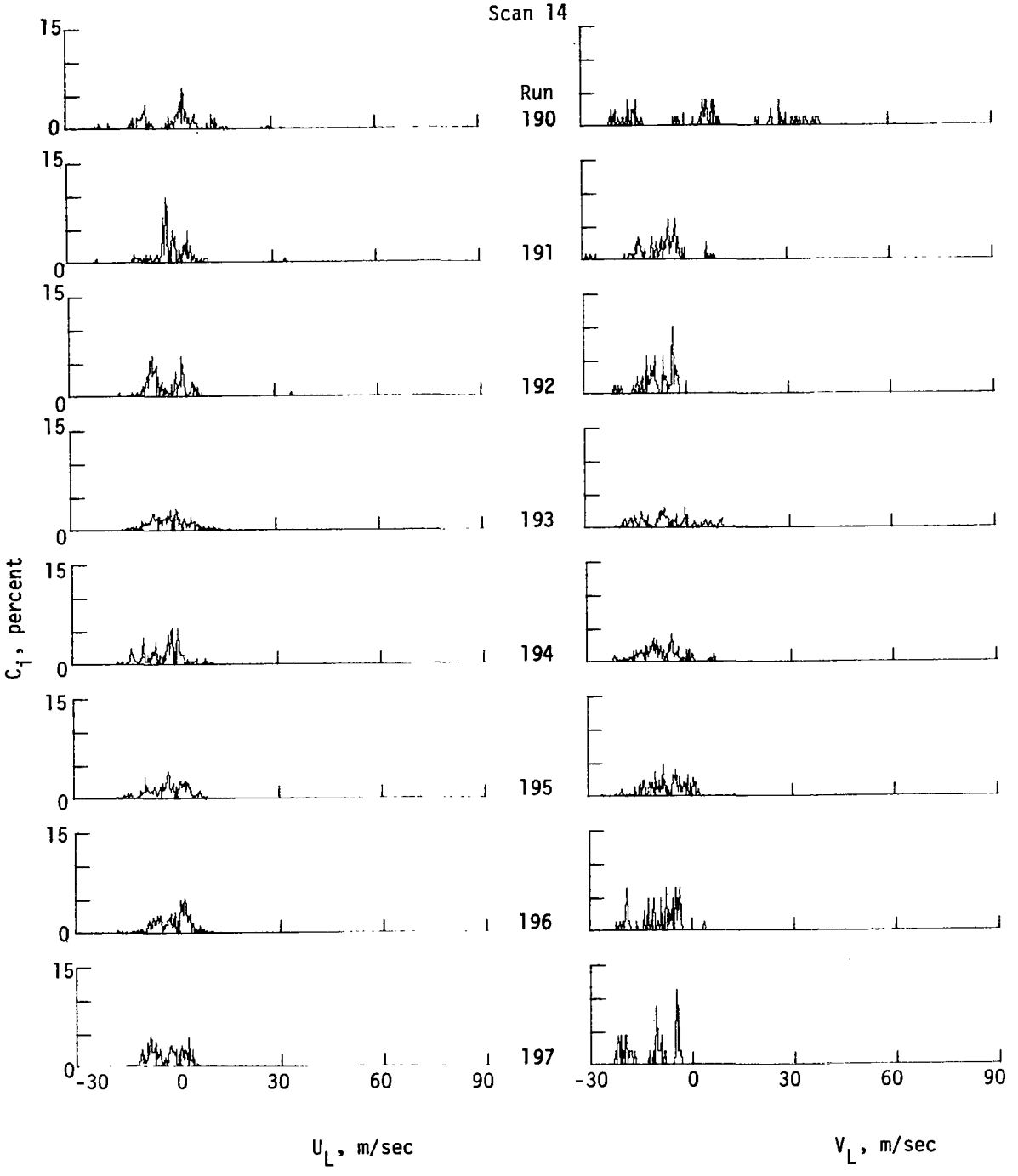

Figure 23.- Concluded.

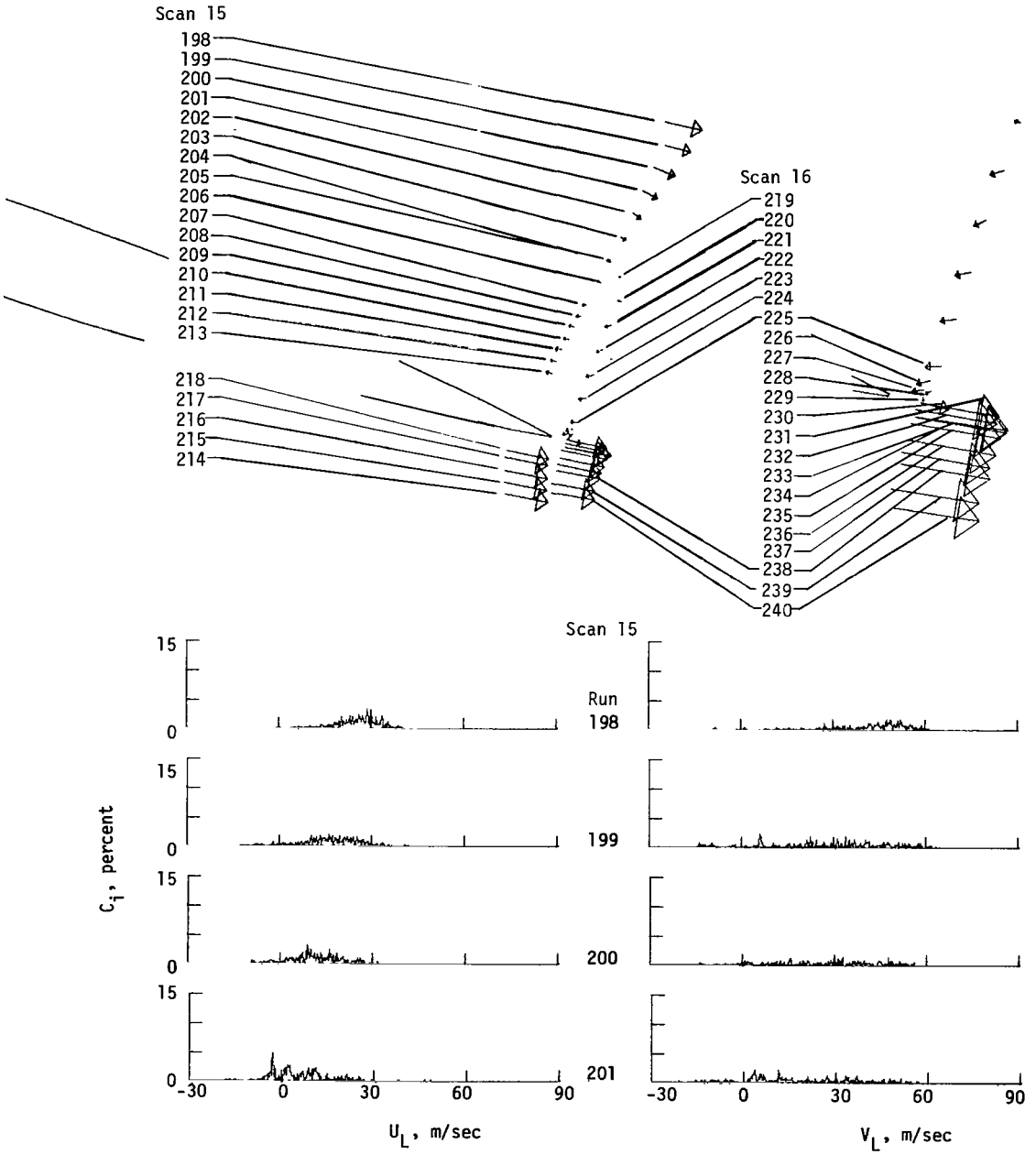

Figure 24.- Histograms in scans 15 and 16.

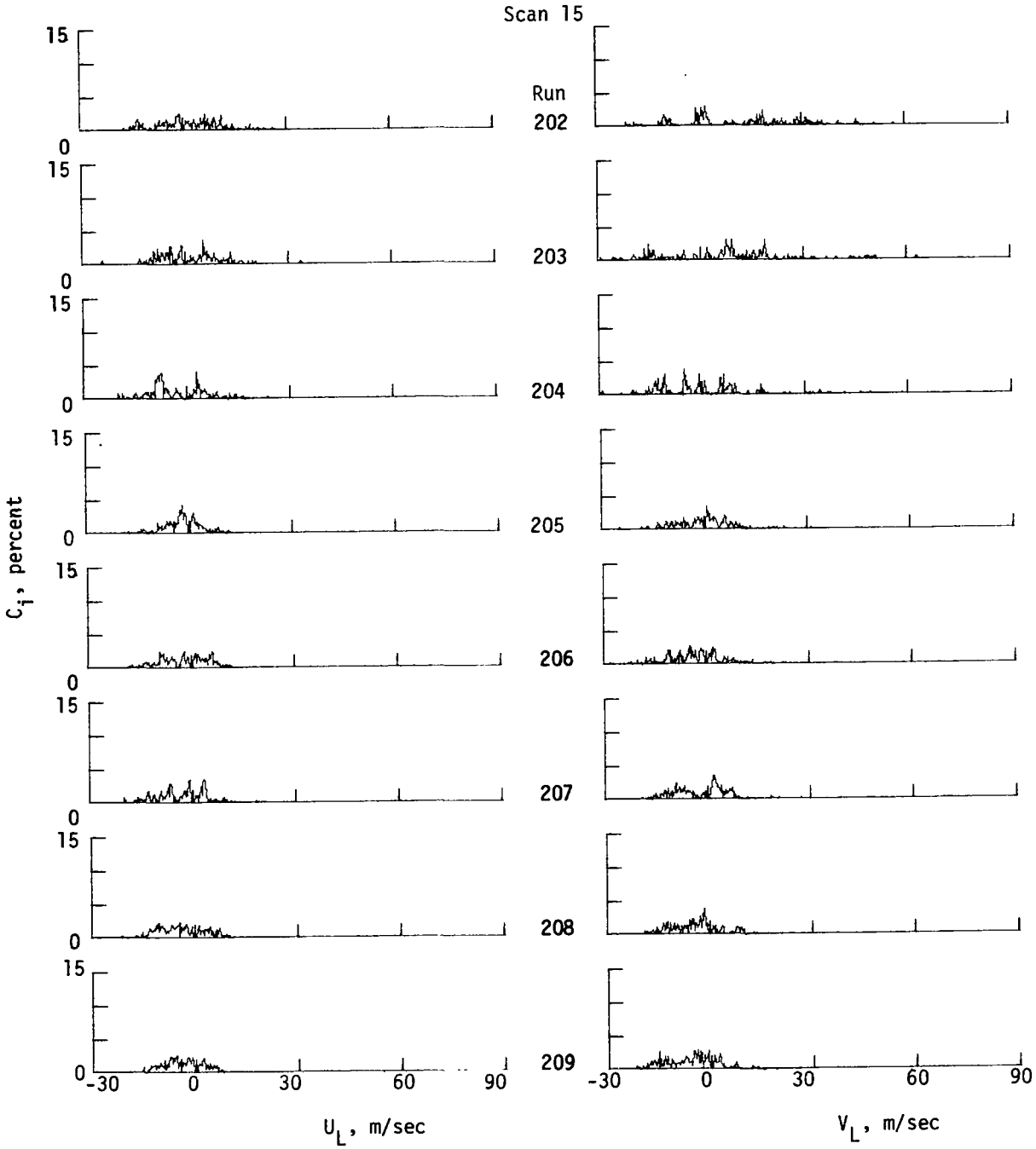

Figure 24.- Continued.

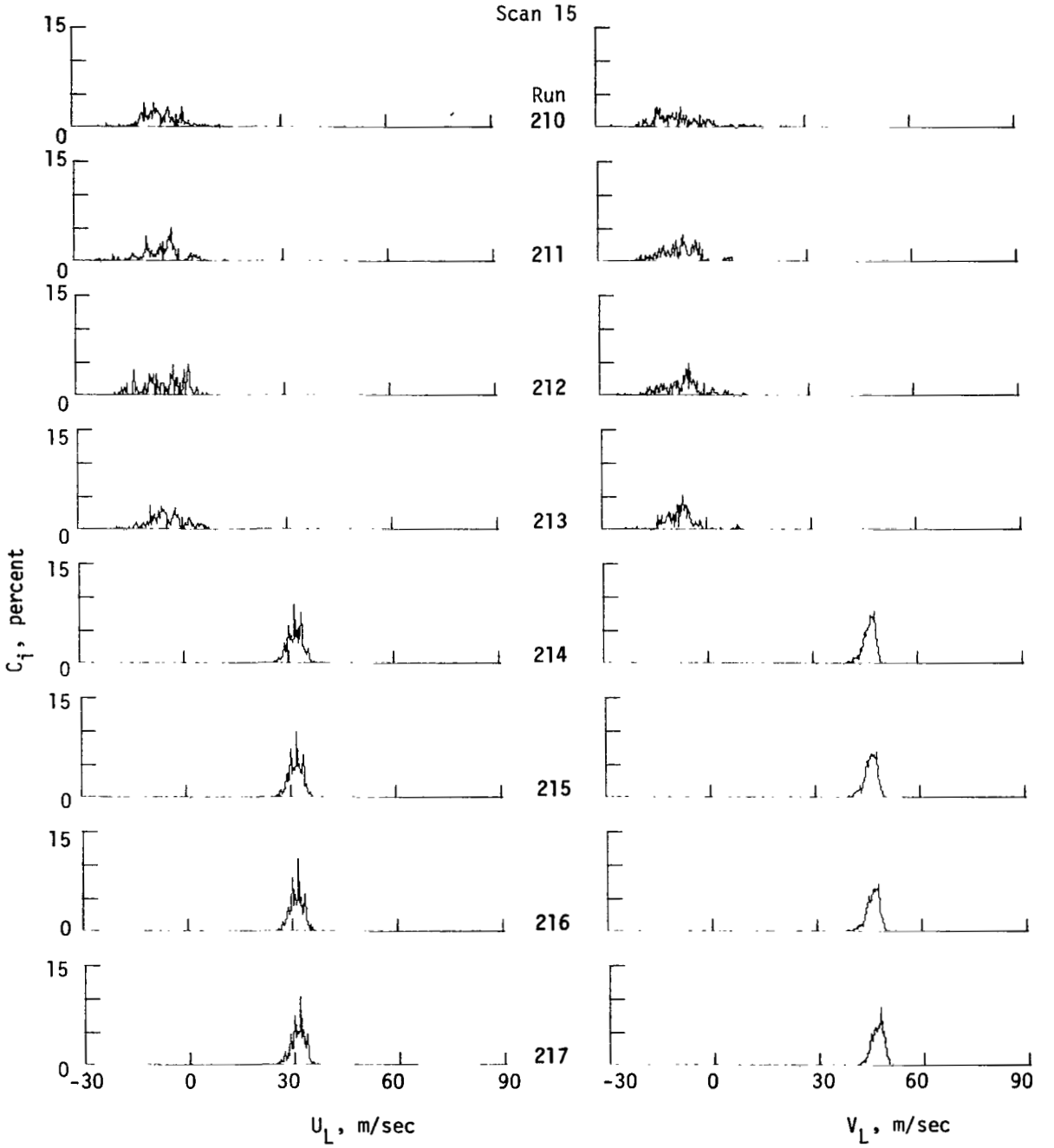

Figure 24.- Continued.

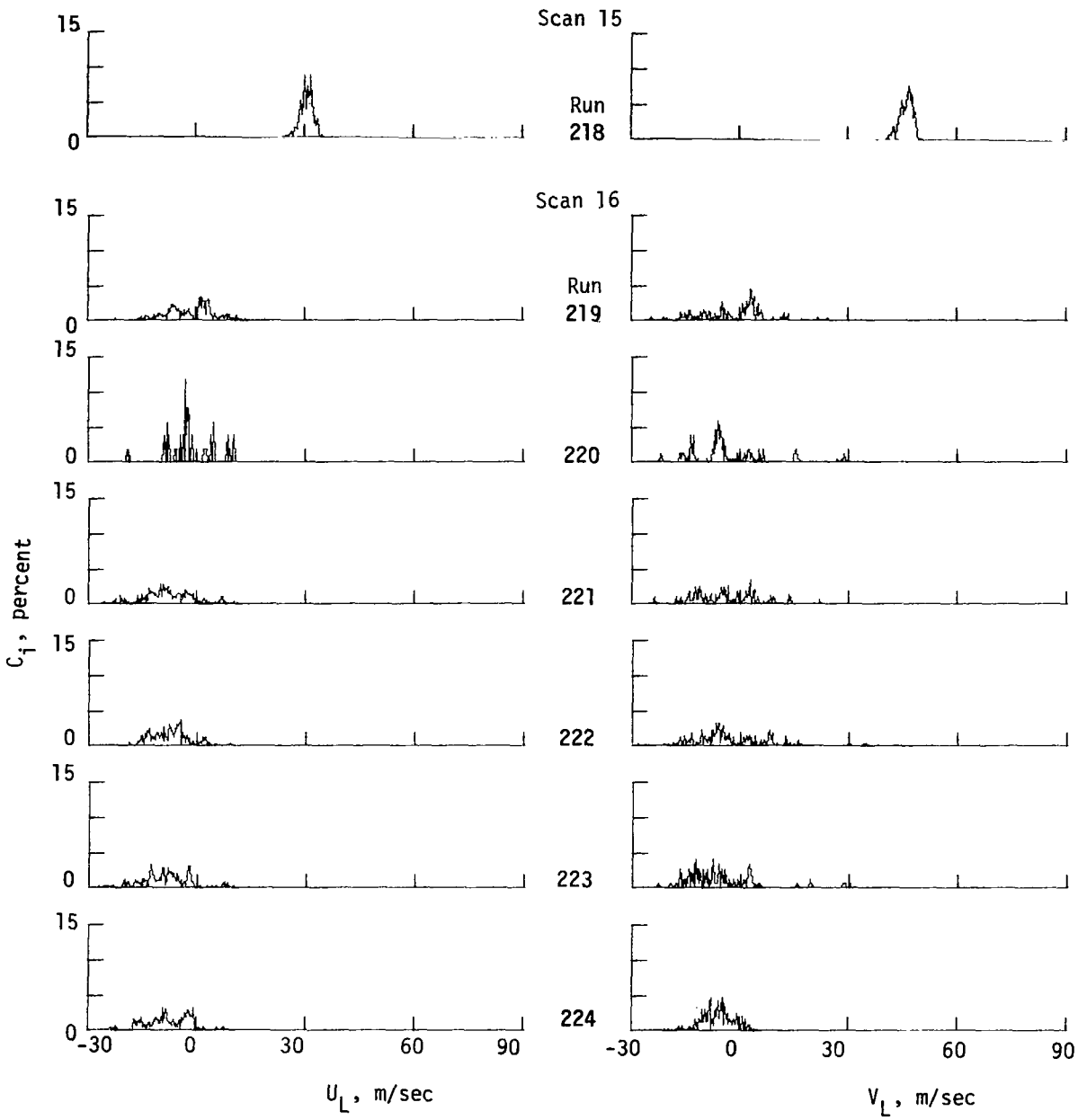

Figure 24.- Continued.

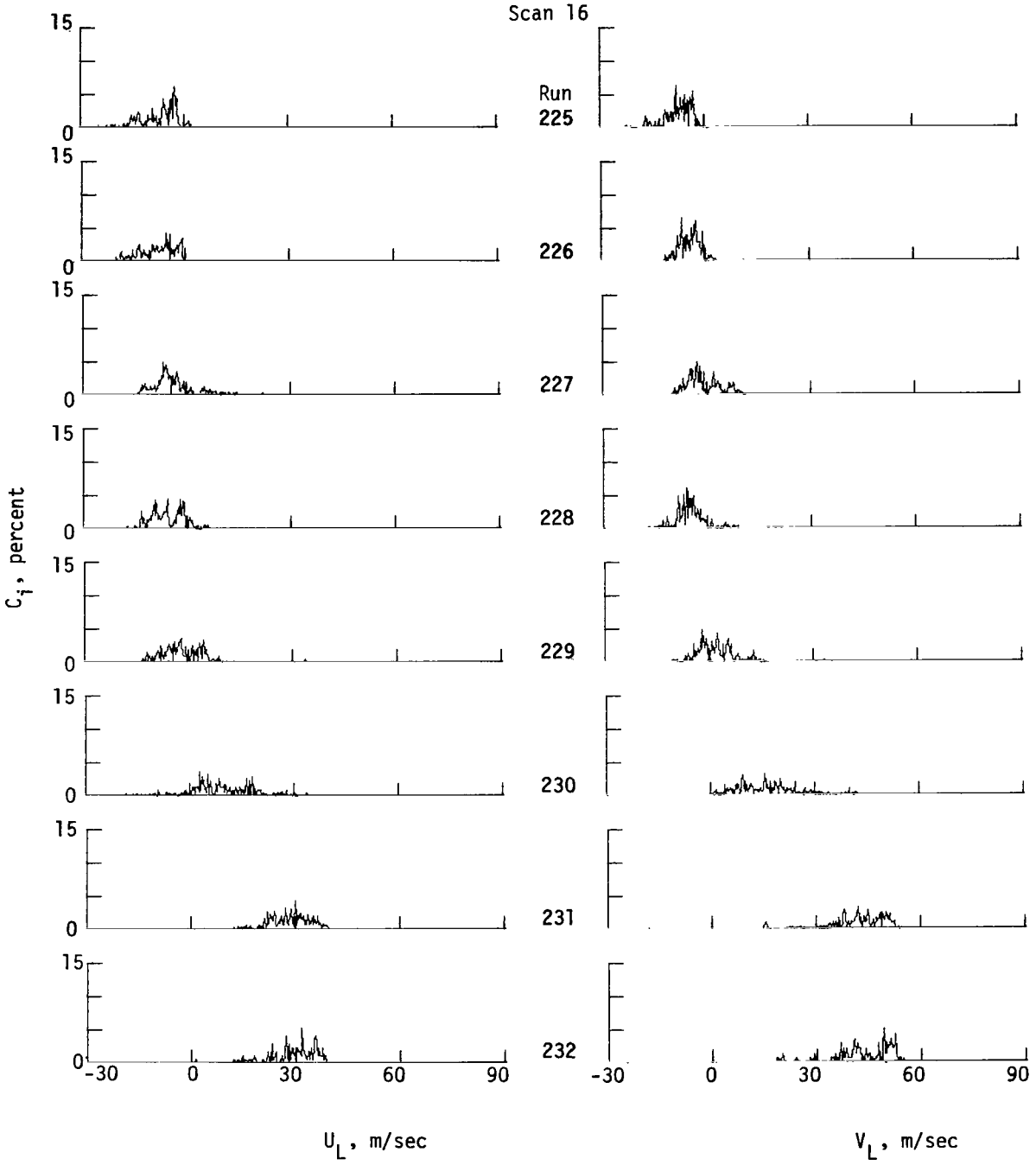

Figure 24.- Continued.

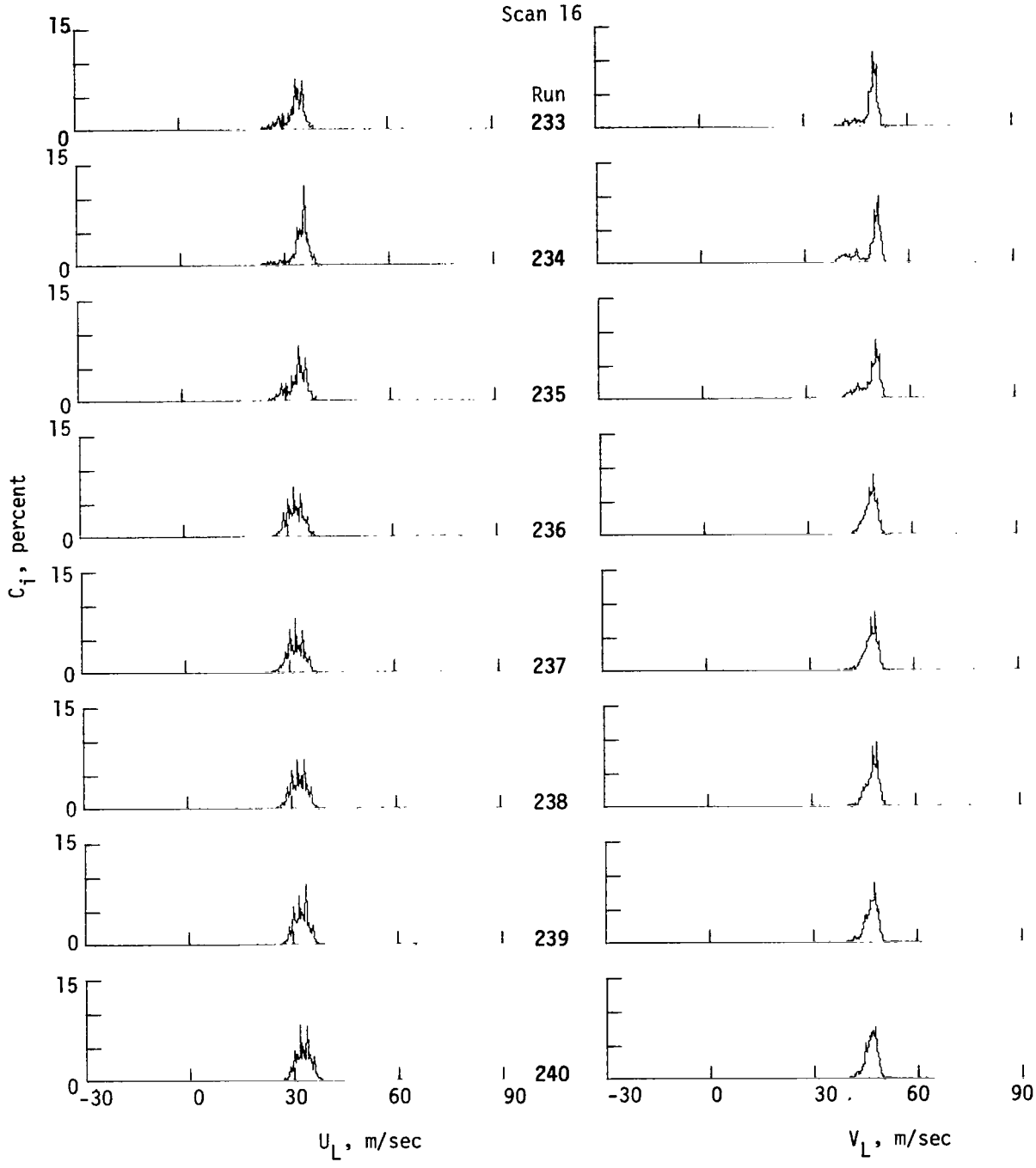

Figure 24.- Concluded.

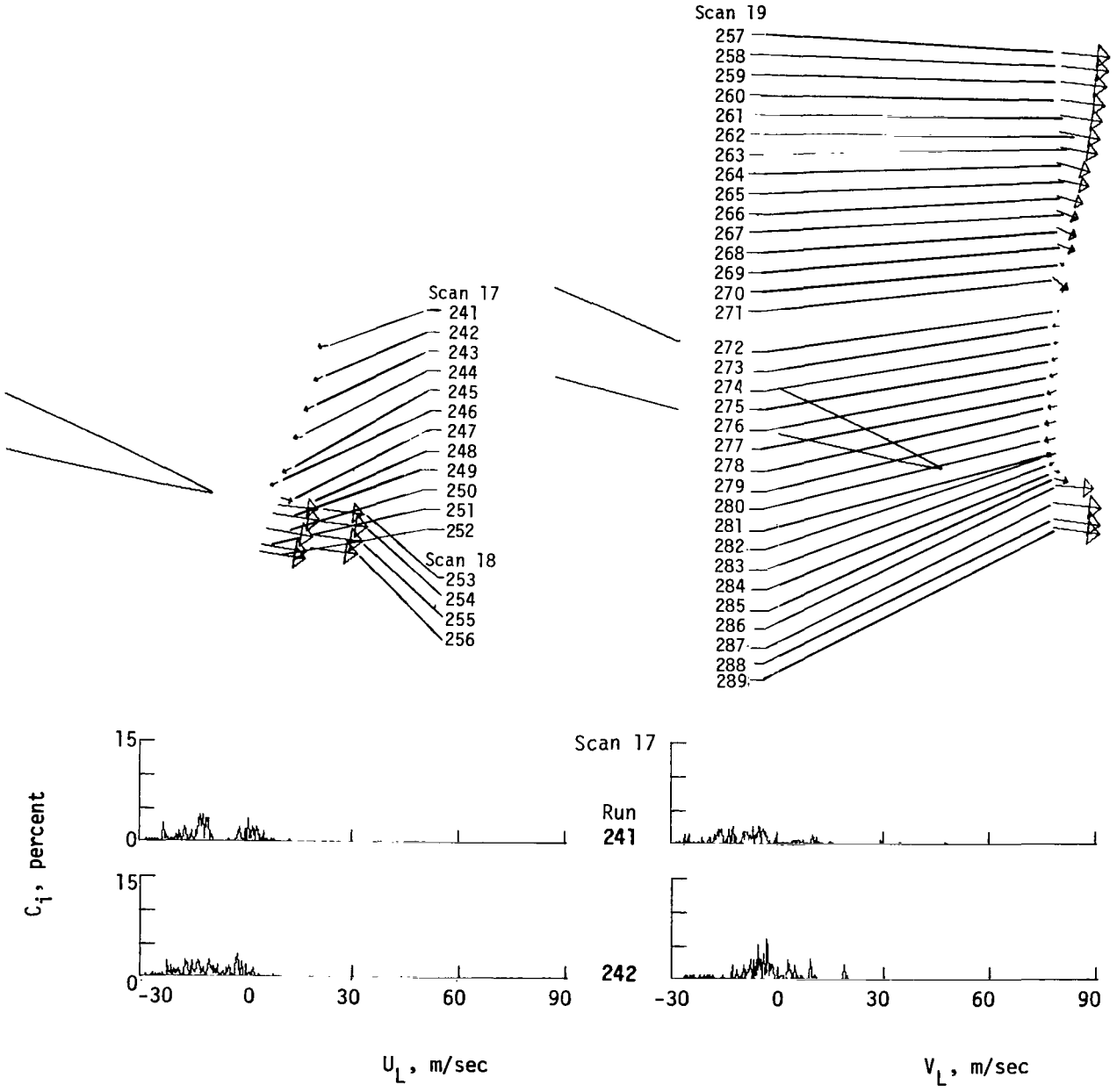

Figure 25.- Histograms in scans 17, 18, and 19.

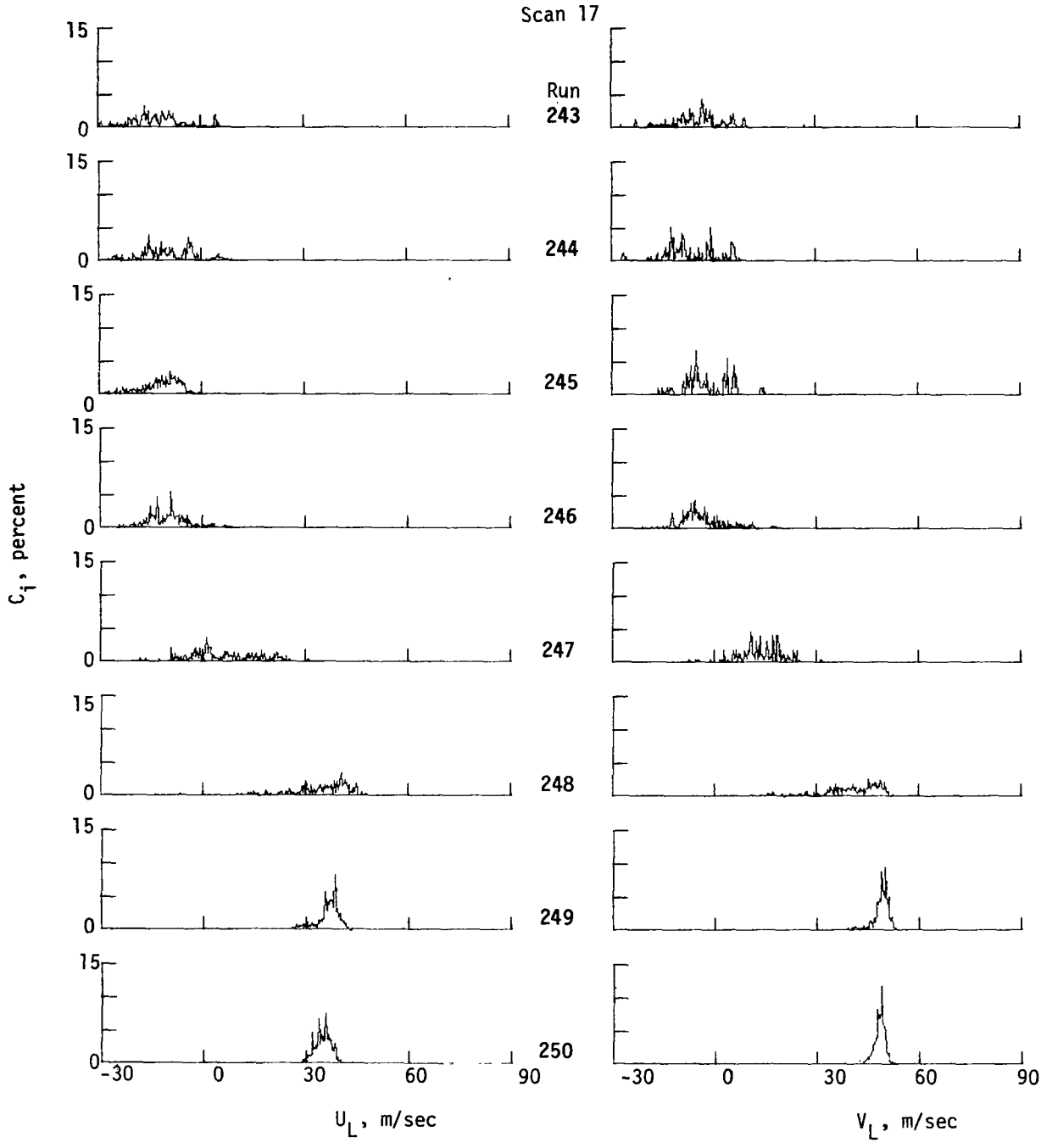

Figure 25.- Continued.

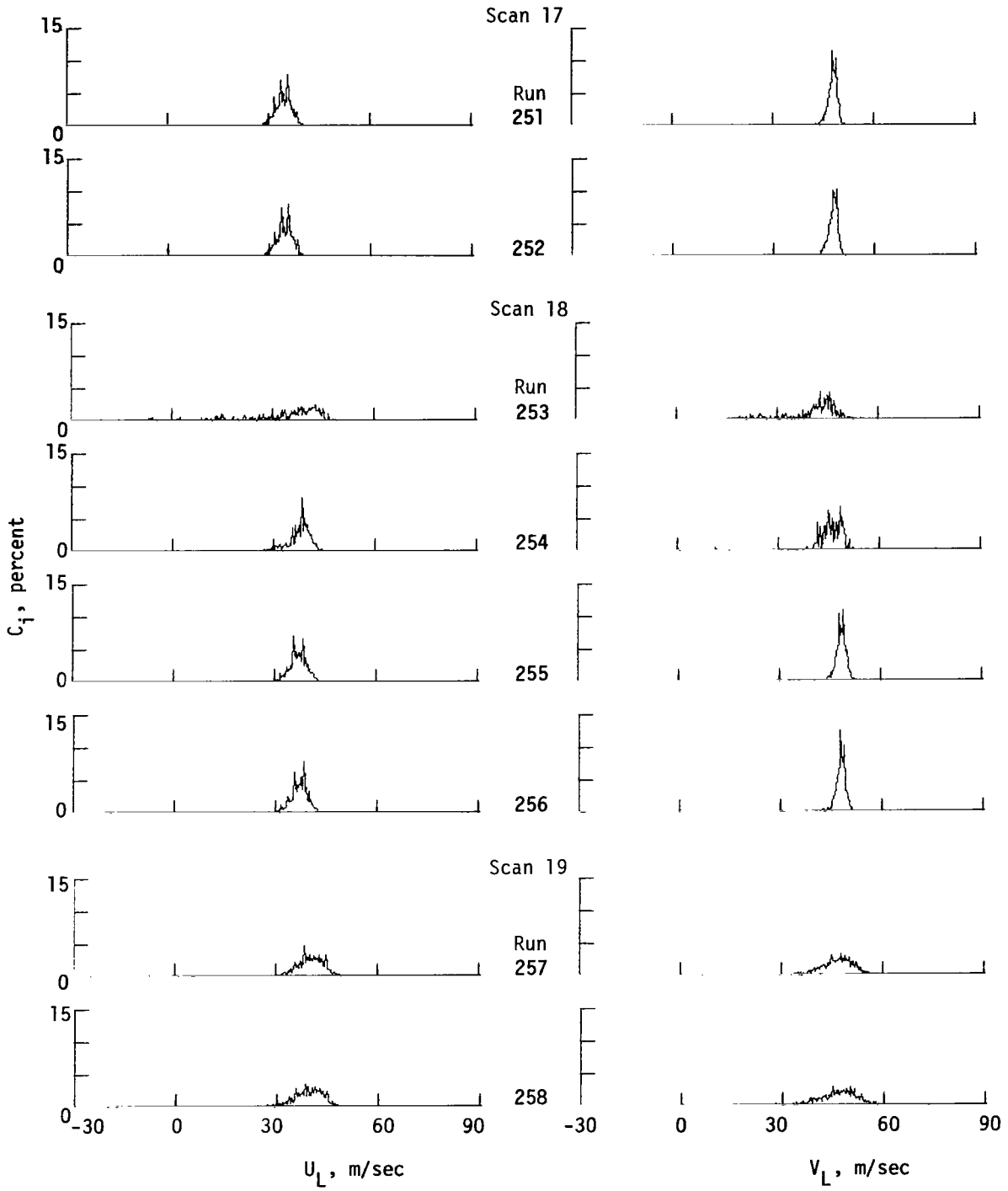

Figure 25.- Continued.

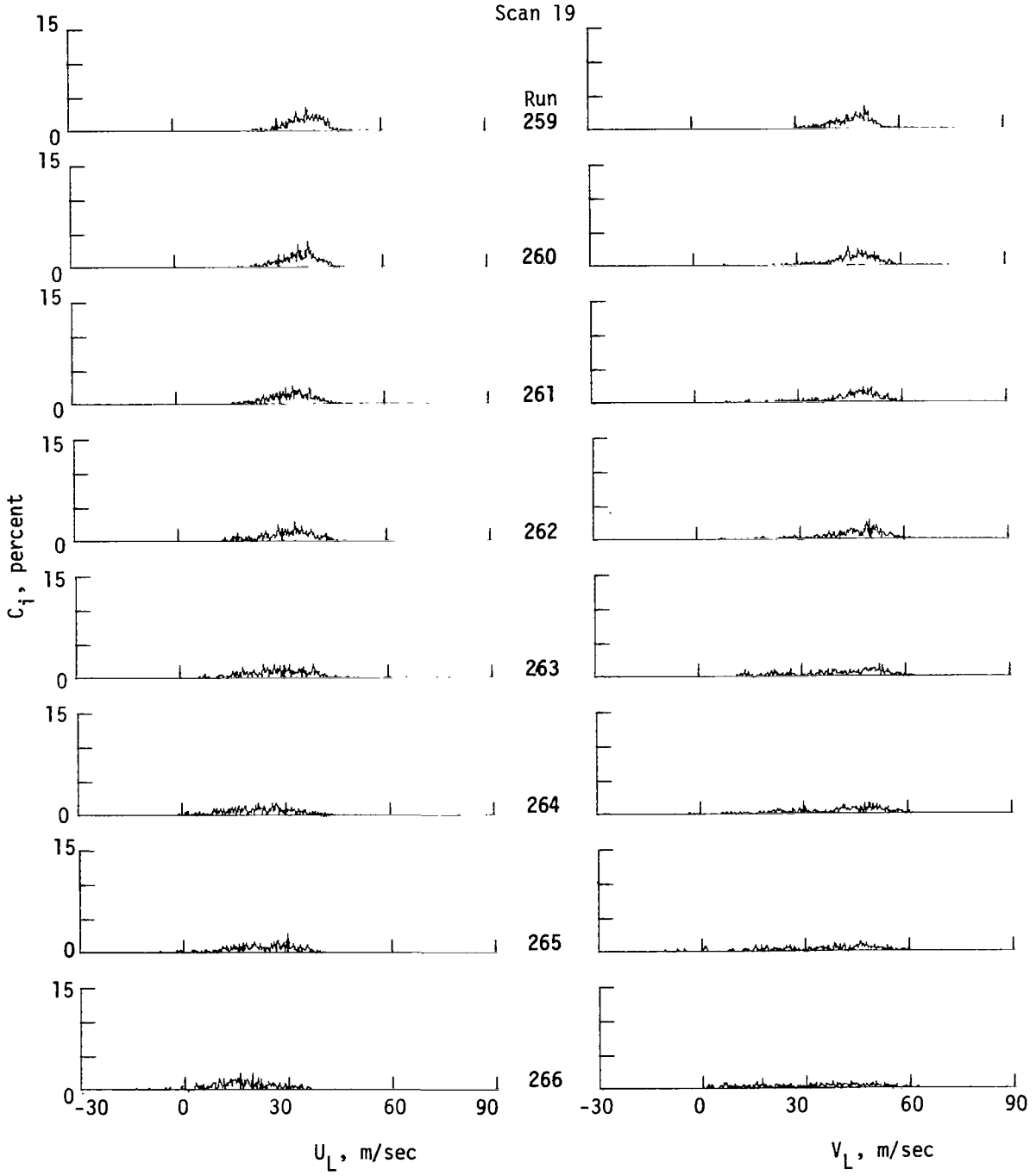

Figure 25.- Continued.

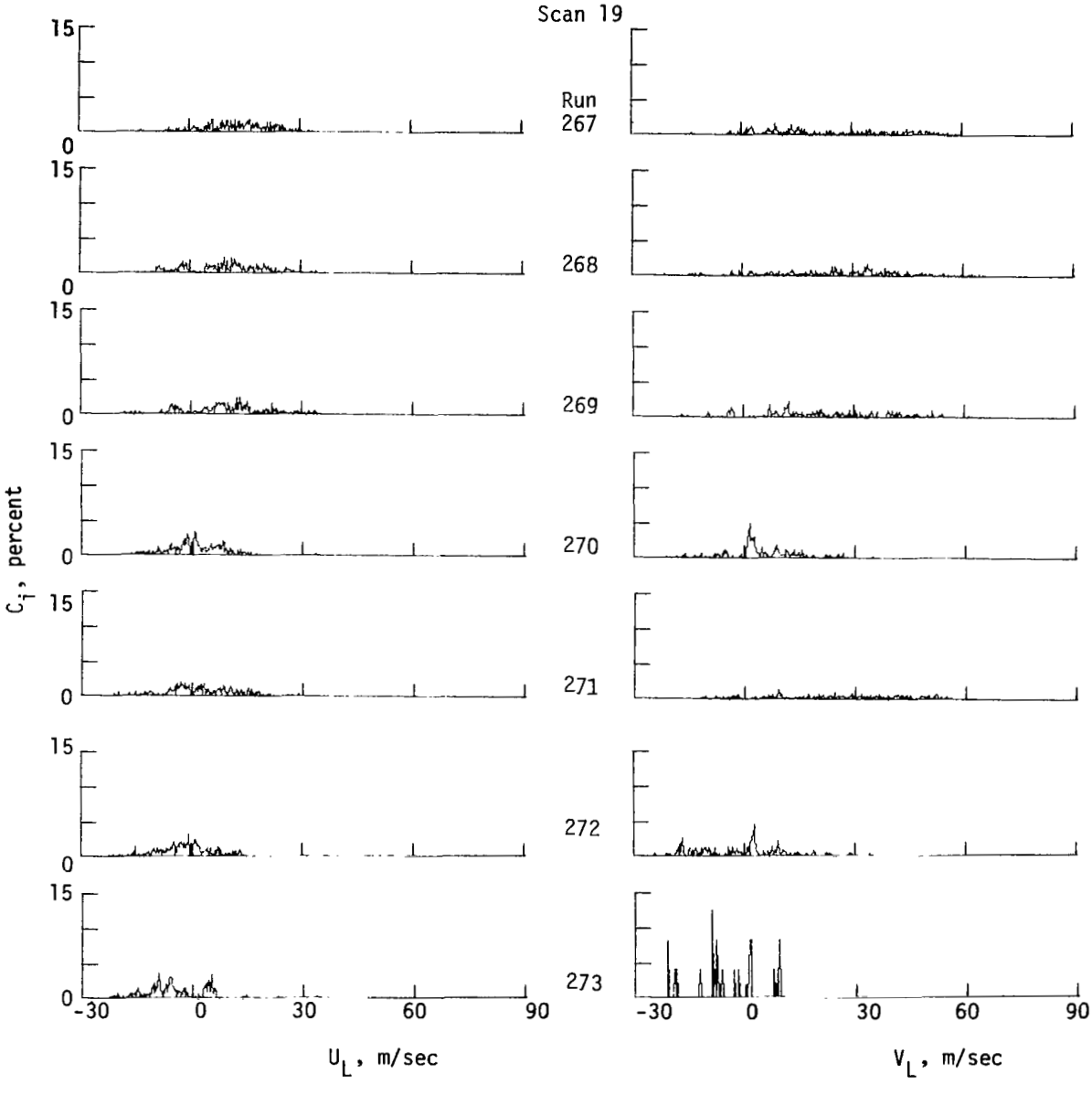

Figure 25.- Continued.

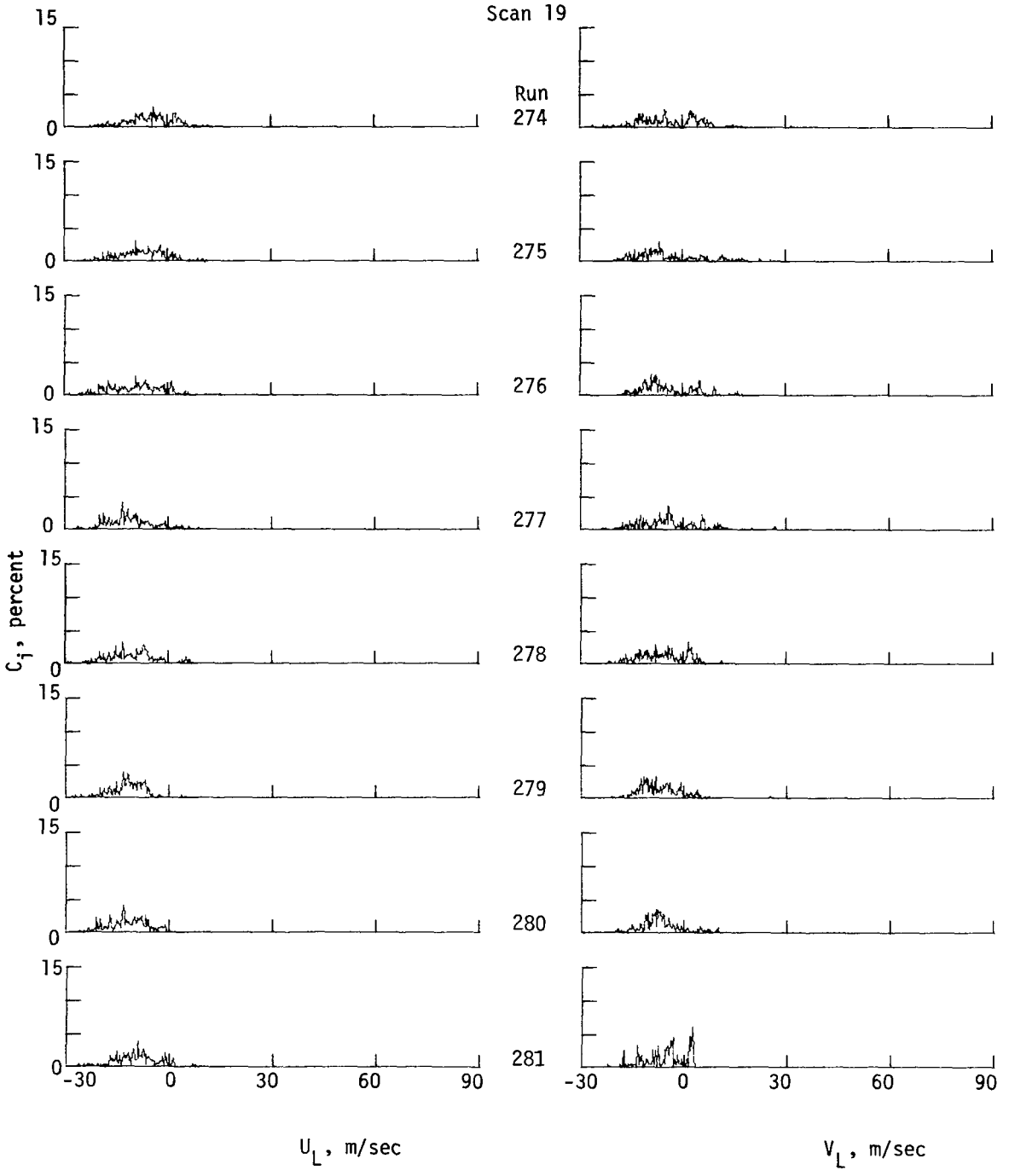

Figure 25.- Continued.

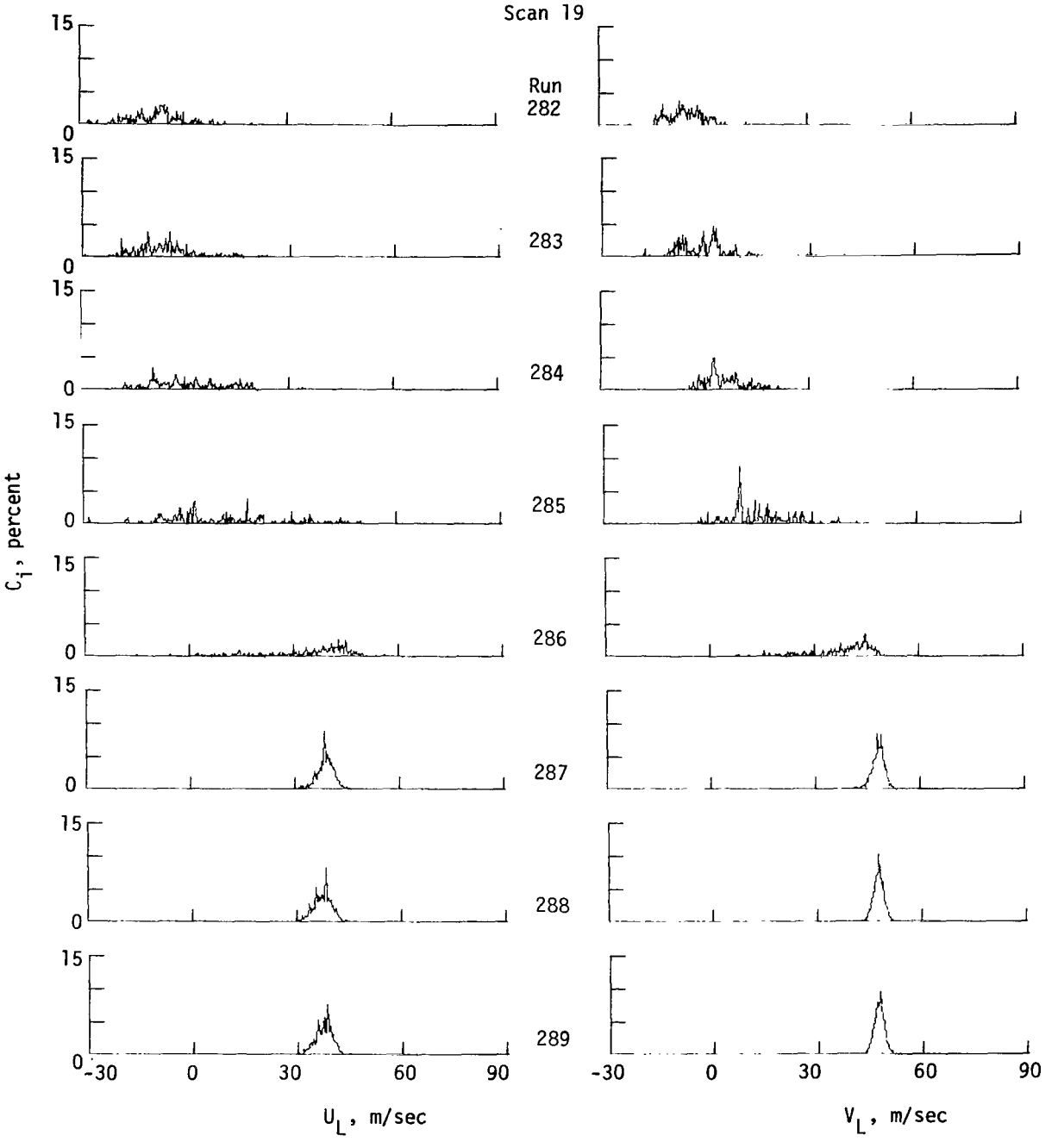

Figure 25.- Concluded.

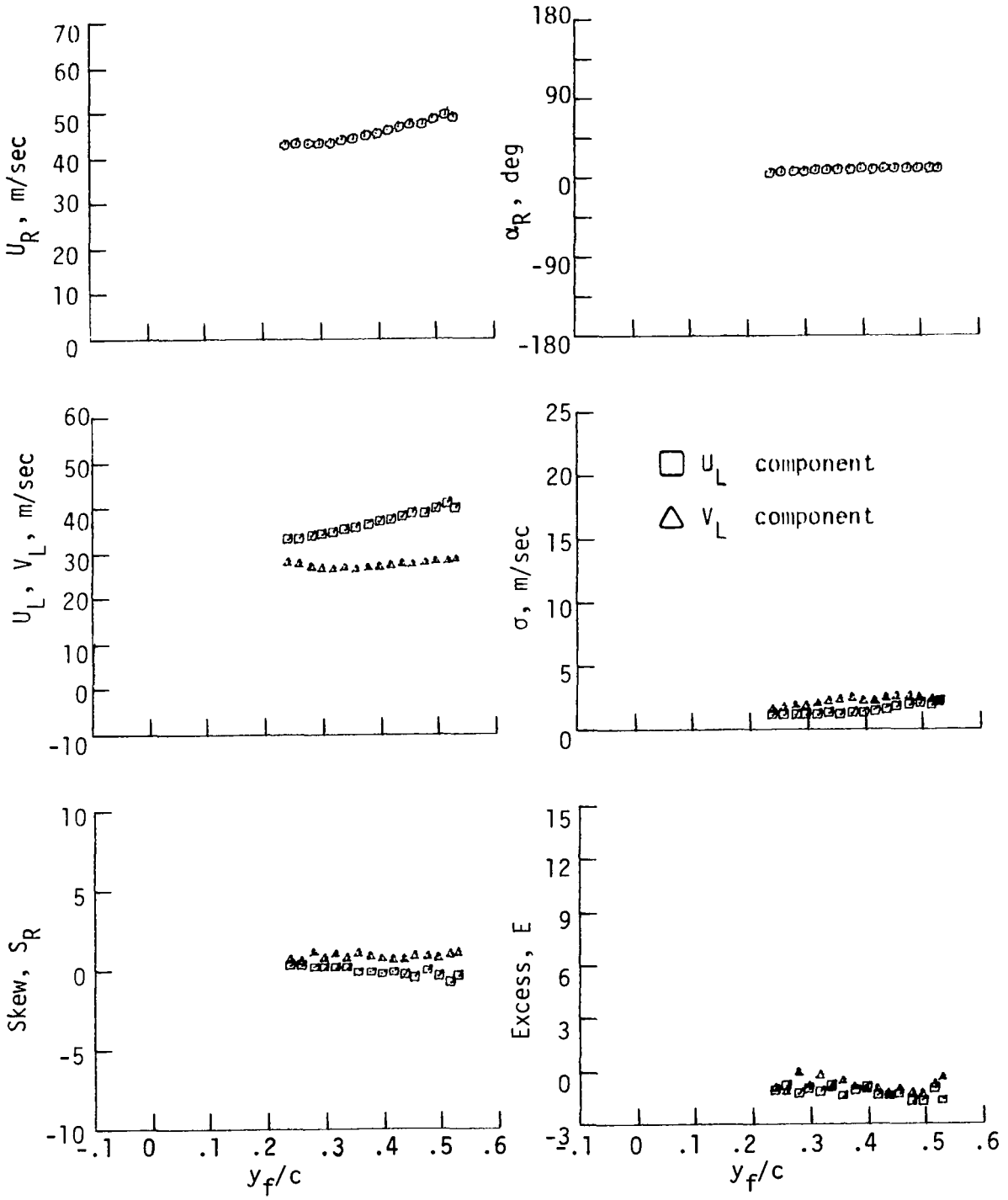

Figure 26.- Statistical moments for scan 1.

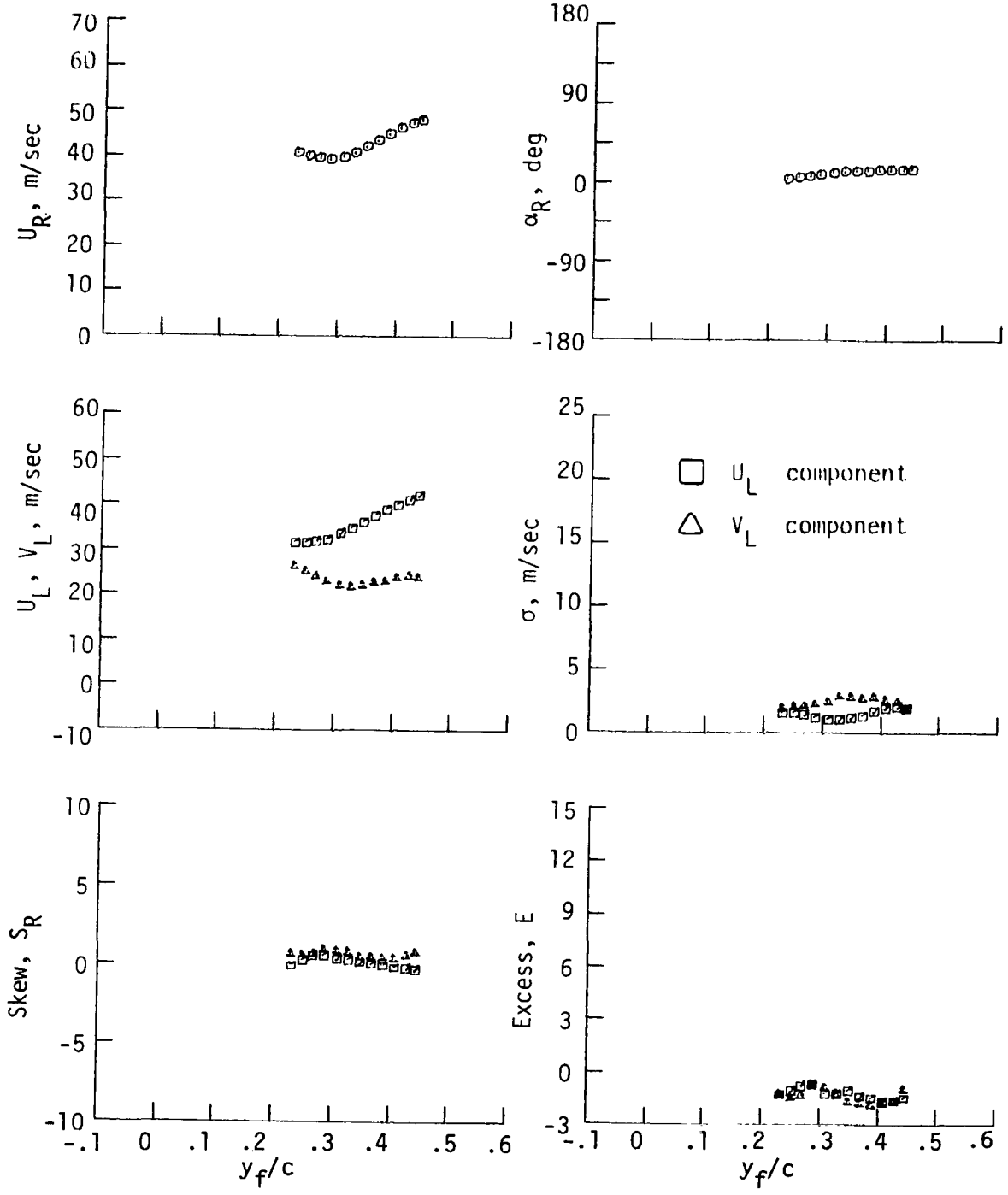

Figure 27.- Statistical moments for scan 2.

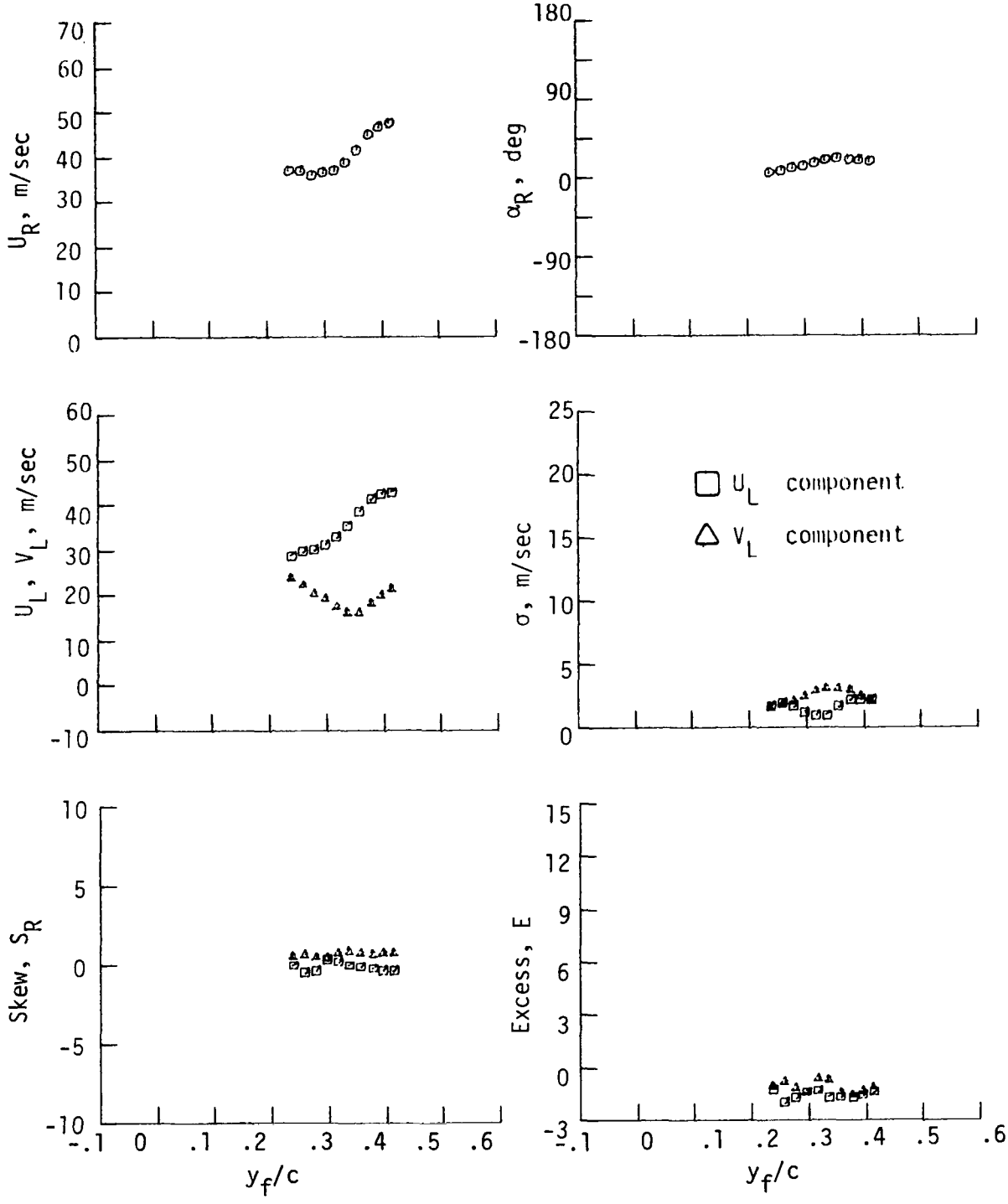

Figure 28.- Statistical moments for scan 3.

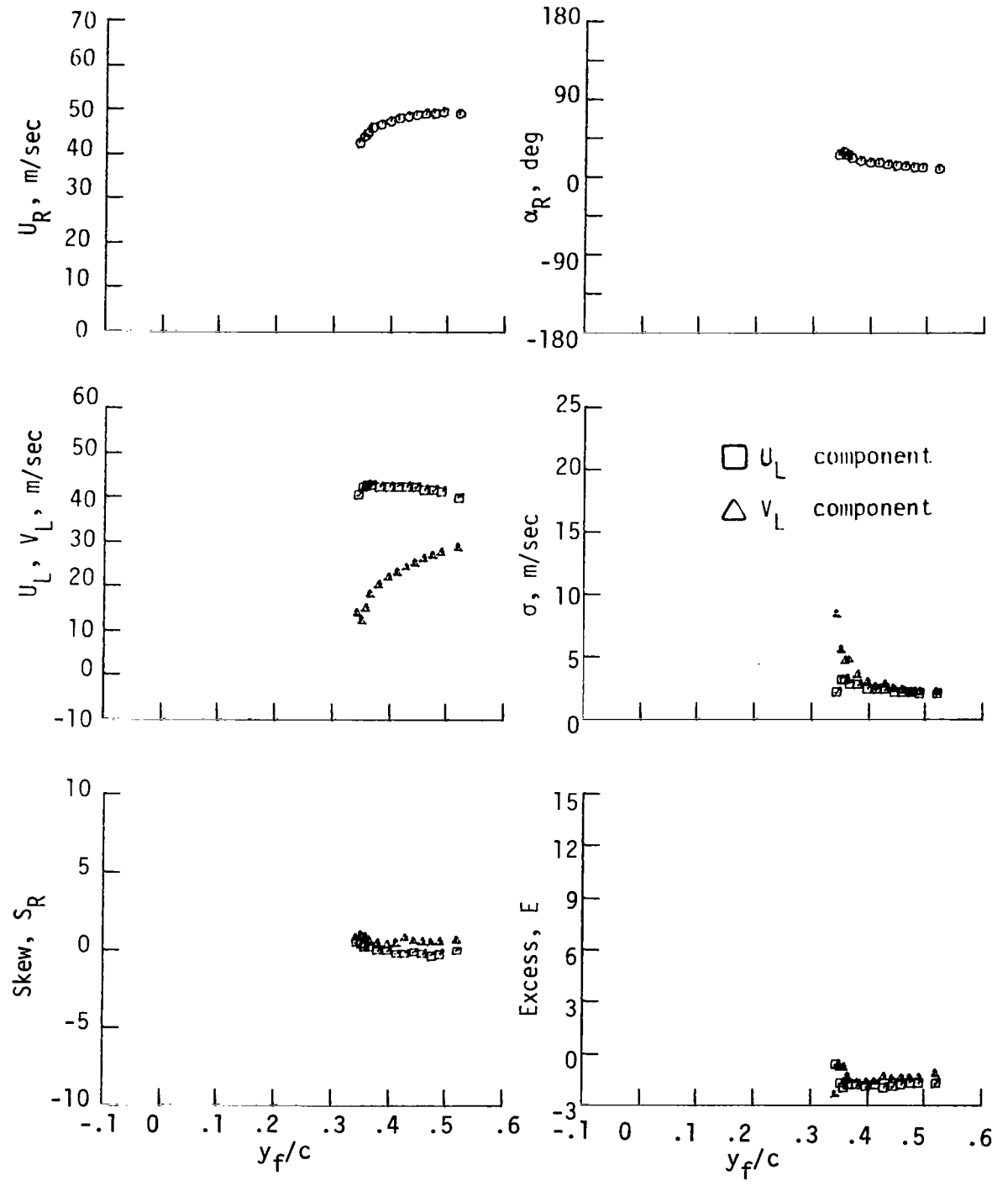

Figure 29.- Statistical moments for scan +4.

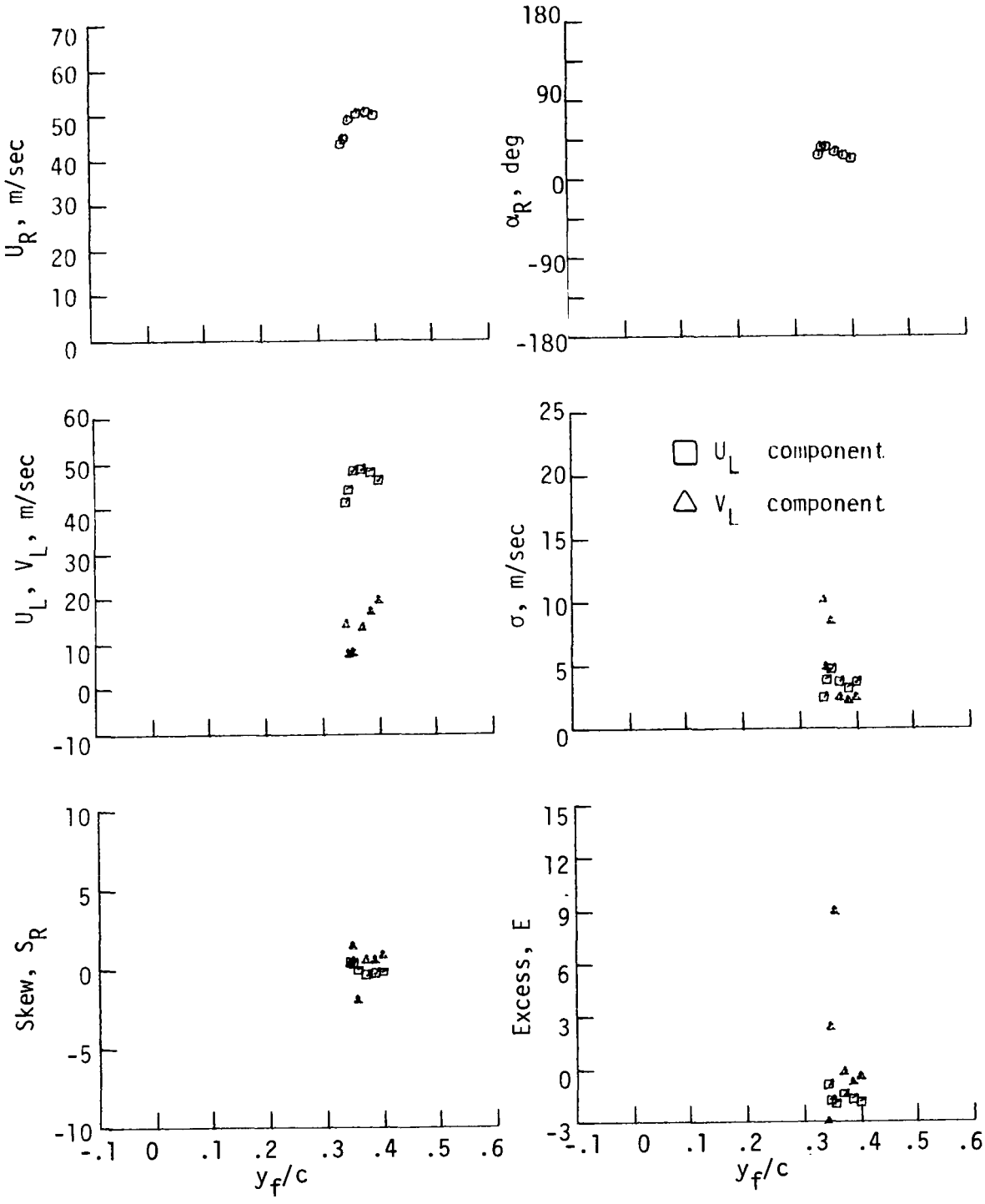

Figure 30.- Statistical moments for scan +5.

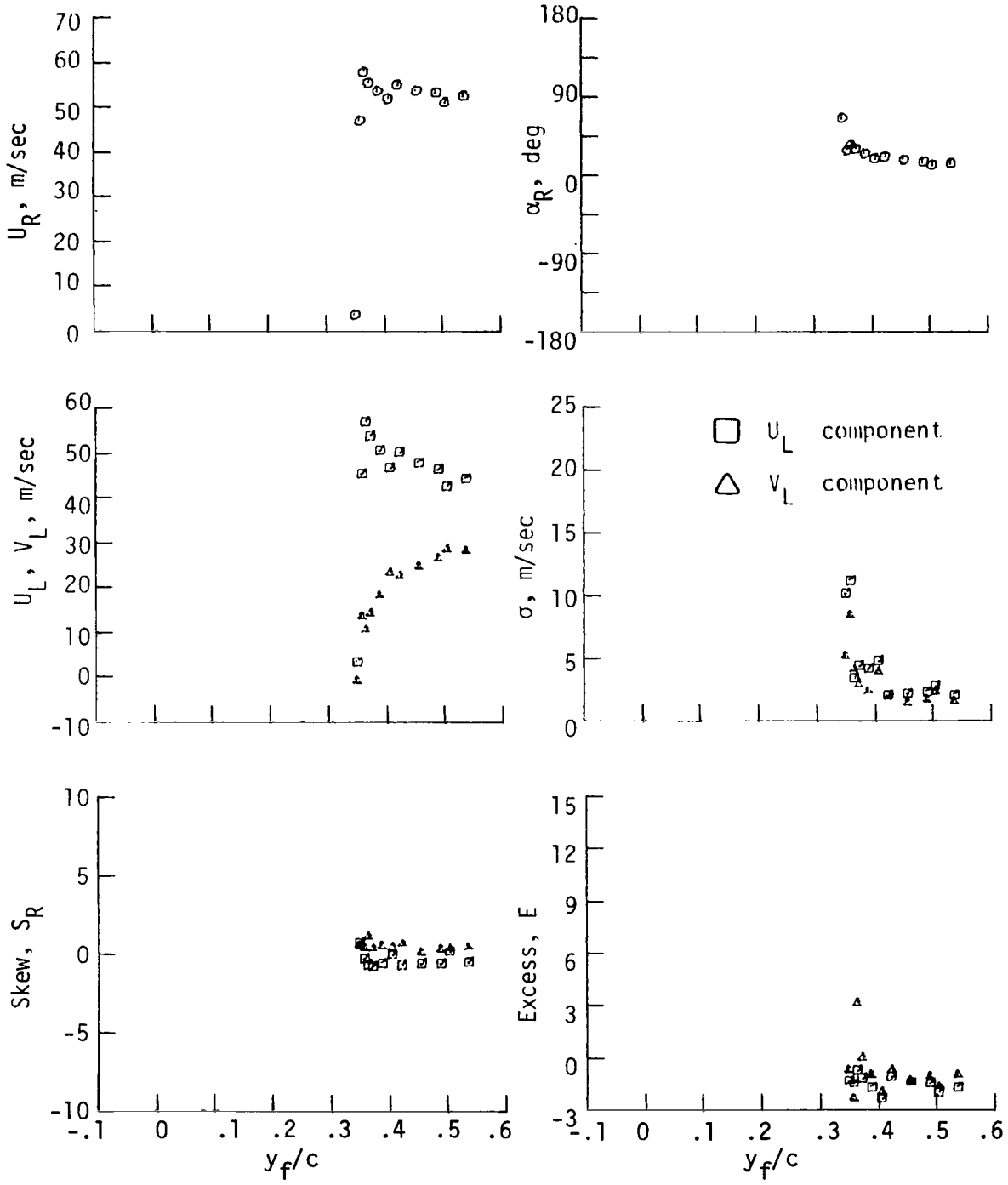

Figure 31.- Statistical moments for scan +6.

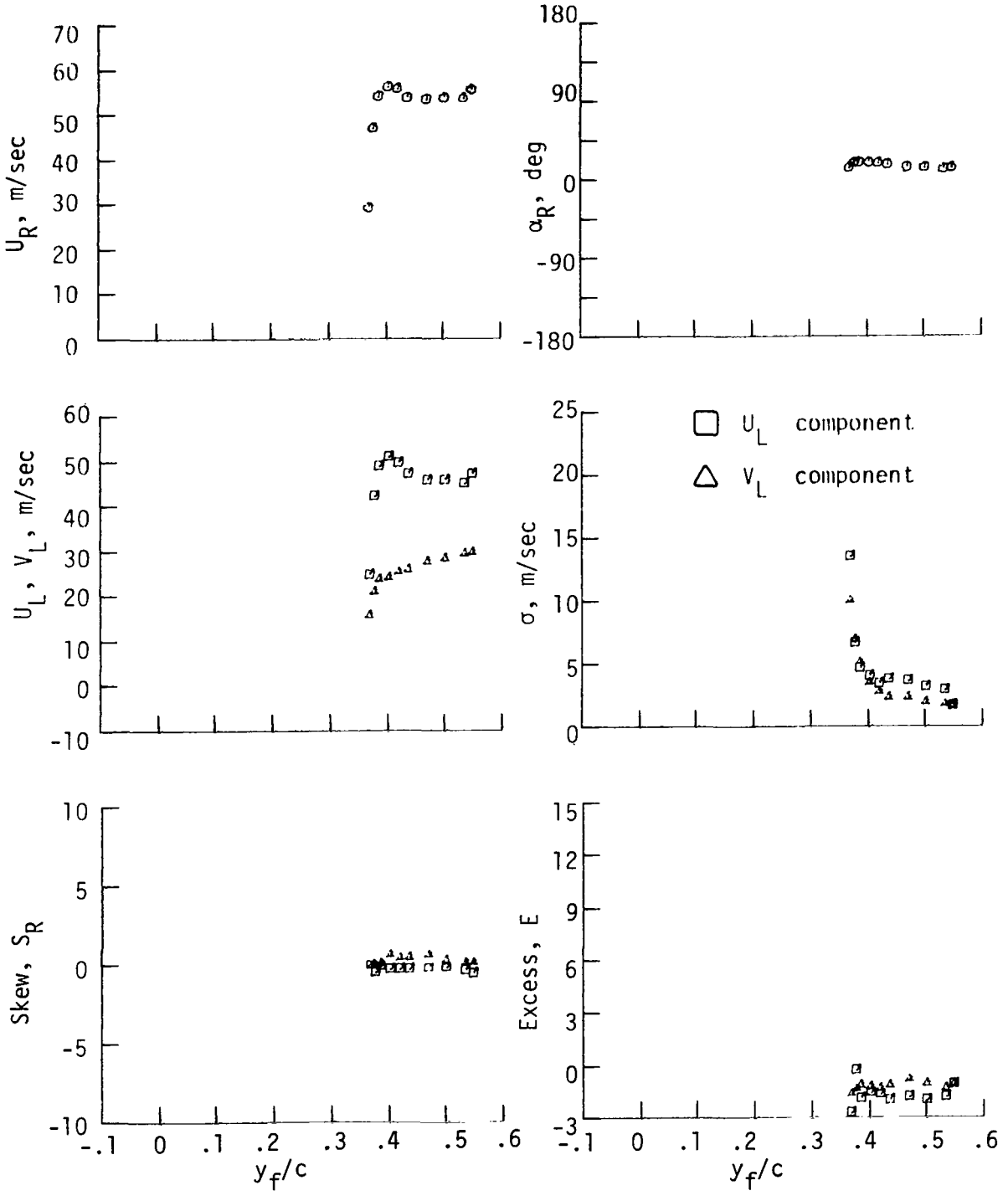

Figure 32.- Statistical moments for scan 7.

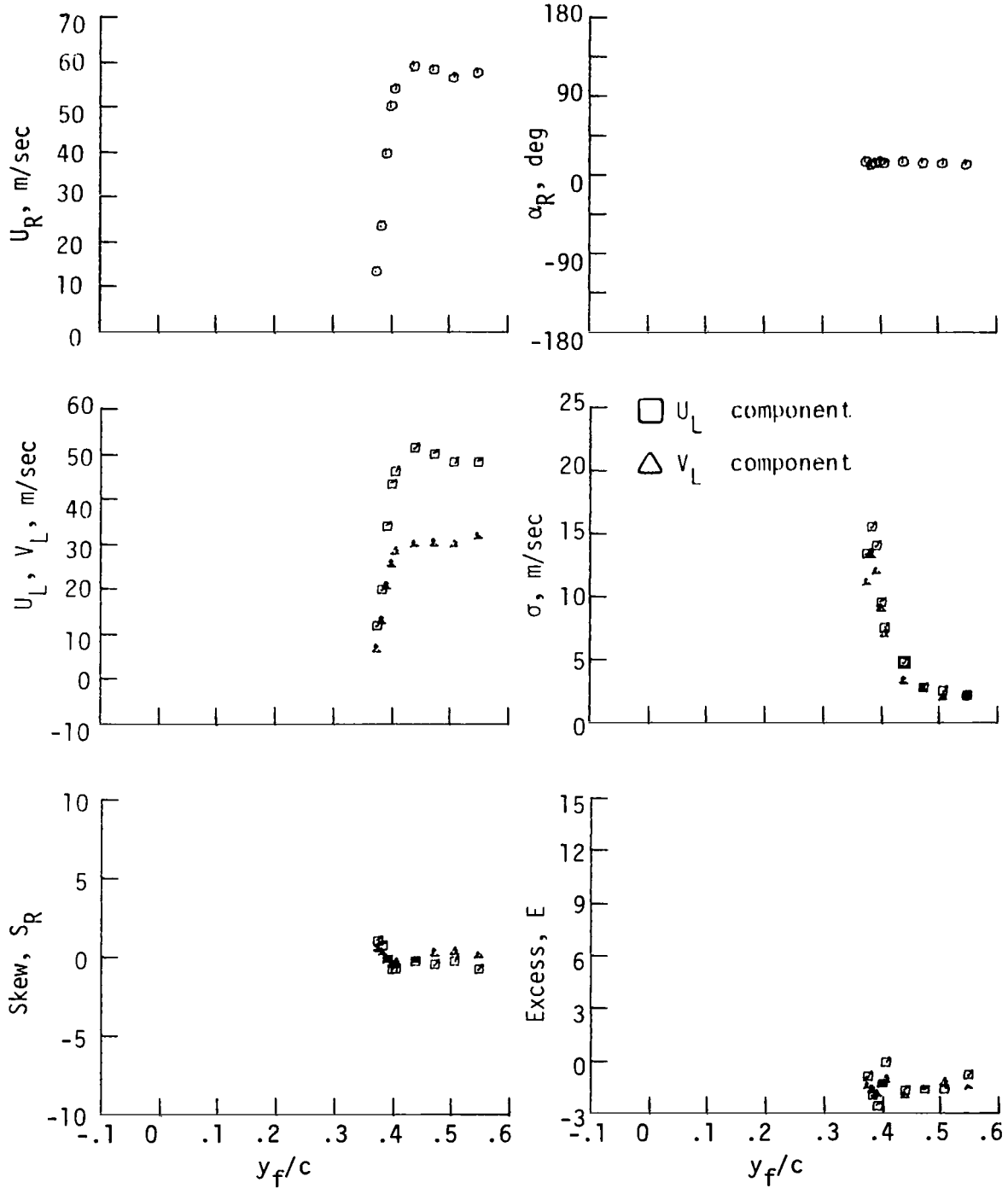

Figure 33.- Statistical moments for scan 8.

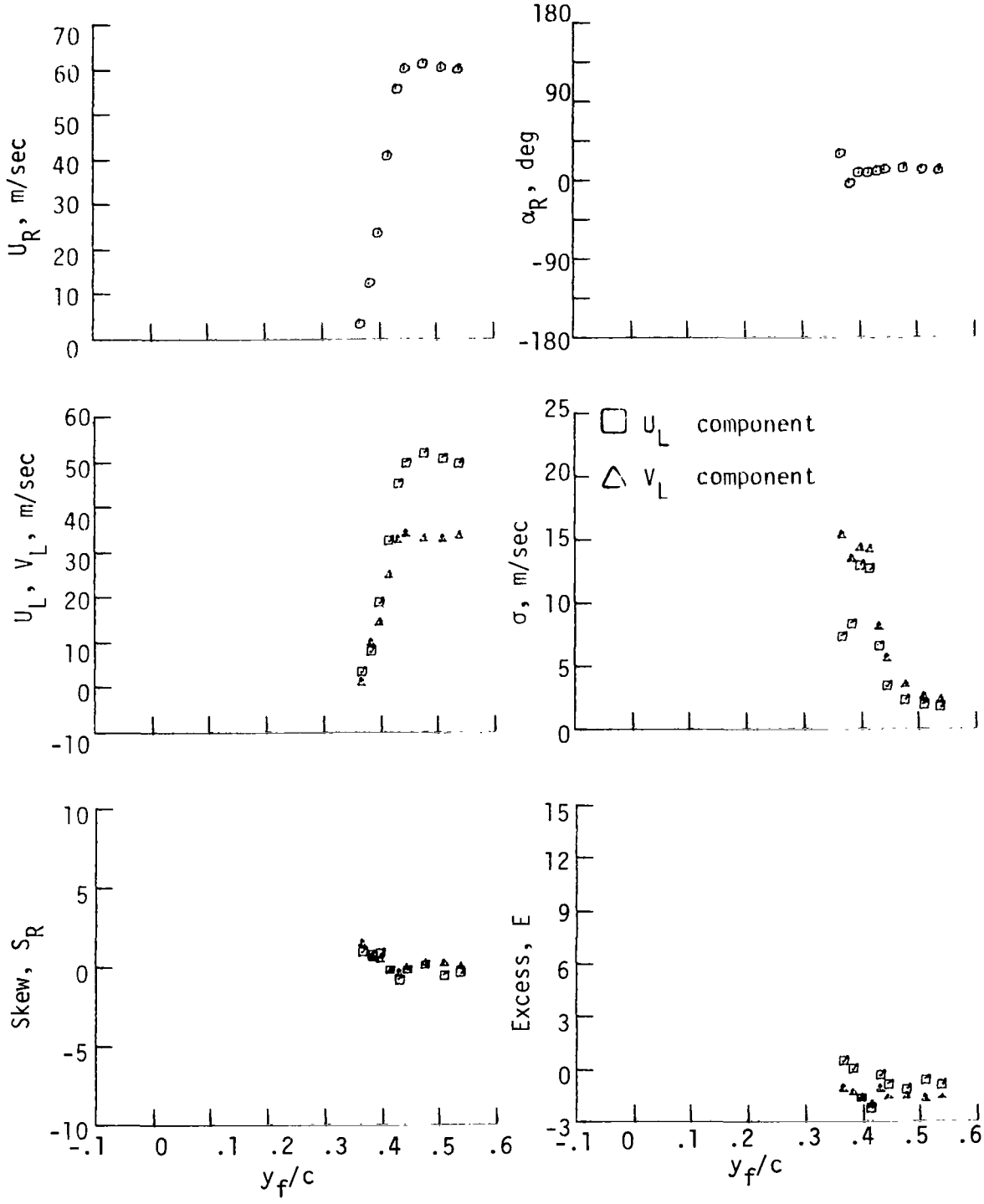

Figure 34.- Statistical moments for scan 9.

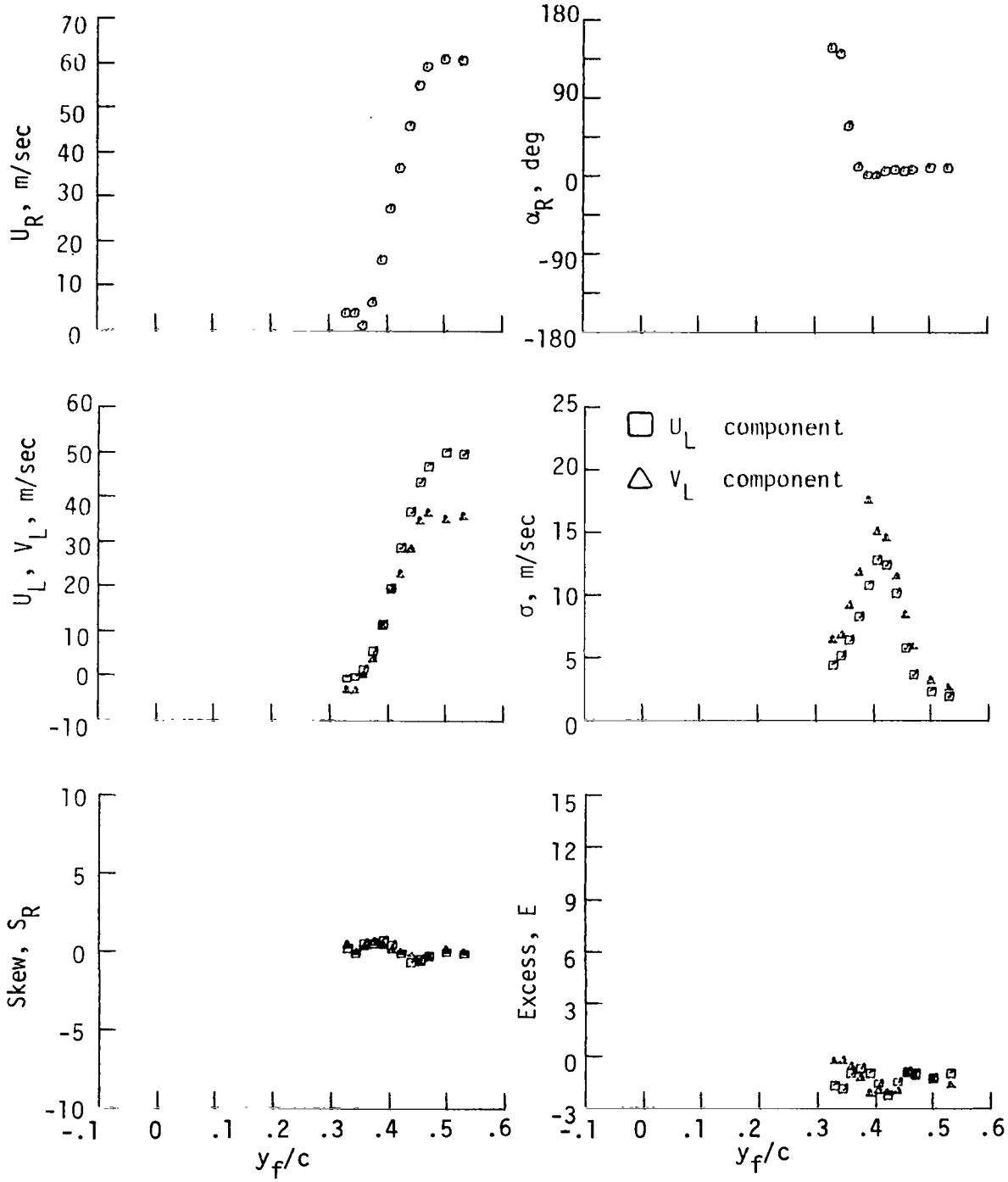

Figure 35.- Statistical moments for scan 10.

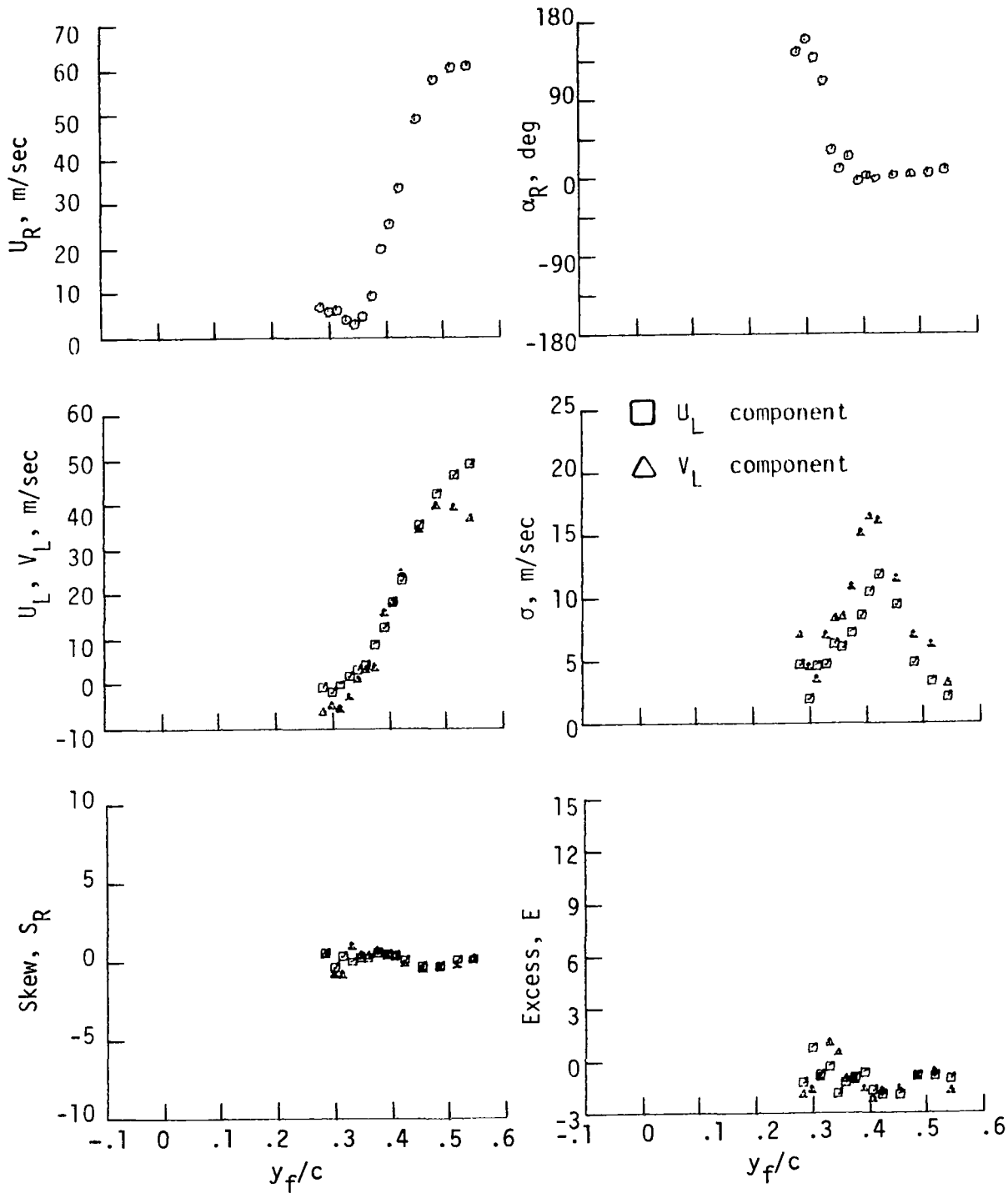

Figure 36.- Statistical moments for scan 11.

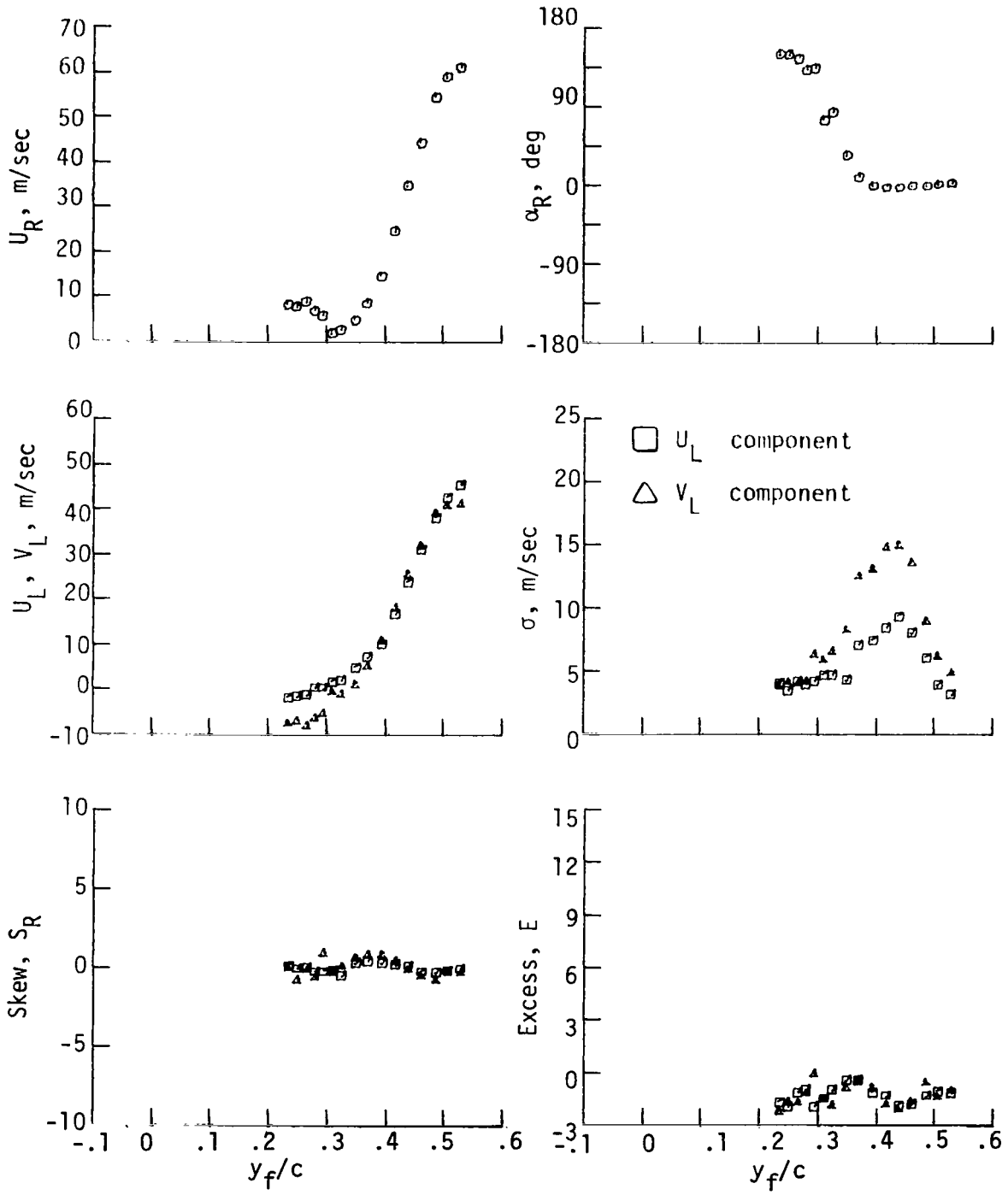

Figure 37.- Statistical moments for scan 12.

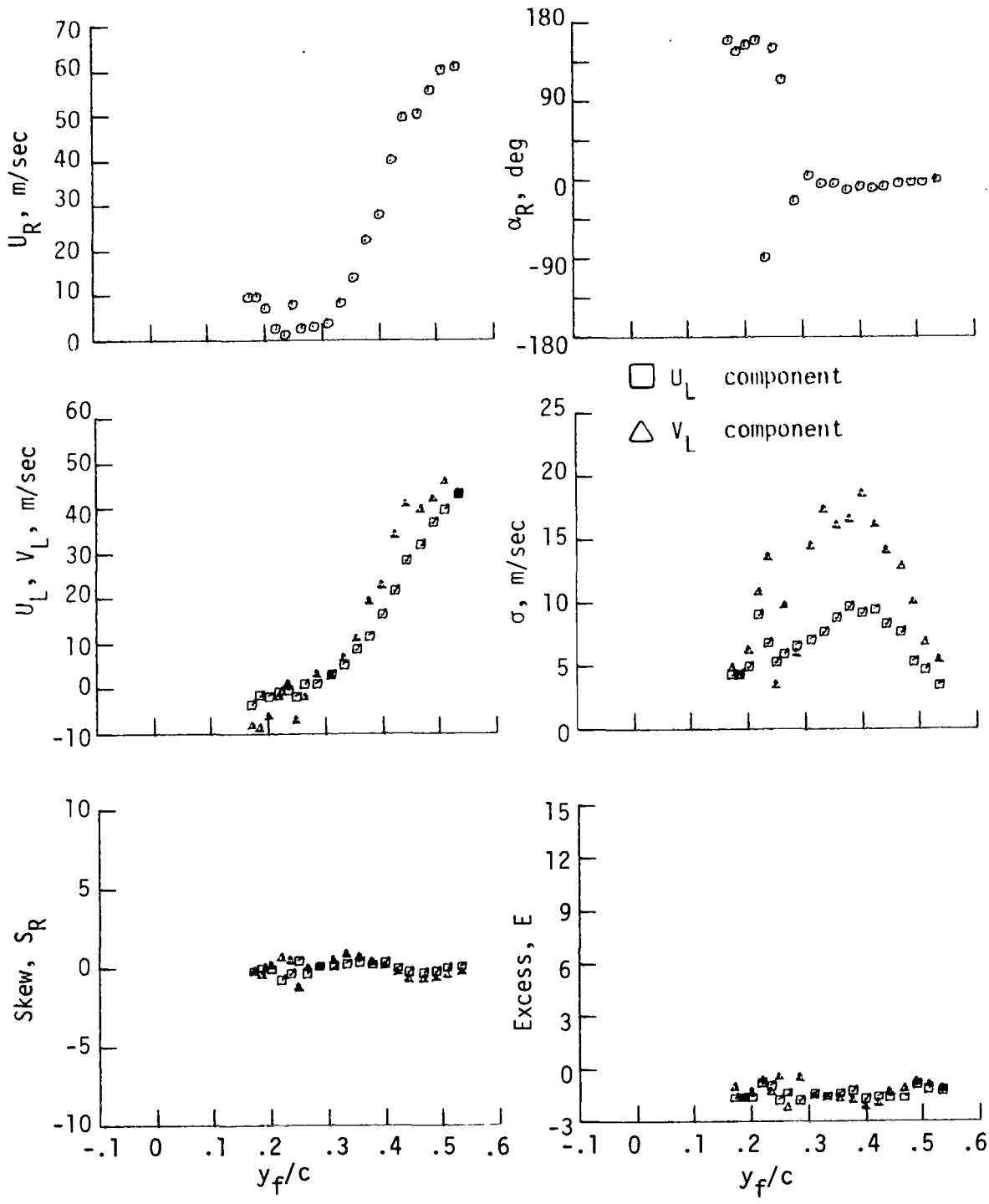

Figure 38.- Statistical moments for scan 13.

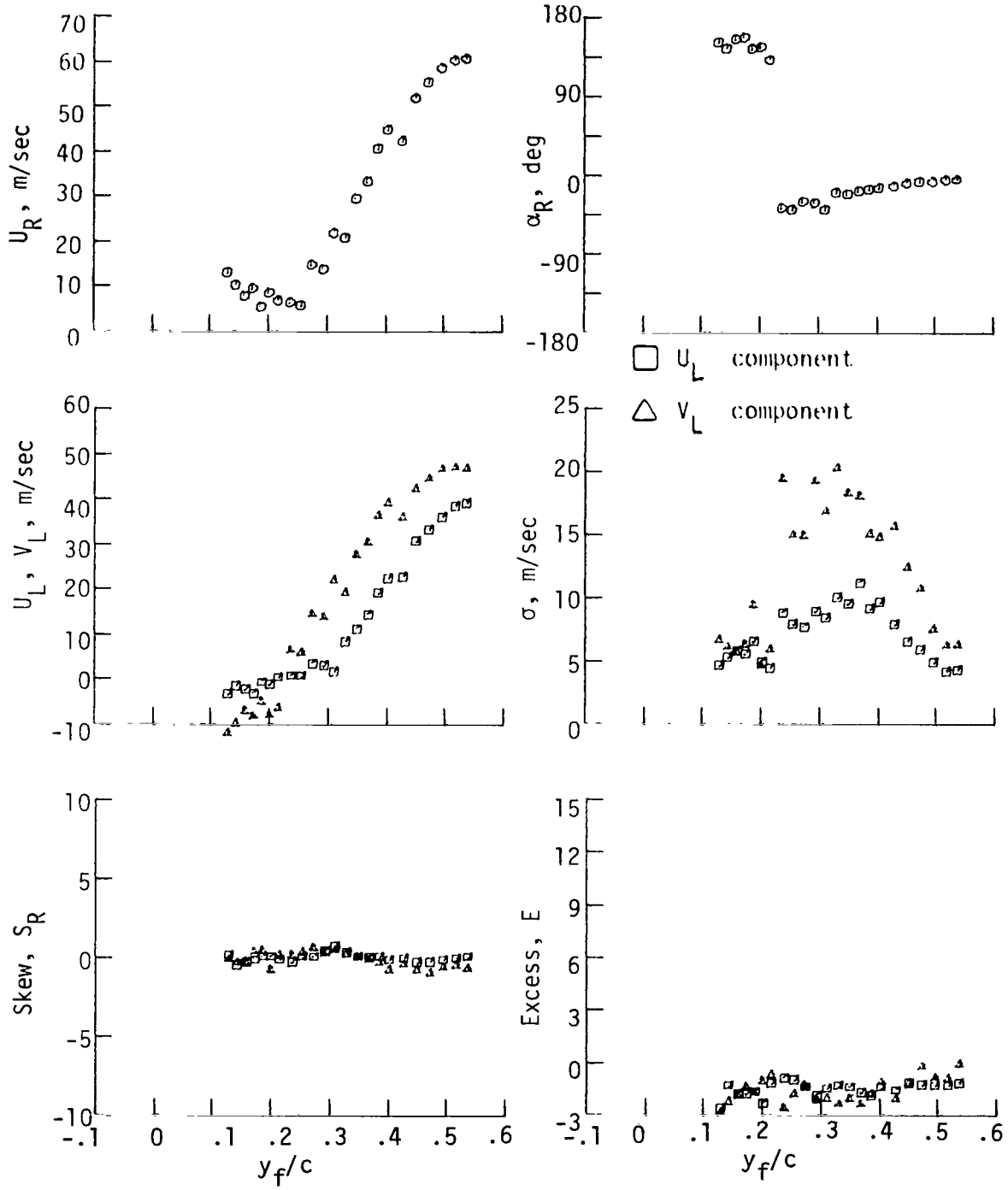

Figure 39.- Statistical moments for scan 14.

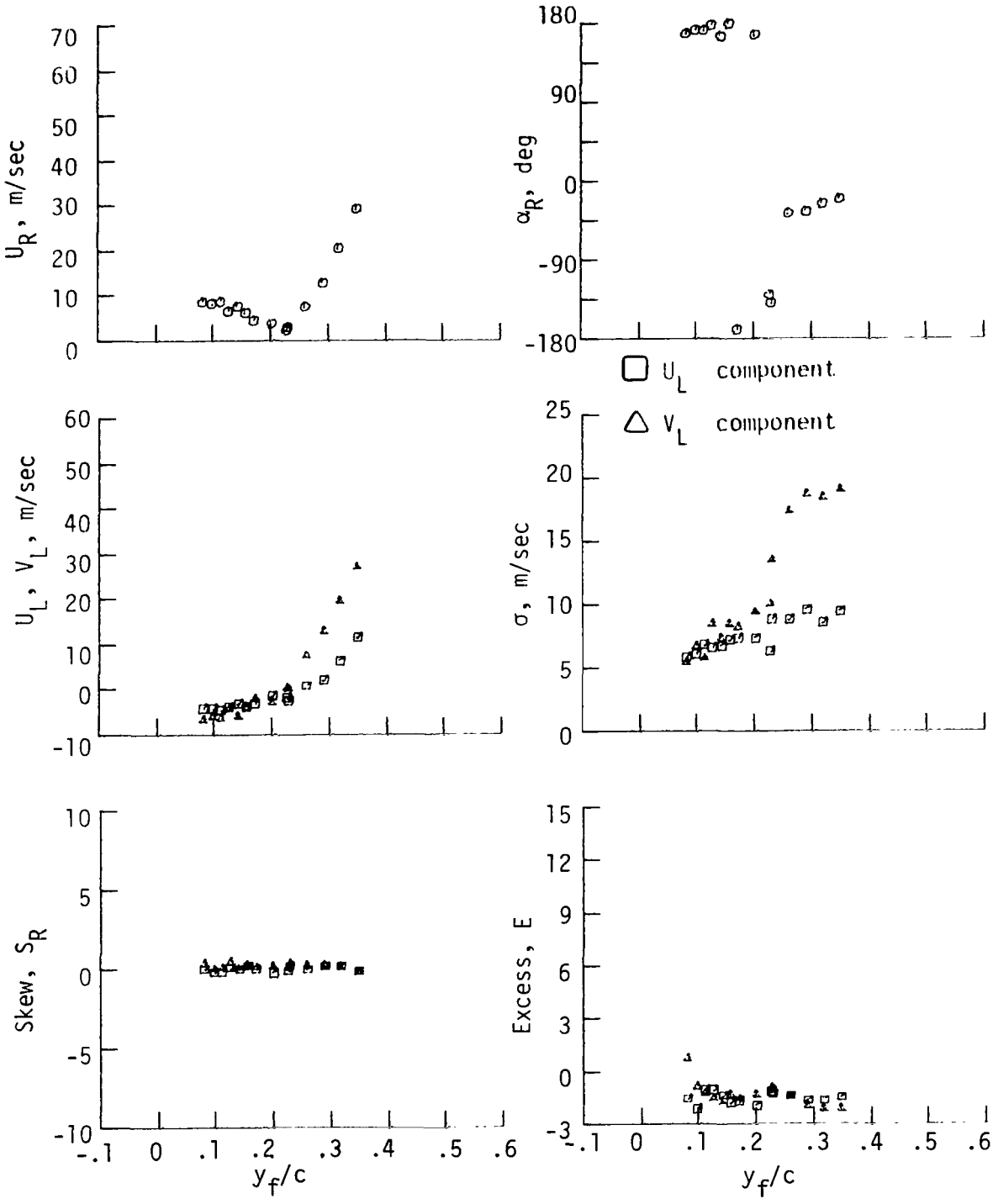

Figure 40.- Statistical moments for scan +15.

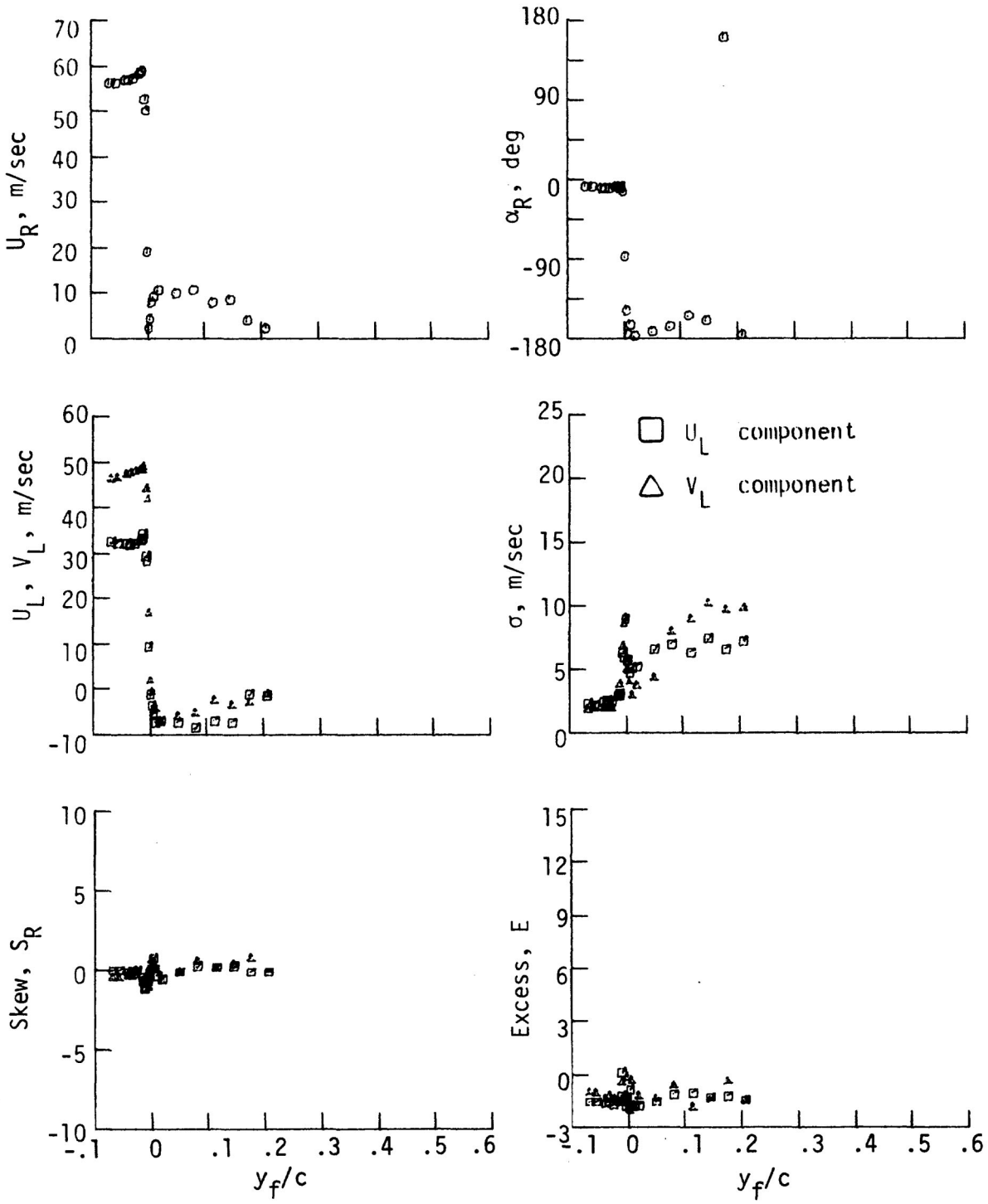

Figure 41.- Statistical moments for scan 16.

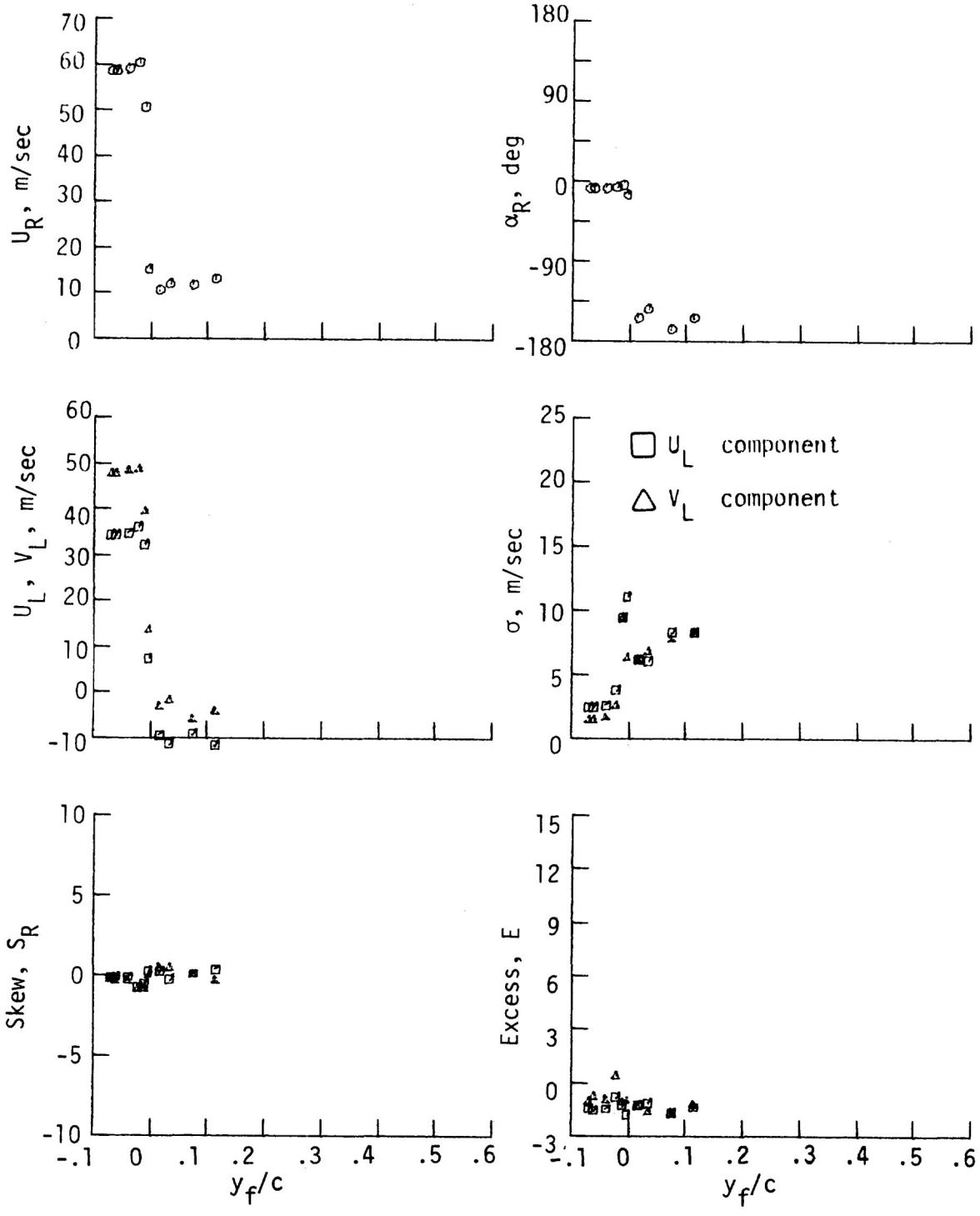

Figure 42.- Statistical moments for scan 17.

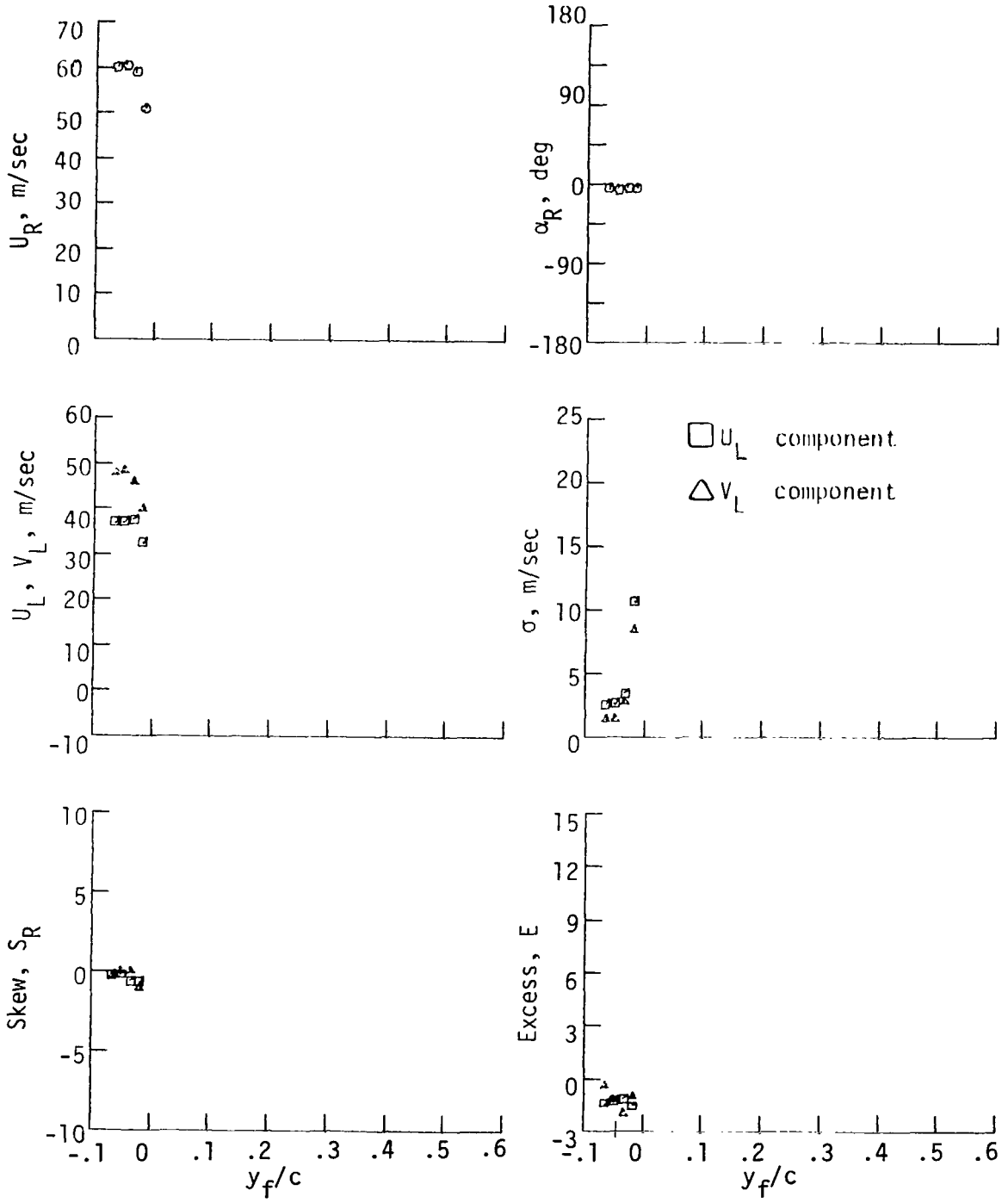

Figure 43.- Statistical moments for scan 18.

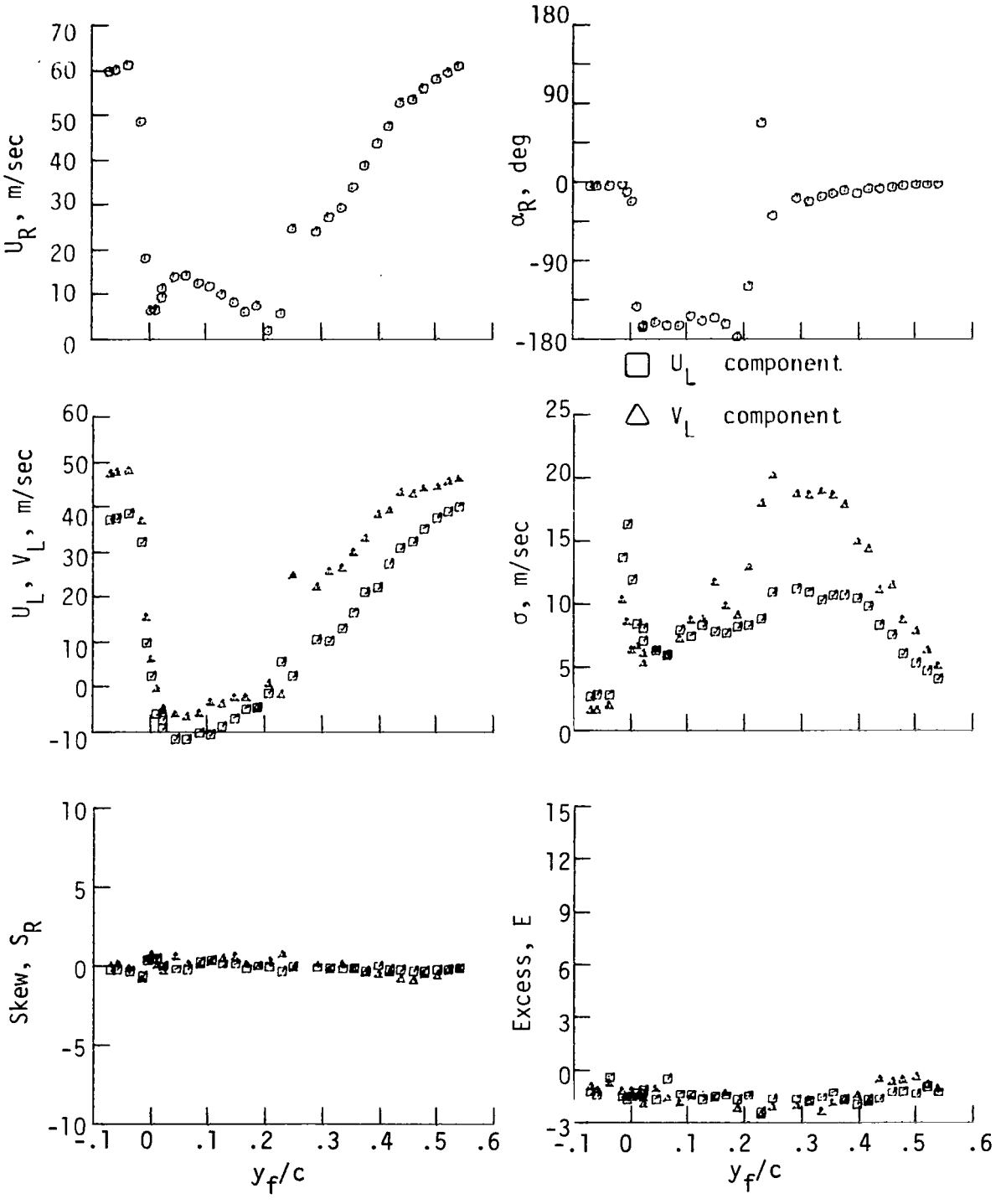

Figure 44.- Statistical moments for scan 19.

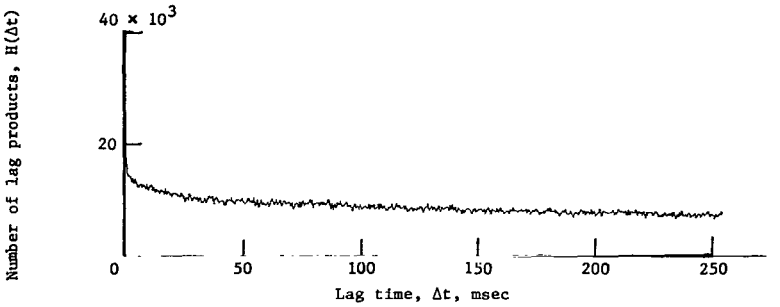

(a) Histogram of number of lag products.

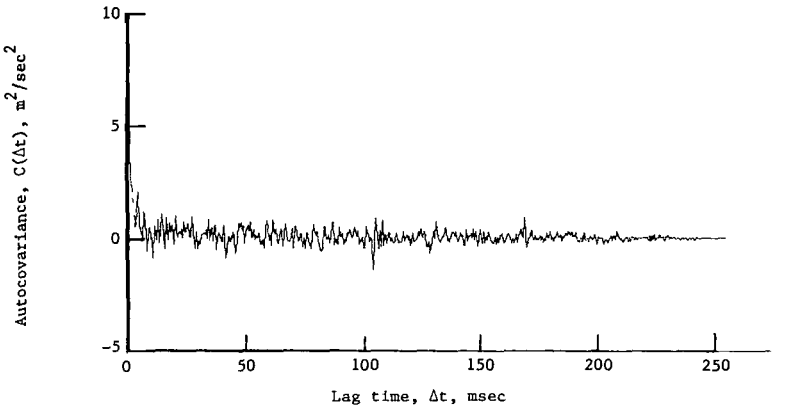

(b) Autocovariance.

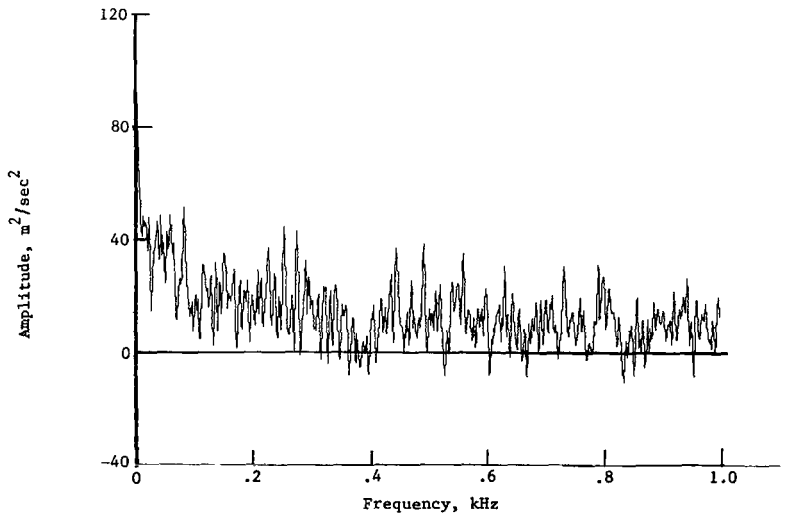

(c) Power spectrum of velocity.

Figure 45.- Calculation of power spectrum for U_L component above airfoil at $x_c/c = 63.2$ percent and $y_c/c = 39.3$ percent.

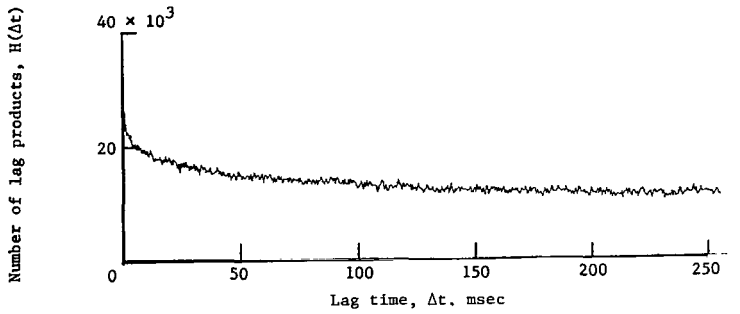

(a) Histogram of number of lag products.

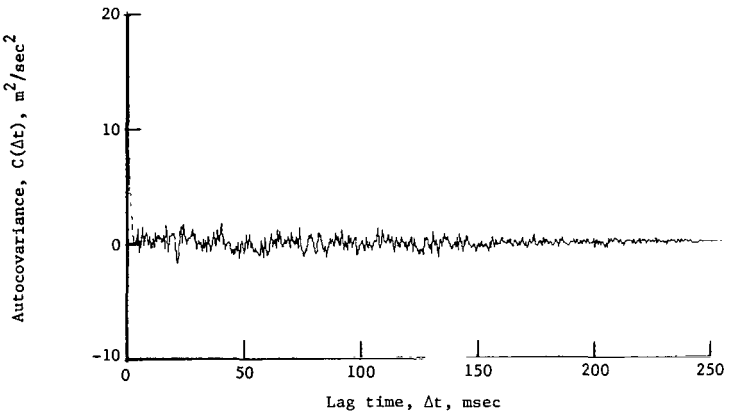

(b) Autocovariance.

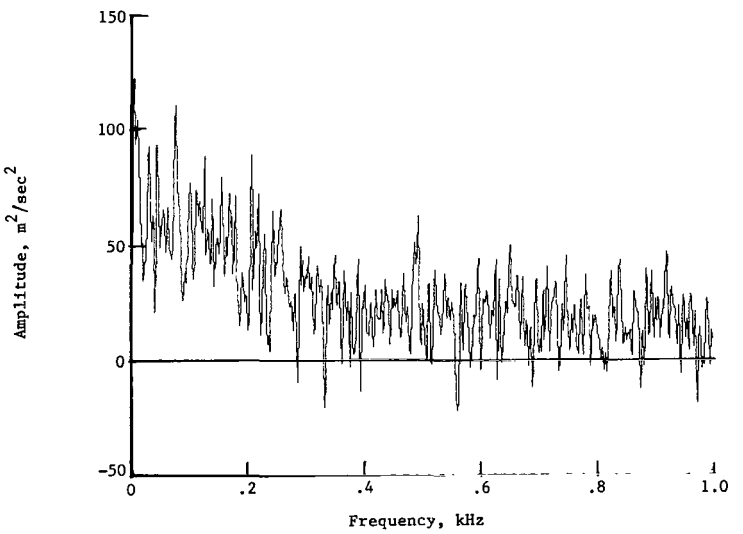

(c) Power spectrum of velocity.

Figure 46.- Calculation of power spectrum for V_L component above airfoil at x_c/c = 63.2 percent and y_c/c = 39.3 percent.

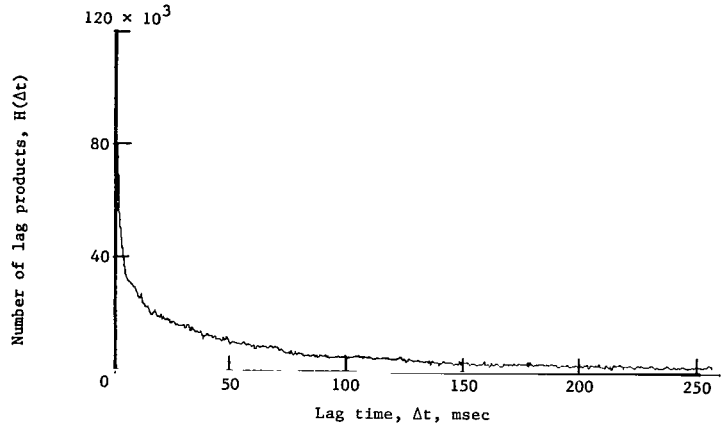

(a) Histogram of number of lag products.

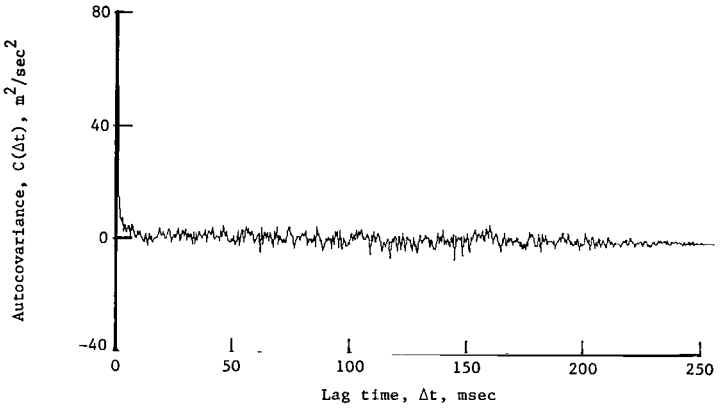

(b) Autocovariance.

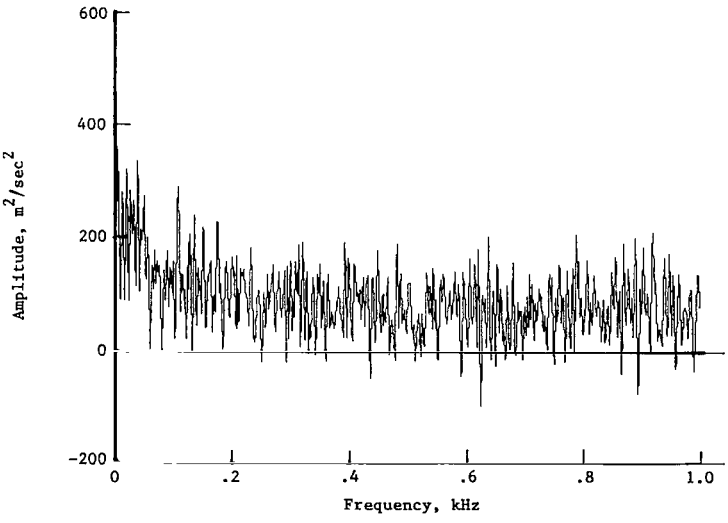

(c) Power spectrum of velocity.

Figure 47.- Calculation of power spectrum for U_L component at x_c/c = 101.6 percent and y_c/c = 0.38 percent.

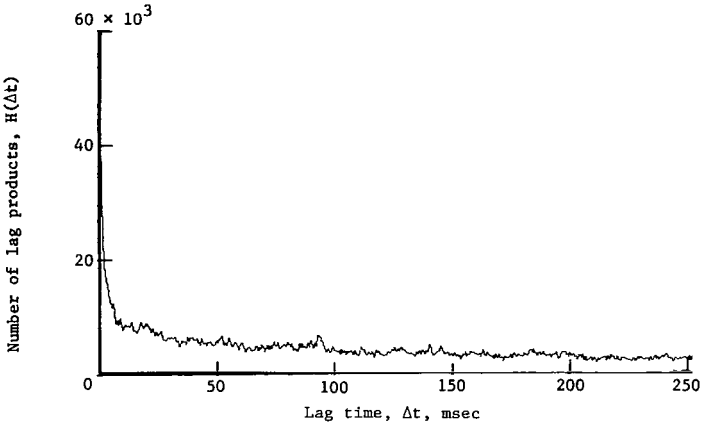

(a) Histogram of number of lag products.

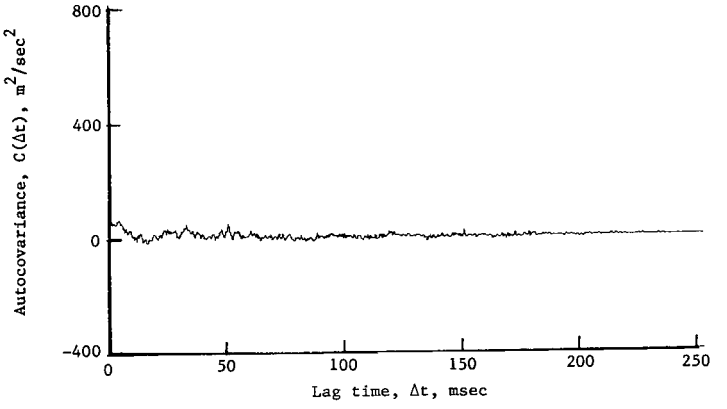

(b) Autocovariance.

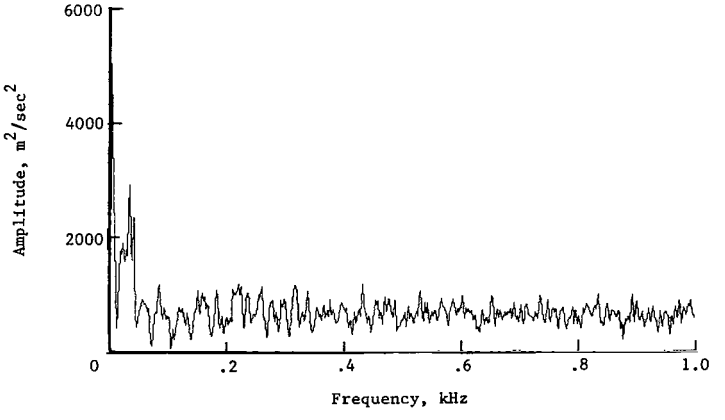

(c) Power spectrum of velocity.

Figure 48.- Calculation of power spectrum for V_L component at x_c/c = 101.6 percent and y_c/c = 0.38 percent.

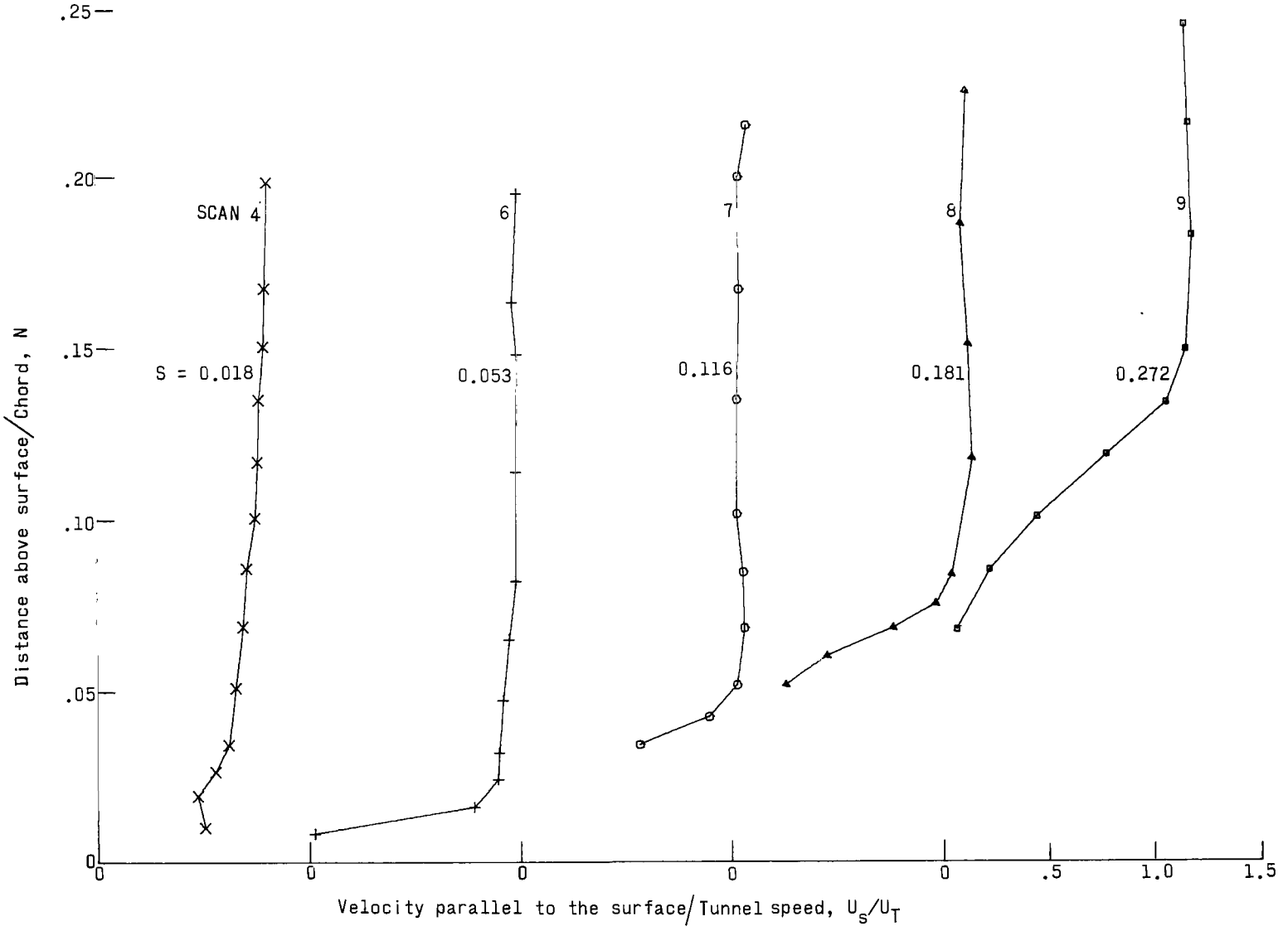

Figure 49.- Velocity profile development above airfoil crest.

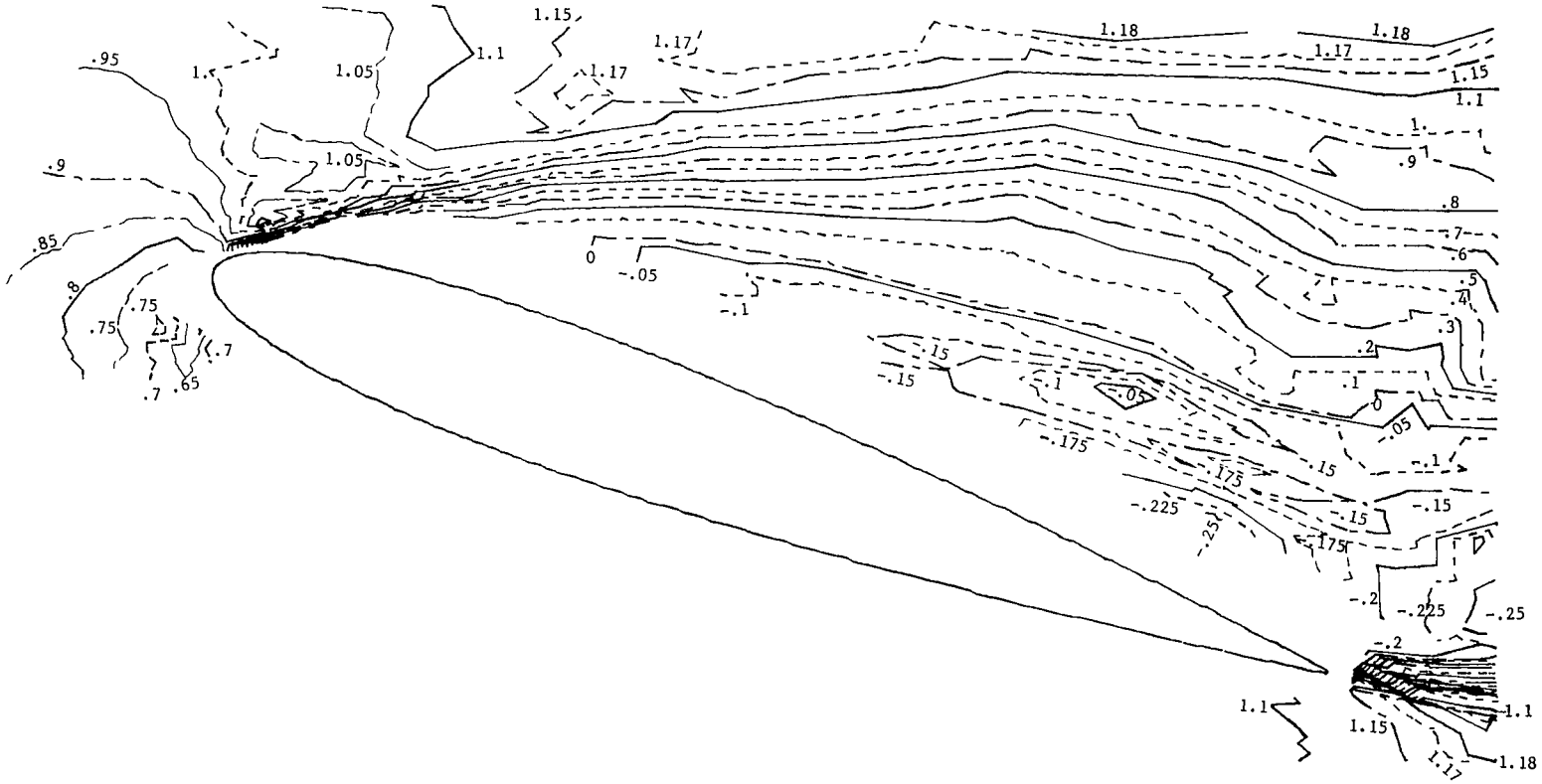

Figure 50.- Contours of constant resultant mean velocity (negative values denote flow upstream).

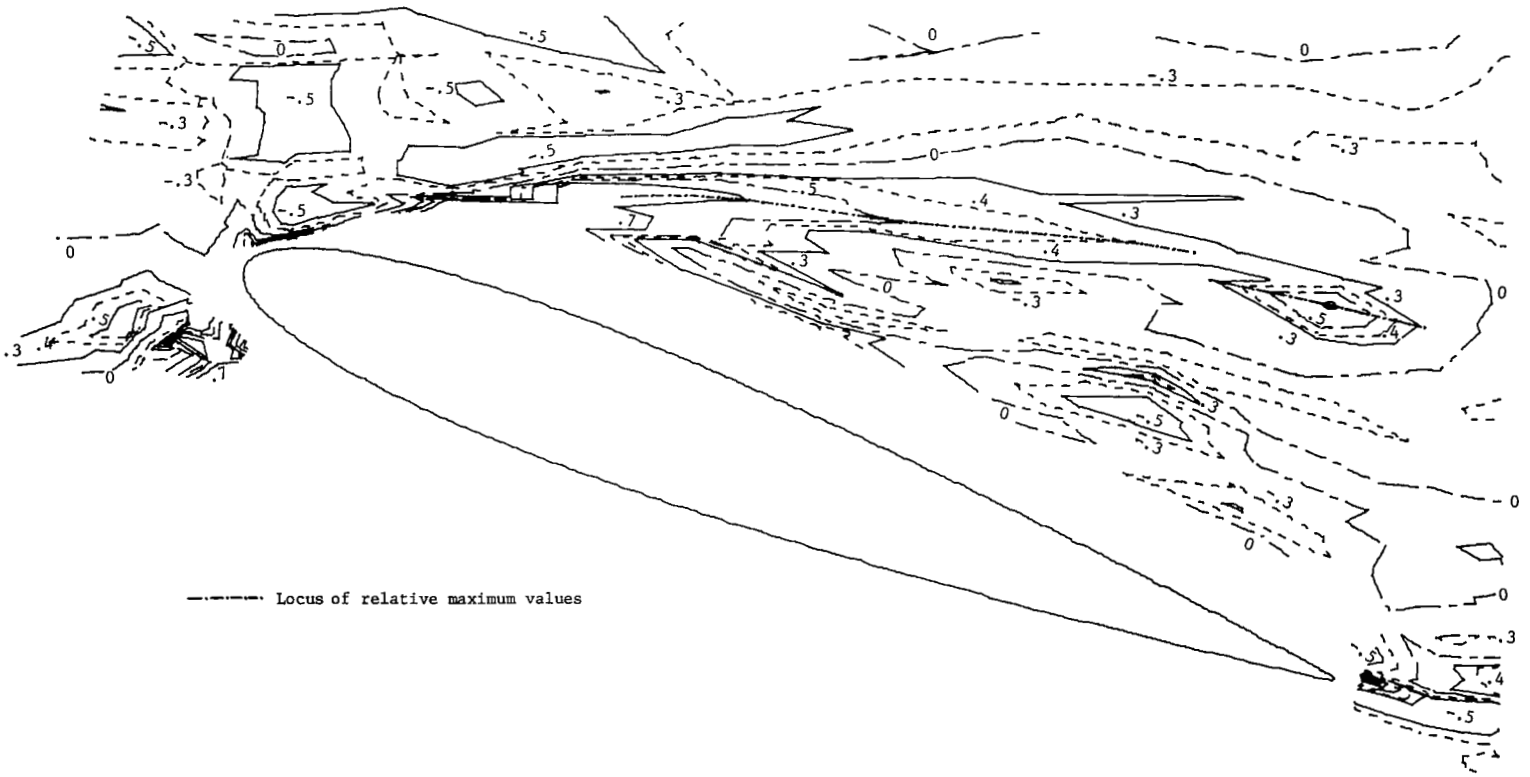

Figure 51.- Contours of constant values of skew in U_L direction.

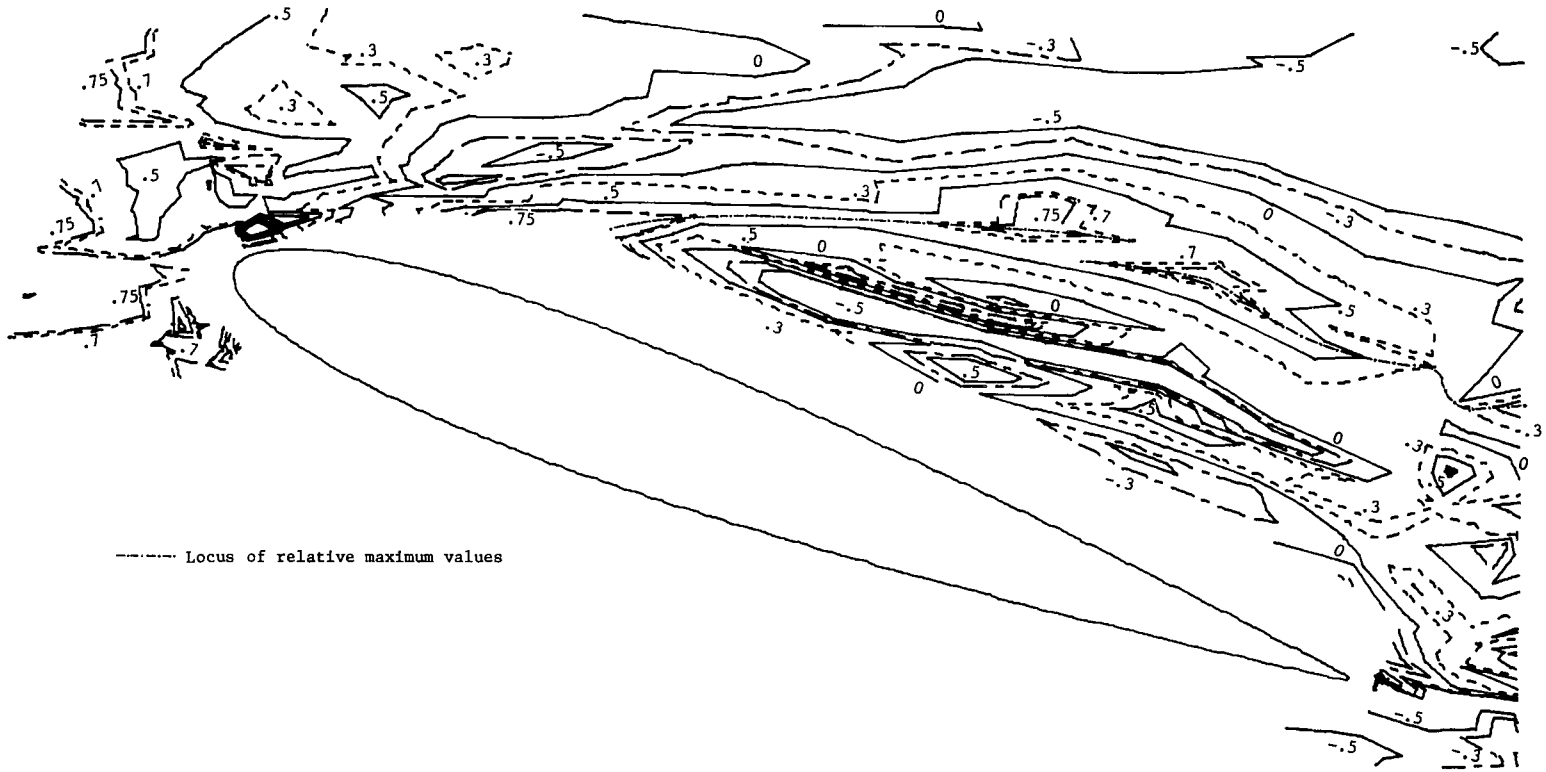

Figure 52.- Contours of constant values of skew in V_L direction.

Figure 53.- Summary of extremums of standard deviation, skew, and excess.

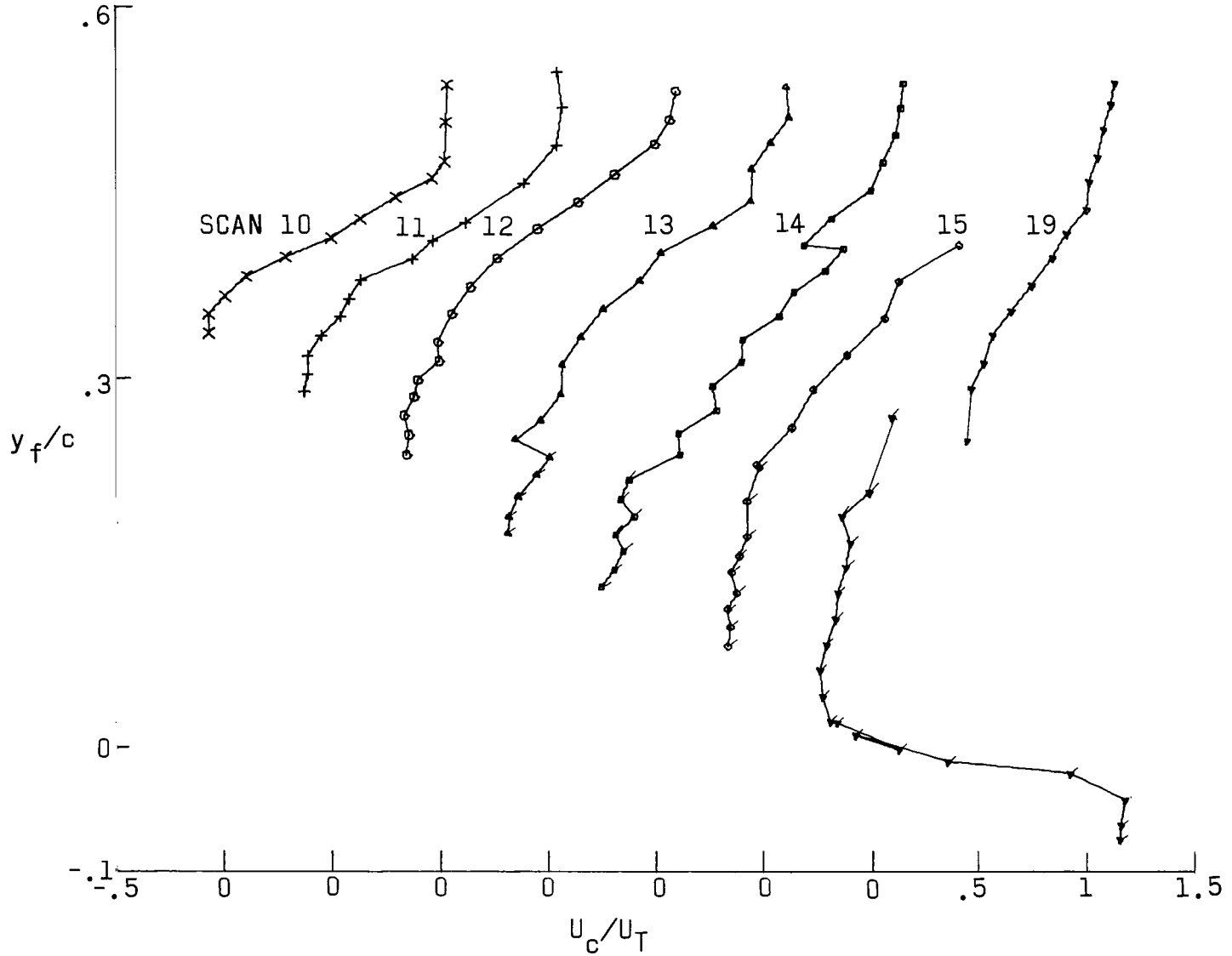

Figure 54.- Chordwise velocity profiles in free-stream coordinates.
Flagged symbols denote raised position of wing.

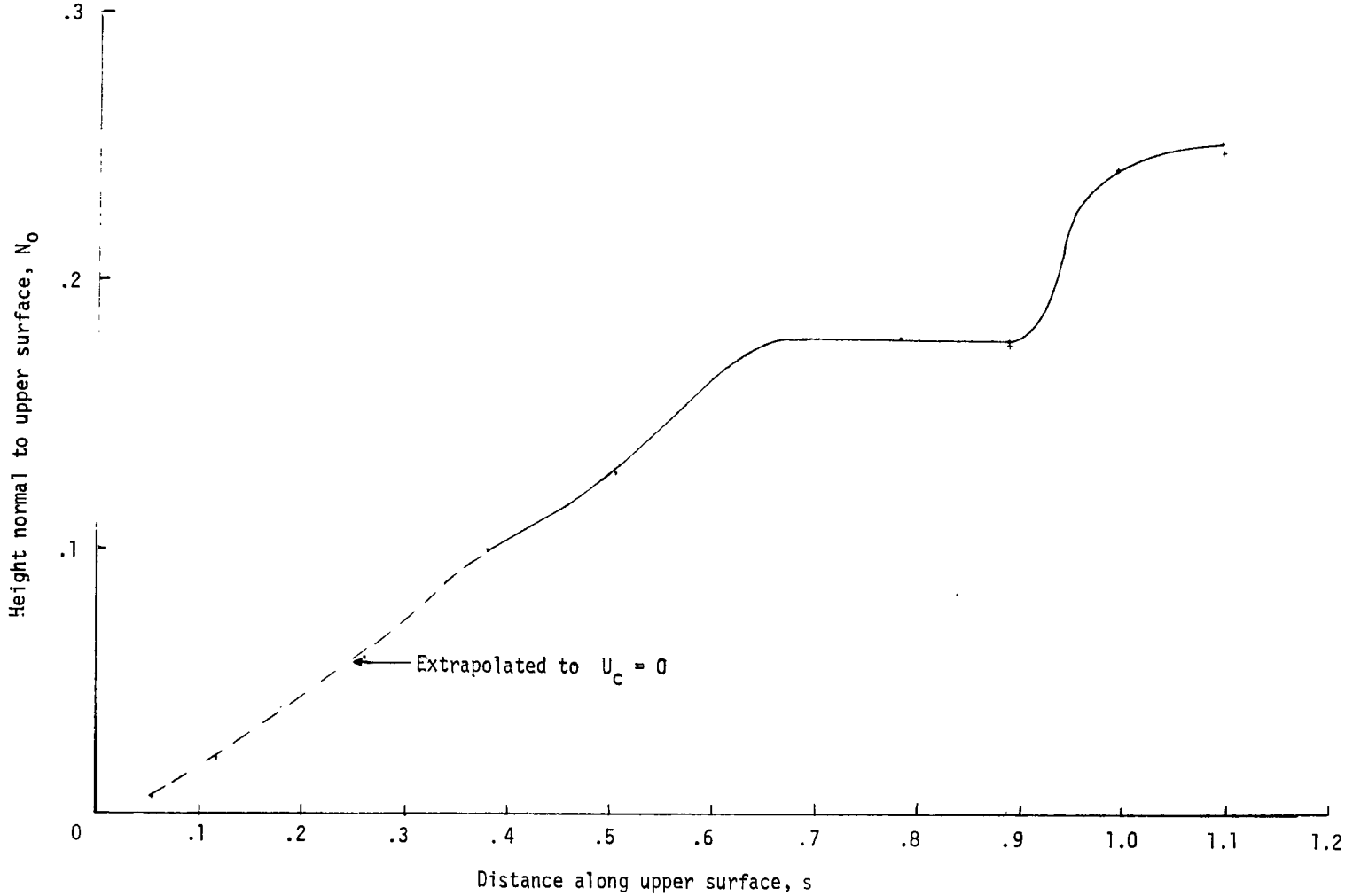

Figure 55.- Boundary of reversed velocity region defined by zero chordwise velocity.

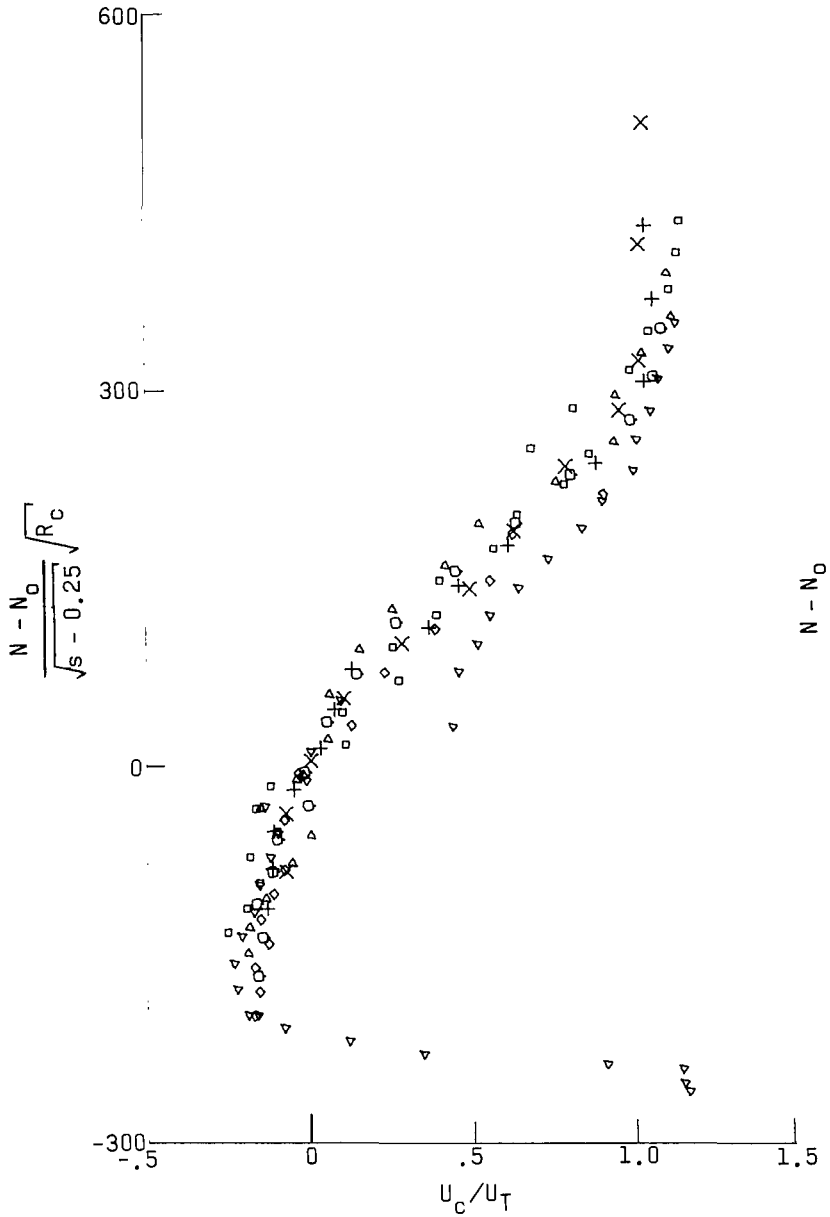

(a) Laminar similarity parameter.

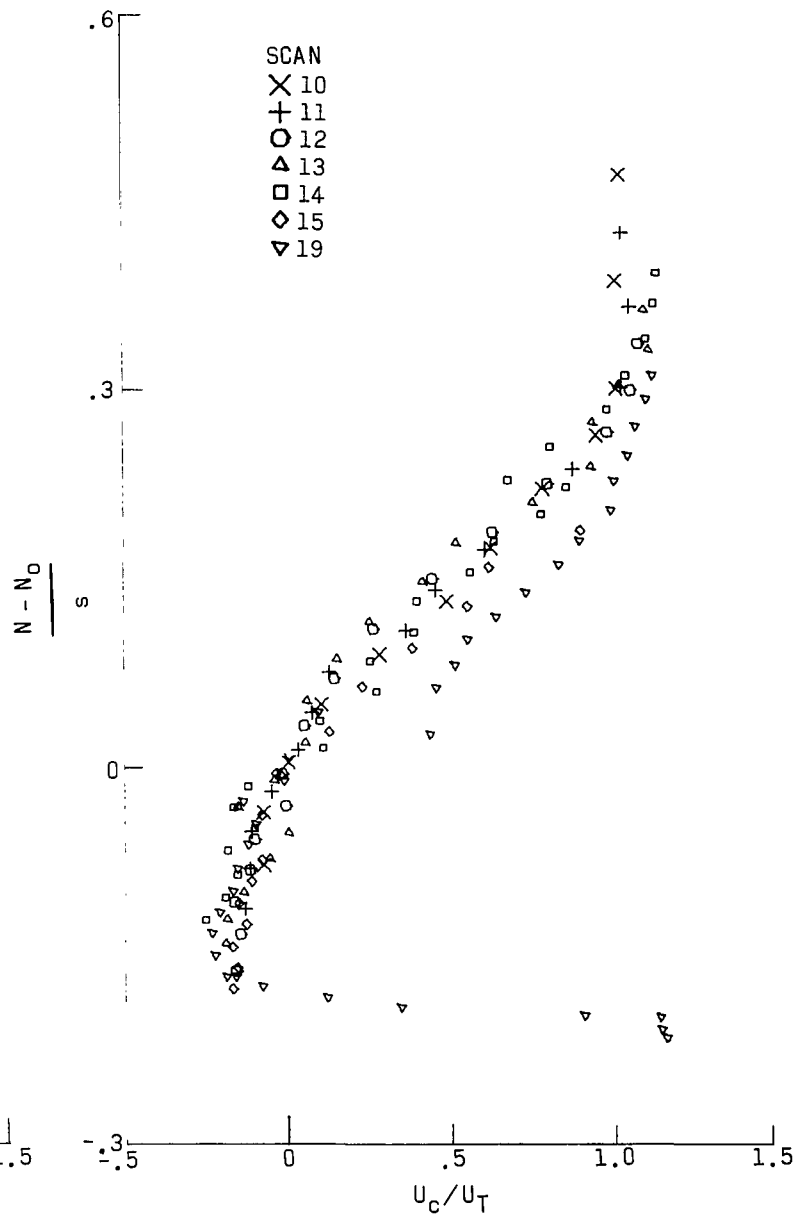

(b) Turbulent similarity parameter.

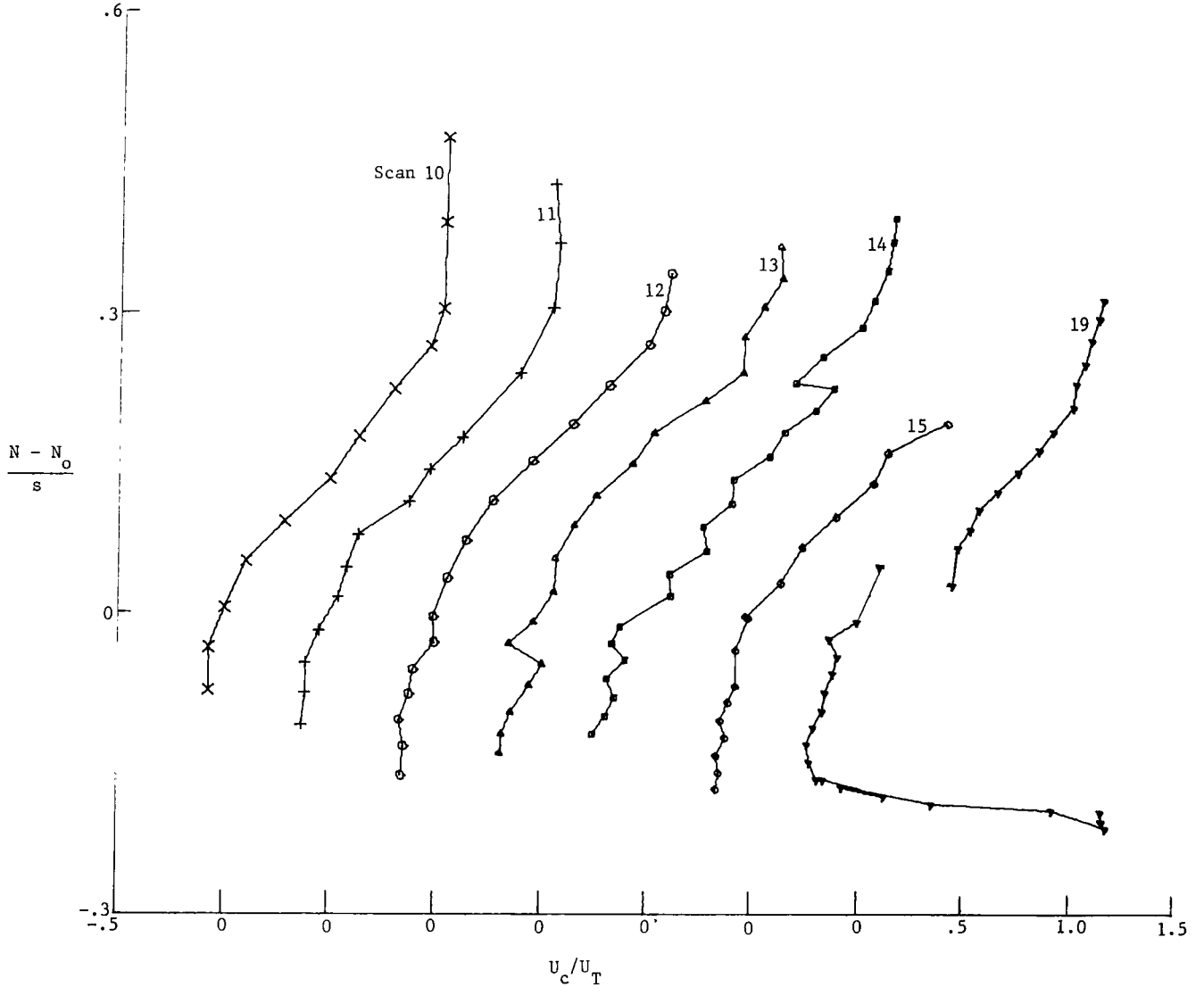

Figure 57.- Similarity of chordwise velocity profiles in mixing layer.

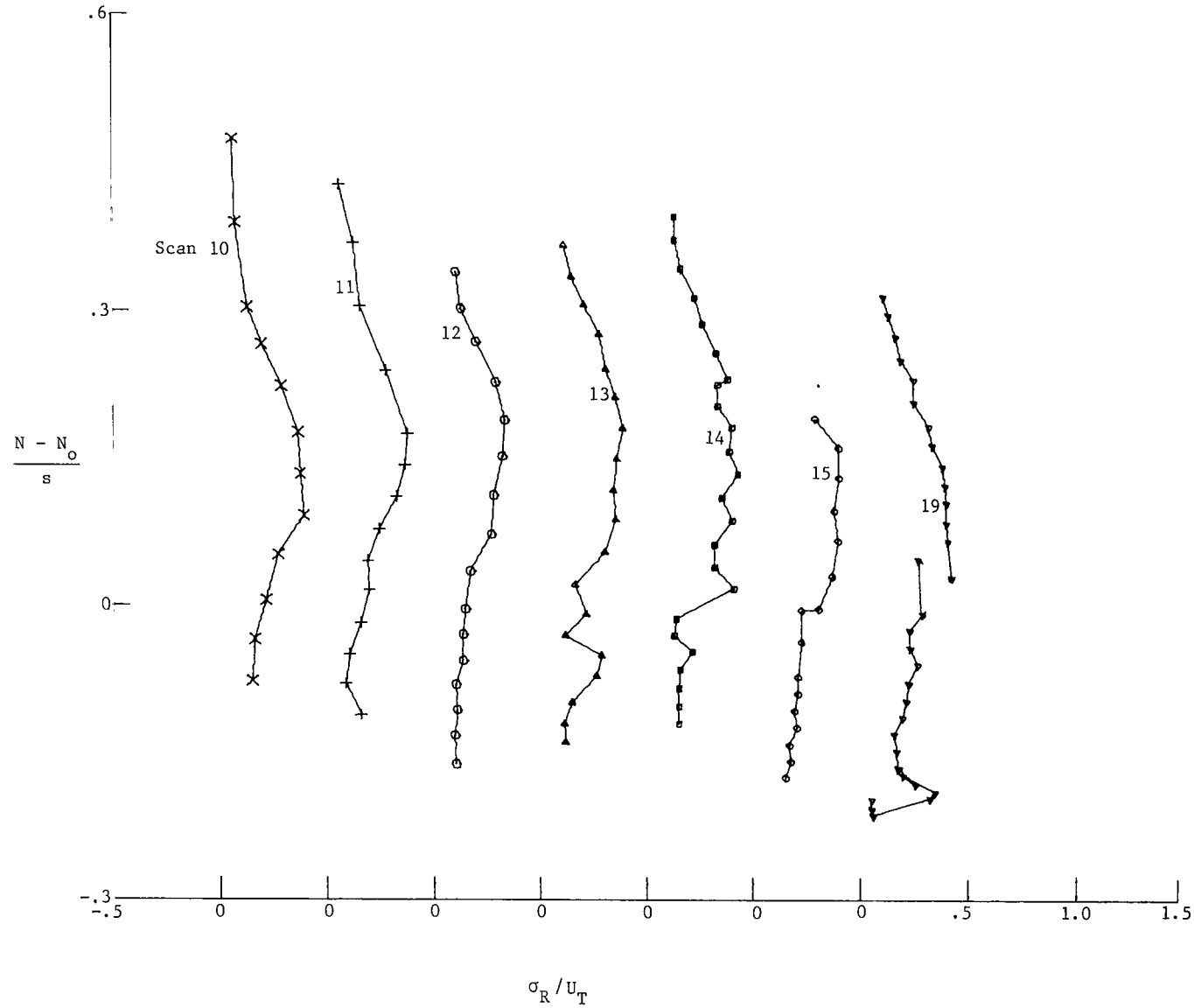

Figure 58.- Profiles of resultant standard deviation in mixing layer.

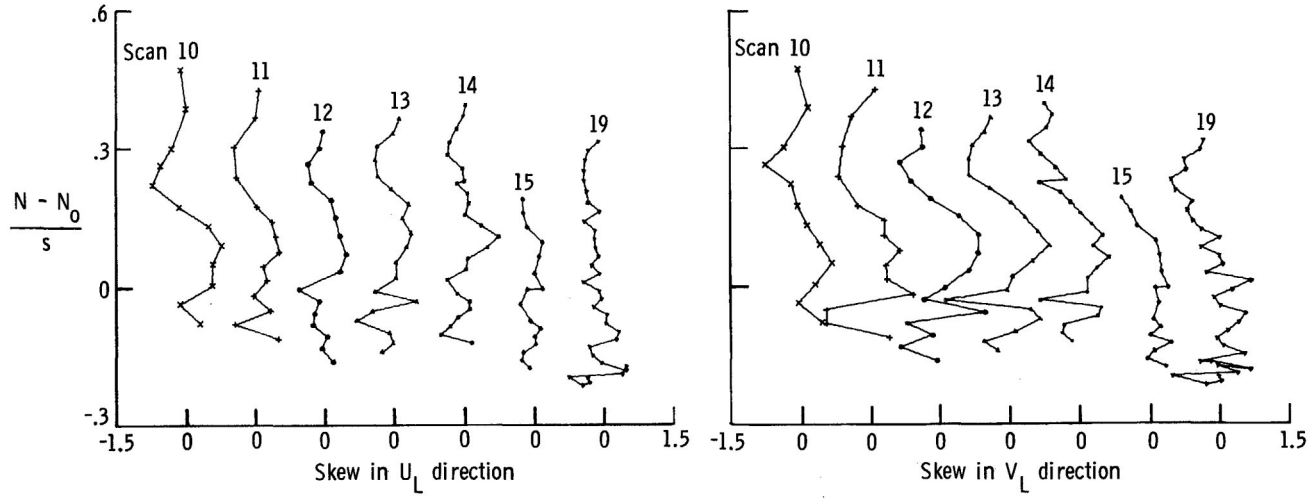

(a) Skew.

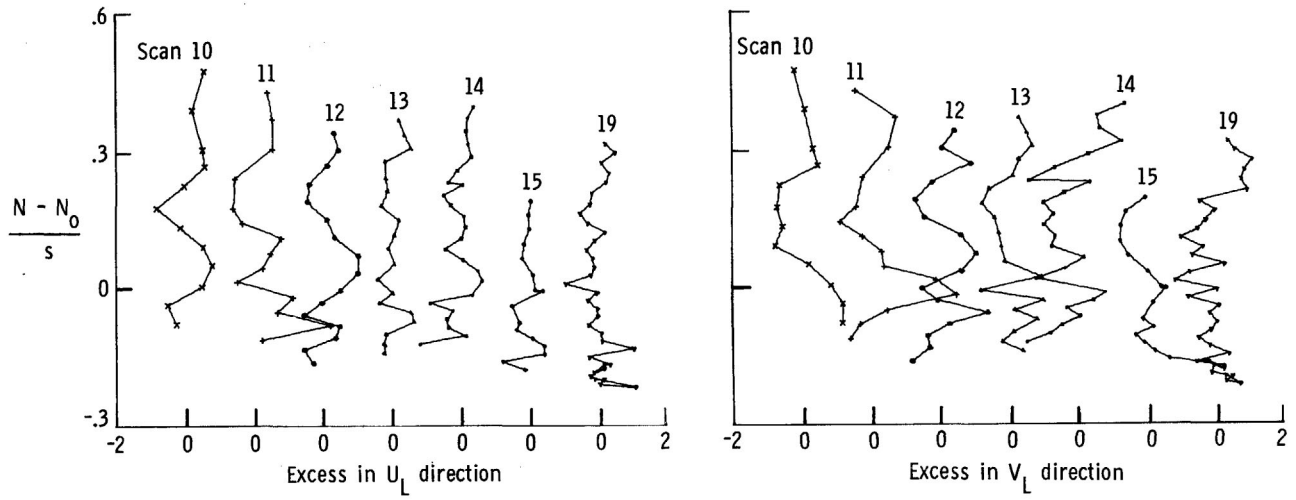

(b) Excess.

Figure 59.- Profiles of skew and excess in mixing layer.

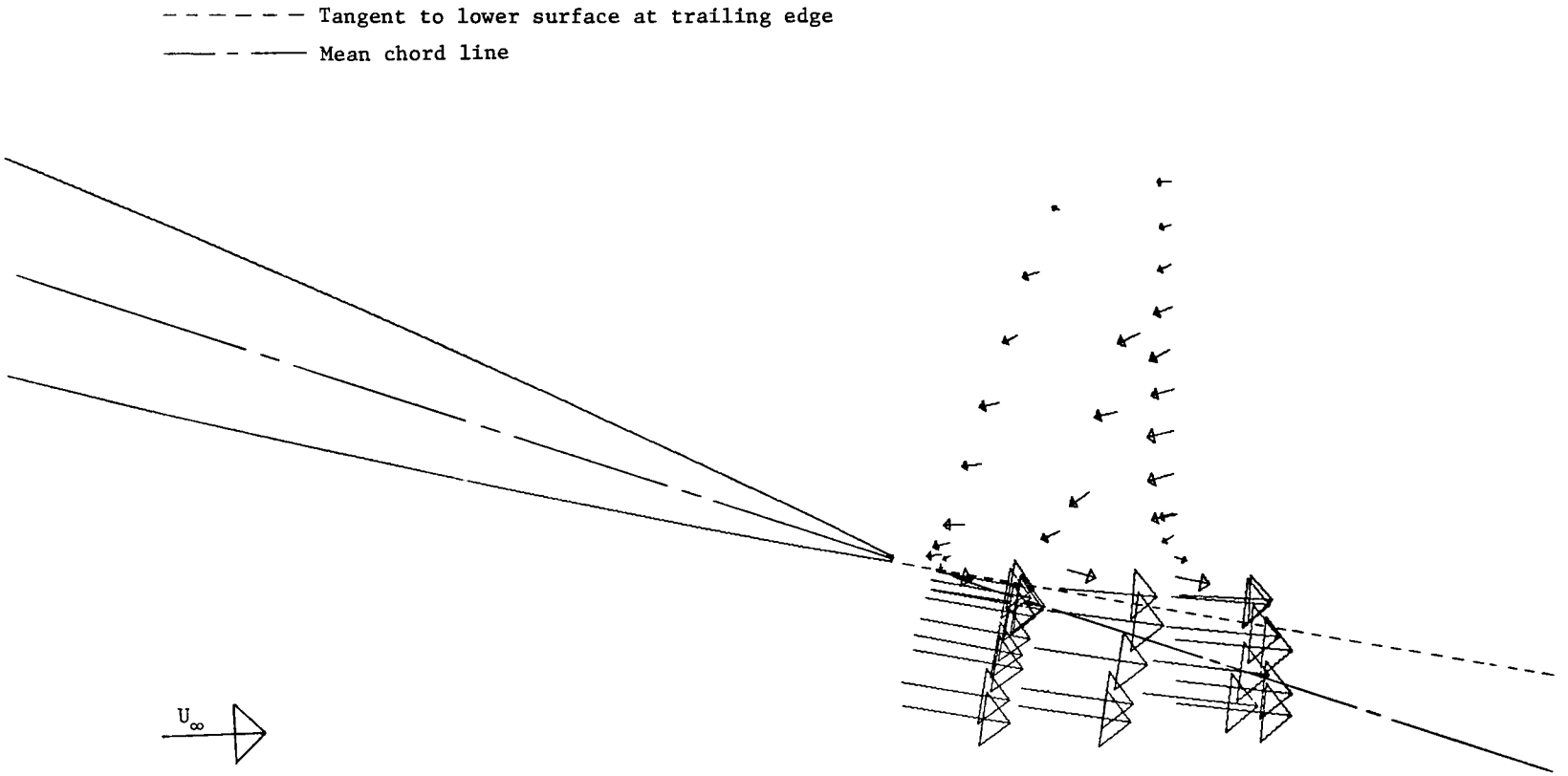

Figure 60.- Details of mean velocity behind trailing edge.

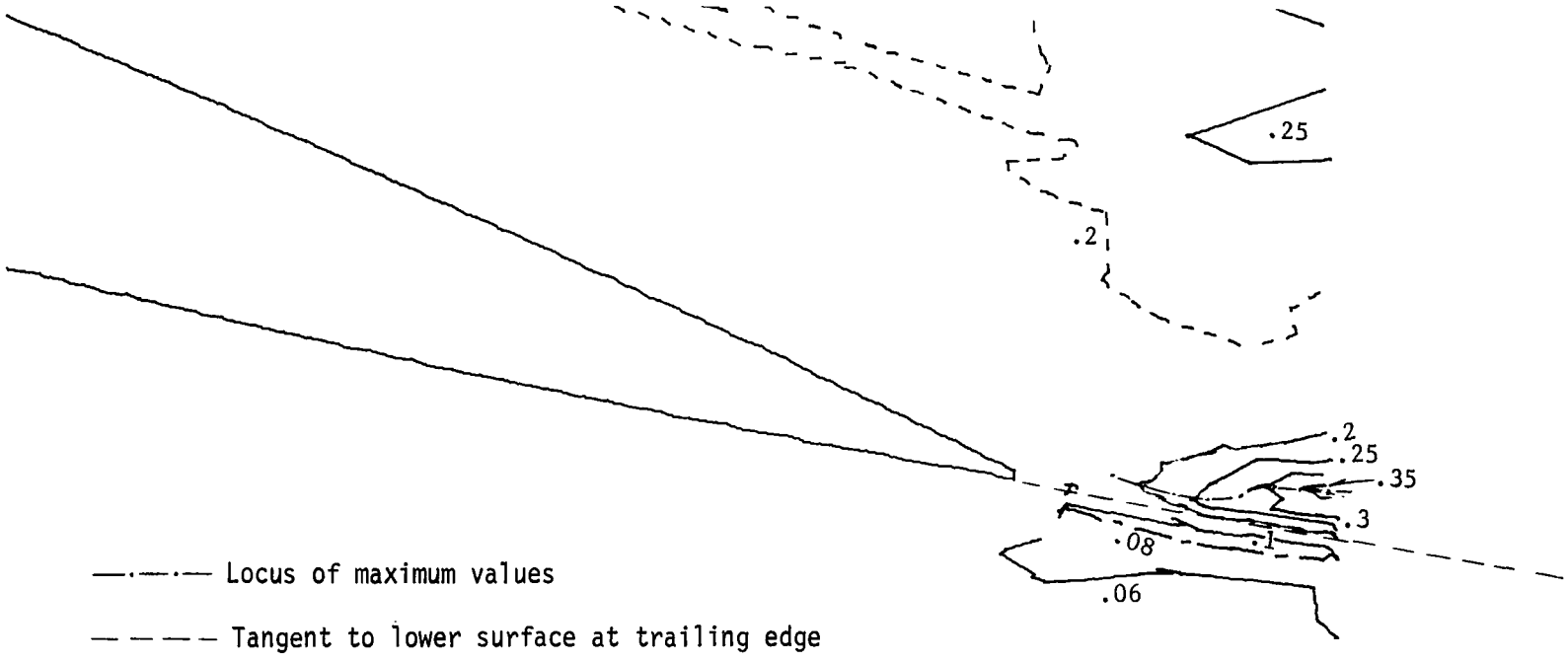

Figure 61.- Details of contours of constant resultant standard deviation behind trailing edge.

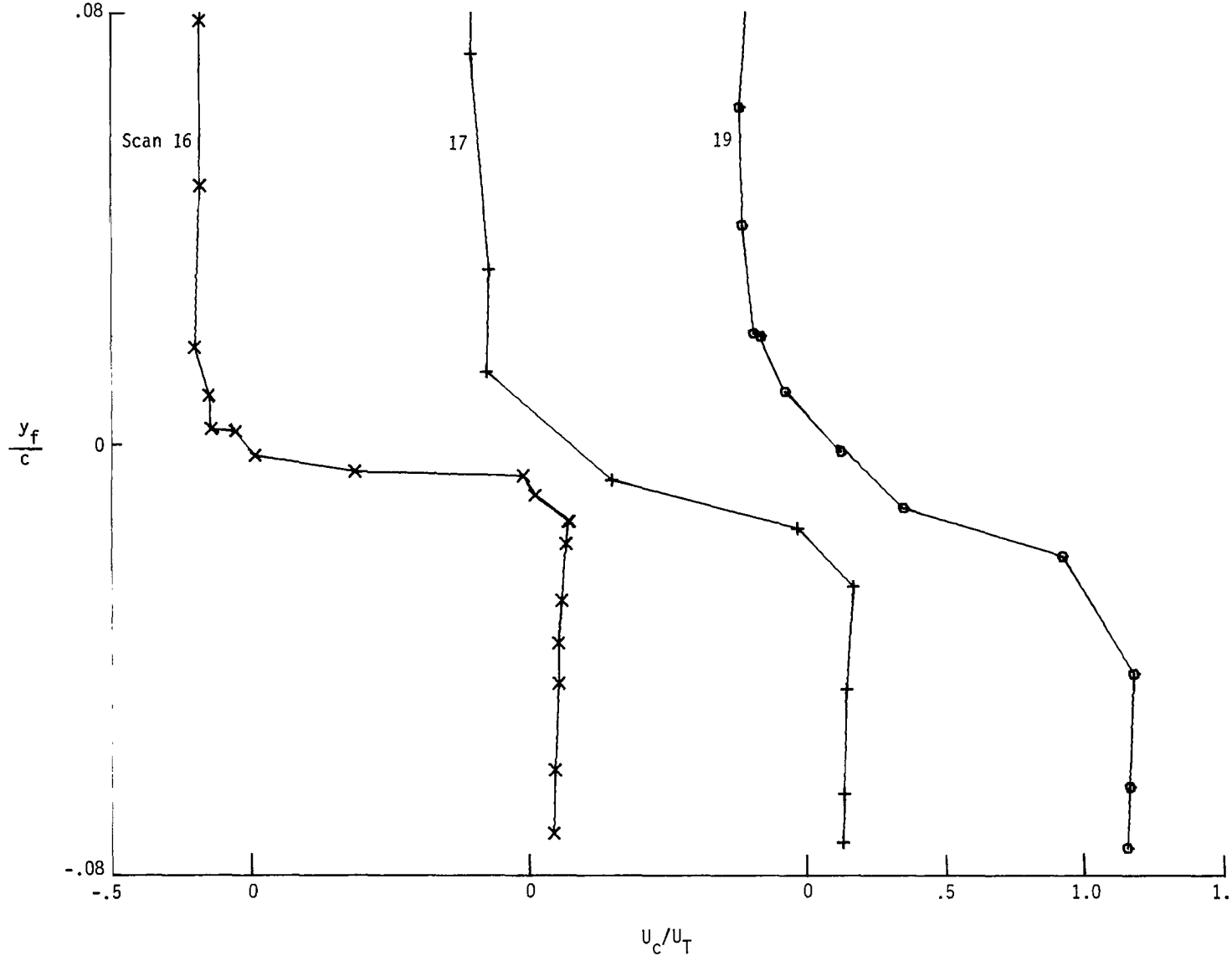
.08
Scan 16
17
19
$\frac{y_f}{c}$
0
-.08
-.5
0
0
0
.5
1.0
1.5
U_c/U_T

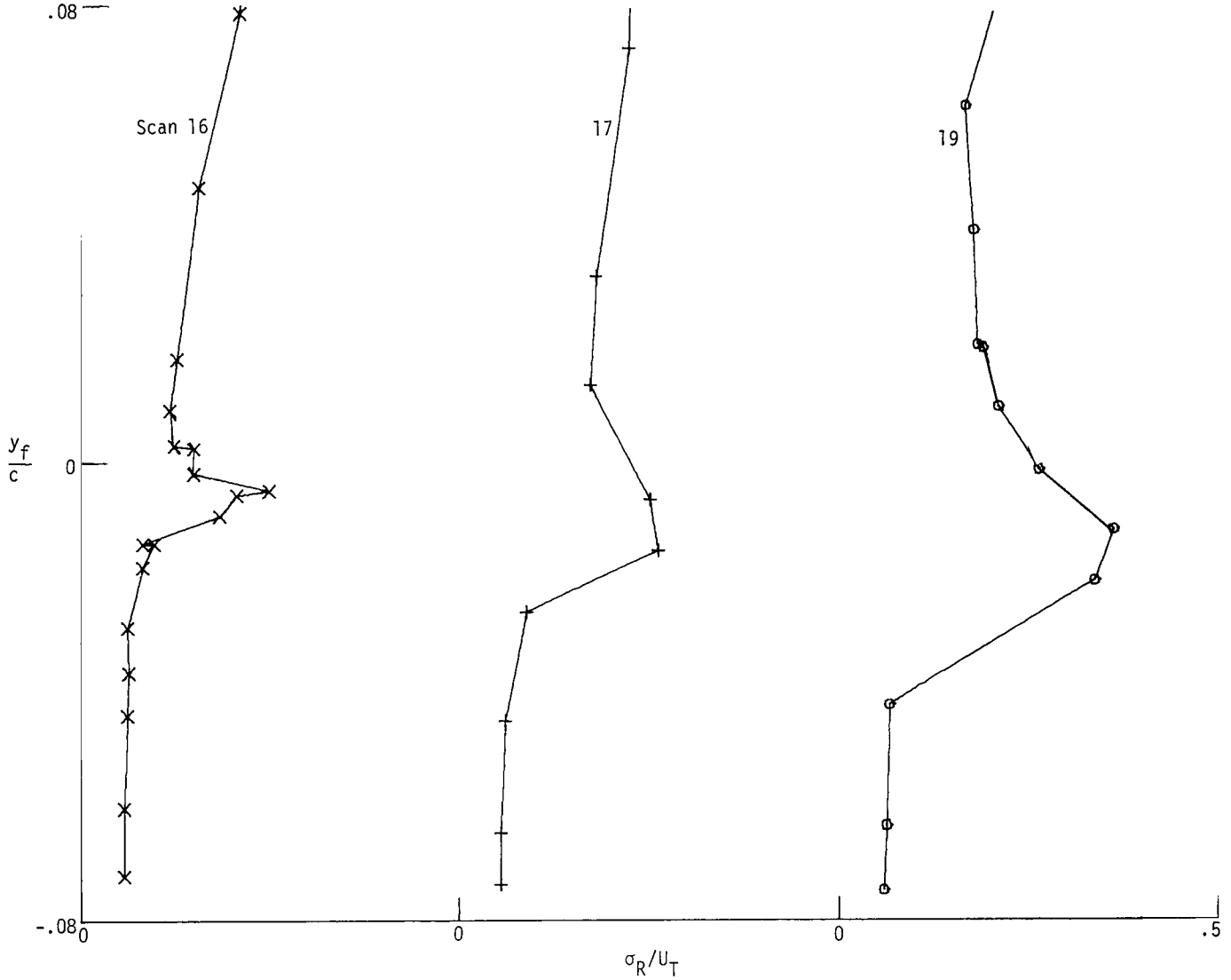

Figure 63.- Profiles of resultant standard deviation in trailing-edge wake.

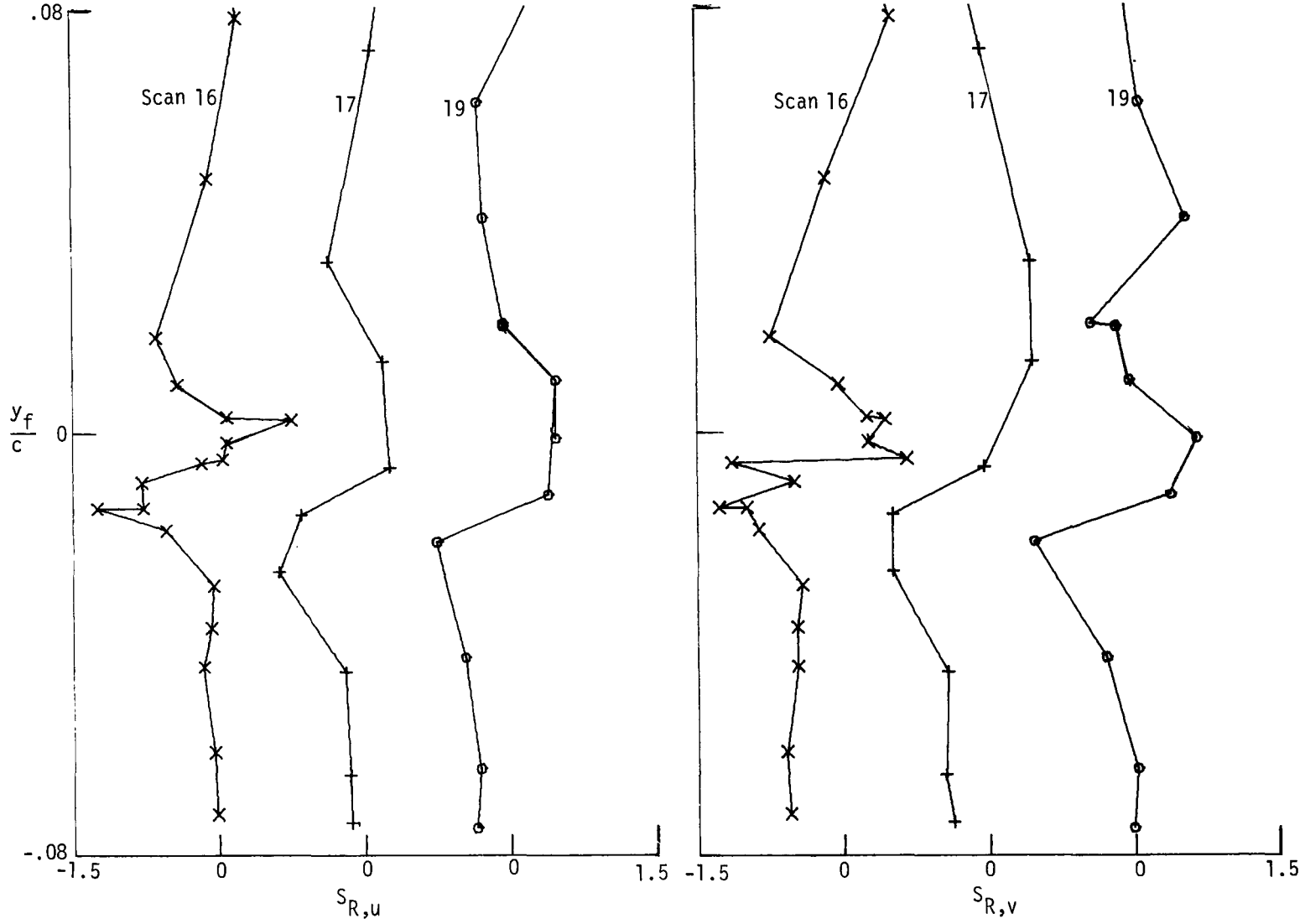

(a) U_L direction.

(b) V_L direction.

1. Report No.	2. Government Accession No.	3. Recipient's Catalog No.
NASA TP-1266 AVRADCOM TR 78-50		

4. Title and Subtitle	5. Report Date
A LASER VELOCIMETER FLOW SURVEY ABOVE A STALLED WING	December 1978
	6. Performing Organization Code

7. Author(s)	8. Performing Organization Report No.
Warren H. Young, Jr., James F. Meyers, and Danny R. Hoad	L-12262
	10. Work Unit No. 505-10-23-00

9. Performing Organization Name and Address	11. Contract or Grant No.
Structures Laboratory AVRADCOM Research and Technology Laboratories and NASA Langley Research Center Hampton, VA 23665	
	13. Type of Report and Period Covered: Technical Paper

12. Sponsoring Agency Name and Address	14. Army Project No.
National Aeronautics and Space Administration Washington, DC 20546 and U.S. Army Aviation Research and Development Command St. Louis, MO 63166	1L161102AH45

15. Supplementary Notes

Warren H. Young, Jr., and Danny R. Hoad: Structures Laboratory, AVRADCOM Research and Technology Laboratories.
James F. Meyers: Langley Research Center.

16. Abstract

A laser velocimeter operating in the backscatter mode was used to survey the flow about a stalled wing installed in the Langley V/STOL tunnel. Mean velocities and magnitudes of velocity fluctuations were calculated from measurements of two orthogonal components of velocity. Free shear mixing layers above and below a large separated flow region were defined. Velocity power spectra were calculated at two points in the flow field. The flow-field survey was carried out about a rectangular aspect-ratio-8 wing with an NACA 0012 airfoil section. The wing angle of attack was 19.4^{o}, the Mach number was 0.148, and the nominal Reynolds number was 1×10^{6}.

17. Key Words (Suggested by Author(s))	18. Distribution Statement
Laser Doppler velocimeter Velocity measurement Aerodynamic stalling Wakes Histograms	Unclassified - Unlimited Subject Category 02

19. Security Classif. (of this report)	20. Security Classif. (of this page)	21. No. of Pages	22. Price*
Unclassified	Unclassified	136	$7.25

*For sale by the National Technical Information Service, Springfield, Virginia 22161

NASA-Langley, 197

2 1 1U,A, 112078 S00903DS
DEPT OF THE AIR FORCE
AF WEAPONS LABORATORY
ATTN: TECHNICAL LIBRARY (SUL)
KIRTLAND AFB NM 87117